Doctoral Dissertation
Doctoral Program in Electrical, Electronics and Communications Engineering
(34th Cycle)

Energy harvesting of low-grade waste heat with colloid-based technology

By

Erik Garofalo

******

Supervisor(s):
Prof. Candido Fabrizio Pirri, Supervisor
Prof. Alessandro Chiolerio, Co-Supervisor

Doctoral Examination Committee:
Prof. Carlos Lodeiro Y Espiño, Referee, Universidade Nova de Lisboa
Prof. Sergey A. Suslov, Referee, Swinburne University of Technology

Politecnico di Torino
2022

Declaration

I hereby declare that, the contents and organization of this dissertation constitute my own original work and does not compromise in any way the rights of third parties, including those relating to the security of personal data.

Some of the work described in this thesis has been previously published in:

- Garofalo, E., Bevione, M., Cecchini, L., Mattiussi, F., Chiolerio, A. Waste Heat to Power: Technologies, Current Applications, and Future Potential. Energy Technology, 2020, 8, 11, 2070113, DOI: 10.1002/ente.202070113;
- Chiolerio, A., Garofalo, E., Mattiussi, F., Crepaldi, M., Fortunato, G., Iovieno, M. Waste heat to power conversion by means of thermomagnetic hydrodynamic energy harvester. Applied Energy, 2020, 277, 115591, DOI: /10.1016/j.apenergy.2020.115591;
- Garofalo, E.; Cecchini, L.; Bevione, M.; Chiolerio, A. Triboelectric Characterization of Colloidal TiO2 for Energy Harvesting Applications. Nanomaterials, 2020, 10, 1181, DOI: 10.3390/nano10061181;
- Bevione, M., Garofalo, E., Cecchini, L., Chiolerio, A. Liquid-state pyroelectric energy harvesting. MRS Energy & Sustainability, 2020, 7, E38. DOI: 10.1557/mre.2020.39;
- Chiolerio, A., Garofalo, E., Bevione, M., Cecchini, L. Multiphysics-Enabled Liquid State Thermal Harvesting: Synergistic Effects between Pyroelectricity and Triboelectrification. Energy Technology, 2021, 9, 2100544, DOI: 10.1002/ente.202100544;
- Garofalo, E., Bevione, M., Cecchini, L., Chiolerio, A. On the pyroelectric and triboelectric phenomena in ferrofluids. Advanced Materials Technologies, 2022, 2200127, DOI: 10.1002/admt.202200127.

Erik Garofalo

2022

* This dissertation is presented in partial fulfillment of the requirements for **Ph.D. degree** in the Graduate School of Politecnico di Torino (ScuDo).

I would like to dedicate this thesis to my loving parents

Acknowledgment

And I would like to acknowledge ...

Abstract

Global energy transitions, exponentially increasing population and complex high-energy societies led the world energy consumption to dramatically increase since the beginning of the 19th century. Because of thermodynamics mechanisms, in any energetic process, a part of the energy employed is always wasted, usually in the form of waste heat, locally increasing the atmospheric temperature and contributing to greenhouse gases emissions, one of the principal drivers of climate change. For these reasons, together with powered devices, several approaches for reducing energy losses have been conceived. In this work, a deep analysis of the state of the art of Waste Heat Recovery and Waste Heat to Power technology is proposed. On the other hand, advancements of materials science and cybernetic systems show that, compared to conventional robotics, colloid-based robots would offer several technical advantages. Here, energy harvesting from the external environment and internal subsystems is fundamental, in order to increase energy efficiency and autonomy level. For this purpose, in this work, the engineering feasibility of a Colloidal EneRgEtic System has been assessed, proposing a starting point to address waste heat to power and energy harvesting with nonconventional solutions, combining the nanoscale properties of solid materials and the advantages of fluids. First, a concise yet exhaustive overview of the physics and materials involved is provided. Then, the milestones of the research project are presented, from the initial conceptual idea and first prototype, its evolution, the test conducted with the main findings, to future optimizations. At last, the investigation of new colloids featuring different physical effects, for the purpose of energy harvesting, is proposed. Since the awareness of unprecedented thermophysical potential of ferrofluids, the first conceptual idea was that of a toroidal device, able to scavenge waste heat from cylindrical surfaces and convert it in electricity, exploiting a combination of thermal gradient and magnetic field to trigger a thermomagnetic advection of the ferrofluid. The first prototype was able to produce 2.9 nW with a thermal gradient of about 5 °C but its performances could be improved 1000 times with several enhancements in the design and selection of the materials employed. The complex fluid dynamics involved led us to deal with a simpler linear and planar geometry. In the linear setup, composed of a pipe and a peristaltic pump, the energy conversion capability of ferrofluid, colloidal titania and barium titanate, by means of different physical effects, was investigated using different extraction systems, accordingly. An inductive coil was employed for the ferrofluid while a capacitive

and a restistive electrode were used for the triboelectric and pyroelectric features of TiO_2 and $BaTiO_3$, respectively. The basic idea was to trigger a Rayleigh-Bénard natural convection by means of a thermal gradient coming from a source of waste heat and then convert the dynamic and thermal energy into electricity. Results show that the electromagnetic induction conversion is least efficient due to magneto viscous effects. Triboelectric conversion shows low output power but high conversion efficiency while the pyroelectric one shows interesting results up to 1 mW/m^3 with low conversion efficiency. The most surprising result is that ferrofluid shows both tribo and pyroelectric-like behaviour. The technology based on these three classes of colloids has been internationally patented for its promising application in wearable, space, domestic, automotive, housing and industrial fields.

Contents

List of Figures

List of Tables

Introduction

In this section, the context in which the current research project lies is outlined highlighting, in particular, energy and climate global issues, the state of the art of technologies trying to address them, as well as the reasons why a novelty in the field of energy harvesting is needed, giving the reader a big picture of the topic.

1.1   Energy transitions, consumption and utilisation

Energy is what powers any anthropic, biological and artificial process, at any level. In particular, any anthropogenic energy system - i.e. any arrangement whereby humans use the Earth's resources to improve their chances of survival and to enhance the quality of life (and also to increase individual and collective power, dominate and kill others) - has three fundamental components: natural energy sources, their conversions and a range of specific uses. In the past, the simplest systems used a small number of sources and inefficient energy conversions for basic and precarious subsistence, while modern systems can draw energy from many natural sources, convert and use it in many and efficient ways in order to power complex high-energy societies. After the conversion of food into muscular power, a segment of naturally cascading energy degradations from solar radiation to dissipation of heat during walking, running, and gathering food, our hominid ancestors used the first extrasomatic energy conversion nearly 800,000 years ago by mastering the control of fire. In contrast, modern societies tap many natural energy stores and flows, convert them by using technologically advanced devices, and use them for purposes ranging from intensive food production to rapid long-distance travel. Nowadays, global final per capita energy consumption ranges over two orders of magnitude, from the miseries of the sub-Saharan Africa to the excesses of the richest urban societies of America, Europe, and Asia. Moreover, in the wealthiest societies even the average per capita energy use is well beyond the level required for healthy and comfortable living (1).

Energies used by current human societies can be classified according to their origins as renewable and non-renewable. Renewable energies include:

- solar radiation and all of its biospheric transformations: phytomass formed by photosynthetic conversion; wind, arising from pressure

gradients created by differential heating of the ground; moving water originating in radiation-driven evaporation and precipitation or as wind-driven waves and ocean currents; thermo-haline gradients in the oceans;

- geothermal energy: the Earth's heat generated by the decay of isotopes (1).

On the other hand, fossil fuels are by far the most important non-renewable form of energy: coals and most hydrocarbons (crude oils and natural gases) are transformations of ancient biomass, buried in sediments and processed by high pressures and temperatures (for millions to hundreds of millions of years). All fossil fuels share the dominant presence of carbon, whose content ranges from nearly 100% in the best anthracite coals to 75% in methane. At the same time, certainty level regarding resources of fossil fuels is not high, and their reserves keep changing as new techniques lower their extraction cost to the point that previously uneconomical deposits become profitable sources of energies (as we see for shale oil and gas). Finally yet importantly, nuclear energy can be produced either by fission of the isotopes of the heaviest natural elements or by fusion of the lightest ones (a process with, up to now, a difficult commercial realization). Since the late 1950s, commercial nuclear stations employed uranium fission to generate electricity by the same means as in fossil-fuelled turbine stations (1).

Energy systems have evolved over time. If, during the preindustrial era only very slow changes in the primary energy supply (dominated by biomass fuels) and in the use of prime movers[1] (dominated by human and animal muscles) occurred, the last two centuries were characterized by a series of remarkable energy transitions. In fact, stasis and stagnation, minimal adjustments and slow innovations marked the entire preindustrial era, while the industrialization and the evolution of post-industrial societies have been marked by rapid diffusion of new inventions and widespread adoption of technical and organizational innovations. As a result, nearly 5000 years of preindustrial history relied on inefficiently burned biomass fuels for heating households, metallurgy, and artisanal manufactures, and by applications of human and animal muscles to provide mechanical energy (sails being the only early exception). The condition did not change essentially even during the early modern era (1500-1800 AC) when some Western European societies began a small-scale

---

[1] Energy converters able to produce kinetic (mechanical) energy in forms suitable for human uses. Human muscles (somatic energy) were the only prime movers (converting chemical energy in food to kinetic energy of walking, running, and countless manual tasks) until the domestication of animals provided more powerful animate prime movers used in fieldwork, transportation, land for some industrial tasks. (1)

extraction of peat while adopting more efficient and powerful water wheels and windmills. The two fundamental transitions, from biomass to fossil fuels and from animate to inanimate prime movers, have taken place only during the last three centuries (in the case of some European societies) or just roughly 50 years ago (in China's and India's case), and the emergence of electricity began only during the 1880s. Inevitably, these transitions, from small local scales, became truly global phenomena (1). Together with an exponentially increasing global population and the formation of complex high-energy societies, as reported by a study performed by Vaclav Smil and displayed in the book "*Energy Transitions: History, Requirements, Prospects*", the global consumption of energy has been following a monotonic increasing trend since the beginning of the 19th century. Since the post-World War II era (1950s), because of the enhancing widespread life standards and with the advent of increasing accessible and sophisticated technologies, this growth has considerably increased its speed (Figure 1).
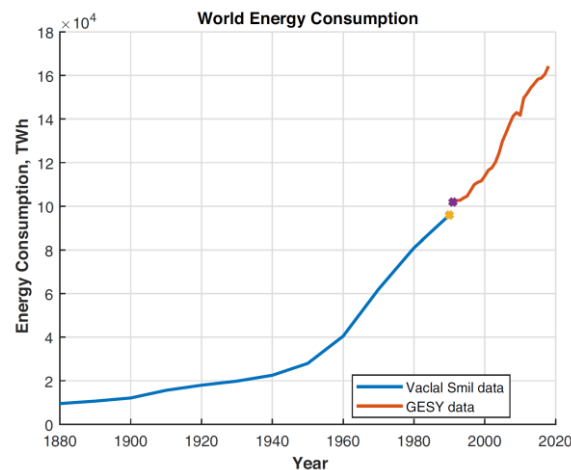
Figure 1: World energy consumption over the last 140 years.[2]

Nowadays, according to the IPCC, one-third of the global energy consumption derives from the industry (corresponding approximately to over 40% of CO_2 emissions worldwide) (2) (3). Data show that in UK industries demand about 3200 TWh per year, which represents about 26% of the total consumption in EU (Eurostat, 2015), while Germany, Italy, France, UK, and Spain, all together accounts for a total amount of about 60% as shown in Figure 2 (4). Analyzing the

---

[2] Coal, crude oil, natural gas, hydroelectricity, nuclear electricity and biofuels have been taken into account until 1990 (blue line). Then, the data provided by the Global Energy Statistical Yearbook (red line) conclude the trend until nowadays and because of the higher precision and comprehensiveness, there is a slight mismatch between the two curves across 1990.

energy utilisation in the industrial sector of the EU28 (member states of the EU before Brexit) (5), it comes out that chemical and steel industries are the main energy-demanding sectors, followed by paper processing, nonmetallic minerals treatment, and food, accounting for about 65% of the total energy consumption in the industry. On the other hand, road freight vehicles and passenger cars play an essential role in today's global economic activity, energy consumption, and environmental impact. According to the International Energy Agency (IEA), transport accounts for more than half of the oil global demand, totaling around 52 million barrels of oil per day (Considering Barrel of Equivalent Oil (BOE) corresponding to 88 TWh per day (6). Furthermore, the global fuel consumption for high-duty vehicles is increasing more rapidly than any other transport mode, especially in emerging markets such as India, China, and Latin America (7).
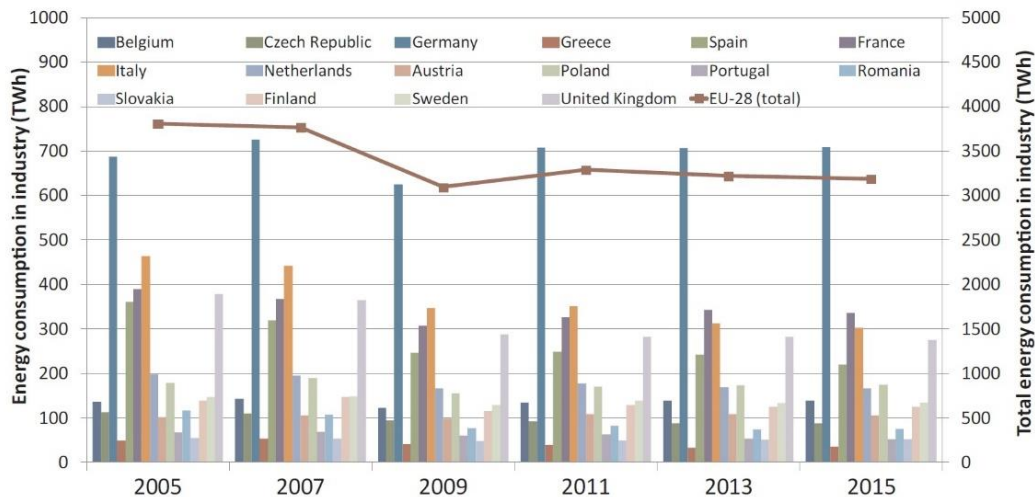
Figure 2: Energy consumption in industry according to the different EU countries and in total (4). Reproduced under the terms of the CC BY NC ND License.

Consequently, energy-related issues, including the location and exploitation of resources, the costs of extraction, transformation, and distribution, accessibility and demand, as well as awareness about use and consumption, are of paramount importance at this moment in time. The governments of every developed nation are increasingly funding research program to evaluate how to overcome these needs. Three key examples of this are 1) the International Energy Outlook 2019 delivered by the US Energy Information Administration, 2) the independent assessment issued by the UK Committee on Climate Change by request of the UK government, and 3) the European Green Deal for a climate neutral EU within 2050, with a plan to invest 1 trillion EUR. Therefore, action plans are required by virtuous

governments to support innovation and make it easier to access financial resources (8). As an example, the world's largest fund manager, BlackRock (close to 2.64 trillion EUR), announced to the US Securities and Exchange Commission the launch of a money-market fund, primarily investing in developed environmental practices (9). In fact, anthropogenic energy systems have a huge environmental impact, from locally devastating deforestation to global changes of the atmospheric composition: most of all, the greenhouse gases (GHGs) emissions coming from fossil fuel combustion that have been the cause of increasing tropospheric temperatures, acid deposition, photochemical smog, and higher ground ozone levels. Although some highly damaging processes have been either completely eliminated or reduced to acceptable levels (e.g. surface coal extraction and flue gas desulfurization), others are yet to be accounted into the real cost of energy.[3]

1.2   Climate action: approaches to fight climate change

The Intergovernmental Panel on Climate Change (IPCC) is the United Nations body for evaluating the science related to climate change. IPCC prepares comprehensive Assessment Reports (AR) about the state of scientific, technical and socio-economic knowledge on climate change, its impacts and future risks, and options for reducing the rate at which climate change is happening. The Working Group I (WGI) contribution to the Sixth Assessment Report (AR6 Climate Change 2021: The Physical Science Basis) addresses the most up-to-date physical understanding of the climate system and climate change. It brings together the latest advances in climate science, and combines multiple lines of evidence from paleoclimate, observations, chemical and biological climate process understanding, and global and regional climate simulations. AR6 WGI assesses new scientific evidence relevant for a world whose climate system is rapidly changing, overwhelmingly due to human influence. The five IPCC assessment cycles since 1990 have comprehensively and consistently determined the rapidly accumulating proof of a changing climate system, with the Fourth Assessment Report (AR4) in 2007 being the first to conclude that warming of the climate system is unequivocal. Sustained

---

[3] All energy systems require infrastructures and their operation consumes considerable amounts of energy. Energy infrastructures comprise not only tangible components (e.g. high-voltage transmission lines or pipelines) but also intangible organizational and managerial arrangements for extracting, storing, and processing fuels and harnessing energy flows. Energy cost is a critical determinant of the viability of any energy system as only high-energy returns can create affluent societies with plenty of time left for leisure. These unavoidable costs of energy are not measured in energy terms but are monetized as capital and operating costs. (1)

changes have been recorded in all the main elements of the climate system: the atmosphere, land, cryosphere, biosphere and ocean. Multiple lines of evidence point out that the recent large-scale climatic changes are unprecedented in a multi-millennial context, and that they represent a millennial-scale commitment for the slow-responding elements of the climate system, resulting in continued worldwide loss of ice, increase in ocean heat content, sea level rise and deep ocean acidification (10). Earth's climate system has evolved over many millions of years, and evidence from natural archives offers a long-term perspective on observed and projected changes over the coming centuries. Global surface temperature has evolved over geological time: beginning approximately 6500 years ago, global surface temperature generally decreased, culminating in the coldest multi-century interval of the post-glacial period (since roughly 7000 years ago), which occurred between around 1450 and 1850 (the so called "Little Ice Age"). Over the last 50 years, global surface temperature has increased at an observed unprecedented rate in the last two thousand years, and probably no multi-centennial period after the Last Interglacial (roughly 125,000 years ago) was warmer globally than the most recent decade. During the mid-Pliocene Warm Period (Figure 3), around 3.3-3.0 million years ago, global surface temperature was 2.5-4 °C warmer, and during the Last Interglacial, it was 0.5-1.5 °C warmer than 1850-1900.
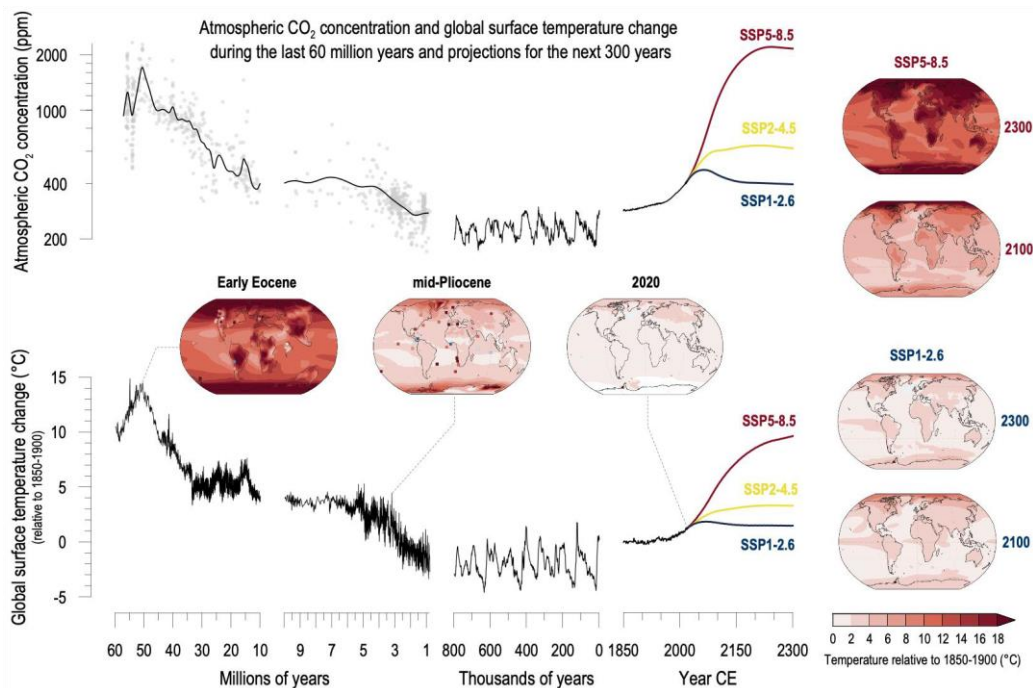
Figure 3: Changes in atmospheric CO_2 and global surface temperature (relative to 1850-1900) from the distant past to the next 300 years (10). Reproduced with permission.

Reconstructions of past climate also reveal that atmospheric CO_2 concentrations and global surface temperature are strongly coupled (Figure 3), based on evidence from a variety of proxy records over multiple time scales. From these data and considering the current socio-economic and environmental scenario, climate projections show that levels of global warming[4] that have not been seen in millions of years could be reached by 2300, depending on the emissions pathway that is followed[5], including high-CO_2 emissions pathways without climate change mitigation as well as new low-CO_2 emissions pathways (10).

Understanding of the climate system's fundamental elements is robust and well established. Scientists in the 19th century identified the major natural factors influencing on the climate system and the main natural drivers of climate change, including variations in incoming solar radiation, volcanic activity, orbital cycles, and changes in global biogeochemical cycles, have been analysed systematically since the early 20th century. They also hypothesized the possible cause for anthropogenic climate change being the carbon dioxide (CO_2) emitted by combustion of fossil fuels (petroleum, coal, natural gas) and other major anthropogenic drivers, such as atmospheric aerosols (fine solid particles or liquid droplets), land-use change and non-CO_2 greenhouse gases, were identified by the 1970s. Since systematic scientific assessments began in the 1970s, the influence of human activity on the warming of the climate system has evolved from theory to established fact. Evidences fortified from the IPCC AR1 in 1990 to the IPCC AR5 in 2013/14, and is now even stronger in the last IPCC AR6 and now, changes across a greater number of climate system components, including changes in regional climate and extremes can be ascribed to human influence. Human effect in the IPCC context refers to the human activities that lead to or contribute to a climate response, such as the human-induced emissions of greenhouse gases, which alter the atmosphere's radiative properties and warm the climate system. Other human activities influencing climate include the emission of aerosols and other short-lived

---

[4] Global warming refers to the change of global surface temperature relative to a baseline. Specific global warming levels, such as 1.5°C, 2°C, 3°C or 4°C, are defined as changes in global surface temperature relative to the years 1850–1900 as the baseline (the earliest period of reliable observations with sufficient geographic coverage). (10)

[5] Five scenarios based on the Shared Socioeconomic Pathways (SSPs, referred to as SSPx-y) are used consistently across the IPCC AR6 WGI: SSP1-1.9, SSP1-2.6, SSP2-4.5, SSP3-7.0, and SSP5-8.5. "SSPx" refers to the SSP describing the socio-economic trends underlying the scenario and "y" refers to the approximate target level of radiative forcing resulting from the scenario in the year 2100. "Radiative forcing" refers to the change in the net, downward minus upward, radiative flux (in W m^{-2}) due to a change in an external driver of climate change, such as a change in the concentration of carbon dioxide (CO_2), the concentration of volcanic aerosols or in the output of the Sun. (10)

climate forcers (substances with a relatively short lifetime in the atmosphere compared with CO_2, e.g. methane and ozone (11), and land-use change such as urbanisation. Progresses in our understanding of human influence is gained from longer observational datasets, improved paleoclimate information, a stronger warming signal since AR5, and improvements in climate models, physical understanding and attribution[6] techniques through a wider range of climate variables and climatic impact-drivers[7] (CIDs). Furthermore, new methods and analyses drawing from several evidence have provided high confidence in attributing changes in regional weather and climate extremes to human influence (Figure 4).
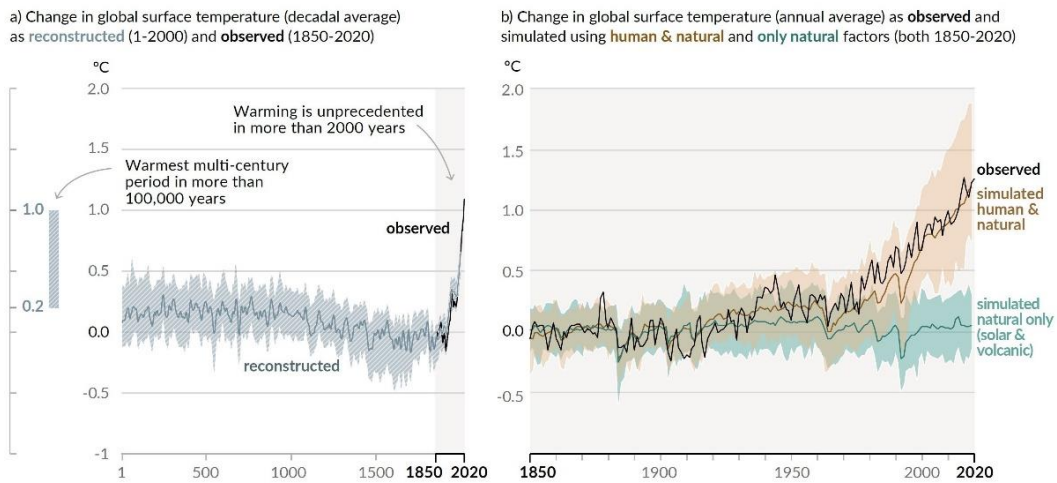
Figure 4: Changes in global surface temperature relative to 1850-1900 (10). Reproduced with permission.

In AR6, global surface temperature during the period of 1850-1900 is used as an approximation for pre-industrial conditions, although recognizing that radiative forcing have a baseline of 1750 for the start of anthropogenic influences. Likely, there was a net anthropogenic forcing in 1850-1900 relative to 1750, linked to a

---

[6] The process of evaluating the relative contributions of multiple causal factors to an observed change in climate variables (e.g., global surface temperature, global mean sea level change), or to the occurrence of extreme weather or climate-related events. Attributed causal factors include human activities (such as increases in greenhouse gas concentration and aerosols, or land-use change) or natural external drivers (solar and volcanic influences), and in some cases internal variability. (10)

[7] Physical climate system conditions (e.g., means, events, extremes) that can be directly connected with having impacts on human or ecological systems are described as 'climatic impact drivers' without anticipating whether their impacts are detrimental (i.e., as for hazards in the context of climate change risks) or provide potential opportunities. (10)

change in global surface temperature of around 0.1 °C, with an anthropogenic component of 0.0-0.2 °C. Later, global surface temperature has increased by 1.09 °C from 1850-1900 to 2011-2020, with a likely range of human-induced warming in global surface temperature of 1.07 °C, while the change attributable to natural forcing is only ±0.1 °C (10).

Climate change projections with climate models need information about future emissions or concentrations of greenhouse gases, aerosols, ozone depleting substances, and land use over time. This information can be estimated by means of scenarios, which are internally consistent projections of these quantities based on assumptions of how socio-economic systems could evolve over the 21st century. Scenarios are used as a method for systematically examining possible futures and allow to follow the cause-effect chain (Figure 5): from anthropogenic emissions, to changes in atmospheric concentrations, to variations in the Earth' energy balance ('forcing', both anthropogenic and natural), to changes in global climate and ultimately regional climate and climatic impact-drivers. Carbon cycle and non-CO_2 biogeochemical feedbacks also influence the ultimate response to anthropogenic emissions. In the AR6, scenario-based climate projections are translated into global warming levels (GWLs) which are closely related to cumulative CO_2 emissions. In fact, as anticipated in Figure 3, a near-linear relationship exists between cumulative CO_2 emissions and the resulting increase in global surface temperature. This implies that continued CO_2 emissions will cause further warming and associated changes in all components of the climate system. Cumulative CO_2 emissions also provide a link to the assessments of mitigation options (10).
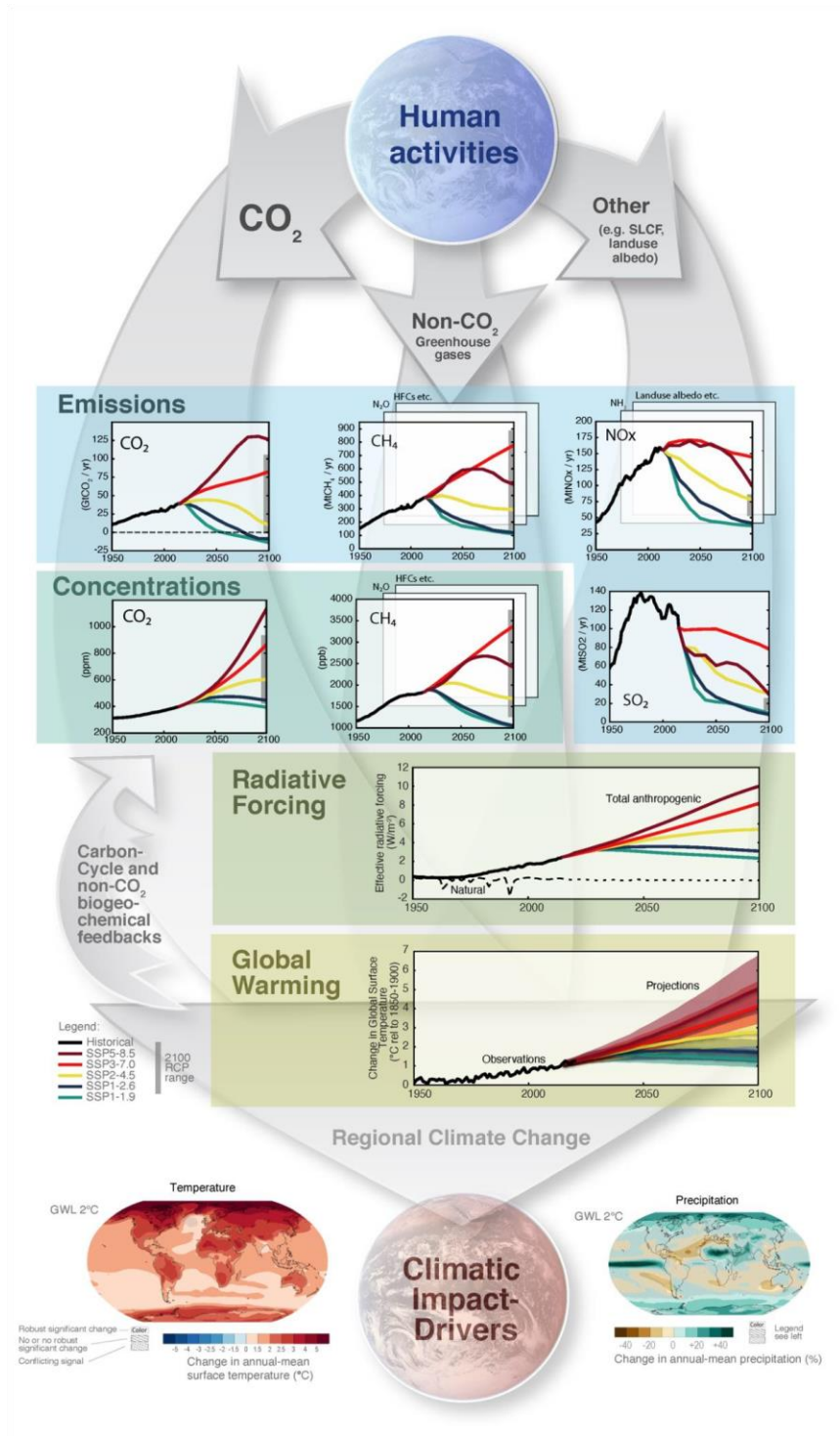
Figure 5: The climate change cause-effect chain. The five SSP scenarios as well as emission and concentration ranges for the previous representative concentration pathways (RCP) scenarios in year 2100 are shown (10). Reproduced with permission.

Since 1750, changes in the drivers of the climate system are dominated by the warming influence of increases in atmospheric GHG concentrations and a cooling influence from aerosols, both coming from anthropogenic activities. By comparison, long-term influence from solar activity and volcanoes has been negligible. Global concentrations of human aerosols peaked in the late 20th century and have slowly declined since in northern mid-latitudes, although they continue to increase in South Asia and East Africa. Concentrations of CO_2, CH_4, and N_2O have increased to levels unprecedented in at least 800,000 years, and current CO_2 concentrations have not been experienced for at least 2 million years (Figure 6a). Although atmospheric CO_2 concentrations have changed substantially over millions of years (Figure 3), during 1750-2019 CO_2 increased by 131.6 ppm (47.3%) and the centennial rate of change of CO_2 since 1850 has no precedent in at least the past 800,000 years, while the fastest rates of change over the last 56 million years were at least a factor of 4 lower than over 1900-2019. Several high-accurate surface observations show that concentrations of CO_2 have exceeded 400 ppm, reaching 409.9 ppm in 2019 (Figure 6c). In the same year, concentrations of CH_4 reached 1866.3 ppb (Figure 6c) with an increase since 1750 of 1137 (157.8%) that far exceeds the range over multiple glacial-interglacial transitions of the past 800,000 years. In the 1990s, CH_4 concentrations plateaued, but started to increase again around 2007 at an average rate of 7.6 ppb yr^{-1}. There is high confidence that this recent growth is largely driven by emissions from fossil fuel exploitation, livestock, and waste, with El Niño-Southern Oscillation (ENSO) driving multi-annual variability of wetland and biomass burning emissions. Since 1750, N_2O increased by 62.0 ppb, reaching a level of 332.1 ppb in 2019. It is estimated that N_2O concentration trends since 1980 are largely driven by a 30% increase in emissions from the expansion and intensification of global agriculture. The total anthropogenic effective radiative forcing (ERF) (Figure 6), including GHGs, halogenated gases, tropospheric aerosols and ozone precursor emissions, in 2019 relative to 1750 was 2.72 W m^{-2}, dominated by GHGs (positive ERF) and partially offset by aerosols (negative ERF). The rate of change of ERF likely has increased since the 1970s, mainly due to growing CO_2 concentrations and less negative aerosol ERF (10).
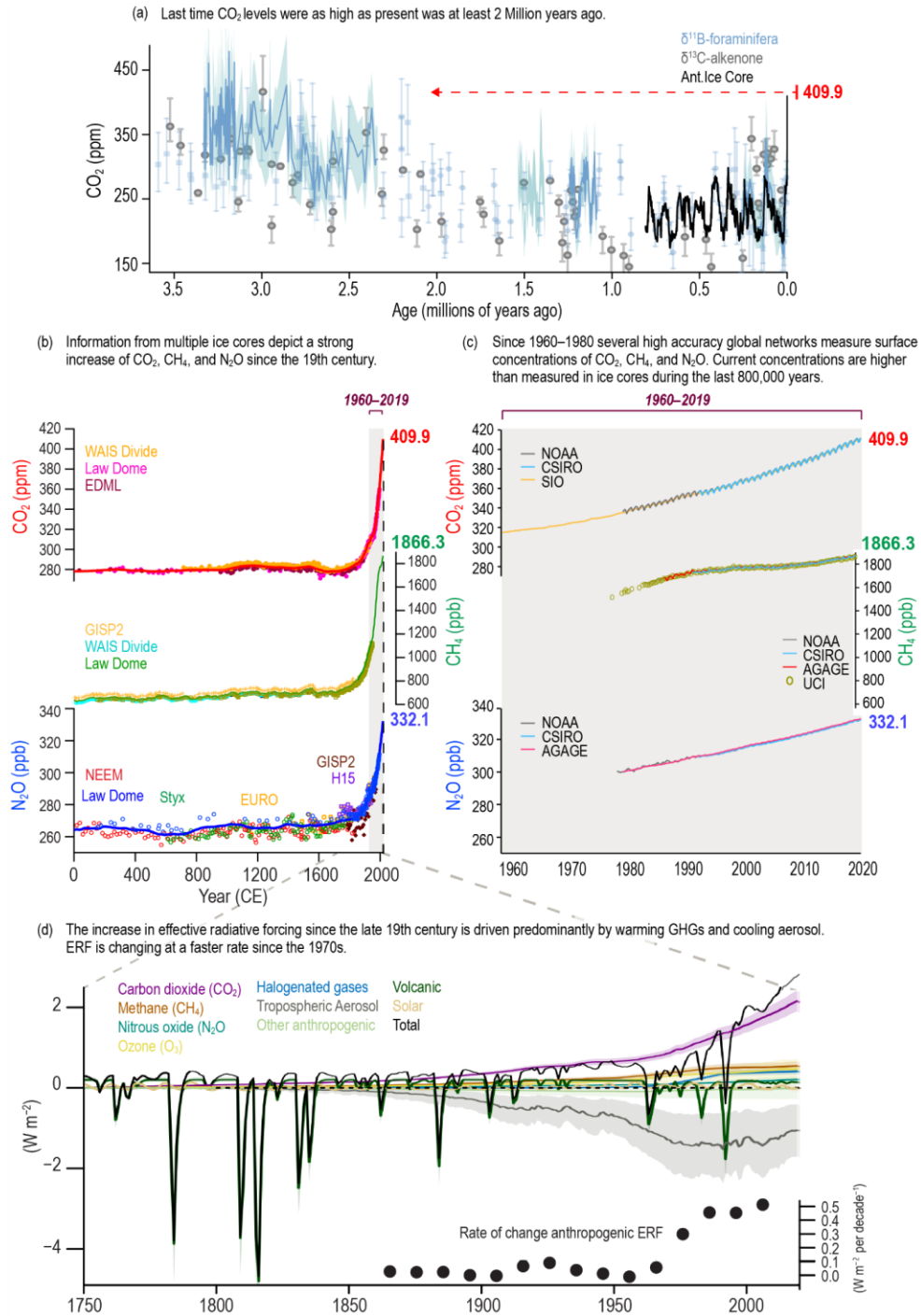
Figure 6: Changes in well-mixed greenhouse gas (WMGHG) concentrations and Effective Radiative Forcing. a) Changes in CO_2 from proxy records over the past 3.5 million years; b) Changes in all three WMGHGs from ice core records over the Common Era; c) directly observed WMGHG changes since the mid-20th century; d) Evolution of ERF and components since 1750 (10). Reproduced with permission.

In addition to global surface temperature, a wide range of indicators (atmospheric, cryospheric, oceanic and biospheric) of the climate system is rapidly changing, with many at levels unseen in millennia. The observed variations provide a coherent picture of a warming world, with many aspects that have now been formally attributed to human influences. It is almost certain that global surface temperature rise and associated changes can be limited promptly and substantially by reducing the global green house gas (GHG) emissions while persistent GHG emissions seriously increase the likelihood of potentially irreversible changes, in particular the contribution of ice sheets to global sea level change. Many indicators are increasingly diverging over the 21st century across the different SSPs and due to the slow response of the deep ocean and ice sheets, this divergence continues long after 2100, and 21st century emissions choices will have implications for global mean sea level (GMSL) rise for centuries to millennia (10).
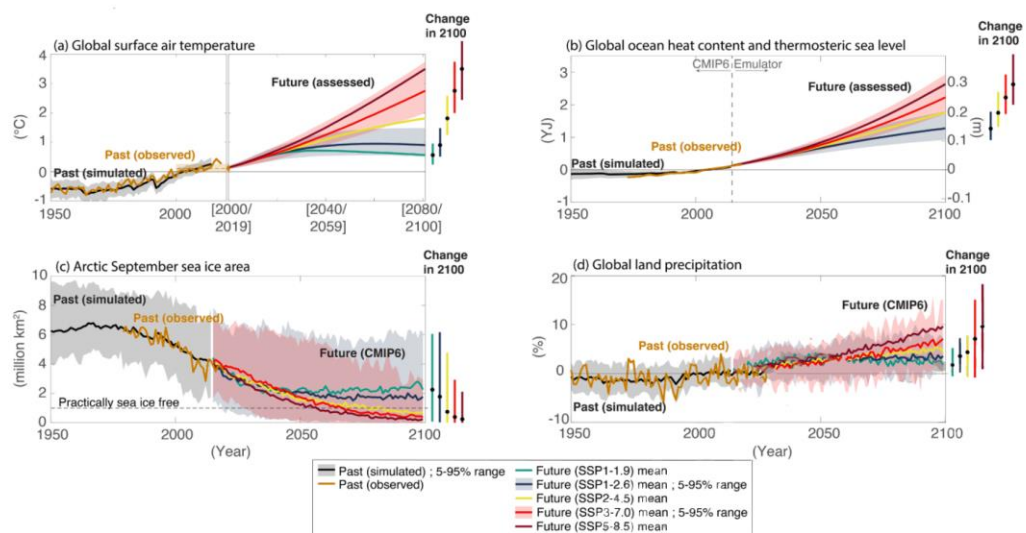
Figure 7: Observed, simulated and projected changes compared to the 1995–2014 average in 4 key indicators of the climate system through to 2100 differentiated by SSP scenario pathway (10). Reproduced with permission.

Current regional climate is already very different from the climate of the early or mid-20th century if considering several climatic impact-drivers (CIDs) resulting in shifting magnitude, frequency, duration, seasonality, and spatial extent of associated climate indices (Figure 8).
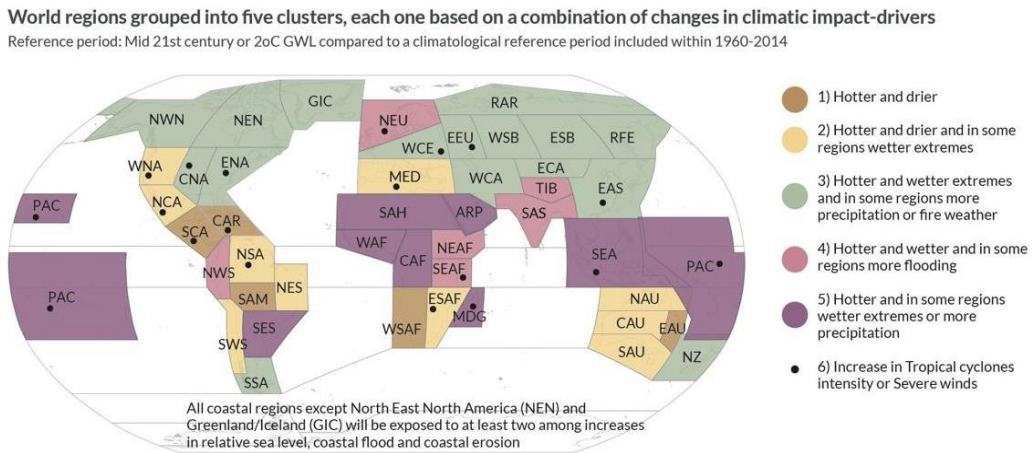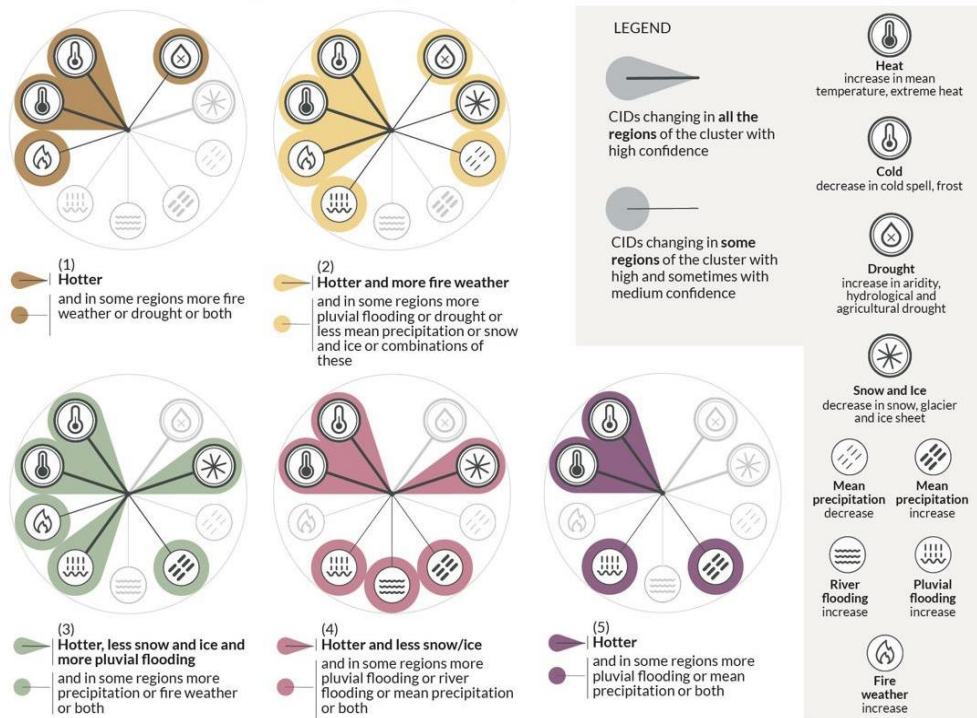
Figure 8: The geographical location of regions belonging to one of five groups characterized by a specific combination of changing climatic impact-drivers (CIDs). The five groups are represented by the five different colors, and the CID combinations associated with each group are represented in the corresponding 'fingerprint' and text below the map (10). Reproduced with permission.

It is very likely that mean temperatures have increased in all land regions and will continue to increase at rates greater than the global average. The frequency of heat

and cold extremes have increased and decreased, respectively and these changes are attributed to human influence in almost all regions and will continue through the 21st century. In particular, extreme heat would exceed critical thresholds for health, agriculture and other sectors more frequently by the mid-21st century with 2 °C of global warming. Relative sea level rise will continue during the 21st century and will continue to rise beyond 2100, contributing to increase coastal flooding in low-lying areas and coastal erosion along most sandy coasts. Every region of the world will experience concurrent changes in multiple CIDs by mid-century (10).

Since the IPCC Fifth Assessment Report (AR5), the international policy context of IPCC reports has changed. The UN Framework Convention on Climate Change (UNFCCC, 1992) has the primary goal of preventing "dangerous anthropogenic interference with the climate system". In response, the Paris Agreement (2015) established the long-term goals of "holding the increase in global average temperature to well below 2 °C above pre-industrial levels and pursuing efforts to limit the temperature increase to 1.5 °C above pre-industrial levels" and of achieving "a balance between anthropogenic emissions by sources and removals by sinks of greenhouse gases in the second half of this century" (10). Because we are already committed to some level of climate change, responding to climate change involves a two-pronged approach, in the best-case scenario, working in synergy:

- mitigation: reducing, preventing emissions of and stabilizing the levels of heat-trapping GHGs in the atmosphere, making the impacts of climate change less severe. Mitigation is achieved either by reducing the sources of these gases, e.g. by increasing the share of renewable energies, or establishing a cleaner mobility system or by enhancing the storage of these gases, e.g. by increasing the size of forests. In short, mitigation is a human intervention that reduces the sources of GHG emissions and/or enhances the sinks (12) (13);

- Adaptation: adapting to the climate change already happening, anticipating the adverse effects of climate change and taking appropriate action to prevent or minimise the damage they can cause, or taking advantage of opportunities that may arise. Examples of adaptation measures include large-scale infrastructure changes, such as building defenses to protect against sea-level rise, as well behavioural shifts, such as individuals reducing their food waste. In essence, adaptation can be understood as the

process of adjusting to the current and future effects of climate change (12) (13).

Parties to the Agreement have submitted Nationally Determined Contributions (NDCs) indicating their planned mitigation and adaptation strategies. However, the NDCs submitted as of 2020 are insufficient to reduce greenhouse gas emission enough to be consistent with trajectories limiting global warming to well below 2 °C above pre-industrial levels (10). Furthermore, the 2030 Agenda for Sustainable Development, adopted by all United Nations Member States in 2015, providing a shared blueprint for peace and prosperity for people and the planet, now and into the future, established the 17 Sustainable Development Goals (SDGs), which are an urgent call for action by all countries, developed and developing, in a global partnership. They recognize that ending poverty and other deprivations must go hand-in-hand with strategies that improve health and education, reduce inequality, and spur economic growth, all while tackling climate change and working to preserve our oceans and forests (14). Goal 13 "Climate action" is defined as "Take urgent action to combat climate change and its impacts" with the following targets and indicators:

- Target 13.1: strengthen resilience and adaptive capacity to climate-related hazards and natural disasters in all countries;
    - Indicator 13.1.1: number of deaths, missing persons and directly affected persons attributed to disasters per 100,000 population;
    - Indicator 13.1.2: number of countries that adopt and implement national disaster risk reduction strategies in line with the Sendai Framework for Disaster Risk Reduction 2015–2030;
    - Indicator 13.1.3: proportion of local governments that adopt and implement local disaster risk reduction strategies in line with national disaster risk reduction strategies.
- Target 13.2: integrate climate change measures into national policies, strategies and planning;
    - Indicator 13.3.1: number of countries with nationally determined contributions, long-term strategies, national adaptation plans and adaptation communications, as reported to the secretariat of the United Nations Framework Convention on Climate Change;
    - Indicator 13.2.2: total greenhouse gas emissions per year.
- Target 13.3: improve education, awareness-raising and human and institutional capacity on climate change mitigation, adaptation, impact reduction and early warning;

- o Indicator 13.3.1: extent to which (i) global citizenship education and (ii) education for sustainable development are mainstreamed in (a) national education policies; (b) curricula; (c) teacher education; and (d) student assessment;
  - o Indicator 13.3.2: number of countries that have communicated the strengthening of institutional, systemic and individual capacity-building to implement adaptation, mitigation and technology transfer, and development actions.
- Target 13.a: implement the commitment undertaken by developed-country parties to the United Nations Framework Convention on Climate Change to a goal of mobilizing jointly $100 billion annually by 2020 from all sources to address the needs of developing countries in the context of meaningful mitigation actions and transparency on implementation and fully operationalize the Green Climate Fund through its capitalization as soon as possible;
  - o Indicator 13.a.1: amounts provided and mobilized in United States dollars per year in relation to the continued existing collective mobilization goal of the $100 billion commitment through to 2025.
- Target 13.b: promote mechanisms for raising capacity for effective climate change-related planning and management in least developed countries and small island developing States, including focusing on women, youth and local and marginalized communities.
  - o Indicator 13.b.1: number of least developed countries and small island developing States with nationally determined contributions, long-term strategies, national adaptation plans and adaptation communications, as reported to the secretariat of the United Nations Framework Convention on Climate Change (14).

Nevertheless, atmospheric concentrations of the major greenhouse gases continued to increase despite the temporary reduction in emissions in 2020 related to measures taken in response to the COVID-19 pandemic. The six years from 2015 to 2020 are likely to be the warmest on record. Furthermore, climate change is making the achievement of many SDGs less likely. To limit global warming in accordance with the Paris Agreement, the world would need to achieve net zero carbon dioxide emissions by around 2050, a goal that, in this moment, looks improbable (14).

Fortunately, as of April 2020, 118 countries and territories had reported the development and adoption of national or local disaster risk reduction strategies, an

increase from 48 countries and territories in the first year of the Sendai Framework. As at 31 December 2020, 190 parties (189 countries and territories plus the European Union) had communicated their first nationally determined contribution to the United Nations Framework Convention on Climate Change, of which 44 were least developed countries and 40 were small island developing States. A further 48 countries and territories, of which one is a least developed country and five are small island developing States, have also communicated a second or updated nationally determined contribution. Of these 48 countries and territories, 39 included adaptation information in their new or updated contribution. The nationally determined contributions demonstrate that countries and territories are articulating more quantified targets and indicators for adaptation and identifying links between adaptation, the Goals and other frameworks. As at 31 March 2021, 125 of 154 developing countries were carrying out measures for national adaptation plans and prioritizing the formulation and implementation of the plans in their adaptation efforts. Moreover, six least developed countries (including three small island developing States) and another four small island developing States have completed a national adaptation plan. Further least developed countries have draft national adaptation plans and are on track to complete and submit these with a view to ensuring that all least developed countries have national adaptation plans by 2021 (14). According to IPCC, global emissions should be cut to 45 per cent below 2010 levels by 2030 in order to limit global warming to 1.5 °C above pre-industrial levels. Emissions from developed countries were approximately 6.2% lower in 2019 than in 2010, while emissions from 70 developing countries rose by 14.4% in 2014 (14). Total climate finance reported by States parties included in annex I to the Framework Convention on Climate Change continues to increase, reaching an annual average of $48.7 billion in the period 2017-2018. This represents an increase of 10 per cent compared to the 2015-2016 period. While more than half of all climate specific financial support in the 2017 and 2018 was targeted at mitigation action, the share of adaptation support is growing, and many countries and territories are prioritizing adaptation in their financial support provision. (14)

During the last United Nations Climate Change Conferences of Parties (COP 26), held in UK, every Party (representing almost 200 countries) agreed the Glasgow Climate Pact that will accelerate action on climate this decade completing the Paris Rulebook, which provides details on how the Paris Agreement pledges can be met. The COP26 achievements can be summarised as follow:

- mitigation: secured near-global net zero (over 90% of world GDP covered by net zero commitments), NDCs (new 2030 emissions targets) from 153

countries and future strengthening of mitigation measures such as move away from coal power, halt and reverse deforestation, reduce methane emissions and speed up the switch to electric vehicles;

- adaptation & loss and damage: boosted efforts to deal with climate impacts (80 countries covered by either Adaptation Communications or National Adaptation Plans to increase preparedness to climate risks). Record amounts of adaptation finance have been pledged, including committing to doubling 2019 levels of adaptation finance by 2025. Nations have announced new partnerships to improve access to finance, including for Indigenous Peoples;

- Finance: developed countries have made progress towards delivering the $100 billion climate finance goal and will reach it by 2023 at the latest. 34 countries and 5 public finance institutions will stop international support for the unabated fossil fuel energy sector next year. Private financial institutions and central banks are moving to realign trillions towards global net zero. Developed countries committed significantly increased funding to vital funds such as the Least Developed Countries Fund;

- collaboration: accelerating collaboration between governments, businesses and civil society to deliver on climate goals faster, whilst collaborative councils and dialogues in energy, electric vehicles, shipping and commodities will help deliver on commitments. Paris Rulebook finalised, agreeing the 'enhanced transparency framework' (common reporting of emissions and support), a new mechanism and standards for international carbon markets, and common timeframes for emissions reductions targets (15).

Although for the first time in a COP text, nations agreed to begin reducing coal-fired power (without carbon capture) and to start to eliminate subsidies on other fossil fuels, some researchers are still dissatisfied considering the lack of stronger commitments to reduce emissions, and failure to agree "loss and damage" finance, a sort of insurance policy for compensating climate-vulnerable countries for damage resulting from emissions that they did not create. Furthermore, following objections from China and India, a promise in earlier drafts of the text to "phase out" coal was changed to "phase down". Even if the deal includes commitments on ending deforestation, reducing methane emissions and a pledge from the financial sector to move trillions of dollars of investments into companies that are committed to net-zero emissions, modelling suggests that it will still not be enough to limit global warming to 2 °C above pre-industrial levels. If countries meet their 2030

targets, global temperatures will still rise 2.4 °C above pre-industrial levels by 2100, according to an analysis published on Climate Action Tracker. "We have kept 1.5 degrees alive. But its pulse is weak, and it will only survive if we keep our promises and translate commitments into rapid action", COP26 president Alok Sharma said. Charlie Gardner, a conservation biologist at the University of Kent in Canterbury, UK, sayd more radical action is needed, such as ending fossil-fuel production more quickly and transitioning economies away from constant growth (16).

Despite the issue of climate finance i.e. funding from wealthy nations to help low- and middle-income countries transition away from fossil fuels was deeply discussed, there was considerable anger over the failure by high-income nations to meet an earlier pledge to provide US$100 billion in climate finance annually from 2020. "The message coming out of this COP is every country for themselves," says Sara Jane Ahmed, a climate-finance researcher. However, the Glasgow Climate Pact includes a commitment to double funding to help the lowest-income countries improve climate resilience to $40 billion by 2025. The deal also commits to continue work on a definition of climate finance that would be acceptable to all countries since, at the moment, different countries define climate finance in different ways (16). COP26 negotiators also finalized the rules that govern international cooperation and carbon markets creating an accounting system that is intended to prevent double-counting of emissions reductions. With a common accounting framework, separate trading schemes, such as those currently operating in Europe, China and parts of the United States will enable connections, creating a more international market. Furthermore, a recent analysis of the climate commitments estimated that if a global carbon market would exist, the world would save around $300 billion annually by 2030 and, if those savings were reinvested in climate mitigation, it would more than double the projected annual emissions reductions in 2030 (16).

1.3   Waste heat recovery, waste heat to power and energy harvesting

Energy is the fundamental source transformed by our everyday life processes, but it also spans from the residential activities, to mobility, to the industrial sectors. The energy produced for heating a material, moving an object or powering an electronic device is always higher than the energy effectively absorbed by the process: this is what the second law of thermodynamics states and the reason lies in the irreversible nature of any thermodynamic transformation and the consequent non-unitary

efficiency. As a result, energy is always wasted in a quantity that depends on the physical or chemical processes governing the system and, usually, in the form of mechanical vibrations, electromagnetic radiations and, above all, thermal dispersions, with a related production of waste heat. Enormous amounts of waste heat injected into the environment also have the side effect of locally increasing the atmospheric temperature, especially in urban environments, slightly moving solution equilibria of several gaseous species. For the purpose of this work, we will mainly focus on:

- water vapour: it is the major contributor among all since it provokes from ≈ 30 to 70% of the overall greenhouse effect, because of the large amount dispersed in the atmosphere despite its low heat capacity (with respect to other GHGs) and the role played in the positive feedback loop influencing the global warming (17);
- carbon dioxide: it is the most popular and the main gas to be monitored because, even if its heat capacity is lower than other GHGs', it is more abundant than water vapour and has longer lifetime in air (thousands of years with respect to the tens of methane). Furthermore, it plays an important role in regulating the pH index of the oceans, and in the positive feedback loop (18) (19).

According to a review of energy consumption at the global level, it is evident that most of the energy we use daily is derived from fossil fuels, whereas renewables account for less than one-quarter of global consumption worldwide (20). Furthermore, the over-exploitation of energy sources have been resulting in criticalities, at the political, social and logistic level. In fact, as introduced in the previous sections, energy consumption, environmental impact, and sustainability have risen fast through the ranks, achieving the first places in driving investments, policies, and concerns of all countries at any developmental stage. Due to global warming, increasing energy costs, and green politics, the search for sustainable, responsible and clean energy represents a highly impacting and exponentially growing sector. In this sense, a reduction of GHGs emissions, implying a conversion of waste heat to more noble forms of energy and a concurrent increase in efficiency of the same devices and processes, is, nowadays, of paramount importance. For this reason, simultaneously with the development of powered devices, several approaches for reducing energy losses exist and nowadays, many of waste heat recovery (WHR), waste heat to power (WHP), energy harvesting and conversion systems are investigated and many of them are already available on the

market. While WHR and WHP technologies are focused only on converting large streams of thermal waste into, respectively, mechanical and electric power, energy harvesting is defined as the process wherein the sources such as mechanical load, vibrations, temperature gradients, heat, light, salinity gradients, wind, etc., are scavenged and converted to obtain relatively small levels of power in the nW-mW range (21). According to the field of interest, energy-harvesting systems differ in the working principles and the employed materials, as direct consequence of the physical effects exploited for the energy conversion. At the same time, regarding the operation of industrial and power plants, dilemmas exist about how to increase efficiency, how to better convert energy between its forms, and how to utilize waste heat arising from thermodynamic inefficiencies. The creation of a common approach with a new attitude towards our fragile natural environment is required. Alongside an increase in the consumption of primary energy, the amount of waste heat increases, therefore representing a greater economic and ecological potential for utilization.

Waste heat is a by-product of various processes and it is released in different forms such as: combustion gases to the atmosphere, heated water into the environment, heated products from industrial processes, heat from hot surfaces and so on. For example, to estimate the amount of waste heat Q [J] released from a continuous hot vapor volume into the environment, it is possible to use the following equation:

$$Q = c \, m \, \Delta T,$$

where m [kg] is the mass of the hot vapour volume, c [J kg^{-1} K^{-1}] is the heat capacity of the vapor, and ΔT [K] is the temperature difference between the hot vapour and the ambient environment. In addition, the heat coming from phase transformations (latent heat) must be taken into account, which is released after the condensation of a gas or the solidification of a liquid. Thus, the higher the mass flow and ΔT between hot and cold reservoirs, the greater the waste heat amount. Other fundamental aspects also play an important role and must be considered in a multivariable optimization model, before any technology is adopted:

- time availability: the temporal distribution of energy availability throughout a day, week, and season, where a more continuous flow is always preferred. To increase heat stability in time, heat storage could be implemented, which is another huge field under development;

- thermoeconomic analysis: it takes into account the Return on Investment (ROI), usually comprising between 5 and 10 years, to pay back the installation;
- energetic and environmental sustainability: it should be evaluated through a full life cycle assessment (LCA), of plant/device life expectancy, development costs, and decommissioning.

Dealing with heat, a form of energy that intrinsically contains entropic (dispersive) terms, is the exergy, by definition: "the total amount of energy that can be extracted from a physical system given its position in an external environment." The concept of exergy brings together two aspects of an energy transformation process: its "quality" and its "quantity." Ideal thermodynamics is conceived as a far-from-reality analysis, where processes are deconstructed as an integral of infinite processes in quasi equilibrium. Exergy analysis is fundamental for WHR processes, as its outcomes take into account the sources of irreversibility, which are intrinsic to real processes (22) (23). To understand the abundance of this source, its economic value, and the importance of converting it into more noble energy forms, we must consider that, because of the average efficiency of industrial processes and thermal machines, the 72% of global energy consumption is lost in the form of heat (24), totaling 12 PWh year^{-1}. Of this, around 66% is available at low temperature (LT) conditions below 200 °C, for a total of about 8 PWh year^{-1}, 25% is available at medium temperature (MT), between 200 and 500 °C, resulting in 3 PWh year^{-1}, and the last 1 PWh year^{-1} is available at high temperature (HT), with conditions above 500 °C. In view of the enthalpy content and distribution of the different sources of waste heat, low/medium temperature sources are considered the most fertile field for research and development, with an impressive industrial growth rate. Considering the average heat to power efficiency in the LT and MT ranges being 15% and 45% respectively, an estimation on the possible amount of electric energy recovered from waste heat and injected into the grid, or used locally, is around 2.5 PWh year^{-1}. This amount can generate a turnover of more than 300 billion EUR if the electricity is sold to industries (at 0.125 EUR kWh^{-1}, which is the 2015 cost toward industrial consumption) or more than 550 billion EUR if sold to households (at 0.221 EUR kWh^{-1}, which is the 2015 cost toward household consumption). A bulk of 2.5 PWh year^{-1} represents 1.5% of the global energy production. However, the cost per kWh generated could be much higher, considering the installation costs for WHR/WHP solutions, and must benefit from intelligent politics aimed at sustaining research, development, and production of highly efficient integrated processes and investment in equipment manufacturing. According to market reports

estimates for the WHP market size, a significant value of 13.2 billion EUR has been pointed out for 2018 and, expecting a current annual growth rate (CAGR) of 13%, its value in 2025 will approach 26.4 billion EUR (25).

Industrial WHR deals with temperatures ranging from 60 °C (cleaning processes) to more than 1700 °C (iron and steel, cement, glass, and ceramic processing industries). For example, in the chemical industry, the typical temperature range is from 100 to 500 °C (in some cases up to 1000 °C) (26). In Figure 9, several industrial processes are associated with the corresponding temperature range.
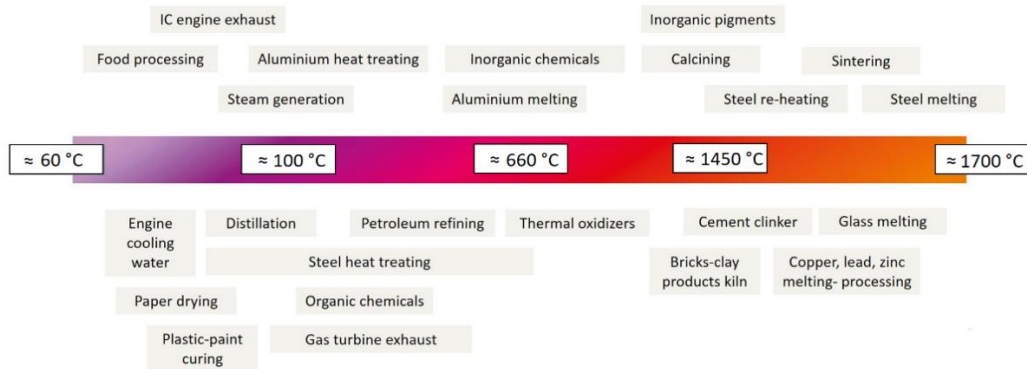
Figure 9: Temperature ranges for different industrial heating processes (25). Reproduced with permission.

Among the various industrial sectors, the amount of waste heat fraction (with respect to the total energy consumption) can vary significantly. The largest amount of waste heat is derived from the food and tobacco, pulp and paper processing, basic metal industries, chemical industry, and nonmetallic mineral processing, and 50% of waste heat is in the temperature range between 300 and 350 °C (5). In the USA, metallurgy and nonmetallic mineral transformation contributes for the 20-50% of the energy used and the recovery potential for energy-intensive industries in the UK is around 10% of the total amount (27). Waste heat potential in the EU has been estimated to lie above 350 TWh year^{-1}, the greatest part between 100 and 200 °C. This is an important amount of energy compared with the 3218 TWh energy consumption of 2016 (4). Waste heat below 100 °C represents a marginal portion, whereas within the 200 and 500 °C range quantities that are more important are found (4). The statistics related to the waste heat potential in percentages per industry sector for all the former countries belonging to EU28 (4) are shown in Table 1.

Table 1: Waste heat potential percentage per industry sector in Europe (4).

Industrial sector	Heat consumption [TWh]	Waste heat [%]
Iron and steel	580	11.4
Chemical and petrochemical	600	11.0
Nonferrous metal	115	9.6
Nonmetallic minerals	390	11.4
Food and tobacco	345	8.6
Paper pulp and print	395	10.6
Wood and products	100	6.0
Textile and leather	50	11.0
Other	660	10.4

Since WHR technologies suffer from long payback periods, high investment requirements, several additional requirements in terms of materials and design due to chemical activity and corrosion, they have been introduced in specific situations without wider diffusion. At the same time, developing countries are experiencing an ongoing industrialization process and can take advantage of experiences and technologies developed in more advanced countries. For sure, the industrial WHR/WHP will definitely be under spotlight for the next years (28).

Regarding the automotive sector, in consideration of the Paris Agreement, many countries are evaluating different solutions to secure improvements in transport efficiency and emissions reductions, both for light-duty vehicles (LDVs) and heavy-duty vehicles (HDVs). In response to this energy and environmental challenges, the automotive industry is focusing on high-efficiency vehicles. In fact,

according to the Global Fuel Economy Initiative objective, within 2030, LDVs should improve the fuel economy by 50% and save 0.5 Gt of CO_2 emissions per year (6). Nowadays, the principal path toward sustainable transportation is the electrification and hybridization of automotive powertrains, while the industry is also focusing on different technical solutions to increase the fuel efficiency of ICE vehicles. A complete physical analysis of fuel consumption in an automotive system was conducted, indicating that 58% of the traction power at the wheel is lost due to vehicle inertia in an urban driving condition. On the contrary, aerodynamic losses become dominant in highway driving conditions (50% of the traction power at the wheel) (7). The US EPA City and Highway Driving Cycles provide an energy loss analysis based on energy utilization in different driving conditions and different size-mass vehicles (Figure 10). It is interesting to note a loss in fuel energy, of around 35% and 30% in exhaust and coolant gases, respectively, representing more than half the losses in wasted heat form (29) (30).
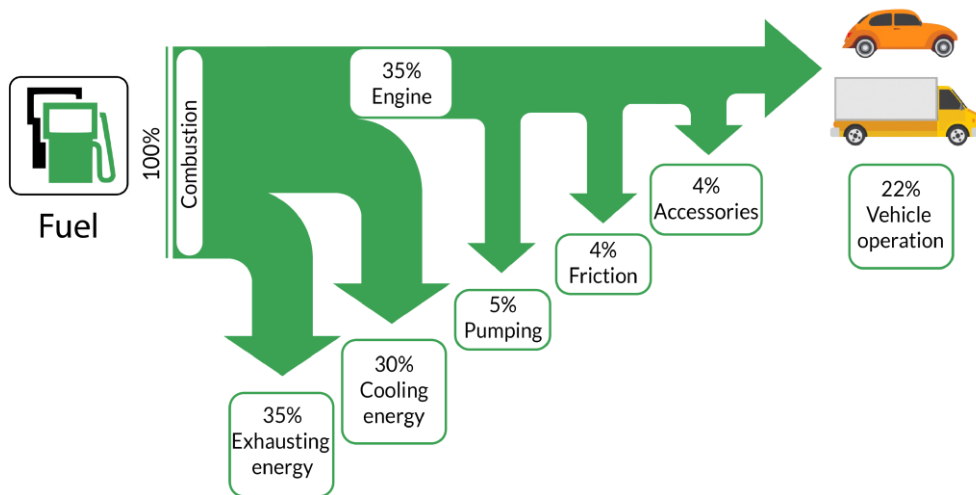
Figure 10: A Sankey diagram showing the fuel energy utilization of an ICE (25). Reproduced with permission.

Nowadays, engine manufacturers concentrate on two different ways to increase the thermal efficiency of an ICE. The first one focuses on improving the thermodynamic cycle of the engine, operating on the choice of fuel, combustion system, and air path. For example, downsized engines deployed in production vehicles improve the fuel economy by 8–10% for LDVs in urban pathways (31). The drawback of this approach consists of a reduction of available power and an increase of fuel consumption, especially in highway conditions. The second trend concerns WHR and WHP. WHR has the important feature to not affect the engine

design and technical features of the vehicle, as it uses the heat rejected by combustion. Therefore, it is suitable for different driving conditions and it can be easily integrated. However, the key point of this technology is to guarantee competing requirements of costs, engine durability, and emissions (32). By considering detailed models and simulations of the thermodynamic behaviour in an ICE (33) (34), it is possible to conclude that the exergy loss (or availability loss) mainly originates by irreversible combustion processes and the energy is mainly conveyed by exhaust gases. This suggests that the best option to maximize energy recovery is to install the recovery plant in close contact with the exhaust gas ducts or the cooling system. A further important feature is thermal availability or rather entropy maximization, representing the maximum amount of work necessary to establish equilibrium in the system (35). This concept is closely related to heat grade (temperature). While HT and MT conditions are widely used for practical power generation, LT sources represent today challenge in the automotive industry. LT sources are mainly localized in the cooling systems (radiator and air conditioning) and in exhaust gases exiting other recovery devices (36).

During the past decades, technology has pointed in the direction of an extreme miniaturization of electronic components and portable devices. Alongside the development of healthcare (37), sport and fitness tracker ultralow-power (ULP) devices (38) (39), approaches for producing electric energy from human body waste heat have become widely analysed (40). Despite the development of new supply technologies, researchers have started to explore a possible definitive solution, battery-less devices integrating an energy-harvesting system where mechanical load, vibrations, temperature gradients, heat and light, are scavenged and converted to obtain relatively small amounts of power. For the purpose of this work, some thermo/tribo/pyroelectric devices are presented. Of course, wearable devices are not comparable with industrial or automotive applications in terms of energy produced, but still they are part of categories of technologies able to convert waste heat into power, which, moreover, can be explored in the sports and space application field, where small amounts of power are enough to power smart devices. Considering that the energy requirements of an average person under 60 years are in the range of 8.8-17.6 MJ day^{-1} (man) and between 7.1 and 14.2 MJ day^{-1} (woman) (41), and assuming to radiate a large part of this energy in the form of heat, a thermal source of some tens of Watts is available (42). Then, the harvest of even a small part of this energy would enable to power wearables devices such as smartwatches that need a few tens of mW to operate (43). In standard conditions, i.e., a body temperature of 36.6 °C (44) and a room temperature of 27 °C, the Carnot efficiency

is $\approx 3\%$, immediately highlighting the limit for the application on the human body. However, even 1% of a total power in the order of 100W still represents an amount of energy sufficient to power wearables.

Although waste heat may be exploited, ideally it should be avoided: this is done through the energy optimization of processes by needs-based controls, process operation and design, improved insulation, the use of highly efficient electric drive systems and a change towards more energy efficient production methods. However, even after energy optimization, significant potential remains (26). A large number of WHR, WHP and energy harvester exist and in the next sections, some of them will be presented.

1.3.1 Thermodynamic machines

In this subsection, the most interesting and promising thermodynamic cycles adopted in a WHR technology are briefly illustrated and commented.

1.3.1.1 Brayton Cycle (BC)

In the BC, a compressor compresses air isentropically. Then it receives heat from exhaust gases at constant pressure and finally it expands isentropically in a turbine to generate electrical power. At this point, the air is discharged back to the atmosphere and the process is repeated. BC represents an optimal choice for WHR systems working at mild temperatures in the industrial sector. This approach has been explored in the 1980s to convert waste heat from adiabatic engines, enabling a reduction of running costs on one side and a reasonable additional capital investment on the other. Recently, a BC system was employed for the blast furnace slag in the iron and steel industry (45). In another case, a BC system was integrated into a diesel engine, connecting the turbocharger compressor with the compressor that operates on the BC. Results showed that the fuel economy of the diesel engine could be improved by 2.6% at fast rotation regimes and 4.6% at lower regimes, at full load (46). The performance of a BC machine operating with internal combustion engine (ICE) exhaust gases was investigated (47).

1.3.1.2 Stirling cycle (SC)

In the SC, the air, helium, or hydrogen is compressed isothermally. Then, it passed through a regenerator (or heat exchanger) that operates at constant volume, where the gas absorbs heat, while its pressure and temperature raise. Then, the gas flow

through an isothermal expansion and finally it goes back through the regenerator, releasing an amount of heat. The application of a Stirling engine (SE) is interesting, especially in conjunction with gas turbine (GT) cycles where waste heath is generated (48). Recently, a double-action thermoacoustic SE-based electrical generator capable of recovering liquified natural gas (LNG) cold exergy was proposed, converting the external thermal energy into acoustic work (49).

1.3.1.3 Organic Rankine Cycle (ORC)

Based on Rankine cycle (RC), ORC system uses organic working fluids instead of water, allowing to manage waste heat at temperatures up to 300 °C (50). A pump pressurizes the working fluid in liquid form; heat is then moved from the heat source to the working fluid through a superheater and an evaporator, where the organic fluid gets vaporized; then, the high-pressure working fluid flows into an expansion turbine, connected to the load (electrical power generator); at the end, the cooling source controls the organic fluid returning back into liquid form in the condenser. Hydrocarbons, siloxanes, refrigerants, and CO_2 can be exploited instead of water, thanks to their advantageous lower boiling and critical points, lower specific volumes, as well as lower viscosities, higher vapour pressures, and higher molecular masses with respect to water-based fluids (50). In addition, ORCs are highly valued in current research for the availability and the simplicity of their components and for the low flammability, corrosion, and toxicity of the working fluids. Currently, several ORC-based plants are installed in many countries (Italy, Austria, Germany, the Netherlands, Sweden, U.S.A., Canada, etc.) and the number of plants is still growing. The adaptability and the scalability of this technology permit to harvest different heat sources, from industrial to domestic applications. To date, there has been a consistent number of ORC manufacturers and commercial applications in industry sectors. Currently, there are many examples of installed plants all over the world such as: the Fonderia di Torbole (Brescia) in Italy, which has been hosting an ORC plant since 1996, updated in 2018, and producing 690 kW; Toscelik Hot Strip Mill in Turkey producing 1MW since 2011; NatSteel in Singapore with an installed plant producing 555 kW since 2013; Elbe-Stahlwerke Feralpi in Germany producing 2.7MW since 2013; ORI Martin in Italy producing 1.9MW since 2016; the Munksjö pulp mill in Sweden producing 750 kW since 2010; and the glass manufacturing plants of Sisecamin in Ostellato, Porto Nogaro, and Manfredonia in Italy, sharing a capacity of 5MW since 2016 for each of the locations. A cement plant in Lengfurt, Germany, burns around 3150 tons of clinkers per day in a rotary furnace at flame temperatures of about 2000 °C. This generates

hot furnace exhaust gases (350 °C, heat flux at around 8 MW) and waste heat from the clinker cooler (275 °C, about 60 MW). Part of this heat is injected back into the furnace. Recently, this technology has been widely used also in the transportation sector (50). In
Figure 11 the schematic of an ORC installation in an industrial plant is shown.
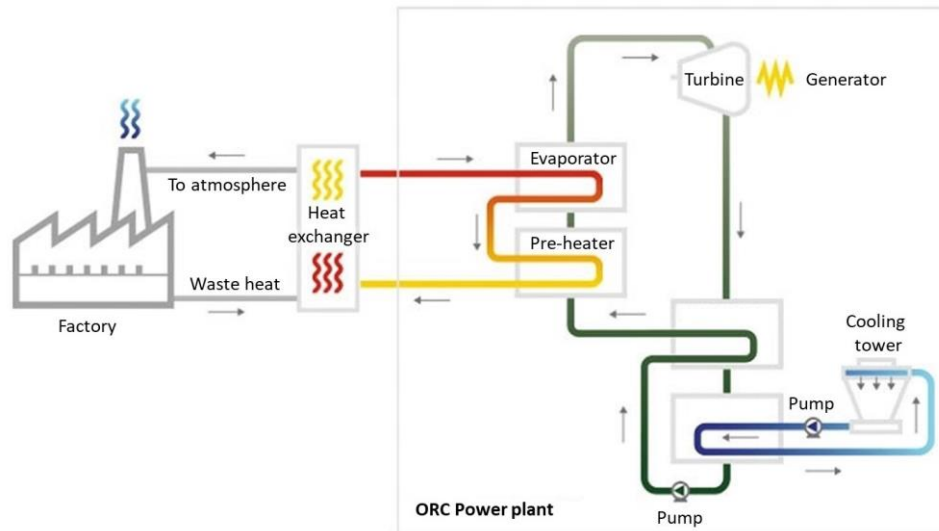
Figure 11: Schematic of ORC installation in an industrial plant (51). Reproduced with permission.

In the automotive research field, BC, SC, ORC and the following KC are currently being analysed. In particular, ORC seems to be most economically advantageous for WHR when the thermal source is below 150 °C (52). In fact, an ORC permits exploiting LT sources in a very efficient way (53). It is also very attractive for large scale production, because of the low cost, the easy integration with the cooling system and the marginal impact on engine design. At the same time, some design challenges exist. The most evident is the miniaturization of the expander machine (54) which operates with organic fluids (55). This is fundamental in reducing the weight-to-power ratio of the dynamic machine (56), decreasing the inertia of the vehicle. The operation conditions of the ORC can be categorized into direct and indirect. In the direct recovery method, the engine block is the heat exchanger, avoiding an additional component (57), exploiting higher temperatures and larger amount of heat rejected by the ICE. Various analyses show how the heat dissipated by the engine block can be coupled with the vaporizer cooling system, enhancing the recovery of about the 3% (58). On the other hand, in the indirect method, heat is transferred from the coolant to the ORC working fluid using an

extra heat exchanger, and the heat dissipated by the coolant fluid can be used for the evaporation system or as a preheater for a HT Rankine-Hirn cycle (59) (60) (61) (62). In this case higher efficiencies are achieved (63), but with a heavier and bulky system, other than economically unfavourable in automotive applications (64). Other approaches (65) involve the use of the heat rejected by the cooling system for the confluent cascade expansions in the ORC system. The matching conditions between working fluid and ORC systems are under analysis to maximize the heat exchange. In LT recovery systems, organic fluids with a low boiling and low freezing temperature are employed, allowing the absorption of the low-temperature heat in the ORC system. However, it is difficult to maintain a high mass flow, since the low stability of organic fluids at HT and low specific heat. Ways to increase the efficiency are designing larger recovery system (as in industrial plants) or using high-specific-heat fluids like water. Furthermore, another important parameter affecting the efficiency is the thermal fluctuation, due to changeable driving conditions. This phenomenon negatively affects WHR systems, limiting the operational range and inducing an efficiency drop during partial load. A solution could be controlling the stream, ensuring a close and safe optimal operational point (66). Finally yet importantly, the net economic advantage involved by using WHR systems has to be compared with the costs of additional volume occupied by an ORC system, affecting the vehicle transportation capacity (67). The main companies that are funding research and development in ORC are BMW, General Electrics, Cummins Engine and United Technologies Corporation and Figure 12 shows the schematic of an ORC standard configuration in automotive system.
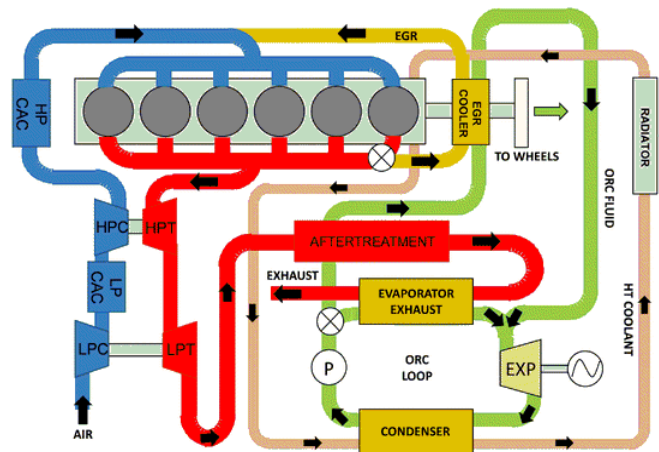
Figure 12: Schematic of ORC installation in an automotive system (68). Reproduced under the terms of the Creative Commons CC BY license.

1.3.1.4 Kalina Cycle (KC)

KC is an absorption-based power generation cycle, based on RC. The working fluid enabling KC systems is a mixture of ammonia and water, which increases the recovery efficiency. Condensed water-ammonia mixture is compressed isentropically and then it is heated at constant pressure while it evaporates (first ammonia and then water); subsequently, it is isentropically expanded into a turbine and finally condensed (first water and then ammonia) at a constant pressure releasing heat. The operating temperature lies between 90 and 500 °C. With respect to ORC and supercritical cycles, KC shows superior performances. Reducing the temperature difference between the working fluid and the heat source, reversibility is increased and dissipation reduced. With respect to RC, where a considerable amount of heat is lost during the isothermal vaporization of water into steam, the binary mixture in the KC vaporizes non isothermally, improving the efficiency of the cycle (69). Moreover, KC has one more big advantage compared with RC, since it is possible to modify the $NH_3:H_2O$ ratio in the working fluid and then pressure levels. In this way, the thermal performances are maximized (70) but, at the same time, the engine is more complex and may require an additional pumping system. With respect to ORC, in the same temperature range, KC are 15-25% more efficient with the tangible outcome that power plants featuring hot fluid below 150 °C are increasingly based on this new technology (50).

Several specific applications have produced adaptations of KC systems, with more than 30 solutions that have been introduced so far. For example, in the cement industry, superheated NH3:H2O vapor is generated, harvesting low-grade heat; it is then expanded in a turbine, condensed in regenerative heat exchangers, diluted and fed into a low-pressure condenser, and finally injected into the high-pressure condenser before reaching the vapor generators again. KCs can recover industrial waste heat in the range from 80 to 400 °C for power generation. Existing industrial WHR applications include: Sumitomo plant in Japan with an installed plant producing 3.5MW since 1999; Husavik, Iceland, plant converting 2.0MW since 2000; Fuji Oil plant in Japan converting 4.0MW since 2005; DG KHAN plant in Pakistan converting 8.6MW since 2013; and Star Cement plant in Dubai producing 4.75MW since 2013. KCs are limited in their industrial applications for some technical issues that have not been solved yet, in particular, for fine tuning the boiler evaporation ratio and the early condensation of the NH_3-H_2O mixture (8). A comparison of performances between KC and transcritical ORC for WHR in different internal combustion engine (ICE) and working conditions shows that,

compared with KC, the transcritical ORC shows evident advantages on the overall thermodynamic efficiency, low operation pressure, and simple component configuration with exhaust temperature from the engine of over 220 °C. The optimal thermal performance of the transcritical ORC is in the range 295–345 °C. Nevertheless, when moving over or under the optimal temperature drop, the performance decreases considerably. Moreover, the extremely high expansion ratio of the turbine requires a complex multistage design and large system size (71). Another comparison between the thermodynamic performances of KC and ORC has been conducted for the case of heat recovery from two diesel engines, each one with an electrical power of 8900 kW. Supposing a mean temperature difference in the heat recovery exchanger of 50 °C, a net electric power of 1615 kW and of 1603 kW can be generated, respectively, for KC and ORC. Although the output levels are almost equal, KC requires a much higher maximum pressure to obtain high performances. Then, at least for a low power level and MT and HT thermal sources, KC appears to be unjustified because the increase in performances is very small (with respect to a properly optimized ORC) and must be obtained with a more complex plant scheme, larger surface heat exchangers, and particular plants featuring pressure and corrosion resistance (72). Nowadays, the number of thermodynamic WHR/WHP systems commercialized in the industry sector is very limited, even though industrial waste heat is available in abundance and the concept of utilization or recovery is not new. The reasons are mainly related to resource constraints and the insufficiency of regulatory, organizational, and business plans (8).

1.3.1.5 Carbon Dioxide Trans-Critical Cycle (CDTCC)

CDTCC systems are based on CO_2, which ensures nontoxic, nonflammable, noncorrosive operation. Since CO_2 reaches the supercritical state at 7.38 MPa and 31.1 °C, it is widely applied to low-grade heat recovery systems (73). The working principle is the same as the ORC but, in this case, heat is rejected below the critical point and absorbed above, having a working fluid in the superheated state under supercritical pressures, maximizing performances (74). CO_2 is isentropically compressed, heated at constant pressure, isentropically expanded, and finally condensed, releasing heat at constant pressure. CDTCC was theoretically compared with a R245fa ORC, operating on a low-grade heat reservoir, and concluded that exergy efficiency would benefit from using a recuperator (73) (75).

1.3.1.6 Trilateral Flash Cycle (TFC)

TFC is a quite recent promising technology having a huge recovery potential in comparison with ORC, as the energy recovered can roughly double over the same temperature difference; an economic outcome of this efficiency is related to the savings generated by avoiding any cooling/heat rejection system in a power plant. A TFC consists of a modified ORC where the organic working fluid is heated up to the saturation temperature under high pressure rather than evaporated, implying that the heat transfer is optimal when no fluid is brought across its boiling point. TFC-based systems can substitute ORC units installed in MT processes between 70 and 200 °C, and they are able to follow any temperature variation on both the inlet and outlet phases of the cycle (28) (5).

1.3.1.7 Supercritical CO$_2$ (SCO$_2$) Brayton Cycle

The SCO$_2$ BC is a standard cycle operating with CO$_2$. It combines the advantages of both steam RC and GT systems. The fluid is compressed in the incompressible region and the higher turbine inlet temperature can be utilized with no material-related issues in comparison with the SRC. Since CO$_2$ is able to sustain intense density variations as a consequence of slight temperature and pressure fluctuations, it allows excellent energy extraction at HT with high energy density of the installed plant, one order of magnitude below GT. SCO$_2$ systems are mainly used in HT applications for direct WHR while driving an electrical power plant. Considering that the heat rejection also occurs at HTs, other systems such as a properly matched ORC could be cascaded. The most typical application is with geothermal sources, accounting for almost 75% of global installed capacity. The diffusion of SCO$_2$ is quite limited, due to the capital-intensive requirements in multi-MW power plants. Nevertheless, small providers cover the niche of small WHR plants ranging from 10 to 150 kW (5).

1.3.2 Thermoelectric devices

Thermoelectric (TE) systems belong to WHP/WHR and energy harvesting technologies as well, but they have significantly different features with respect to the thermodynamic cycles. First, TE systems are solid-state devices able to convert heat into electricity by means of the Seebeck effect. They are adopted in several application domains such as factories, power plants, computers, vehicles, stoves, and wearable devices (50). The Seebeck effect is due to from the capability of

specific materials to produce current when subjected to a temperature gradient. The propensity of a material to manifest this effect is a nonlinear function of the temperature, and it is specific for each different material and crystalline configuration. TE materials are currently commercialized for integration into high-performance cooling systems needed to realize high heat fluxes to very LTs at precise rates (50). In general, the materials can be divided into three categories depending on the temperature of operation: since the first device was developed, bismuth has been the most widely used material for LT applications. Furthemore, antimony–telluride Sb_2Te_2 or its alloys are used for p-type composition instead of bismuth–telluride, because of their tunable high carrier mobility, resulting in stronger and optimized Seebeck effect.

Several industrial companies have focused on TE technologies as these devices can compete with fluid-based systems, like compressors or heat pumps. Furthermore, solid-state energy conversion is more appealing because of its simplicity, if compared with compressing or expanding two-phase fluid systems. Although their limited efficiency, several commercial uses have been realized. The reasons behind this success are the relatively small size and complexity, vast scalability, robustness, rapid response time, lack of toxic operational emissions, long reliability and lifetime, inertness, and lack of moving components (50) (76). Many countries, such as the USA, UK, Australia, Ukraine, Japan, and South Korea, are focusing their attention on this field (77) (78) and several researches have been already accomplished to characterize the TEGs performances under various heat sources like diathermal oil heaters, cook stoves, and waste heat from industrial process. Recently, the concept of the hybrid power-generation system was introduced. It is composed of one TE module held by two copper layers with four heat pipes generating the temperature difference between the two TEG sides (79). Another application of TEG modules is in support of the industrial wireless sensor networks (IWSNs), clusters of wireless sensor nodes in industrial plants and commercial areas. They consist of a high number of sensor nodes, including sensor units and control electronics, communication, and power supply. Most of these are powered by means of batteries having strong limitations in terms of energy because of the constrained node and battery size. Therefore, several researchers explore the possibility of coupling IWSNs with TEGs to harvest energy and extend batteries' lifetimes, achieving higher power densities with respect to other energy harvesters. It has been concluded that with $0.6ms^{-1}$ of air flow on the TEGs and without using any heat sink, the hot side being at 50 °C and the cold one at 20 °C, the output power is around 80 µW. A TE component was employed to supply an autonomous

sensing node for T measurement (80) and others were produced and characterized to power systems for environmental monitoring, in the order of 10mW for a temperature difference of 10 °C (81). In another application domain, 52% of Australian households hot water heaters are powered using natural gas and liquified petroleum gas (LPG) systems. By exploiting the thermal gradient generated between hot exhaust gas exiting and cold water from ducts, it would be possible to generate power by means of TEGs. Through the testing conducted, a power generation unit including 60 TE cells would be able to produce more than 40W and more than 20W in case hot water is around boiling temperature and 80 °C, respectively. In the latter case, the efficiency of the system is estimated to fall in the range 0.37–1.03% (82). Furthermore, some hybrid concept and devices have been analyzed for enhancing the performances of a geothermal-based ORC and proposed two novel systems in which, in the first case, part of the waste heat is recovered using a TEG for power generation whereas in the second for hydrogen production (by means of a proton-exchange membrane electrolyzer). Results indicated that the proposed system has exergy efficiencies higher than that of the basic ORC by 21.9% and 12.7%, respectively. They also reveal that the specific product cost for the proposed solutions is lower than that for the basic ORC, despite a higher total cost rate (83). The possibility of using TEG to recover waste heat from a KC was analysed revealing an improvement of around 7.3% of the net output power and higher energy and exergy efficiencies. Furthermore, they evaluated economically the integration of TEG with the KC, indicating modest profitability (84). Recent studies by Pacific Northwest National Laboratory considered some well-known industrial activities, such as aluminum smelting, glass manufacturing, and cement production, concluding that small internal combustion engines (ICEs) could be profitably replaced by external combustion TE engines. This technology is vibration free and less acoustically impacting and can be fueled using propane, butane, liquefied natural gas, bio alcohols, and not necessarily ones based on fossil sources (76). Both US and Japan Governments have introduced new regulations to encourage companies to introduce TE devices in trucks and cars to partially convert waste heat from the exhausts into electricity, powering steering, brakes, water pumps, turbochargers and so on. Although efficiency depends on the level of system integration and driving conditions, diesel consumption could be reduced by 5-10% (76). Several leading automotive manufacturers such as Volvo, Volkswagen, BMW, and Ford are introducing WHR systems able to provide around 1 kW of electrical power and increase consequently the thermal engine overall efficiency using TE generators (TEGs). A WHR system for automotive exhaust heat recovery composed of 24 TE modules was tested with an output of ≈12W with

a ΔT of 30 °C (85), and another very efficient TE module (15% efficiency) was produced (86). Furthermore, solar thermoelectric generators (STEGs) have been developed efficiently, coupling thermal solar collectors with TE devices, as the absorbed heat is conveyed on the TE devices by means of a diathermal fluid.

Regarding the automotive sectors, in order to improve vehicle efficiency some WHR systems exploiting the TE effect have been proposed, since TEGs allow to recover heat from ICE, reducing fuel consumption and with no increase in the emissions. In particular, exhaust TEG (ETEG) is the most promising technology, because it has no moving parts, it requires less maintenance in comparison with ORC systems, and it is silent in operation. Despite the light weight of ETEG and its versatility, main issues exist. The main are the low efficiency (5-10%), high cost and large temperature differences required for considerable energy conversion. In particular, the cold side of the ETEG module should be at a temperature as low as possible to maximize efficiency and then, cooling mechanisms are required to maximize the thermal gradient. In a typical ICE application, the system is composed of four modules: a TEG module, a heat sink, a heat exchanger, and a power-conditioning unit (PCU). A typical configuration is illustrated in Figure 13. Exhaust gases flow through the heat exchanger placed on the exhaust pipe, warming the hot side of the TEG module, while the cold side can be refrigerated using a liquid or an air-cooled heat tank system. The generated electric power is stored in a battery, matched with the car electrical system through a PCU (87) (88). This component is essential to guarantee the maximum power transfer in different driving conditions (idle or operational).
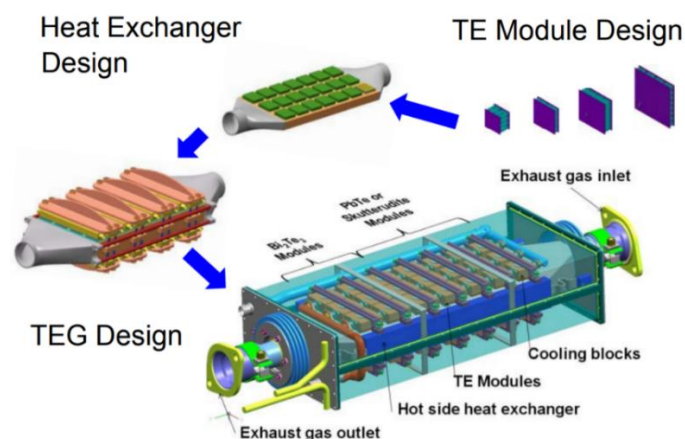
Figure 13: Example of ETEG design. Reproduced with permission (89). Reproduced with permission.

Komatsu (Japan), Marlow (USA), and HiZ (USA) are the main producers and seller of TEG modules using Bi_2Te_3 as active material. In particular, HiZ produces several devices working with a maximum temperature of 250 °C and ΔT of 200 °C, producing from 2 to 20 W of electrical DC power, at a cost between 18 and 80 EUR per module, depending on size and application. An important factor affecting the efficiency is the installation position. In general, it is possible to adapt both size and shape of the TEG module according to the recovery application. Several installation positions were tested, finding that for LT applications the optimal position is after the catalytic and filtering blocks of the exhaust system (90). As example, if using six Bi_2Te_3 TEG modules on a 3696 c.c. gasoline engine with hot and cold sides at 225 and 255 °C, respectively, the generated output power is higher than 40 W (91), improving the fuel economy of a vehicle up to 2% (92) (93). A different approach similar to the ORC case, substitutes the radiator with 72 TE modules (Bi_2Te_2 with an area of 4x4 mm) and 128 heat pipes, recovering energy from the engine coolant. The coolant flows in contact with the modules, transferring heat to the hot side, reaching 95 °C. To keep the cold side at 25 °C, a common air-cooling system is used. With this configuration, almost 30 W of electrical DC power is generated during the idle condition and almost 75 W during the driving condition, recovering 0.4% of wasted heat (93). Currently, the main limit in the commercialization of TEGs is the cost ranging between 2500-3500 EUR kW^{-1} while, to be competitive, the cost per energy capacity should be 395 EUR kW^{-1} (94). BMW, Nissan, Jaguar, Land Rover, and Porsche are some of the manufacturers investing in this field, although only HDVs can benefit from TEG systems, as it is easier to lower the installation cost, considering both the driving conditions (long driving distances) and the higher amount of energy from exhaust gases with respect to LDVs.

In the wearable domain, TEGs for LT waste heat harvesting do not use bulky material but rather thin layers of material and then, they are typically referred as micro-wearable TEG (μ-WTEG). Initially, TEGs employed rigid substrate for example a multistage thermopile (95), or a completely self-powered device to measure the oxygen content in blood embedded in a wristwatch (Figure 14) (96). In this case, a commercial sensor is placed on the forefinger. The wristwatch TEG charges a storage capacitor able to provide 0.7-2 V as output voltage while a DC/DC converter, ensuring stable and higher open circuit voltage, is mounted after the capacitor. A potential of 2.05 V is obtained, sufficient to supply the wireless sensor. The maximum power extracted is more than 100 μW during daily activities.
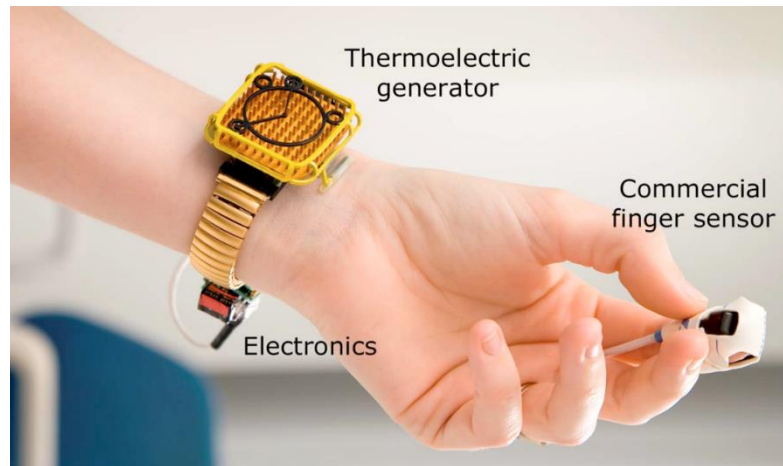
Figure 14: Fully powered wireless pulse oximeter (97). Reproduced with permission.

Then, an electroencephalography (EEG) system was proposed (98) and a battery-less device specific for EEG, electrocardiography, and electromyography data transfer was investigated (99). More recently, two different devices, a TE and piezoelectric energy harvester were characterized, to obtain a self-powered system (100). Results show that a 9 cm^2 TEG system is able to generate up to 20 µW at RT with respect to 3.7 µW of a 5 cm^2 piezoelectric one. By properly setting the parameters, they reached an output voltage (V_o) of 12 mV and open circuit voltage (V_{oc}) of 24mV, with a ΔT of 0.5 °C. The main drawback of rigid WTEGs is the incapability of adapting to the human skin curves, with consequent heat transfer losses. Moreover, the integration of rigid WTEGs into clothes is not easy and makes them uncomfortable and therefore, flexible devices have taken place. About wearable applications, comfort is not the only constraint. The low thermal difference extremely affects the overall efficiency. To overcome this limit, a local absorber placed below the TEG legs onto the layers was introduced (101), increasing the ΔT from the usual 2 ÷ 4 to 20 °C. A prototype with 10 p–n couples developed an output of around 4.44 µW and a V_{oc} of 55.15 mV. However, the local temperature increment could result uncomfortable for the user but this solution paves the way for future implementation in WTEGs. Another important step involves the integration of harvesting systems directly into the clothes fibers. Textile TE materials were analysed from both application (monitoring, computing, energy harvesting) and production (fabric finishing and coating or fibers/yarns coating technologies) points of view. Thanks to the easy integration, comfort, and air permeability they represent good alternatives.

1.3.3 Pyroelectric devices

Pyroelectric (PE) systems can be classified as energy harvester more than WHR/WHP systems since their application is still not adopted in large scale plants but on miniaturized device. The working principle is based on the pyroelectric effect i.e. the capability of specific materials to displace electrical charges from a temporal temperature variation, unlike thermoelectricity, where a stationary temperature gradient triggers the process. PE allows to avoid the main issue of TEGs that is the need of huge heat flows to maintain a large temperature gradient. For this reason, PE are under consideration because they have promising efficiency and ease in installation.

TEGs and PEGs performances were compared showing that even though the power generated by PEGs is low, their efficiency is much higher than that of TEGs (102). Recently, the innovative method for low-grade WHR based on nanogenerators has been deeply investigated and, even though a large margin for improvements is still present, some interesting results have been reached. For example, a hybridized pyro-vortex device, realized in polyvinylidene fluoride (PVDF), was realized, with an area of 2 cm^2 (103). The idea behind this work is to exploit the energy of the wind to realize an inexpensive and efficient harvester providing an uninterrupted energy output. In particular, the vortexes generated by this give rise to two conversion mechanisms: molecular transport, proportional to the gradients of the averaged velocity of the wind and heat fluxes, and convective transport, which gives rise to turbulent stresses caused by the momentum transfer produced by velocity fluctuations. In fact, this device allows to produce a stable output current, reaching a maximum power density of 2.82 μWcm^{-2}. A combination of PE and triboelectric hybrid energy harvesters has been also proposed with the idea of harvesting useful energy from low-grade waste fluids (104). In practice, drops of fluid can fall onto the device surface and energy can be recovered, exploiting both their thermal and kinetic energy. In fact, the drop hitting the surface will release its energy on it, provoking friction and thus triboelectrification to take place, but also have a certain temperature that will provoke temperature variation, allowing pyroelectrification. The maximum power produced per unit area is similar to the one proposed by Rouadi, lying around 2.6 μWcm^{-2}. Interesting is to notice that all these devices have been realized in PVDF, which seems to be a promising material in LT waste heat harvesting, and are in the solid state.

As already pointed out, heat constantly flows out from our body because of self-thermal regulation. Thanks to the homeostasis process, the human body is able

to maintain always an external temperature of about 36 °C, in a range of 1 °C. Furthermore, the physiological temperature changes are slow. Then, PE devices are clearly unsuitable for human body energy harvesting, because of the very efficiency. Nevertheless, a feasibility study on using a nanogenerator as a self-driven power supply for wearable devices was conducted (105) but it is evident that a combination of more effects, in particular triboelectric and PE, is the best solution to partially overcome this limit. At the same time, hybrid systems exploiting piezo and pyroelectric effects have been analysed (106). As an example, a mouse powered by means of human heat, was proposed, exploiting just the PE effect (107). In this case, the current generated by the PE effect was so low that was completely dominated by the one due to the piezoelectric effect, intrinsic of pyroelectric materials, that was provoked by the user's hand. Furthermore, a commercial PE device was investigated, composed of a piezoceramic foil placed between two conductive electrodes, proving the feasibility of of using water vapour to power the device, with a maximum output power of 0.034 μWcm^{-2} (108). Recently, a very interesting hybrid device was proposed, implementing a thermocell and a PE harvester, with the aim of recovering heat by both stable gradient and temporal variation of temperature (109). This device consists of two layers of PVDF, coated with carbon nanotube/cellulose nanocrystals composites, that serve as the electrode and absorber, and a block of polyurethane (PU), installed under the two PVDF films. The first deals with heat recovery from T variation, which is the PE part, while when the temperature gradient is established in the thermocell, a redox of ferrous/ferric chloride acid develops and converts it into useful electric energy. The cell has shown a current density production of 1.2 Am^{-2} for a ΔT of 100 °C. Assuming an illumination of AM 1.5G, the PVDF film generates up to 200 V of output voltage under illumination and -120 V with no illumination. The main advantage is then in the versatility as the device can harvest energy in different conditions, being operational 24/7. The harvester has shown a maximum output power produced, of 1.86 and $0.9mWm^{-2}$, for the thermogalvanic and PE components, respectively. Recently, a wearable PEG based on human breathing was proposed (110), where a thin film of PVDF was introduced in a mask. Exploiting the heat contained in the breadth, the maximum temperature variation recorded was 12 °C and the maximum power extracted reached 0.68 ΩWcm^{-2}.

1.3.4 Triboelectric devices

The triboelectric effect is a friction-induced electrification between two materials (see 2.2 for a more detailed description) and triboelectric nanogenerators (TENGs)

exploit contact electrification to convert mechanical energy into electricity (111), and they have been proposed to drive hundreds of light-emitting diodes (LEDs) (112), and charge lithium-ion batteries for powering wireless sensors and commercial cell phones (113). Recently, new devices have been conceived in order to collect energy from other environmental sources, such as wind (114), human motion (115), ocean waves, and tides (116). So far, TENGs have been designed employing solid-state materials whose optimal performances are obtained under dry conditions. However, triboelectricity has also been observed when liquids flow through pipes or polymeric films made of dielectric materials (117). As examples, voltages up to 300 mV have been observed when deionized water (DIW) flows through a 1 m long rubber tube (118), and surface charge densities of 4.5 C/cm^2 have been measured on water droplets injected by a polytetrafluoroethylene (PTFE) tip (119). Recently, with the advent of low power electronics (recovery systems, environmental monitoring, Internet of Things), triboelectric devices have found to be used as a renewable energy source, to harvest energy from several types of mechanical energy, including vibrational, rotational, wind, and tidal wave energy. The important features of these devices consist in their ease of fabrication, stability, and high-energy conversion efficiency (120). Therefore, the right functionalization of TENGs is important in order to build a marketable device for recovery applications, even from unexplored energy sources such as waste heat.

1.3.5 Magnetocaloric machines

In equilibrium conditions, a magnetic colloid (a suspension of magnetic nanoparticles in a liquid carrier) is a system where magnetization is thermodynamically coupled with temperature. At rest and at a specific temperature, some energy is transferred from phonons to the magnetic domain structure; if an external magnetic field is applied adiabatically, the magnetic domains align and reduce their number (entropy is consumed). When the field is removed, in the absence of energy exchanges with the environment, the material cools down. This is the so-called magnetocaloric effect (MCE). Considering a sample of ferromagnetic material, for example $MnCr_2S_4$ crystals: if no magnetic field is present, it is at thermal equilibrium with the surrounding environment and the magnetic dipoles are randomly oriented; then, if a magnetic field is switched on, the sample starts heating up, whereas the dipoles become aligned in the direction of the applied field. Subsequently, heat is transferred to the surrounding environment by means of a heat-transfer medium, but when the external magnetic field is removed, the dipoles orientations randomize, which translates into a further

temperature reduction of the sample. Possible heat-transfer materials are water or, for very LT, liquid He (121).

1.3.6 Technological overview

After this in-depth analysis, all the identified technologies have been sorted according to their typical application and optimal temperature range in Figure 15, in order to give an immediate, qualitative glimpse on the statistics of technology application. For this reason, the reader should focus on the temperature ranges rather than on the specific temperature values.
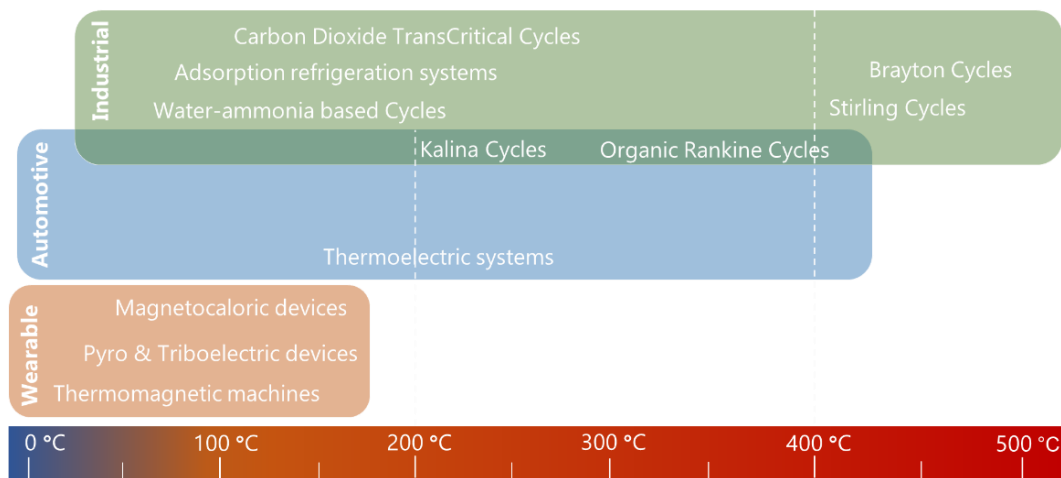
Figure 15: WHP and energy harvesting technologies sorted according to their typical application and optimal temperature range.

Furthermore, a comparison in terms of efficiencies, post-installation costs per kW, and typical installed power output is shown in Table 2. In the table, data relative to CDTCC are not given at MT due to the intrinsic properties of CO_2, implying that the cycle operates at cryogenic temperatures. The TE efficiencies are computed using conventional physical models and assuming reasonable temperature ranges in operating conditions (55 °C of ΔT for LT and 150 °C of ΔT for MT). For PE efficiency, data have been derived by a previous study and the same temperature ranges as above have been considered. The reader should never forget that closed-loop thermodynamic cycles based on any specific fluid feature intrinsic installation costs that strongly limit their power output lower bound, whereas purely solid-state systems such as TEGs and PEGs suffer from the specular limit, toward the upper bound.

Table 2: Efficiency and installation cost/kW comparison between the mentioned technologies.

	BC	SC	KC	CDTCC	ORC	TE	PE
η @ LT	0.40[a]	0.13	0.10[d]	0.15[f]	0.12[g]	0.037	0.15
η @ MT	0.40[a]	0.20	0.15[d]	–	0.20[g]	0.073	0.13
Cost per kW [kEUR kW⁻¹]	1[b]	12-2.5	6.5-2.5[e]	N.A.	2.8-1.2[h]	2.5	N.A.
Installed power [MW]	7.8[i]	0.0015[j]	0.4[k]	0.0046l	0.35[m]	0.012[n]	N.A.

The references are reported as follows: a (122), b (123), c (124), (125), e (126), f (125), g (74), h (127), i (128), j (129), k (130), l (131), m (132), n (86).

Once the available WHP technologies have been analyzed, the question arises on whether they could represent a valid approach to increase the quota of "green" installed power, working in conjunction with both fossil fuel-based processes and renewable resources-based processes. Considering their costs per kW and comparing them with photovoltaic systems (on average the cost per kW is 1.4 kEUR kW⁻¹ as of December 2018), two technologies are already competitive: BC and ORC. On the other side, the higher production costs of wind turbines (on average 1.4 kEUR kW⁻¹ as of 2017 for onshore plants and 3.5 kEUR kW⁻¹ for offshore ones), of biomass-based power plants (3.3 kEUR kW⁻¹), and of hydroelectric power plants (3.6 kEUR kW⁻¹) give already a strong evidence of the bright future this sector will experience. Parallel to industrial development and technology readiness level, the most statistically relevant results in all ranges of reviewed current solutions mainly involve optimization through thermoeconomic, exergetic, and LCA analyses, as well as material development. A completely different approach is seen for emerging technologies, where basic studies and theoretical developments are frequent. In conclusion, WHR/WHP technologies have reached a maturity level that could significantly boost their mass application in close relationship with industrial processes and wherever waste heat is generated, such as in the automotive field, regardless of the policies enforced at the local/global

level. Scientific research, on the other hand, is rapidly expanding and casting light on less explored multidisciplinary fields, where combined effects (such as pyro + thermo + magneto) have been shown to greatly enhance conversion efficiencies and volume/mass specific power/energy. In particular, the most promising directions to explore are 1) magnetocaloric and thermomagnetic hydrodynamic machines on the one side and 2) TE, triboelectric, and PE devices on the other side. The former group is suitable for small-scale systems and the latter suitable for wearables (25).

1.4   A novel concept for energy harvesting

Up to now, we discussed energy and climate issues, waste heat to power and energy harvesting. Surprisingly, this is not where the project was born. In fact, it was conceived far away from these topics. So, let's step back for a moment to see where everything started: the space exploration in extreme environments.

Extreme planetary environments represent the next frontier for in situ exploration, where future missions will be characterized first by robotic reconnaissance and, later, by human interventions (133). In these harsh scenarios, several factors, such as temperature, pressure and radiation, make many missions hard to conceive at present. In fact, extreme environments, on Earth and other locations in the solar system, are characterized by very low or very high temperatures, high radiation, high pressure, corrosive and toxic chemicals, where autonomous robotic missions need increasing complexity and ultra-advanced technology (133) since interactions with robots are difficult to model due to reasons such as dynamics, uncertainty, complexity and unpredictability (134). Although humans have already successfully placed rovers, landers and probes respectively on the Moon, on Mars, on the comet 67P/Churyumov–Gerasimenko, on Jupiter, on Titan - just to give some examples - robotic system development for planetary surface exploration is still at the dawn (133) mainly due to unstructured, sandy and rocky terrain and micro-gravity. In these environments, sustained damages to robots are too costly to fix and rescue efforts are unavailable for robots trapped in the environment due to their remoteness (134). Even if a larger robot would better suits for traversing most surfaces, the increased size of present-day rovers limits their mobility capabilities and the need for developing a whole new generation of small, agile, and rugged robots, performing unconventional mobility including hopping, climbing, rolling and crawling, is increasing (135). Furthermore, planetary robotics must also address several conflicting demands. First, high levels of system robustness are required despite time delays for Earth communication that

necessitates high levels of autonomy. Second, the operational environments are both very complex and yet only partially known. Finally, the variability of technology needs across the expanse of prospective surface missions is immense, yet technology development funding is extremely limited (133).

Advancements of material science and cybernetic technology in the field of Smart Fluid Systems (SFS) show that, compared to conventional robotic systems, liquid or colloid-based robots would offer advantages in terms of versatility, adaptability, resiliency, mobility, distributed architecture and autonomy, especially for applications in harsh environments, such as gas giants, comets and asteroids, or deep-sea and post-earthquake areas for search and rescue applications (133) but also for oil and gas pipes and nuclear waste inspections (136). In fact, a soft and deformable robot would be suitable, as example, for traversing unpredictable terrain, moving through small holes and many other applications in the exploration of gas giant planets or small bodies like comets and asteroids, oceans and lakes depths, post-earthquake areas, and so on. For example, it is worth considering Venus, where a spherical and deformable shape would better suits in high-pressure environments (90 bar) and an inert, non-metallic, shell would be fundamental for surviving a corrosive atmosphere (containing sulfuric acid), where conventional electronics would not be able to withstand high temperatures (up to 473 °C). A smart fluid (SF) is defined as a liquid-state system featuring unprecedented properties thanks to the cooperation of two phases, whose single constituents enable smart distributed functionalities such as information processing capabilities, self-powering, sensing capabilities, and mobility (133). Thus, complex systems based on liquid media, named colloidal autonomous systems (CASs) represent a new paradigm in the field of cybernetic systems, joining the versatility of conventional robotics and the advantages of soft robotics. Here, energy harvesting, storage and management capabilities play an essential role. Indeed, in order to increase the energy efficiency and the autonomy level of intelligent robots, harvesting energy from the external environment and internal subsystems has become fundamental (137) (138) (139). In particular, with the advent of soft robots, composed of highly compliant materials similar to those found in living organisms (140), energy harvesting from many sources has been explored, mainly for mobility purposes (141) (142). For this purpose, the engineering feasibility of an energy harvesting and storage system applicable to SFS, named Colloidal EneRgEtic System (CERES), has been assessed, proposing a starting point to address waste heat to power and energy harvesting with nonconventional solutions (143), combining the nanoscale properties of solid materials and the advantages of fluids.

Physics

As preview, the main materials involved in the CERES project are colloids featuring, in particular, magnetic, triboelectric and pyroelectric properties. Thus, in this section, the physical phenomena governing the system are described to provide a better understanding of the initial conceptual ideas and further development, during the design and characterization of the prototypes.

2.1   Magnetic phenomena

2.1.1 Magnetism

In nature, different materials respond differently to the influence of an external magnetic field, $\vec{H}$. The capability of certain materials, like mineral magnetite (Fe_3O_4), to attract iron (Fe) is known since ancient times. However, apart from this macroscopic effect, the magnetization generated within the material depends on the nature of the material itself. In fact, magnetism depends on the atomic/crystalline structure of the sample, the orbital momentum and spin of electrons, and macroscopic geometry, and it is classified as (144):

- diamagnetism: it appears in all materials and is the propensity of a material to oppose an applied magnetic field and to be repelled. However, in a material featuring also paramagnetic/ferromagnetic properties (a tendency to enhance an external magnetic field), the paramagnetic/ferromagnetic behavior dominates. Thus, diamagnetism is observed only in a purely diamagnetic material, such as water, wood and heavy metals (gold, mercury), where there are no unpaired electrons and the intrinsic electron magnetic moments cannot produce any bulk effect. In these cases, the magnetization arises from the electrons' orbital motions, understanding of which requires a quantum-mechanical description. Since these materials have a very small relative magnetic permeability μ_r [H/m], their particles tend to develop an induced magnetic field in the opposite direction of an external magnetic field. Typically, this effect is very weak and no macroscopic consequence are observed. However, if it is the only magnetic contribution, i.e. in diamagnetic materials, the repulsive force can be so strong to cause levitation;

- paramagnetism (Figure 16a): typical of materials weakly attracted by the external magnetic field such as aluminum, titanium and iron oxide. In paramagnetic materials, there are unpaired electrons, i.e. atomic or molecular orbitals with exactly one electron in them, which is free to align its magnetic moment in any direction. When an external magnetic field is applied, these magnetic moments tend to align themselves in the same direction as the applied field, reinforcing it. This phenomenon can be described by means of the Curie's law, indicating that the susceptibility, χ, of paramagnetic materials is inversely proportional to their temperature, i.e. that paramagnetic materials become more magnetic at lower temperatures;

- ferromagnetism (Figure 16b): typical of few materials such as iron, nickel, cobalt, their alloys, and some alloys of rare-earth metals that, like paramagnetic materials, have unpaired electrons which tend to align parallel to the external magnetic field. However, additionally, they also tend to orient parallel to each other to maintain a lowered-energy state, even in the absence of an applied field. So, contrarily to paramagnets, ferromagnets retain the magnetization once the external field is removed making possible to realize permanent magnets, since the magnetic moments of atoms stick together and align themselves into small regions called magnetic domains. At the same time, every ferromagnetic substance has its own Curie temperature, or Curie point, above which it loses its ferromagnetic properties. This is because the thermal tendency to disorder overwhelms the energy-lowering due to ferromagnetic order;

- antiferromagnetism (Figure 16c): typical of few materials such as hematite, chromium, alloys such as iron manganese (FeMn) and oxides such as nickel oxide (NiO) that, unlike a ferromagnetic materials, have magnetic moments of neighboring valence electrons which tend to point in opposite directions, arranged so that each neighbor is anti-parallel. Antiferromagnets have a zero net magnetic moment, meaning that the material itself produces no field. Antiferromagnets are less common compared to the other types of behaviors and are mostly observed at low temperatures. In varying temperatures, antiferromagnets can be seen to exhibit diamagnetic and ferromagnetic properties;

- ferrimagnetism (Figure 16d): typical of few materials such as magnetite (the oldest known magnetic material), yttrium iron garnet (YIG), cubic ferrites composed of iron oxides with other elements such as aluminum, cobalt, nickel, manganese and zinc. Like ferromagnets, they retain their magnetization in the absence of a field but, like antiferromagnets,

neighboring pairs of electron spins tend to point in opposite directions. These two properties are not contradictory, because in the optimal geometrical arrangement, there is more magnetic moment from electrons pointing in one direction, than from those pointing in the opposite one and the overall magnetization is partially counteracted by a population of atoms developing a weak opposite magnetic field;

- superparamagnetism: typical of ferromagnetic or ferrimagnetic nanoparticles (NPs), where magnetization can randomly flip direction under the influence of temperature, with a typical flipping time called the Néel relaxation time. In the absence of an external magnetic field, when the time used to measure the NPs magnetization is much longer than the Néel relaxation time, their magnetization appears to be in average zero: they are in the so called "superparamagnetic state". In this situation, an external magnetic field is able to magnetize the NPs, similarly to a paramagnet. However, their magnetic susceptibility is much larger than that of paramagnets. Ferrofluids (FFs) behave as superparamagnetic materials.
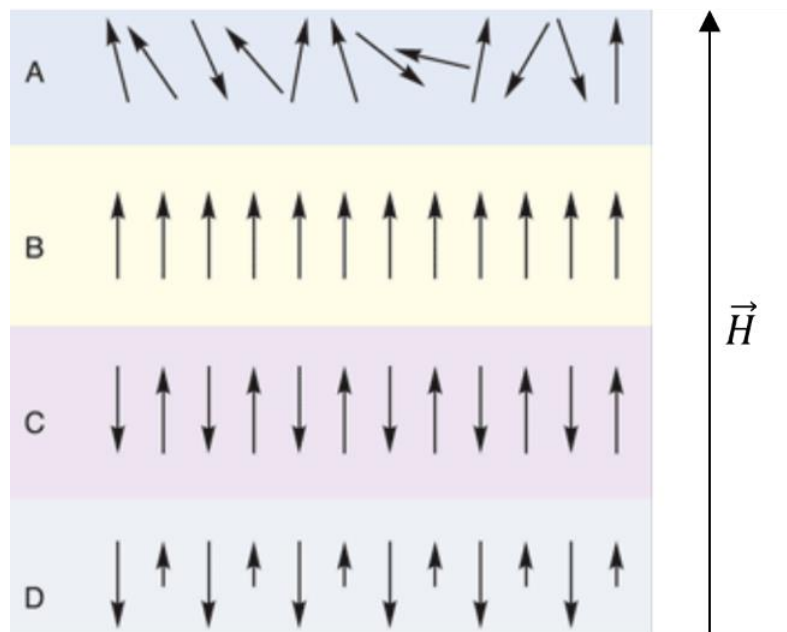
Figure 16: Different types of magnetism in materials: (A) paramagnetism, (B) ferromagnetism, (C) antiferromagnetism, (D) ferrimagnetism.

2.1.2 Magnetization

The term magnetization, typically denoted by with $\vec{M}$ [A/m], is defined as the total magnetic moment per unit volume, i.e. the vector expressing the density of magnetic dipoles formed spontaneously or because of the external field. It also represents the ability of the material to re-orient its magnetic dipoles according to the direction of the applied magnetic field, $\vec{H}$ [A/m], creating an additional contribution to t*h*e magnetic flux density, $\vec{B}$ [T], and having the general form:

$$\vec{B} = \mu_0(\vec{H} + \vec{M}).$$

Since the magnetization is a function of the applied magnetic field, in the case of paramagnetic/ferromagnetic materials, provided that the magnetic relaxation time of the material is much shorter than that of magnetic field variation, the relation between $\vec{H}$ and $\vec{M}$ can be expressed as:

$$\vec{M} = \chi\vec{H}.$$

In a paramagnetic material, where the magnetic moments are initially randomly oriented and slightly re-orient in the presence of magnetic field, the magnetization behaviour can be described by the Langevin relation. It represents a theoretical magnetization curve as function of an external applied magnetic field in the case of ideal paramagnetic gas of particles, without considering any dipole-dipole interaction. Neglecting the mutual action of the magnetization field generated by the paramagnetic particles, the mechanical work, W [J], done on a magnetic dipole by an external magnetic field is:

$$W = -\vec{m} \cdot \vec{B} = -m B \cos\theta,$$

where m [A m^{-2}] is the magnetic moment of a magnetic dipole. According to Boltzmann statistic, the probability of occupation of a state with energy W is:

$$p_B = exp\left(\frac{-W}{k_B T}\right) = exp\left(\frac{m B \cos\theta}{k_B T}\right) = e^{\beta\cos\theta},$$

with
$$\beta = \frac{m B}{k_B T}.$$

In superparamagnetic particles, m re-orient almost immediately with the application of an external field. The Boltzmann statistics states that thermal

fluctuations counteract the action of the magnetic field generating a randomness of the orientation (angular distribution) of the magnetic dipoles due to the thermal agitation of the particles. In this case, we assume that the magnetization magnitude is constant and only its direction can change, rotating on a sphere of radius $\vec{m}$.

The net magnetization is the average component of the total magnetization moment along the direction of the external magnetic field. From a statistical mechanics point of view, it can be defined as the ensemble average over the surface of the sphere (phase space in spherical coordinates):

$$M \ = \ n\,m \ \frac{\int_0^{2\pi} d\varphi \int_0^{\pi} e^{\beta \cos\theta} \cos\theta \sin\theta \, d\theta}{\int_0^{2\pi} d\varphi \int_0^{\pi} e^{\beta \cos\theta} \sin\theta \, d\theta},$$

where $n = N/V$ is the volume concentration of magnetic dipoles, N is the number of dipoles and V is the control volume. Assuming identical and non-interacting particles:

$$n\,m \ = \ \frac{N}{V} V_{NP} M_d \ = \ \Phi M_d = M_s,$$

where Φ is the volume packing fraction of NPs within the system ($0 \leq \Phi \leq 1$), $M_d = \frac{m}{V_{NP}}$ is the domain magnetization of the bulk magnetic particle, V_{NP} is the volume of the particles and M_s is the saturation magnetization, which corresponds to the value of magnetization when all dipoles are aligned with the external magnetic field. For magnetite particles $M_d = 4.46 \times 10^2$ kA/m (145).

By solving the integral, we obtain the Langevin relations (Figure 17):

$$M \ = \ M_s \left(\coth \beta - \frac{1}{\beta} \right),$$

$$L(\beta) = \frac{M}{M_s} = \coth \beta - \frac{1}{\beta},$$

with
$$\beta = \frac{\pi}{6} \frac{M_d H d^3}{\kappa_B T}.$$

In the weak-field limit (Figure 17), the Langevin relation can be expressed as:

$$M \ \simeq \ M_s \frac{m\,B}{3\,k_B T} \ = \ n\,m \ \frac{m\,B}{3\,k_B T}.$$
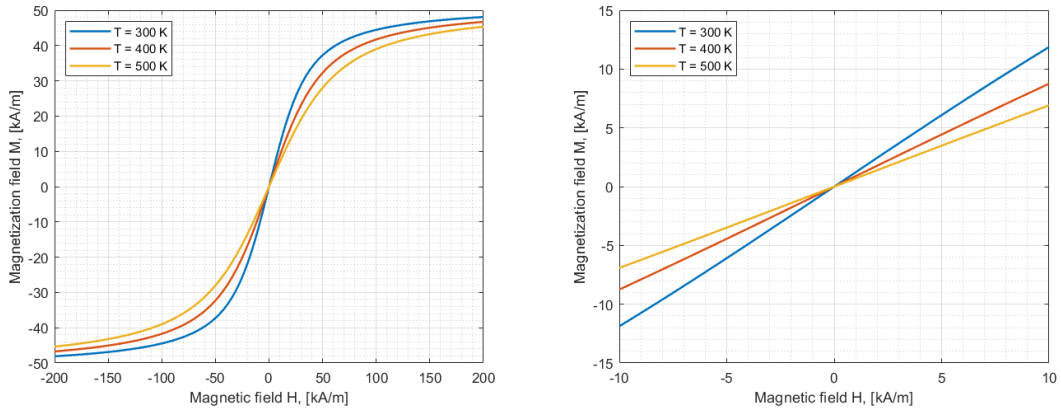
Figure 17: Langevin relation at different temperatures for FF EMG 901 with NPs concentration $\mathbf{\Phi}$ = 0.12. Left: full magnetization curve, right: linearization in the weak field limit (146). Reproduced with permission.

2.1.3 Magnetic flux

One way to harvest energy in the CERES project is by converting the momentum generated by the motion of a magnetic fluid into electro-magnetic energy (see 4.1) in a two-steps recovery system: first thermal to dynamic and then, dynamic to electromagnetic energy conversion. In this case, the extraction system is based on the Faraday-Neumann-Lenz law, in which a variation in time of the magnetic induction flux, Φ [Wb], over an open surface will generate an induced electromotive force according to:

$$\phi_{m(t)} = -\frac{\partial \Phi(\vec{B})}{\partial t} = -\frac{\partial}{\partial t} \iint_{\Sigma(t)} \vec{B}\left(\vec{r}(t)\right) \cdot \hat{n} \, dS.$$

Due to the linearity of the derivative and integral operators, it is possible to decouple the time variation with respect to the magnetic induction (transformer) and to the open surface (motional):

$$\phi_{m(t)} = -\left(\frac{\partial \Phi(\vec{B})}{\partial t}\bigg|_{\Sigma = const} + \frac{\partial \Phi(\vec{B})}{\partial t}\bigg|_{B = const}\right),$$

$$\phi_{m(t)} = -\underbrace{\iint_{\Sigma} \frac{\partial \vec{B}(\vec{r}(t))}{\partial t} \cdot \hat{n} \, dS}_{Transformer} + \underbrace{\oint_{\partial\Sigma} \vec{v}_{\Sigma}(\vec{r}(t)) \times \vec{B}(\vec{r}(t)) \, d\vec{l}}_{Motional}.$$

The transformer part represents power generated by the variation of particle magnetization in time, in a fixed region, Σ, while the motional part can represents

the effects of the surface motion or the surface deformation in time. The motional electromotive force represents the action of the Lorentz force on the free charges (electrons) in the conductive material that defines the open surface. Note that this effect can be observed only if the charges have a velocity component perpendicular to the magnetic induction field. Therefore, the velocity term represents the variation in time of the open surface Σ along a generic path.

Assuming that a static magnetic field is differentiable and defined at each point of the domain, the magnetic induction is defined as:

$$\vec{B}(\vec{r}(t)) = \mu_0\big[\vec{H}(\vec{r}(t)) + \vec{M}(\vec{r}(t))\big] = B(\vec{r}(t))\,\hat{u}_B,$$

where $\hat{u}_B$ is the unit vector in the direction of the magnetic field, and $\vec{r}(t)$ represents the displacement vector.

In the transformer part, the first term is a derivative of a vector field with respect to a scalar term and it is developed as:

$$\frac{\partial \vec{B}}{\partial t} = \frac{\partial B}{\partial t}\hat{u}_B + \vec{\omega}_B \times \vec{B},$$

where $\vec{\omega}_B$ is the angular velocity of the vector $\vec{B}$. Considering the magnetic induction field oriented along the normal vector of the surface in order to maximize the magnetic flux ($\hat{u}_B \cdot \hat{n} = 1$):

$$\left(\vec{\omega}_B \times \vec{B}\right) \cdot \hat{n} = 0.$$

Then, supposing a static external magnetic field, the time derivative of the magnetic induction is:

$$\frac{\partial B}{\partial t} = \mu_0 \frac{\partial M}{\partial t}.$$

Since in the CERES system is a way to harvest energy by means of static coils defining a static open surface, Σ, the motional part of the equation is negligible. So, the temporal definition of the electromotive force, $\phi_{m(t)}$, is:

$$\phi_{m(t)} = -\iint_\Sigma \mu_0 \frac{\partial M(\vec{r}(t))}{\partial t}\hat{u}_B \cdot \hat{n}\, dS.$$

It is now possible to use the chain rule in order to reduce the variation of the scalar field M into its spatial and temporal components:

$$\frac{\partial M(\vec{r}(t))}{\partial t} = \nabla M(\vec{r}) \cdot \vec{v}_{\mathrm{p}}(t),$$

where $\vec{v}_{\mathrm{p}}(t)$ is the particle velocity distribution as function of time and $\nabla M(\vec{r})$ is the gradient of the magnetic induction. Note that all the parameters are defined only in the integral domain Σ. Thus, the closed-form equation of electromotive force is:

$$\phi_{m(t)} = -\iint_{\Sigma} \mu_0 [\nabla M(\vec{r}) \cdot \vec{v}_{\mathrm{p}}(t)][\hat{u}_B \cdot \hat{n}] \, dS.$$

Now, the magnetization field can be defined by the Langevin relation so that the role of temperature, magnitude of the external magnetic field and particle concentration is highlighted (also influencing the motional part of the system). Extending the domain of integration using a solenoid coil structure for the energy harvesting, a "volumetric domain" is defined, where ϕ_m is proportional to the number of coil of the solenoid N:

$$\phi_{m(t)} = -\sum_{i=1}^{N} \iint_{\Sigma_i} \mu_0 [\nabla M(\vec{r}) \cdot \vec{v}_{\mathrm{p}}(t)][\hat{u}_B \cdot \hat{n}_i] \, dS.$$

Supposing the magnetization and velocity contribution uniform along the solenoid:

$$\phi_{m(t)} = -N \iint_{\Sigma} \mu_0 [\nabla M(\vec{r}) \cdot \vec{v}_{\mathrm{p}}(t)][\hat{u}_B \cdot \hat{n}] \, dS.$$

So, the electromotive force is generated by the variation of the relative magnetic permeability or by the movement of the ferromagnetic core inside a solenoid.

Supposing that the magnetization field is parallel to the normal surface vector and the velocity of the particles is collinear with respect to the gradient of the magnetic induction and M is a symmetric function with respect to the center of the solenoid:

$$\phi_{m(t)} = -N\mu_0 \frac{\Delta M}{L} \Sigma \, v_{\mathrm{p}}(t),$$

where $\langle M \rangle$ is the mean value of the magnitude of the magnetization along the length of the solenoid, L is the length of the solenoid and Σ is the area of the solenoid. The term $n = N/L$ is the linear coil density. In the weak-field limit and with constant temperature:

$$\phi_{m(t)} = -n\mu_0 \frac{C}{T} \Delta H \Sigma \, v_{\mathrm{p}}(t).$$

Thus, for optimizing the design of a CERES harvester, the velocity changes in function of temperature and magnetic field must be investigated. This can be done by means of a holistic approach, mainly based on the experimental knowledge of the physical mechanisms that are involved in the motion generation, or by simulating the behaviour of the fluid inside the device, or by characterizing the extraction system in a controlled way as in 4.3.1 (146).

2.1.4 Ferro-hydrodynamics: conservation equations

When dealing with fluids, the principle of mass conservation states that for any closed system (no transfer of energy and matter), the mass of the system must remain constant over time. So:

$$\frac{d\rho}{\rho} = \left(\frac{\partial ln\rho}{\partial P}\right)_T dP + \left(\frac{\partial ln\rho}{\partial T}\right)_P dT,$$

where ρ is the density [kg/m^3], P the pressure [Pa] and T [K] the temperature. The first term represents the bulk compliance, while the second term is the negative of the volume coefficient of thermal expansion. In the case of colloidal systems moving far from sonic velocity, the finite compressibility of the fluid is negligible. So, the fluid is considered incompressible, i.e. no variation of density in time is observed (no expansion or compression).

The coefficient of thermal expansion plays an important role in the system dynamics and the density is linearized, around the working point temperature, using a first order Taylor expansion:

$$\rho = \rho_0[\, 1 - \alpha_V(T - T_0)],$$

where α_V is the coefficient of thermal expansion.

Adopting an Eulerian approach, it possible to demonstrate that:

$$\frac{D\rho}{Dt} + \rho \nabla \cdot \vec{u} = 0,$$

where $\vec{u}$ is the velocity and the term $\frac{D}{Dt}$ is the material derivative, defined as:

$$\frac{D}{Dt} = \frac{\partial}{\partial t} + \vec{u} \cdot \nabla,$$

and considering an incompressible fluid:

$$\nabla \cdot \vec{u} = 0.$$

The presence of superparamagnetic NPs like magnetite generates a strong response to external magnetic fields leading to the so called magneto-convection effect. In ferro-hydrodynamics the ponderomotive Kelvin force plays a fundamental role pulling the more magnetised portion of fluid to move toward the region where B is stronger. In the case where FF is non-uniformly heated, i.e. a thermal gradient is set across the fluid layer:

- in case of non-uniform field, e.g. generated by placing a permanent magnet in proximity to the liquid layer, ∇H is directly responsible for the fluid motion since a gradient of magnetic forces act on the NPs;
- in case of uniform field, e.g. generated by means of an electromagnet or Helmholtz coils, the magnetic induction, $\vec{B}$, is expressed as the sum of magnetization, $\vec{M}$, and magnetic field, $\vec{H}$. In this case, since $\vec{M}$ changes as function of the temperature, T, the internal magnetic field of the NPs, $\vec{H}$, has to lower where the magnetization is stronger, generating a gradient of magnetic field.

The momentum equation for a magnetic fluid under gravitational and magnetic fields is obtained considering the internal and external forces acting on the system: inertial forces, pressure forces, viscous forces plus gravitational and magnetic forces. For an incompressible Newtonian fluid in the Eulerian frame, the momentum equation is:

$$\rho \frac{D\vec{u}}{Dt} = -\nabla p + \rho \vec{g} + \eta \nabla^2 \vec{u} + \vec{f}_m,$$

where t is the time, $\vec{g}$ the gravitational body force, η the dynamic viscosity and $\vec{f}_m$ the magnetic body force. In the case of dispersed paramagnetic colloidal particles, in addition to the force induced on a magnetic dipole by an external magnetic field, the internal magnetization of the fluid induces a variation of the external magnetic field. Therefore, in this case, it is better considering the action of the magnetic induction on the single magnetic dipole. Using the separated magnetic charge model for a magnetic dipole the force acting on a single domain NP, represented as a magnetic dipole, is evaluated (147). Thus, the local force is defined as:

$$\vec{F}_m = (\vec{m} \cdot \nabla)\vec{B},$$

where $\vec{m}$ is the magnetic moment of a single dipole and $\vec{B}$ the magnetic induction. Since, in the case of FF, the NPs dimension is below the critical diameter (about 10 nm (148)), the particle is considered as a single domain structure and the magnetic force per unit volume is:

$$\vec{f}_m = (\vec{M} \cdot \nabla)\vec{B},$$

with $\vec{M}$ representing the magnetization density of the whole fluid. Note that this term does not represent the macroscopic Kelvin body force, since it takes into account the magnetic dipole interaction that is not negligible in FFs.

In the quasi-stationary limit, the magnetized particles react to the applied magnetic field almost instantly. Therefore, the magnetization vector $\vec{M}$ will be collinear with $\vec{H}$ in each instant of time, so that:

$$\vec{M} = \frac{M}{H}\vec{H} \qquad\qquad \vec{M} = \frac{M}{B}\vec{B}.$$

Owing to these assumptions:

$$(\vec{M} \cdot \nabla)\vec{B} = \frac{M}{B}(\vec{B} \cdot \nabla)\vec{B},$$

and considering the vector equality:

$$(\vec{B} \cdot \nabla)\vec{B} = B\nabla B - \vec{B} \times (\nabla \times \vec{B}).$$

Considering a non-conducting fluid, with no displacement currents, it is possible to express the Maxwell's equations as:

$$\nabla \cdot \vec{B} = 0 \qquad\qquad \nabla \times \vec{H} = \vec{J} + \frac{\partial \vec{D}}{\partial t} = 0,$$

and combining the above mentioned equations:

$$\nabla \times \vec{B} = \mu_0 \nabla \times (\vec{M} + \vec{H}) = \mu_0 \left(\frac{M}{H} + 1\right)\nabla \times \vec{H} = 0.$$

Summing up:

$$\rho\frac{D\vec{u}}{Dt} = -\nabla p + \rho\vec{g} + \eta\nabla^2\vec{u} + M\nabla B.$$

Since $\vec{M}$ is both function of the magnetic field and the temperature:

$$\nabla M(H, T) = \frac{\partial M}{\partial H} \nabla H + \frac{\partial M}{\partial T} \nabla \mathrm{T},$$

with:

$$\chi \equiv \frac{\partial M}{\partial H}, \qquad K \equiv -\frac{\partial M}{\partial T},$$

where χ is the differential magnetic susceptibility and K the pyromagnetic coefficient. The Langevin relation and the Curie law highlight the dependence of χ on the magnetic field intensity and the temperature. However, it is possible to decouple the temperature dependence using the pyromagnetic coefficient:

$$\chi = \mu_0 \frac{C}{T}, \qquad K = \mu_0 \frac{C}{T^2} H.$$

Finally, the magnetic force per unit volume can be written as:

$$M \nabla B = \mu_0 M \nabla M + \mu_0 M \nabla H = \mu_0 M [(1 + \chi) \nabla H - K \nabla T]].$$

Considering a small variation of the magnetization with respect to the magnetization around the working point, M_0, it is possible to use a first order approximation for describing the intensity of the magnetization field:

$$M = M_0 + \chi \Delta H - K \Delta T,$$

with:

$$\Delta H = H - H_0, \qquad \Delta T = T - T_0,$$

with H_0 being the applied magnetic field at temperature T_0.

Finally, applying the Boussinesq approximation (valid for small variation of density $\Delta \rho \ll \rho_0$), assuming that variations in density have no effect on the flow field, except for buoyancy forces:

$$\rho \frac{D \vec{u}}{Dt} = -\nabla p + \rho_0 \alpha_V \Delta T \vec{g} + \eta \nabla^2 \vec{u} + \mu_0 M [(1 + \chi) \nabla H - K \nabla T].$$

Regarding both thermal and mechanical energy, combining the approach for the electrodynamics of moving media and the thermodynamic approach, the temperature equation for an incompressible magnetizable fluid is:

$$dU = TdS - pdV + \mu_0 H \cdot dI,$$

where U is the internal energy per unit mass, T the temperature, S the entropy per unit of mass, V the specific volume, p the pressure and $I = MV$.

For an incompressible fluid:

$$\frac{dU}{dt} = T\frac{dS}{dt} + \mu_0 \vec{H} \cdot \frac{d\vec{I}}{dt}.$$

According to Finlayson (149), it is possible to express the entropy as:

$$\rho T \frac{dS}{dt} = -\nabla \cdot \vec{q} + \Phi,$$

where $\vec{q} = -\kappa \nabla T$ is the heat flux and Φ is the viscous dissipation. Considering the continuity equation, the Fourier's law for thermal conduction and the Maxwell relations:

$$\left[\rho C_{p,H} - \mu_0 \vec{H} \cdot \left(\frac{\partial M}{\partial T}\right)\right]\frac{DT}{Dt} + \mu_0 T \left(\frac{\partial M}{\partial T}\right) \cdot \frac{\partial \vec{H}}{\partial T} = \kappa \nabla^2 T + \Phi,$$

where $C_{p,H}$ is the heat capacity at constant volume and magnetic field and κ the thermal conductivity (assumed constant). Supposing that conduction, natural convection and magneto-convection are the main heat transfer mechanisms in the colloid, neglecting the magnetocaloric effects and the viscous dissipation:

$$\rho C_p \frac{DT}{Dt} = \kappa \nabla^2 T.$$

2.1.4.1 Thermomagnetic convection

In magnetic fluid, it is possible to generate convection motion by means of spatial variation of magnetization, which depends on temperature and a large enough temperature gradient across the volume containing the fluid is applied. The maximum possible variation in the particle magnetization occurs in the neighborhood of phase transition where the particle have null magnetization. However, the effect is still present even if we are far away from it. If dealing with

colloidal suspensions of paramagnetic particles in a carrier liquid, the pyromagnetic coefficient can play an important role in the convection mechanism. Supposing to have a one-dimensional converter, filled with FF, in which a homogeneous magnetic field is applied along the x-direction and a thermal gradient is set across the isothermal boundary layers of the reactor (along the x-axis), as per Figure 18.
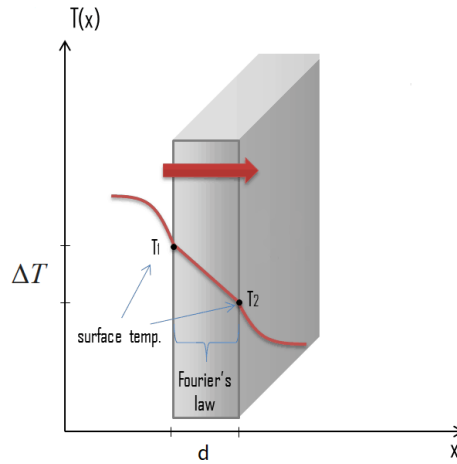
Figure 18: Linear temperature decay in one-dimensional reactor (146). Reproduced with permission.

Since:

$$\nabla \cdot \vec{H} = -\nabla \cdot \vec{M},$$

and:

$$\frac{\partial H_x}{\partial x} = -\chi \frac{\partial H_x}{\partial x} + K \frac{\partial T}{\partial x} = \frac{K}{1+\chi} \frac{\partial T}{\partial x},$$

where H_x is the x-component of the internal magnetic field, a spatial variation of temperature will induce a gradient of magnetic field intensity (the cooler part having a higher magnetization than the warmer part), so an induced force acting on the magnetic particles along the x-direction. Note that even if a uniform magnetic field is applied to a non-isothermal ferrofluid, Kelvin force driving thermomagnetic convection will arise.

Supposing the distance between the two isothermal walls being small enough, the thermal gradient is considered linear:

$$H(x) = H(0) + \frac{K}{1+\chi}\frac{\Delta T}{d}x,$$

where $H(0)$ is the value of the external magnetic field intensity. Thus, the crucial term affecting the effect of the thermo-magnetic force is the difference of temperatures across the layer, ΔT, and the distance between the walls, d.
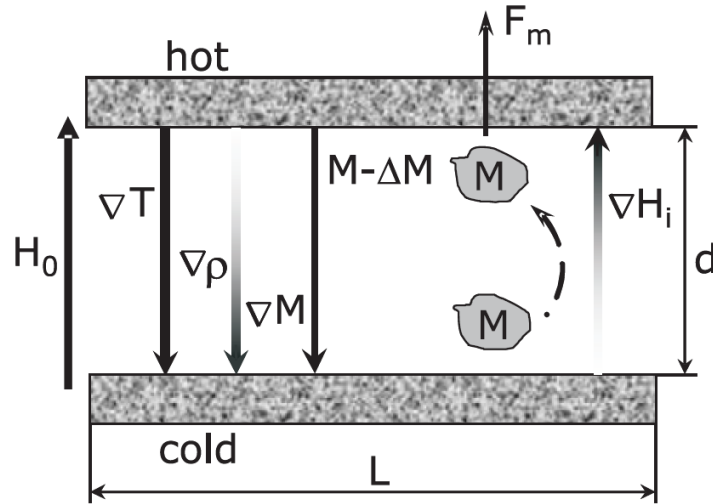
Figure 19: Sketch of thermomagnetic effect (150). Reproduced with permission.

Therefore, thermomagnetic convection is the result of the ponderomotive force due to non uniform magnetization. As per natural convection, this phenomenon arises as consequence of non uniform heating along the direction of the thermal gradient. This can be exploited in the case of reduced gravity conditions (in orbit), where non-conducting FF with high pyromagnetic coefficient, far from its Curie's temperature, can be employed in heat exchange application when natural convection is not possible.

An analysis on the ΔT required to induce natural and thermomagnetic convection in magnetite-based FFs (with different solvents as carrier fluid) has been conducted, showing that, in a geometric configuration similar to the one in Figure 19 with thin layers ($\leq$ 1mm), magnetic convection predominates over the buoyancy mechanism (Table 3), giving precious indications for the CERES design and optimization.

Table 3: Temperature difference required to induce natural (N) and thermomagnetic (T) convection in magnetite-based FFs (149).

	Water		Kerosene		n-Heptane	
			ΔT [K]			
d [cm]	N	N+T	N	N+T	N	N+T
1	0.1	0.1	0.05	0.05	0.008	0.008
0.5	0.9	0.9	0.4	0.4	0.06	0.06
0.2	15	7	6	5	1	1
0.1	120	17	51	19	8	5

Furthermore, the interaction between of thermal and magnetic fields and the combination of their directions can be exploited to impose a specific direction to the magnetic fluid activated by a thermal gradient. Suslov et al. (151) developed a computational and experimental analysis in a vertical layer of an oil-magnetite based FF imposing isothermal surfaces and setting the thermal gradient. Then, a homogeneous and isotropic magnetic field orthogonal to the surfaces and parallel to the thermal gradient vector was imposed using a Helmholtz coil. Results show different possible motional patterns of the magnetic colloid, with a strong dependence to the magnitude of the magnetic field and the intensity of thermal gradient. Four types of characteristic motions have been observed, reported in Figure 20 and for the cases of natural convection and vertical thermomagnetic rolls experimental infrared images are shown in Figure 21.
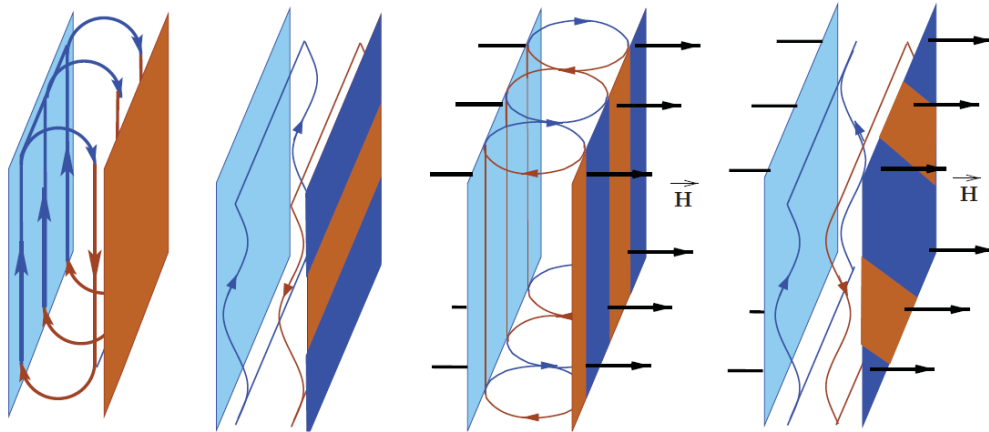
Figure 20: Schematics of main flow patterns (from the left to the right): natural convection (*H*=0); thermogravitational waves; stationary vertical thermomagnetic rolls; oblique thermomagnetic waves (151). Used with permission.
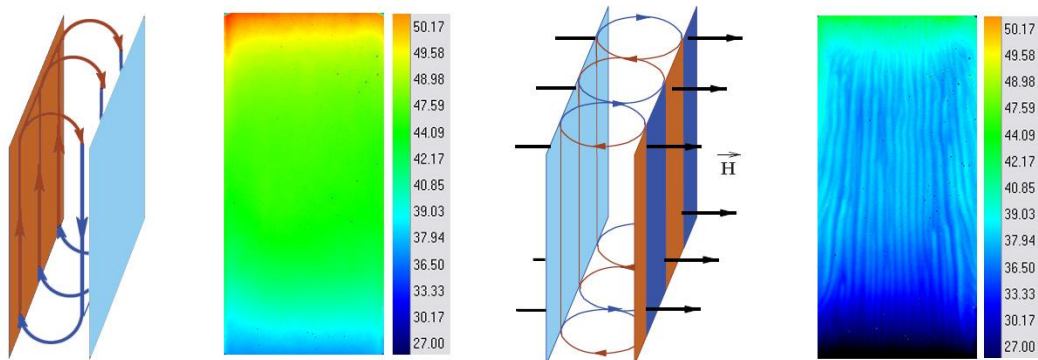
Figure 21: Schematic and infrared image of thermo-gravitational rolls when *H* is null (left) and *H* = 35 kA/m (right). In both cases, **ΔT** between the hot and cold sides is 40 °C (152).

Thus, in the case of the CERES harvester geometry, thermal and magnetic fields can be combined in order to generate the desired periodic flow along the toroidal axis of the tank (see 4.1). The most suitable solution would be a geometry in which the ΔT guarantees the natural convection, while *H* triggers concatenated stationary vertical thermomagnetic rolls, and the combination of the two effects defines a spiral-like motion along the converter which suits well with the device shape.

2.2   Triboelectricity

Triboelectricity is defined as a contact-induced electrification in which a material becomes electrically charged when friction with a different material occurs. Every day we experience this effect since it generates electrostatic phenomena. Nevertheless, the mechanism behind triboelectrification is still under debate between a solid-state and a more holistic approach, mainly based on an engineering modeling (146). Theoretically, triboelectricity is described as a phonon-induced phenomenon (153). In fact, the viscous friction forces generate vibrations in the polymeric structure of the pipe (phonon generation), electron-transfer (triboelectric effect) and dissipation in the form of heat. Other approaches (168) define the number of charge carriers extracted by triboelectric effect as a function of energetic compatibility (affinity, Fermi level, etc.) which influences directly the triboelectric series. This means that a system constituted of same colloid flowing at the same velocity would produce electrical power with a different efficiency according to the different material of the pipe (FEP, PTFE, PVC, etc.). In fact, when two materials come in contact, a chemical bonding is established between the surfaces and if the process is slow enough, allowing electrons, holes, or ion/molecules to flow in order to reach the thermal equilibrium, the electrochemical potential of the two materials equalizes. The sign of the charges carried by a material depends on its relative polarity in comparison to the second material (118). During the separation process, some of bonded atoms have the tendency to keep electrons, mainly due to the difference of electronegativity between the two materials, producing a charge accumulation on the surfaces. Furthermore, the active area plays an important role, since the process is strictly related to the friction coefficient. In order to maintain this charge, the characteristic time of discharge can be modeled as an RC circuit where $\tau = 1/RC$. Then, material choice is driven by high resistivity and high relative dielectric constant (good electric insulator), geometrical parameters, high difference in electronegativity and high active surface. Almost any material we know undergoes triboelectrification: synthetic polymers, metals, wood and silk. The ability of a material for losing/gaining electrons depends on its polarity and the tendency to gain or lose electrons is usually described using the so called triboelectric series (3.2.2). Once the most suitable material, according to the application, has been selected, also the surface morphology can be modified by physical and chemical treatments for creating nano patterns or functionalizing the surface using NPs, molecules, nanotubes or nanowires, effective for enhancing the contact area and the triboelectrification process (146).

Recently, with advances in low power electronics (recovery systems, environmental monitoring, IoT and so on), triboelectric devices have found employment as energy harvesters from mechanical energy, wind and tidal wave energy featuring ease of fabrication, stability and high-energy conversion efficiency. Therefore, the right functionalization of a triboelectric nanogenerator (TENG) is important in order to build a marketable device for recovery applications. TENGs have four basic modes of operations, represented in Figure 22, that can be used in different operating conditions, according to the specific application. For sake of simplicity, only the Single-electrode mode (SEM) is explained in detail, since it is the only one adopted in the CERES project.
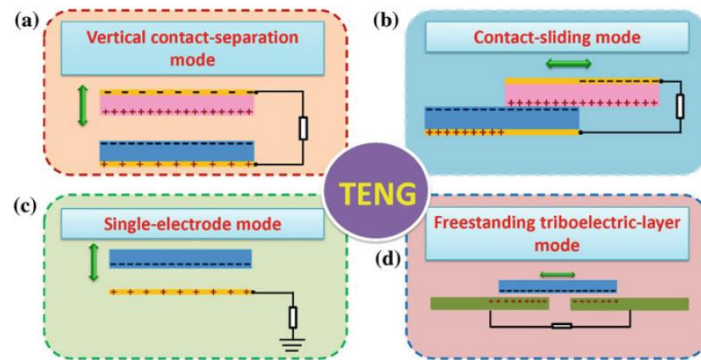
Figure 22: Operational modes of TENGs. a) Vertical contact-separation mode, b) Contact-sliding mode, c) Single-electrode mode, d) Freestanding triboelectric-layer mode (154). Reproduced with permission.

SEM features only one electrode connected to a load. This characteristic is fundamental for mobile applications, such as human walking or fluid motion, where only one object is moving. The second electrode is set as a reference, which can be placed anywhere in the space but, during characterization, it is usually plugged to the same ground of the measurement systems (154). The operating principle can be described by the coupling of contact electrification and electrostatic induction. Considering a conductor-to-dielectric system, e.g. an aluminum primary electrode in contact with a fluorinated ethylene propylene (FEP) pipe: surface charge transfer takes place on the contact area of the two materials. Since, according to the triboelectric series, the FEP have a tendency to accumulate electrons due to the presence of fluorinated groups (high electronegativity), a net positive charge is transferred to the aluminum surface. Because of the insulating properties of the polymers, a long-time retention of triboelectric charges (hours or even days) is expected (154). Considering a reference electrode, a potential difference is

established between the two electrodes. The open circuit voltage, V_{OC}, keep increasing until reaching the maximum value and when a load is connected in between the two electrodes, an instantaneous current will flow. This effect can be observed in presence of a continuous contact-separation between the two materials (contact mode) or if a continuous charge accumulation because of a flowing medium, as in the case of water-based, applications takes place (154).

In the CERES project, the idea is to exploit the positive charging of colloidal titania (TiO_2) in a FEP pipe (negative material in the triboelectric series) in order to have an accumulation of electrostatic energy from the fluid motion, that is generated by wasted sources. In Figure 23, a graphic representation of the working principle is shown and it will be better explained in 4.3.2.
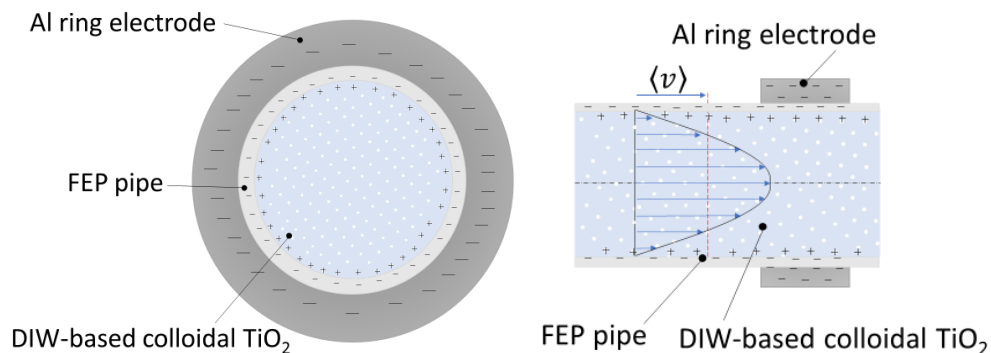
Figure 23: Graphic representation of triboelectric phenomenon in cross (left) and lateral section (right) views of the pipe (155). Reproduced under the terms and conditions of the Creative Commons Attribution (CC BY) license.

2.3   Pyroelectricity

Pyroelectricity (PE) was investigated for the first time thousands of years ago even though an effective comprehension of the effect came out with the thermodynamics studies on the of matter during 18-19th century. The working principle, reported in Figure 24, is described by a spontaneous polarization occurring when temperature conditions are unsteady, bringing the dipoles to reorient according to the thermal gradient. Thus, PE is the ability of a material to spontaneously polarize when a temperature variation occurs and it represents the changes in surface charge density due to heating or cooling. This ability does not depend only on the material employed but also on its crystal structure since, in order for the pyroelectric effect to occur, an unbalance between the centers of charges needs to be established. For

this reason, only some configuration, are suitable for pyroelectric devices, such as triclinic, monoclinic or tetragonal structure.
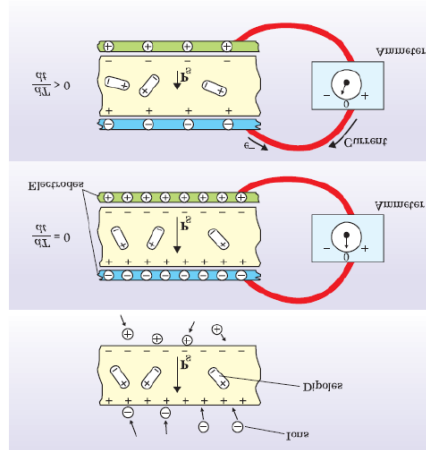
Figure 24: schematic of pyroelectric effect phenomenon (156). Reproduced with permission.

Several types of PE materials have been analysed, trying to find the best compromise to enhance efficiency in the realization of PE generators (PEGs). Currently, lead zirconate titanate $(Pb,Zr)TiO_3$ (PZT) or barium titanate $BaTiO_3$ (BT) features the highest-known PE coefficients (-268 and -200 μCm^{-2} K^{-1}, respectively). With linear materials, having an increasing dielectric constant with an increasing applied electric field, are able to produce just few μWcm^{-3} for temperature variations of 20 °C. However, using nonlinear materials, featuring particular thermodynamic path cycles (Figure 25), the performance can be strongly increased:

- Ericsson cycle: it consists of two isobaric transitions, isoelectric in the polarization-E plane (157) and two isothermal transitions, a compression and an expansion (158);
- Olsen cycle that is formed by two isoelectric processes and two isothermal ones. Several experiments have been conducted with different materials under different crystalline forms (e.g. single crystals and thin films) (159) (160) (161);
- Lenoir cycle, a cycle formed by three transitions: isochoric heat injection, isentropic expansion, and isobaric heat rejection. This cycle was demonstrated to be more performing than the Ericsson one (162).
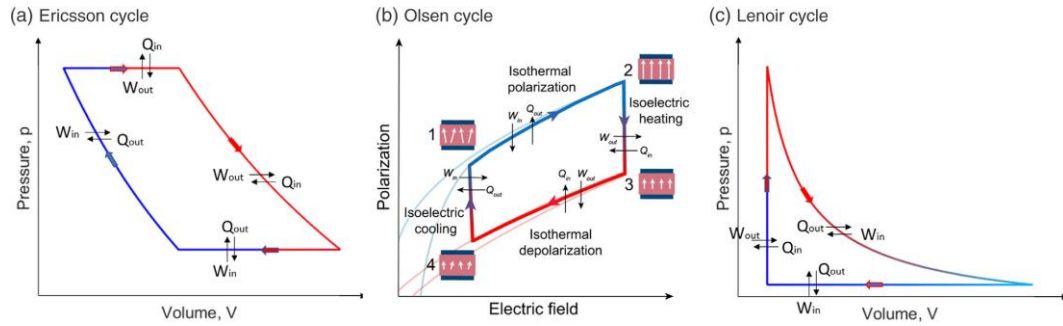
Figure 25: The typical trend of an Ericsson (a), Olsen (b) and Lenoir (c) cycle (163). Reproduced under the terms of the a Creative Commons Attribution CC BY 4.0 license.

In the CERES project, the idea is to exploit the polarization of colloidal barium titanate (BaTiO$_3$) when undergoing a thermal gradient, the same exploited to generate the colloid motion within the device, generated by wasted sources.

Materials

In this section, an introduction about the class of materials under analysis for the CERES project is provided and then the specific materials employed for the experimental campaign are described in detail.

3.1   Colloidal systems

If a fluid is a substance with no resistance to shear deformation and a liquid is a nearly incompressible fluid with adapting shape but almost perfect volume retention, soft-matter systems react much more sensitively to mechanical perturbations (such as shear) as compared to pure molecular materials. Research activities in this field has exhibited rapid growth and strong diversification because soft-matter systems are essential in many technical applications and play a key role in medical, pharmaceutical and biological problems (164).

In this work, we focused on colloids, complex condensed matter system, lying at the boundary between completely homogeneous systems such as solutions, and completely heterogeneous systems such as suspensions (133). Usually defined as a stable suspension of solid nanoparticles (NPs) in a carrier fluid (both in liquid or gaseous form), colloids are classified according to the aggregation state of their components (S = solid, L = liquid, G = gaseous):

- S-S (solid sol);

- S-L (sol);

- S-G (solid aerosol);

- L-S (gel);

- L-L (emulsion);

- L-G (liquid aerosol);

- G-S (solid foam);

- G-L (foam),

where the first letter refers to the dispersed phase and the second to the dispersion medium. Sols (S-L), also named colloidal suspensions, are characterized by a solid

suspended phase with the ability to confer specific unique physical properties according with the nature of the NPs (magnetic, thermal, photo, tribo, pyro, etc.), maintaining the liquid nature of the solution.

3.1.1 Complexity

Even if colloidal suspensions represent the simplest complex fluids, important questions in confining geometries and additional external fields are still open since soft matter reacts sensitively to external perturbations and manipulations and stable colloids are rare in real case scenarios, where colloidal matter is usually exposed to external perturbations. The sensitivity of colloidal soft matter to external fields has been exploited empirically in many different applications but the systematic scientific understanding is still immature. In contrast to molecular condensed matter systems, working with colloids provides the fascinating opportunity to control and tailor the external perturbation and study their influence on scales of length and time, which are typically associated with the particle structure, with the final goal of systematically control properties of colloidal matter using external fields (164). Distinguishing between the complexities of the colloid itself (complexity of the system) and that of the circumstances under which the colloid is investigated (complexity of the problem), it is possible to schematically visualize (Figure 26) possible research directions (arrows in Figure 26 parallel to x and y-axis).
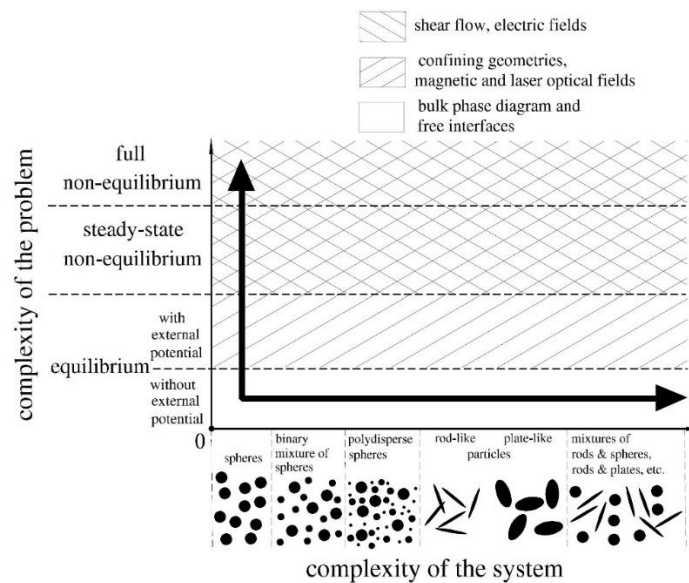
Figure 26: Schematic diagram of complexity: the x-axis shows the complexity of the system, the y-axis the complexity of the problem. The problems associated with different kinds of external field are indicated (164). Reproduced with permission.

The simplest situation is a system composed of equally sized spherical particles in equilibrium corresponding to a one-component classical system with a radially symmetric pair potential in the absence of any external field. Problem complexity is enhanced analysing the same system in an external potential (confining geometries, magnetic and laser optical fields). Then, by turning from equilibrium to steady-state non-equilibrium problems and finally, for fully non-equilibrium situations with explicit time-dependent processes (shear flow, electric fields). On the other hand, system complexity is increased in a binary or multicomponent (polydisperse) mixture of spherical particles. Even more complexity arises from cylindrically symmetric (rod-like or plate-like) particle shapes featuring orientational degrees of freedom, mixtures of spheres/rods/plates, flexible particle shapes (164).

In the present work, we dealt mainly with spherical NPs or a binary/trinary mixture of spherical NPs, under the influence of shear flow, thermal, magnetic and electric field representing a complex system in a high-complex, full non-equilibrium problem.

3.1.2 Stability

A big advantage of employing colloidal suspensions is that, in the limit of stability, the global system can be considered as single-phase, since the mutual interaction among the particles and the molecules of the carrier liquid are balanced by the Brownian motion (induced by the thermal effects) and by the physico-chemical properties of the carrier phase. However, colloids feature non-trivial collective properties and can present some phase transitions, such as:

- flocculation, occurring when the dispersed phase coalesces;

- gelation, occurring when the dispersant changes viscosity.

These phase transitions can be reversible, also depending on exogenous inputs (133). In fact, in a suspension, three main forces act on the solid particles:

- attractive electrostatic dipole-dipole interactions, i.e. Van der Waals forces, inversely proportional to the sixth power of the separation distance between two particles;

- repulsive electrostatic forces that arise from the interaction in electric double layer;

- repulsive force among adsorbed molecules on the surface of the particles, i.e. steric force (165).

These physico-chemical effects are exploitable for avoiding agglomeration, for example by adjusting the solution pH and the ion concentration, or by using surfactants (surface-active agents), dispersing agents added to the suspension to improve the separation of the particles and to prevent their settling or clumping (166).

Homogeneity is one of the main feature of colloidal systems. Considering a generic system where gravity and Van der Waals forces (attraction forces among NPs) plus an external magnetic field (characterizing the current work) tend to destabilize the suspension, two main effects can guarantee its stability:

- brownian motion, the random movement of fine particles in a carrier liquid;

- steric or ionic repulsion.

Therefore, it is possible to say that a colloidal system is stable if there is an energy balance between stabilizing and destabilizing mechanisms. In particular, it is possible to define the thermal energy, expressing the magnitude of the Brownian motion, associated to a spherical particle in colloidal suspension as:

$$E_T = k_B T,$$

where k_B is the Boltzmann constant (1.38×10^{-23} m^2 kg s^{-2} K^{-1}) and T is the temperature. For providing sufficient mixing, the gravitational energy or the magnetic energy has to be lower than the thermal energy.

In a suspension, the effect of sedimentation due to gravitational effects is evaluated by means of the difference of potential energy, ΔE_P, related to the balance between Archimedes force and gravity of a NP:

$$\Delta E_P = (\rho_s - \rho_l)Vgh,$$

where ρ_s and ρ_l [kg m^{-3}] are the densities of solid NPs and of the carrier liquid respectively, V [m^3] is the volume of the particle, g [m s^{-2}] is the standard gravity constant and h is the relative height between the top and the bottom of the reservoir containing the suspension. Considering a spherical NP with diameter D [m] so that:

$$V = \frac{\pi D^3}{6}.$$

It is possible to define the critical diameter of the NP, i.e. the maximum diameter that the particle can have in order to be gravitationally stable ($E_T > \Delta E_P$):

$$D < \left(\frac{6\,k_B T}{\pi\,(\rho_s - \rho_l)\,gh}\right)^{\frac{1}{3}}.$$

Furthermore, if dealing with magnetic NPs, the application of an external magnetic field could induce sedimentation. Defining the magnetic potential energy as:

$$E_H = -\vec{m} \cdot \vec{B}.$$

For moving a magnetic particle, a difference of magnetic field intensity within the solution is needed. Hence, we can define a variation of potential energy ΔE_H proportional to the difference of the magnetic field intensity. Supposing the magnetization collinear to the external magnetic field:

$$\Delta E_H = -\mu_0\,m\,\Delta H.$$

The magnitude of the magnetic moment is:

$$m = MV = \frac{\pi M D^3}{6},$$

where M is the domain magnetization of the constitutive material. In our case, for magnetite-based FFs this value is equal to 4.46×10^2 kA/m. Thus, the critical diameter is ($E_T > \Delta E_H$):

$$D < \left(\frac{6\,k_B T}{\pi\,\mu_0\,M\,\Delta H}\right)^{\frac{1}{3}}.$$

In addition, the application of a magnetic field trigger the magnetic dipole-dipole interaction, increasing the probability of NPs agglomeration, that should be avoided to prevent sedimentation and guarantee the homogeneity of the medium. Consider the motion of a NP in the magnetic field generated by another NP. In order to minimize the potential energy, the two particles tend to get closer and the dipole-dipole energy, E_{dd}, can be expressed as:

$$E_{dd} = -\frac{\mu_0}{4\pi}\left(3\frac{(\vec{m}_1 \cdot \vec{r})(\vec{m}_2 \cdot \vec{r})}{r^5} - \frac{\vec{m}_1 \cdot \vec{m}_2}{r^3}\right),$$

where $\vec{r}$ is the position vector with respect to the center of gravity of the two NPs. Assuming the two NPs being close enough, they reach the minimum of energy when they are in contact. Thus, replacing r with D and introducing m in terms of M and V:

$$E_{dd}{}^{min} = -\frac{\pi \mu_0 M D^3}{72}.$$

Since the stability condition is defined considering the thermal energy of two NPs, the critical diameter is ($2E_T > \left| E_{dd}{}^{min} \right|$):

$$D < \left(\frac{144 \, k_B T}{\pi \, \mu_0 \, M^2} \right)^{\frac{1}{3}}.$$

3.1.3 Viscosity

In a suspension, the viscosity depends on the carrier liquid and on the suspended particles. In the case of non-interacting particles in highly diluted solutions (volume fraction $\Phi < 0.11$), a linear relation developed by Einstein is used (145):

$$\eta_0 = \eta_c \left(1 + \frac{5}{2} \Phi_s \right),$$

with η_0 and η_c [kg m^{-1} s^{-1}] representing the dynamic viscosities of suspension and carrier liquid in absence of a magnetic field and Φ_s the modified volume concentration of NPs, dependent on the geometrical dimensions of the surfactant so that:

$$\Phi_s = \Phi \left(\frac{d + 2s}{d} \right)^3,$$

where d [m] is the NPs diameter and s [m] the surfactant thickness.

When the concentration of the suspended phase is increased, the particles interact each other, generating complex chained structures (145) and influencing the viscosity in a way that:

$$\eta_0 = \eta_c \left[1 - \frac{5}{2} \Phi_s + \left(\frac{5}{2} \Phi_c - 1 \right) \left(\frac{\Phi_s}{\Phi_c} \right)^2 \right]^{-1},$$

where Φ_c is the critical volume fraction (usually 0.74, when the above expression is used for comparison with experiments). In Figure 27, the linear (Einstein) and

quadratic (Rosensweig) models for viscosity are compared in the case of FF EMG 901 (see 3.2.1.1)
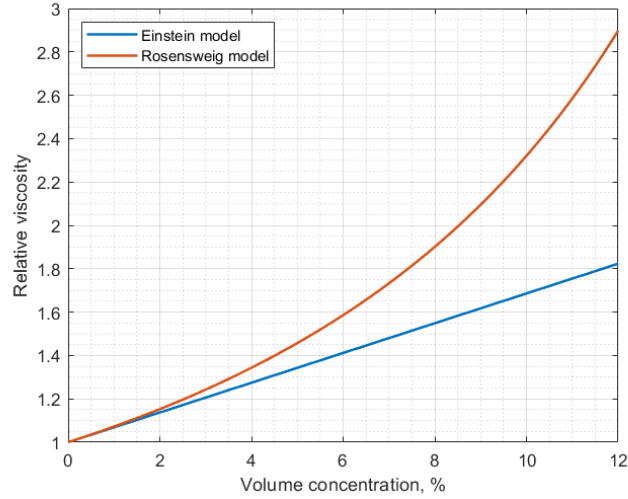
Figure 27: Comparison between Einstein and Rosensweig models for viscosity, in the case of FF EMG 901 (146). Reproduced with permission.

Furthermore, if dealing with superparamagnetic fluid, the application of a magnetic field increases the interparticle interaction introducing magnetoviscous effects modeled (145) as a variation of local concentration of bidisperse systems, containing a small fraction of large particles (d ≥ 10 nm) forming chains in presence of an external magnetic field, and a large fraction of smaller particles (d < 10 nm) with weak interparticle interaction. So, if no magnetic field is applied, the relation between stress and shear rate is linear and the FF behaves as a Newtonian fluid, as is it were a suspension of non-magnetic NPs. On the other hand, if a magnetic field is applied, the fluid has a strong magnetoviscous behaviour due to particle/particle interactions and the relation between shear and stress is not anymore linear (146).

3.1.4 Specific heat and heat capacity

In a suspension, the presence of a solid phase modify the thermodynamic response of the material. Modeling the fluid as a single-phase mixture in thermal equilibrium, as preliminary analysis, the specific heat of a generic colloidal suspension, C_P [J kg^{-1} K^{-1}], with volume concentration of NPs, Φ, is defined as:

$$C_P = \frac{(1 - \Phi)\rho_f C_{Pf} + \Phi\rho_p C_{Pp}}{\rho},$$

with
$$\rho = (1 - \Phi)\rho_f + \Phi\rho_p,$$

where ρ_f and ρ_p [kg m^{-3}] and C_{Pf} and C_{Pp} are the densities and specific heat of carrier fluid and NPs, respectively. Adopting the same approach, the thermal conductivity, κ [W m^{-1} K^{-1}], of a colloidal mixture is defined as:

$$\kappa = \kappa_f \frac{2\,\kappa_f + \kappa_p - 2\,\Phi(\kappa_f - \kappa_p)}{2\,\kappa_f + \kappa_p + 2\,\Phi(\kappa_f - \kappa_p)},$$

where κ_f and κ_p are the thermal conductivities of carrier fluid and NPs, respectively. However, a more complex analysis could also consider Brownian motion and magnetic interaction between particles. In fact, the application of an external magnetic field can generate short-chained structures of NPs, changing the distribution from homogeneous dispersion medium to non-uniform aggregated particles (146).

3.1.5 Magnetic permeability

If dealing with a magnetic colloid, the magnetic susceptibility is defined in function of the volume concentration of ferromagnetic NPs. With respect to the classical Langevin relation (2.1.2), M_L, the magnetization is considered as a combination of the external field H_0 and the collective magnetic field produced by the NPs (167). Furthermore, all the magnetite particles are equal in volume, the internal magnetic field inside the droplets is uniform and the fluid is homogeneous. For describing the magnetization of a superparamagnetic fluid, the first order modified mean-field model is used, taking into account a linearization of the inter-particle interaction:

$$M(H) = M_L H_e,$$

with
$$H_e = H + \frac{4\,\pi}{3} M_S L\left(\frac{mB}{k_B T}\right),$$

where $L(x)$ is the Langevin equation, $M_L(x)$ is the Langevin relation and M_s is the saturation magnetization.

So, the relative magnetic permeability, μ_r [H m^{-1}], is defined as, taking into account that the magnetic permeability of the carrier liquid is equal to the unity:

$$\mu_r = 1 + \Phi \frac{M_p(H_p)}{H_0}.$$

In the case of spherical NPs and in the weak-field limit, where the linear magnetization relation, $M_p = \chi_i H_p$, is valid, the initial magnetic permeability of superparamagnetic fluid is defined as:

$$\mu_r = 1 + \frac{\chi_i \, \Phi}{1 + \frac{1}{3}\chi_i \, (1 - \Phi)}.$$

However, in order to have an accurate quantitative model, demagnetization related to the NPs eccentricity and inter-particle aggregation, should be considered especially if vol. concentration is $> 8\%$, since NPs start to aggregate and the local fields generated by the aggregates influence the orientation of NPs moment along the direction of the applied magnetic field (146) (168).

3.2   Employed colloids and materials

3.2.1 Ferrofluids

In nature, no spontaneous magnetic materials in a liquid state are found since the melting point of ferromagnetic materials is higher than their Curie's temperature. In fact, higher temperatures make magnets weaker, as spontaneous magnetism only occurs below the Curie temperature. So, even if natural magnetic fluid exist (melts and solutions of salts, oxygen), it was not possible to have a liquid with high magnetic susceptibility until 1938, when William Cronk Elmore prepared the first satisfactory colloidal magnetite (Fe_3O_4) (169). Only later, in 1965, at NASA laboratories, Steve Papell, exploiting the properties of colloids, developed and patented a process to synthesize a superparamagnetic fluid, named ferrofluid (170). According to Rosensweig (171), ferrofluids (FFs) are colloids containing NPs of ferromagnetic material suspended in a carrier liquid. This allows the substance to be highly susceptible to the presence of an external magnetic field (Figure 28) but once the magnetic field is removed, the magnetisation is completely lost. Thus, FFs are classified as superparamagnetic materials.
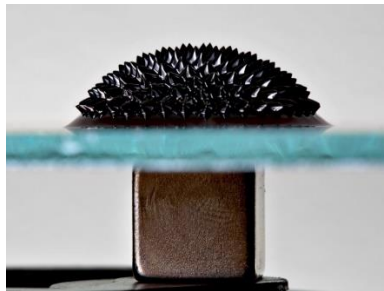
Figure 28: Picture of FF under the influence of a static magnetic field.

Nowadays, in the most common FFs NPs of maghemite (Fe_2O_3 cubic lattice), hematite (Fe_2O_3 trigonal lattice), magnetite (Fe_3O_4 cubic lattice) and other ferrites (MFe_2O_4, with M identifying a transition metal), are dispersed. Several solvents are adopted, mainly:

- organic solvents: hexane, benzene, toluene, kerosene, nitrated and halogenated hydrocarbons;

- water.

The NPs are coated with a surfactant, amphiphilic molecules having a hydrophobic and hydrophilic part (oleic acid for oil-based, anionic or cationic dispersant for water-based), acting as stabilizing agents and preventing agglomeration. At the same time, surfactant makes the overall fluid not electrically conductive. Furthermore, in order to guarantee the stability of NPs suspension the diameter of spherical NPs has to be small enough so that gravitational sedimentation is balanced by thermal agitation as per 3.1.2. Therefore, their typical dimension is ≈ 10nm, making them single-domain magnetic NPs. Their final structure is schematically represented in Figure 29.
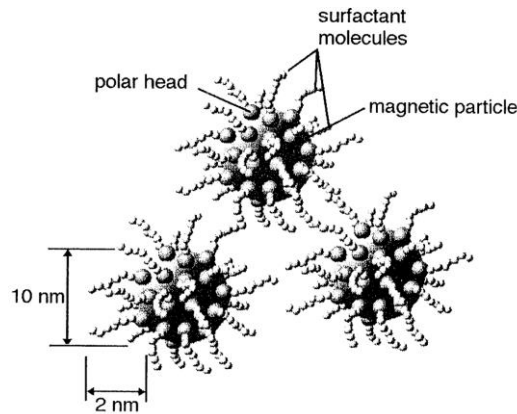
Figure 29: Schematic representation of the FF NPs (172). Reproduced with permission.

The interest to FFs arises because their flow can be significantly controlled by the influence of moderate magnetic fields (173). Controlling a fluid using an external magnetic field opens a wide spectrum of possibilities in different application fields, from passive cooling systems in low gravity environments to biomedical, vibration damping, magnetic sealing and cancer treatment applications. Moreover, it is possible to recover and harvest electrical energy from the motion of the magnetic fluid, exploiting its magnetization and demagnetization properties as explained in 4.1.

3.2.1.1 FF EMG 901

In our inductive tests, we employed a FF purchased from Ferrotec, with a solid phase of magnetite (Fe_3O_4 cubic lattice) chosen for its ferromagnetic properties in a large temperatures range, since the Curie point of Fe_3O_4 is at ≈ 675 °C. The NPs are coated with oleic acid and are dispersed in a light hydrocarbon oil (kerosene-like). Its main characteristics are reported in Table 4.

Table 4: Physical Properties of FF EMG 901

	Unit	Value
Appearance	-	Black-brown fluid
Carrier liquid	-	Light hydrocarbon oil
Nominal particle diameter	[nm]	10
Magnetic particle concentration	[% vol.]	11.8
Density	[kg m^{-3}]	1.43×10^3
Flash point	[°C]	89
Saturation magnetization	[mT]	66
Viscosity @ 27°C	[mPa s]	8
Initial magnetic susceptibility	-	6.79

3.2.2 Triboelectric colloids

As mentioned in 1.3.4, triboelectricity has also been observed when liquids, such as water, flow through polymeric pipes/films made of dielectric materials. In fact, water plays an important role in the electrification of materials and a particular kind of contact electrification (flow electrification) has been reported in different studies

where insulating liquids cause electrification of electronic components or determine shock problems in petroleum pipeline hazards (174) (175). However, other interesting triboelectric phenomena can be associated with pure water flowing between hydrophobic surfaces, such as polytetrafluorethylene (PTFE) (146). The charging process that occurs in polymers is not completely clear, as in depth as in metal but several consistent charging patterns are observed. In particular, insulators and organic polymers can be arranged in the triboelectric series from those that charge most positive, like nylon, to those that charge most negative, like the halogenated polymers (176). Fluorinated ethylene propylene (FEP) is defined as a negative element in the triboelectric series (Figure 30), also due to its fluorinated groups in the polymeric structure (177) (178).

Positive		Negative
	Aniline-formol resin	Polyvinyl alcohol
	Polyformaldehyde 1.3-1.4	Polyester (Dacron) (PET)
	Etylcellulose	Polyisobutylene
	Polyamide 11	Polyuretane flexible sponge
	Polyamide 6-6	Polyethylene terephthalate
	Melanime formol	Polyvinyl butyral
	Wool, knitted	Formo-phenolique, hardened
	Silk, woven	Polychlorobutadiene
	Polyethylene glycol succinate	Butadiene-acrylonitrile copolymer
	Cellulose	Nature rubber
	Cellulose acetate	Polyacrilonitrile
	Polyethylene glycol adipate	Acrylonitrile-vinyl chloride
	Polydiallyl phthalate	Polybisphenol carbonate
	Cellulose (regenerated) sponge	Polychloroether
	Cotton, woven	Polyvinylidine chloride (Saran)
	Polyurethane elastomer	Poly(2,6-dimethyl polyphenyleneoxide)
	Styrene-acrylonitrile copolymer	Polystyrene
	Styrene-butadiene copolymer	Polyethylene
	Wood	Polypropylene
	Hard rubber	Polydiphenyl propane carbonate
	Acetate, Rayon	Polyimide (Kapton)
	Polymethyl methacrylate (Lucite)	Polyethylene terephtalate
	Polyvinyl alcohol	Polyvinyl Chloride (PVC)
	(continued)	Polytrifluorochloroethylene
		Polytetrafluoroethylene (Teflon)

Figure 30: Triboelectric series (154). Reproduced with permission.

Since water tends to charge positively in presence of electronegative elements, FEP is the perfect candidate for the study of triboelectric effects. Although the work is based on the use of FEP, the same approach could be extended to several other

polymeric materials having a broader employment in general piping systems such as polyvinyl chloride (PVC), since they are defined as negative element in the triboelectric series (154) (176). A complete outlook on the electrification processes in pure water states that ion-partitioning near solid-liquid interfaces (hydroxyl adsorption of water-hydrophobic surfaces) is fundamental in material electrification (179), and an example of water-based TENGs using a Ti-mesh, operating in single electrode mode (SEM) is provided in Figure 31 (120).
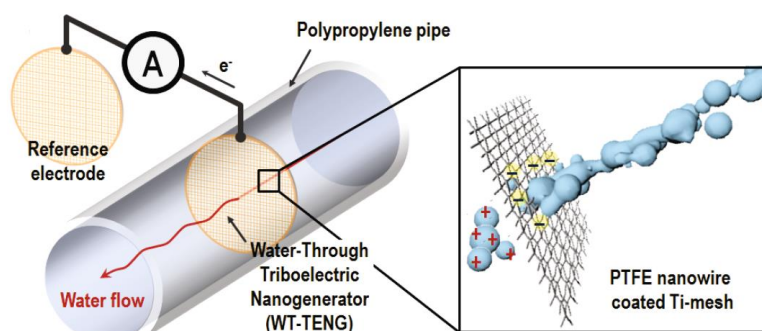
Figure 31: Example of water-based TENG using a Ti-mesh in SEM (120). Reproduced with permission.

Furthermore, titanium oxide powder has been employed in a solid-state TENG exploiting the contact electrification between a PTFE thin film and a layer of TiO_2 nanomaterial (nanowire and nanosheet) array. The as-developed TENG has been systematically studied and demonstrated as a self-powered nanosensor toward catechin detection, with output voltage and current density increased by a factor of 5.0 and 2.9 respectively, demonstrating the good triboelectric match between PTFE and TiO_2 (180) (181).

3.2.2.1 Colloidal TiO₂

In our triboelectric tests, we employed colloidal titania (TiO_2 or T), prepared starting from TiO_2 powder, purchased from Degussa, featuring extremely high purity (TiO_2 content > 99.5%) and a composition of 40% rutile and 60% anatase. TiO_2 was chosen for its triboelectric properties and for its chemical compatibility with water-based suspensions. TiO_2 was dispersed in DIW, purchased from Carlo Erba, featuring an electrical resistivity of 12.8 MΩ/cm, by means of a 30 minutes long ultrasonic bath operating at 40 Hz (Bransonic® M, Branson Ultrasonics).

Two samples of colloidal TiO_2 at different vol. concentrations were prepared, featuring an excellent stability toward sedimentation avoiding electrostatic

aggregation of the NPs, even without adding surfactants (that would have hindered electronic transfer phenomena) or balancing pH.

Table 5 shows the physical properties of colloidal TiO$_2$ at 1% vol. concentration.

Table 5: Physical Properties of colloidal TiO$_2$ at 1% vol. concentration.

	Unit	Value
Appearance	-	White fluid
Carrier liquid	-	Deionized water
Nominal particle diameter	[nm]	30
Triboelectric particle concentration	[% vol.]	1
Density	[kg m^{-3}]	1.03×10^3
Viscosity @ 27°C	[mPa s]	0.91

3.2.3 Pyroelectric colloids

In addition to solid-state pyroelectric energy harvester, in the recent past liquid-state PEGs were proposed using a liquid-based switchable interface (182), and a hybridized pyro-piezo ferrofluidic wearable harvester exploiting vibrations induced by the body motion, during walking or running, and body temperature variations was conceived. The combination of all these currents resulted in 11.4 mA with a pyroelectric current of 3.03 nA (183). Furthermore, a colloidal wurtzite structure CdSe/ZnS quantum dots photodetector based on photoinduced-PE effect was employed in a layer placed between two gold electrodes producing a current whenever the light at a specific wavelength hit the device, showing low-cost, easy-fabrication and high-speed independent self-power without any external source (184).

3.2.3.1 Colloidal BaTiO$_3$

In our pyroelectric tests, we employed colloidal barium titanate (BaTiO$_3$ or BT), prepared starting from BaTiO$_3$ powder, purchased from Inframat® Advanced Materials™, chosen for its excellent pyroelectric performances. BaTiO$_3$ was dispersed in the FF EMG 901, purchased from Ferrotec, for guaranteeing the dispersion of BT NPs, by means of a of horn sonicator (Branson Digital Sonifier® Model 450) operating at 100 W, with a duty cycle of 10 s of rest each 10 s of operation. FF EMG 901 was diluted with Kerosene (Carlo Erba), compatible with the FF carrier fluid, in order to reach a 2% vol. concentration of Fe3O4. BaTiO$_3$ NPs were added to reach a 0.5% vol. of BT, resulting in a colloid whose physical properties are reported in Table 6.

Table 6: Physical Properties of colloidal BaTiO$_3$ at 0.5% vol. concentration.

	Unit	Value
Appearance	-	Black-brown fluid
Carrier liquid	-	Light hydrocarbon oil
Nominal particle diameter	[nm]	300
Particle structure	-	Tetragonal
Pyroelectric particle concentration	[% vol.]	0.5
Density	[kg m^{-3}]	0.92×10^3
Viscosity @ 27°C	[mPa s]	2.13

CERES project

In this section, the main steps and milestones related to the PhD project are described and discussed. Starting from the initial conceptual idea and the first prototype, showing how and why the design has evolved, the test conducted and the main findings and, finally, future optimizations, the following subsections illustrate how the project has evolved: first, designing, building and testing new prototypes and then, changing the approach of the analysis, simplifying the experimental setup. Finally, the investigation of new colloidal materials exploiting different physical effects, for the purpose of energy harvesting, is proposed.

4.1   Toroidal converter

The first conceptual idea of a CERES prototype was that of a toroidal energy harvester and converter, with geometry similar to that of Tokamak fusion reactors, (185) able to scavenge waste heat, from cylindrical surfaces, and convert it to electricity. The idea behind this work comes from the awareness of unprecedented thermophysical potential of FFs (186). In fact, the goal was to exploit the combination of thermal gradient and magnetic field to trigger a driven thermomagnetic advection of FF within the device, and with dedicated induction coils, coupled with permanent magnets, extract electromagnetic induction forces and then electrical power, ready to be used, accumulated in supercapacitors or stored in batteries. For all these reasons, it was named ThermOmagnetic hydRODYNAmic energy harvester (TORODYNA). Of course, considering the particular geometry, hot pipes would be the most suitable applications for such device.
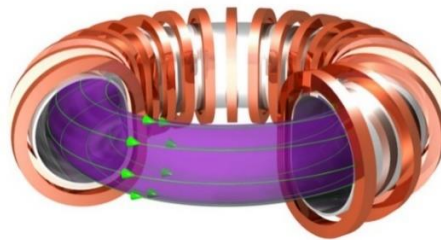
Figure 32: Concept of TORODYNA converter, inspired by the Tokamak structure (146). Reproduced with permission.

Some FF-based solutions already exist but they include an active pumping system that adsorbs energy from an external source and are not optimized for energy production only, but are conceived to dissipate heat and to recover a tiny portion of the energy available as kinetic energy (187). The energy output is typically low, 20 µV across a 1000 turn copper-wire of 130 µm diameter (1300 Ω/km leading to around 50 Ω) corresponding to 80 fW (188). Another interesting application based on electromagnetic induction by FF is that of oscillating heat pipe, a device that exploit the thermal gradient between a heat source and a heat sink using a closed-loop serpentine filled with FF, magnetized by permanent magnets and forced to move across an extraction coil (189). In this case, the required thermal gradient must be high enough to induce a phase transition in the FF solvent, creating vapour that pumps the fluid in the circuit, with a resulting figure of merit of 10 pW/K. Steady oscillations are established with rather high thermal power, above 70 W, thus preventing applications in wearable/portable devices/appliances (190). Furthermore, thermomagnetic cycles on Gd rotors were able to convert waste heat starting from 2 °C of ΔT with the output of 52.5 µW/K cm^3 (191). Another interesting device, operating with 20 °C of ΔT, was fabricated to exploit thermomagnetic effects and induce currents in a coil, with a remarkable output of 1 mW under certain conditions, with the drawback of requiring exotic materials, like La-Fe-Co-Si (192). With 40 °C of ΔT the technology of thermo-osmotic WH have promising power densities in the order of 1 Wm^2 (193), while much lower power could be extracted (550 fW/K) if, instead of using special membranes, conical holes are drilled to separate the two reservoirs (194). Other relevant examples involve a thermomagnetic based device exploiting the magnetic fluid motion to drive a mechanical rotor (195), and a thermo-magnetic driven motor exploiting a magnetic fluid (196), although, in both cases, the devices are not able to harvest electrical energy.

This highlights the need of a novel and first closed-loop thermomagnetic hydrodynamic energy harvester, based on thermomagnetic advection and exploiting a commercial FF. Such new robust and low-cost energy harvester exploits minimal temperature gradients and converts them into electricity employing non-toxic materials, thanks to the stabilization of magnetic particle density waves known as "Hopfions" (Figure 33), whose layout is that of knots twisted around the toroidal cycle (i coordinate system) p times and twisted around the poloidal cycle (j coordinate system) q times. A homogeneous, with high magnetic permeability core moving inside the induction coils would generate no electromotive force in case the magnetic flux variation is negligible with respect to

the coil volume. Therefore, in a toroidal container filled with a homogeneous magnetic fluid set in motion, we will measure no electromotive force on poloidal windings. Density waves appear and move in the structure and self-organize into clusters from whose movement it is possible to extract electromagnetic energy. Using a curved geometry instead of a flat one and closing the loop offer the FF a circular trajectory useful for electromagnetic conversion as described later. Thus, the torus appeared as a natural choice. The thermal gradient and the magnetic field are set across the container walls, so the resulting density waves twist along the toroidal and poloidal axes and generate a stable helical flow of magnetically charged particles, similar to the helical plasma flow in nuclear fusion reactors (197).
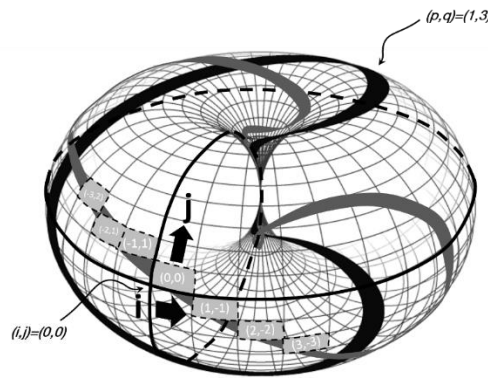
Figure 33: TORODYNA concept based on Hopfions phenomenon.

4.1.1 TORODYNA prototype 1.0

4.1.1.1 TORODYNA 1.0: design and fabrication

The main guidelines for the design of the first prototype were:

- light, easily transportable and movable apparatus, with inner diameter (ID) = 20 cm and outer diameter (OD) = 40 cm;
- thermally conductive and magnetically transparent structure;
- delta of temperature of, at least, 50 °C generated by means of heating modules, such as Peltier cells or thermal tapes;
- permanent magnets to generate a static magnetic field, eventually solenoids to allow tunability;
- commercial FF as principal material;
- measurement ports for fluid and wall temperature sensors;

- very low roughness of the internal surface of the device;
- visualization windows for looking inside the device;
- stand-alone, expandable USB data acquisition system (DAQ) with multiple channels;
- sield programmable gate array (FPGA) for managing and controlling thermal and magnetic fields.

The initial basic sketch is illustrated in Figure 34.
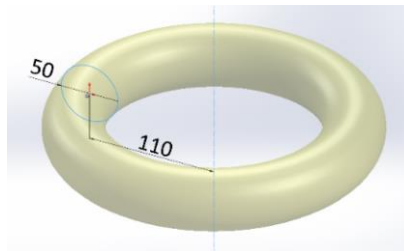
Figure 34: Initial sketch of the prototype.

With such dimensions, the internal volume of the prototype would have been of about 7 liters and considering the cost of FF being about 6000 €/L, it was necessary to find a compromise. Therefore, the internal volume was reduced to 1 L, the best trade-off between the FF cost and the volume needed to keep the physics at the macroscopic scale, giving also the advantage of increasing the thermal gradient for a given ΔT and enhancing the thermomagnetic advection. In order to do so, only the cross-section was squeezed while maintaining the same global dimensions, maintaining appropriate fluid dynamic parameters. So, four different lenticular configurations have been proposed and are shown in Figure 35.

(a)   (b)   (c)   (d)
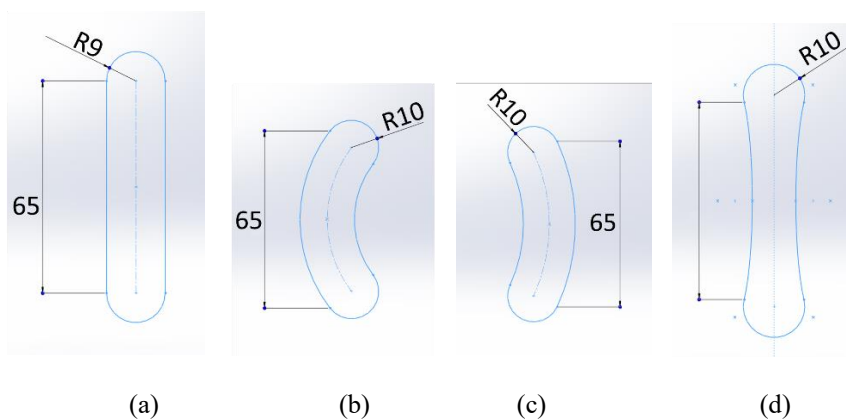
Figure 35: Lenticular cross section configurations.

Considering that, a convective symmetric motion was expected, in order to guarantee a suitable geometry, the first configuration has been selected.

In Figure 36, the front view of the final configuration is shown.
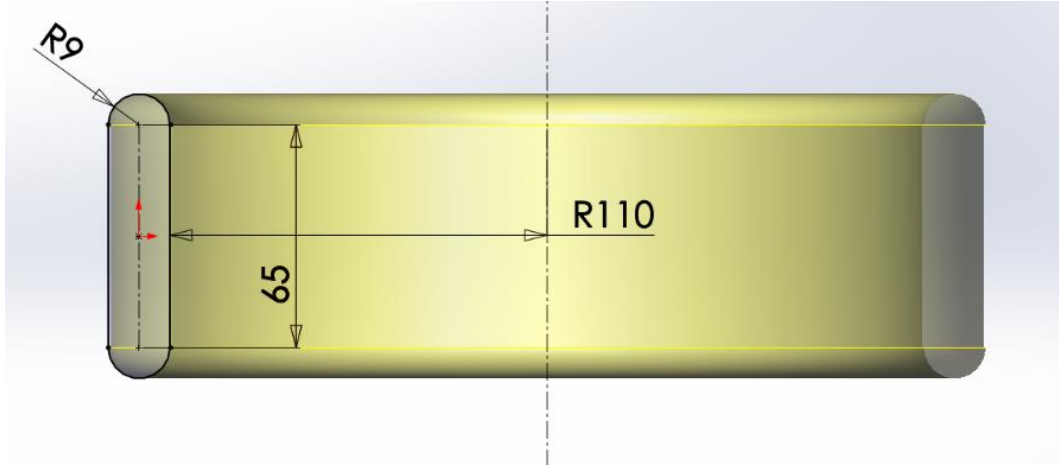
Figure 36: Front view of TORODYNA 1.0 structure with final dimensions.

4.1.1.1.1   Polylactic acid (PLA) 3D printed structure

Since the early stage of the project, for the first apparatus, a 3D printed structure was preferred so that we could produce different prototypes at low cost before reaching the optimal configuration. To meet the requirements of lightness and manoeuvrability, a polymeric material was preferred and, in order to assure chemical compatibility with the FF employed in the device, which is an oil-based one dilutable in kerosene, the polylactic acid (PLA) has been selected, being also thermally resistant and biodegradable. Finally, a polytetrafluoroethylene (PTFE) or Teflon spray layer was applied to allow high smoothness on the internal surface. Moreover, to finalize the design the wall thickness was sized in function of the material deformability, temperature probes size and consequent fluid dynamic disturbance. The global structure has been divided in two separate parts to create an assembly easy to be inspected: a main body with a top cover. The main body is an open hollow ring developed revolving for 360° the cross-section configuration shown in Figure 35a. The bottom is drilled to permit the drainage of the FF while the top cover presents two holes for the fast-on connectors installed to fill up the ring and venting the air. Each part is matchable with the other by using a silicone sealant avoiding screws holes, difficult to be generated with a 3D printer.

The isometric and section view of both parts are shown in Figure 37.

(a)

(b)

(c)

(d)
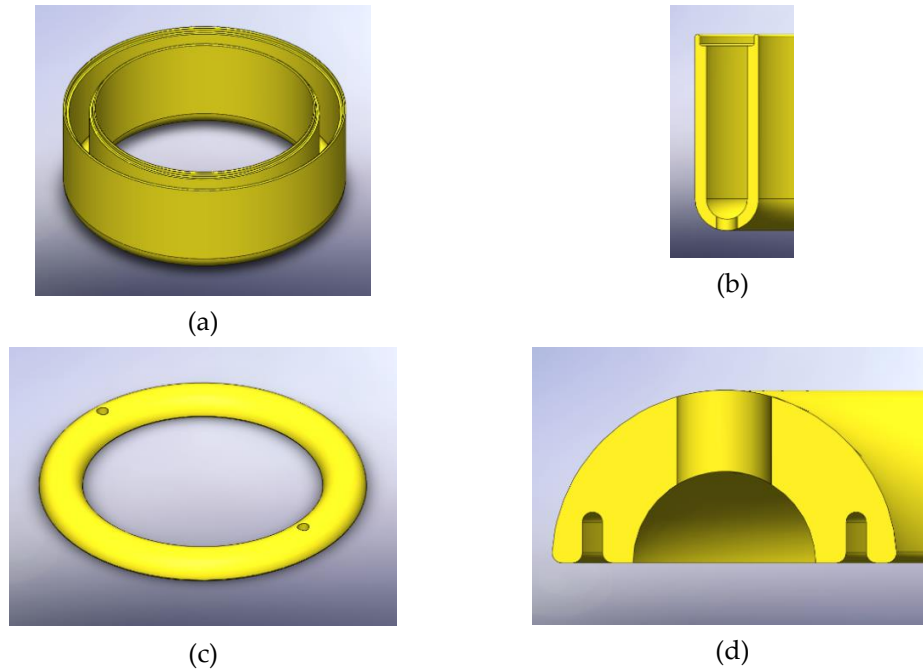
Figure 37: (a) Main body isometric view; (b) main body section; (c) top cover isometric view; (d) top cover section, modeled in Solidworks^TM environment.

Finally, a bottom base has been designed to support the prototype on the testbed. Its 3D model is shown in Figure 38.
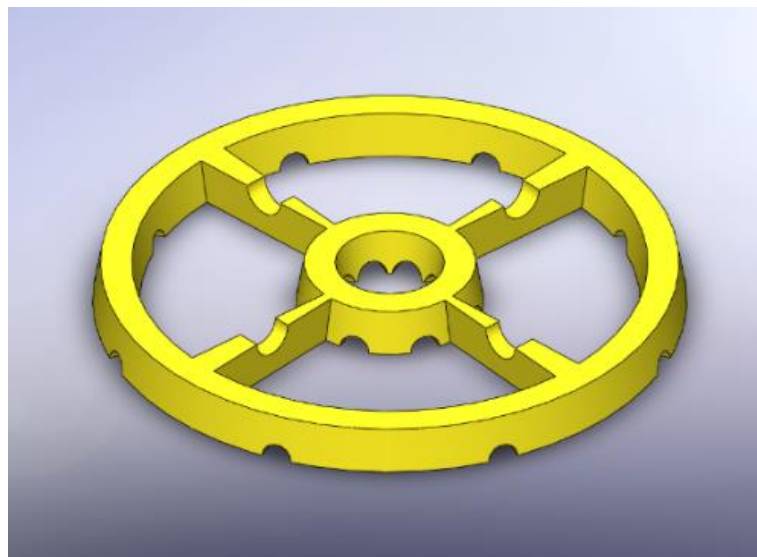
Figure 38: Isometric view of the bottom base.

4.1.1.1.2   Thermomagnetic region

Regarding the thermal and magnetic field, initially, we decided to generate a thermal gradient across the lateral sides of the prototype by means of thermoelectric modules (Peltier cells) and to apply a static magnetic field parallel to the thermal gradient, by means of permanent magnets. In optimal conditions, when the Peltier cells were steadily switched on, the inner wall was heated and the outer cooled down but it was possible to invert the thermal gradient by inverting the polarity of thermoelectric modules. They were arranged taking into account the available space, the modules dimensions and desired number, the clearance needed for installation, measurement ports and maintenance. For each TORODYNA's side, 8 equally spaced "thermomagnetic regions" are present, each of them composed of a 2x3 matrix, where the columns are filled by magnets, Peltier cells and magnets, respectively, according to Figure 39.
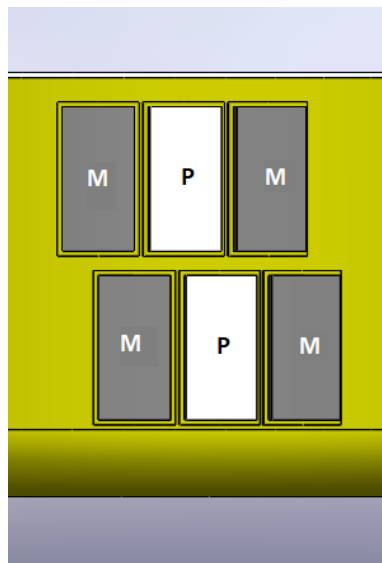
Figure 39: Front view of a "thermomagnetic region". "M" represents the permanent magnet, "P" the Peltier cell.

To install the modules, specific housings were designed, where the modules were installed by using a water soluble thermal grease. The two rows are staggered of "half module" in order to generate a non-equilibrium in the magnetic and thermal fields and trigger the motion, choice verified in experiments. The modules, both thermal and magnetic, measure 30x15 mm, choice driven mainly by the available space and modules cost. Table 7 shows the specifications of the 32 Peltier modules, while the 64 magnets are made of AlNiCo$_5$ (Aluminium-Nickel-Cobalt) alloy

(usually composed of 8–12% Al, 15–26% Ni, 5–24% Co, up to 6% Cu, up to 1% Ti, and the balance is Fe), thermally resistant up to 500 °C, and axially magnetized through the thickness dimension. In Figure 40 the global TORODYNA structure is shown.

Table 7: Peltier modules main specifications

	Unit	Value
I_{max}	[A]	3.9
V_{max}	[V]	7.8
Pc_{max}	[W]	19
ΔT_{max}	[K]	74
Length x Width x Thickness	[mm]	30 x 15 x 3.6
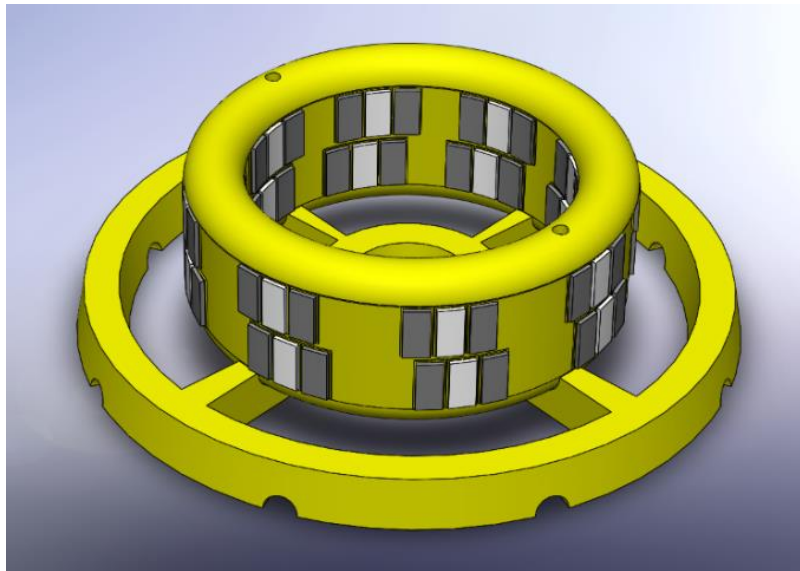
Figure 40: TORODYNA structure: bottom base, main body and top cover.

4.1.1.1.3 Power supply system

Initially, the 32 Peltier modules were powered by 8 power suppliers (Bel), one every four modules. The power supplies were grouped in two groups of 4 and their metallic supports was also used as electric GND. For more details on the power supply, the reader is referred to Figure 41 and Table 8.

Figure 41: Stack of power suppliers (198). Reproduced with permission.

Table 8: Power supply main specifications.

	Unit	Value
Type	/	HN12-5.1-AG
Input voltage	[V_{ac}]	$100 \div 264$
Output voltage	[V_{dc}]	12
Output current	[A]	5.1
Nominal power	[W]	66
Efficiency	[%]	55
Operating temperature range @ 100% load	[°C]	$0 \div 50$

Being cost-effective, implies a limit in the number of power suppliers and considering the high level of current absorbed by the TE modules, 2 to 2.5 V were set as input for the Peltier cells, enough to generate a significant thermal gradient (in the order of 1000 K/m) between the two sides of the converter. Therefore, two additional stages of voltage regulators were installed between the power supply and the Peltier cells to guarantee electrical compliance. The first stage involves a LM7805 (Fairchild) in order to lower the voltage from 12 V to 5 V, with an output current comprised between 5 mA and 1 A, with an output power up to 15 W. Since these voltage regulators can reach very high temperatures (up to 130 °C) due to the large power dissipation, thermal heat sinks were installed as shown in Figure 42a. Furthermore, a medium size fan was installed near the circuits, providing a continuous air flux. The second stage is composed of ADP7157 (Analog Devices) and lowers the voltage between 1.2 V and 3.3 V, according to the resistors added in the circuit, with an output current up to 1.2 A. Since this regulator presents an exposed pad on the bottom side, acting both as ground and as thermal heat sink, we need to solder it on a proper socket with an integrated circuit, to adapt the linear regulator to the breadboard (Figure 42b). Each regulator circuit contains two 10 kΩ resistors, and five 10 µF capacitors used to by-pass some pins to ground in order to have a lower noise. Therefore, the measured output voltage was $V_O \approx 2.34$ V sufficient to power one Peltier module. In Figure 43, the schematic of the circuit is shown: from the power supply output (12 V) which is the input of the LM7805 that reduces it to 5V (VOUT_1). Then, the ADP7157 lowers it to about 2.34 V (VOUT_2). The potential divider, composed of 10 kΩ resistors, adjusts the output voltage at the desired value.
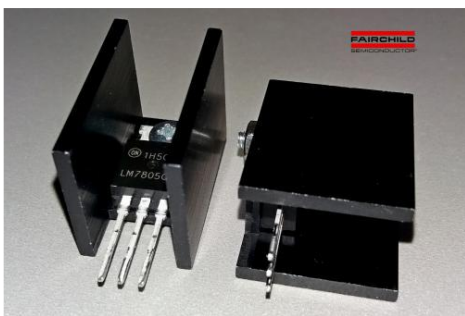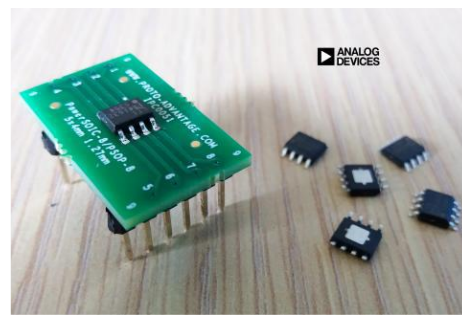
| (a) | (b) |

Figure 42: (a) LM7805 and (b) ADP7157 voltage regulators (198). Reproduced with permission.
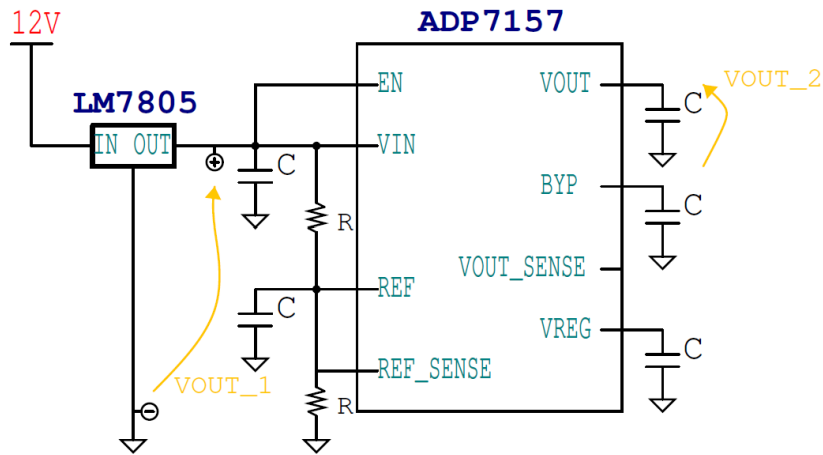
Figure 43: Schematic of the two stages of voltage regulators (198). Reproduced with permission.

The final implementation on a breadboard is shown in Figure 44, where the reader can notice two resistors, five capacitors, LM7805 with its heat sink (behind) and ADP7157 mounted on its IC socket. In addition, the coloured jumpers are used to make the circuitry connections. Here, the cables coming from the power supply are missing just for clarity reasons.
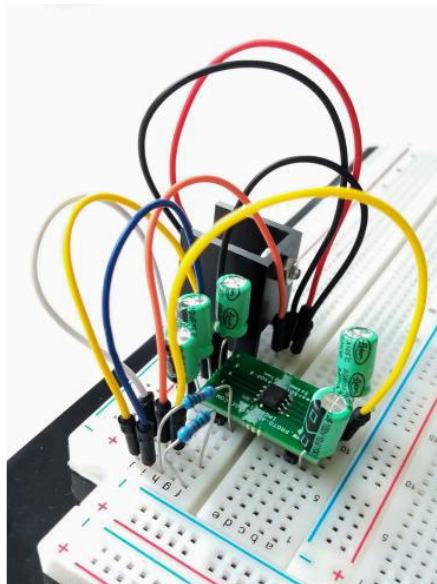
Figure 44: Implementation of two stages of voltage regulators on the breadboard (198). Reproduced with permission.

4.1.1.1.4   Temperature monitoring system

To monitor and control the fluid and walls temperature, on each side, 8 equally spaced measurement ports are present. For the fluid, 16 N-type (complaint with the magnetic field) glassfibre exposed welded tip thermocouples probes (RS component) are installed between two thermomagnetic regions, where a clearance of 60 mm is left. The fluid temperature probes are the least possible invasive in order to avoid disturbance flow. In are illustrated.

Table 9, the main specifications are illustrated.

Table 9: Fluid thermocouples main specifications.

	Unit	Value
Type	/	N
Operating temperature range	[°C]	-60 ÷ +350
Time constant	[s]	1.5

For the wall, 16 negative temperature coefficient (NTC) ND03N00103KCC thermistors (AVX) probes are fixed with thermal grease at the center of each heating region, assuming the temperature almost constant and uniform within this region. The connection between the thermistor and the DAQ system is made through a dedicated channel providing 5 V, where the potential difference on the thermistor is read thanks to a voltage divider between a 10 kΩ resistor and the thermistor itself.

Table 10 shows the specifications. Both thermocouples and thermistors were previously calibrated.

Table 10: Wall thermistors main specifications.

	Unit	Value
Type	/	NTC
Operating temperature range	[°C]	-50 ÷ +150
Thermal time constant	[s]	6
Probe Length x Width x Thickness	[mm]	7 x 3 x 2

In Figure 45 a close-up view of a thermomagnetic region of the TORODYNA converter is provided, where the sensors are visible.
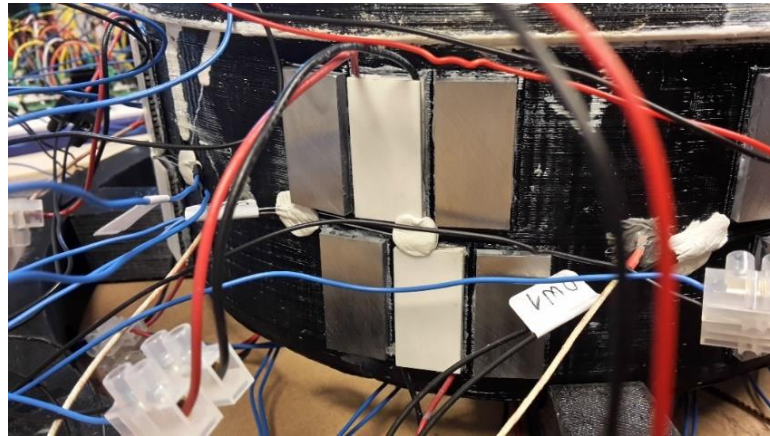
Figure 45: Close-up view of TORODYNA converter.

4.1.1.1.5   Data Acquisition system

The temperature sensors are connected to the Data Acquisition System, which is the National Instruments 6289 M Series Data Acquisition with 18-bit of resolution,

sample rate of 625 kS/s, and 32 single ended channels. For more information, please refer to Table 11.

Table 11: DAQ System main specifications

	Unit	Value
Type	/	NI 6289
Number of channels	/	32 single ended
Digital output	/	48
Analog output	/	4
Aggregate sample rate	[kS/s]	500
Timing resolution	[ns]	50

All the sensors are controlled and monitored by LabVIEW^{TM} routines. In this case, a block diagram (Figure 46) was used to acquire analogical signals, selecting the desired sample rate and channels. A start/stop button was inserted in order to initiate (or terminate) the data acquisition. The 32 channels were divided into two groups, one for the thermocouples and one for the thermistors. The thermistors channels show resistance values that are properly converted into temperature ones by means of the Steinhart-Hart equation (199); in order to perform this conversion, 16 function blocks are used. Then, the 16 thermocouple and the 16 thermistor signals are put together and sent to a Write to Measurement File block, in order to write the future collected data into a spreadsheet .xlsx file, meanwhile their instantaneous values appears live in windows and graphs. Then, the data were manipulated with other software, such as Origin or MATLAB, performing detailed data analysis.
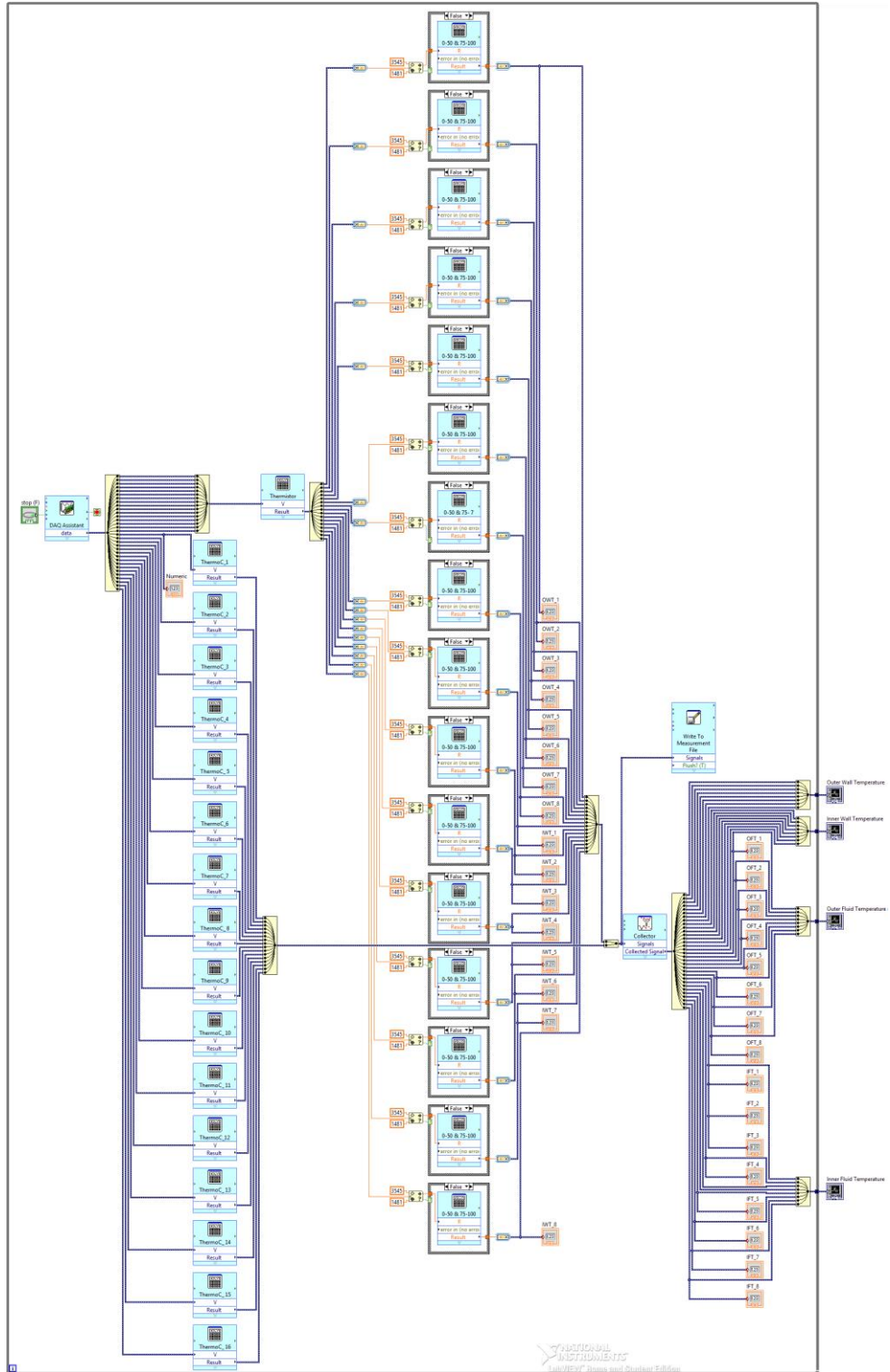
Figure 46: Block diagram for temperature monitoring realized in LabVIEW™ (198). Reproduced with permission.

In Figure 47 the data collected are represented in MATLAB graphs, showing an entire acquisition period lasted about 21 h.
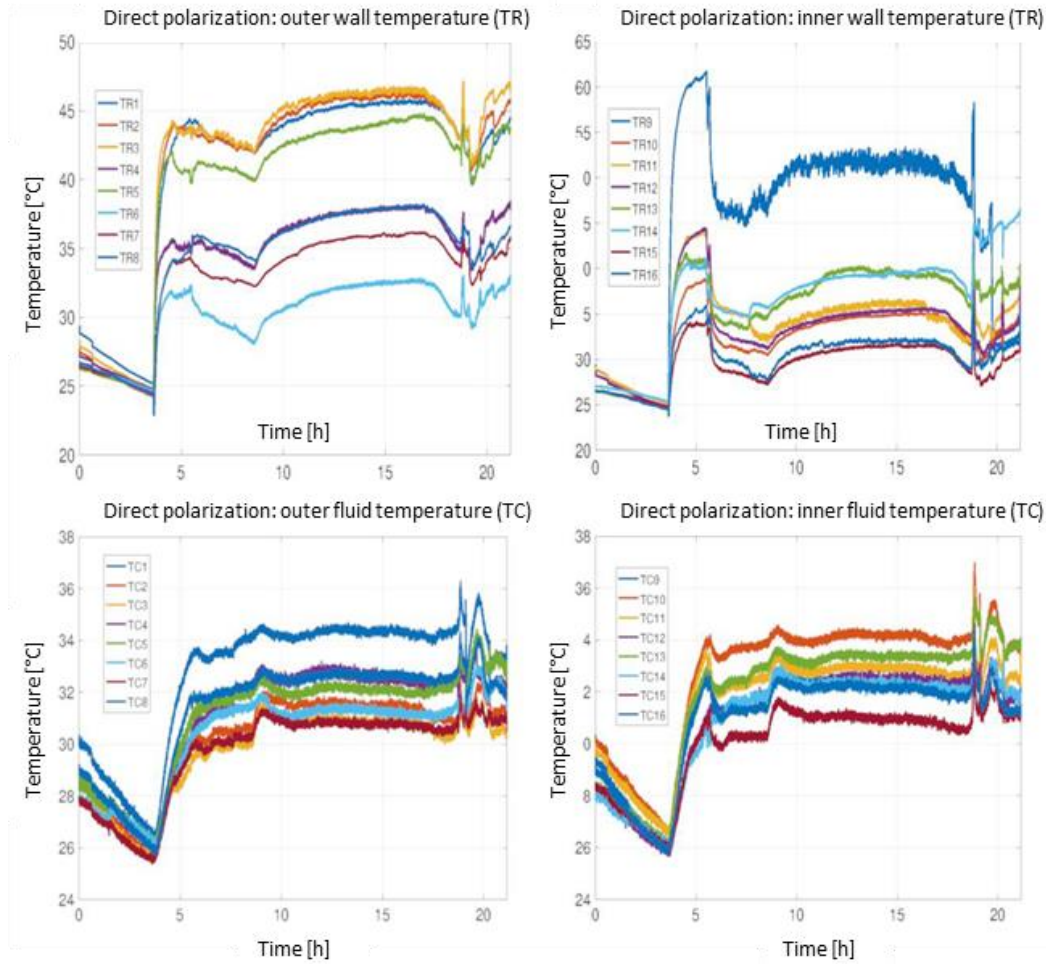
Figure 47: Temperature graphs developed in MATLAB. Top: thermistors (TR), bottom: thermocouples (TC) (198). Reproduced with permission.

4.1.1.1.6   Extraction system

Finally, inductive coils made from Oxygen Free Copper (OFC) wire, chosen to minimize the extraction losses due to wire resistance, wrapping the structure and coupled with the permanent magnets, compose the extraction system, as shown in Figure 48. Here, it is clear that the permanent magnets have a dual function: while triggering the thermomagnetic advection of the FF along the converter, they locally magnetize the FF where it flows through the coils, so that it can induce an

electromotive force that, otherwise, would be null because of its superparamagnetism.
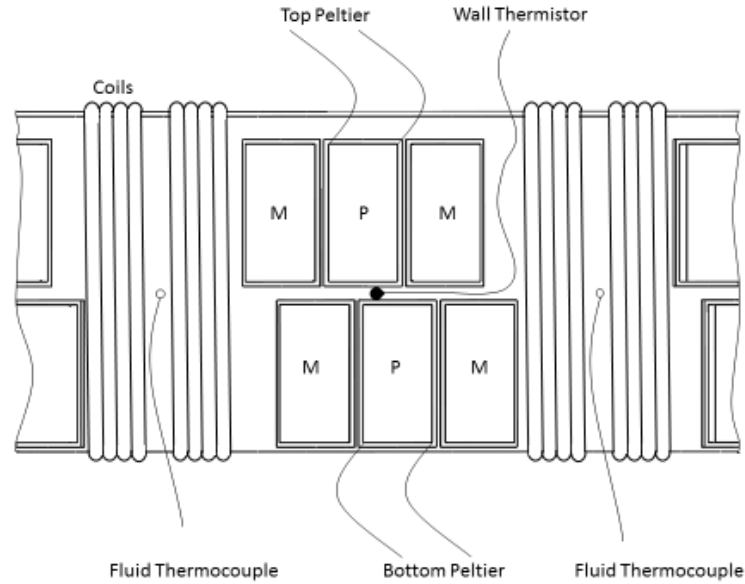
Figure 48: Frontal view of a TORODYNA section, showing thermomagnetic region, inductive coils and temperature sensors.

The coils are wrapped up along the entire ring in the poloidal direction (as shown in Figure 49) or in a and a mixed poloidal/toroidal configuration (Figure 50), in the free space between two adjacent thermomagnetic regions.

Figure 49: TORODYNA prototype in operating conditions with poloidal coils.
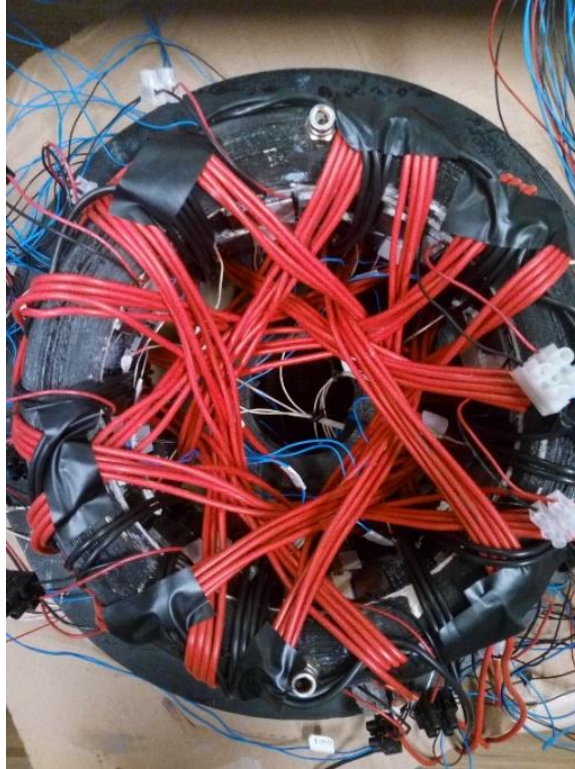
Figure 50: Mixed toroidal/poloidal coils.

Therefore, if the FF motion inside the torus has a purely toroidal component, then purely poloidal coils can optimally intercept all of its magnetic flux. On the other case, if the FF motion is helical (hence the velocity field having both a toroidal component and a poloidal one), then mixed poloidal/toroidal coils are more suitable. Other two coils (one poloidal and one toroidal) are used to induce a magneto-static field helping in the starting phase to trigger a net clockwise flow along the toroidal coordinate. After a few minutes, both coils are disconnected to measure the pure harvesting component of electromotive force.

4.1.1.1.7   Characterization system

The output power generated by the TORODYNA extraction system is measured by a source meter, to measure the intensity of the current induced by EMF, and a precision impedance meter, used to measure the inductive, capacitive and resistive behaviours of the extraction coils, respectively the Keithley 2635A and the Agilent E4980A (Figure 51). The latter has been equipped with an Agilent test fixture 16047A, in order to have a better coupling between coils and instrument. All the instruments are controlled and monitored by LabVIEW^{TM} routines.

Figure 51: Keithley 2635A SourceMeter (left) and Agilent E4980A LRC meter (right).

4.1.1.1.8   Overview

The assembled experimental is shown in Figure 52, where the inductive coils, the measurement system and the laptop are the only missing components.
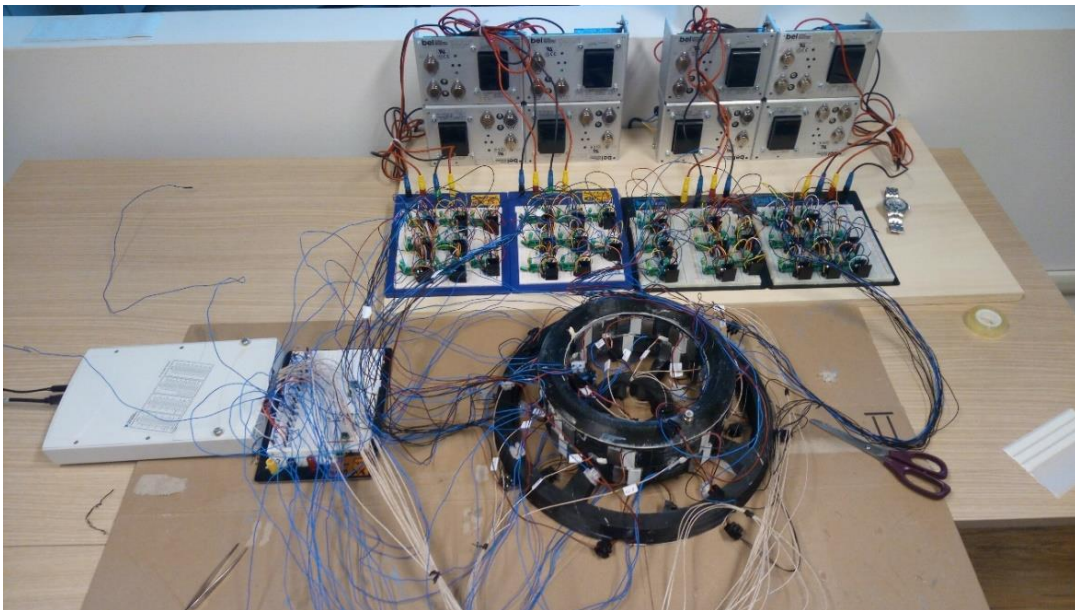
Figure 52: Experimental apparatus for the characterization of TORODYNA 1.0.

For a clearer understanding of the connections, the user is referred to Figure 53 in the following page.
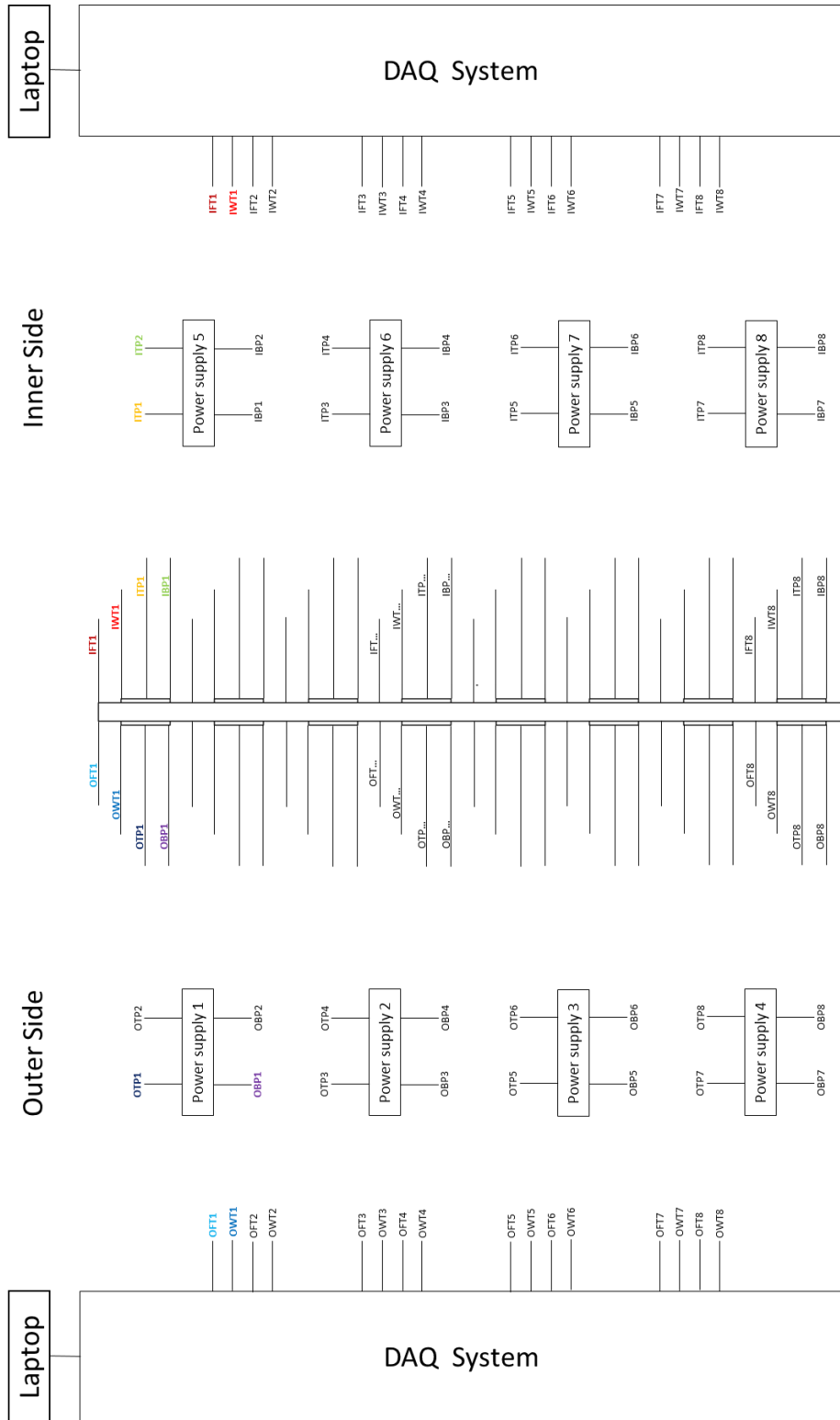
Figure 53: Schematic of the experimental apparatus.

4.1.1.1.9   Upgrades

At a second stage, the Peltier cells were controlled by a Peltier array controller (PAC) electronic system (Figure 54), capable of pulse width modulation (PWM) control of the cells and at the same time capable of measuring the temperature from the thermocouples/thermistors with commercial I2C read-out components. The motherboard integrates all AC/DC modules to power the cells and the read-out electronics, including a commercial FPGA with embedded ARM A9 microprocessor. The FPGA interfaces all the microprogrammed components on the motherboard and probes the hardware using ad-hoc Linux drivers and a mainline Kernel.
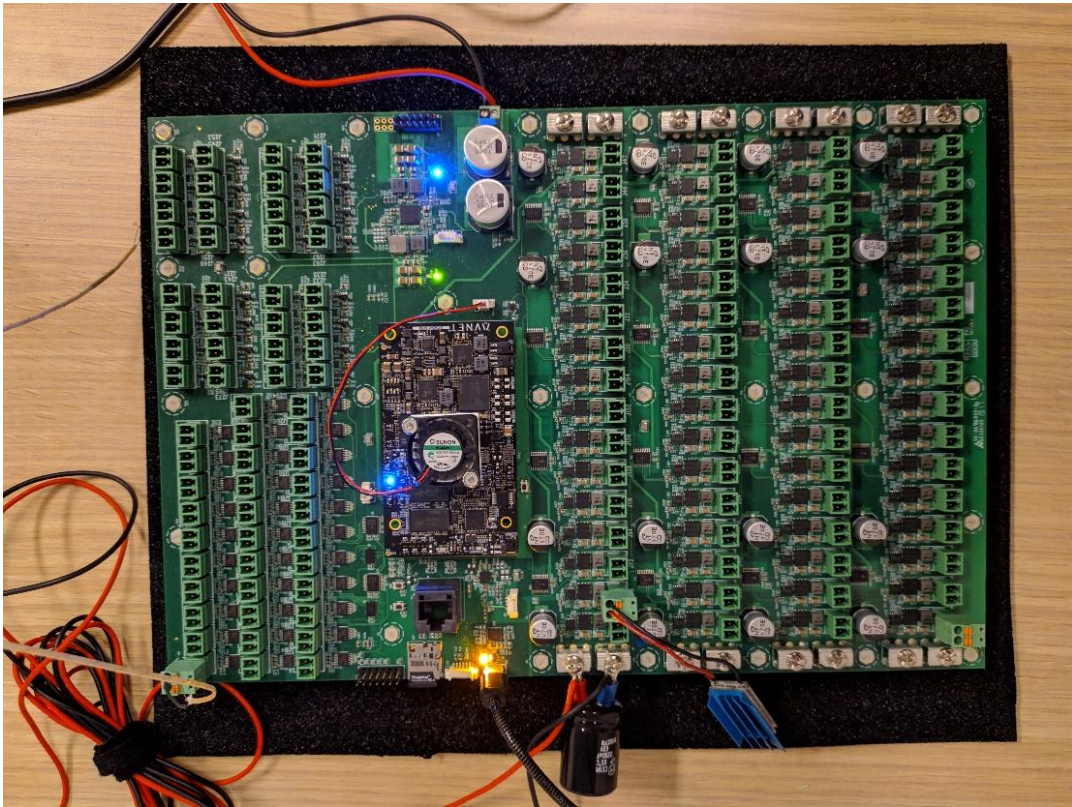
Figure 54: Peltier Array Controller.

Other future upgrades of the setup involve the utilization of thermal camera for thermal infrared imaging (Figure 55) of the prototype and the employment of ultrasound velocity profile probes for the analysis of the fluid velocity within the converter.
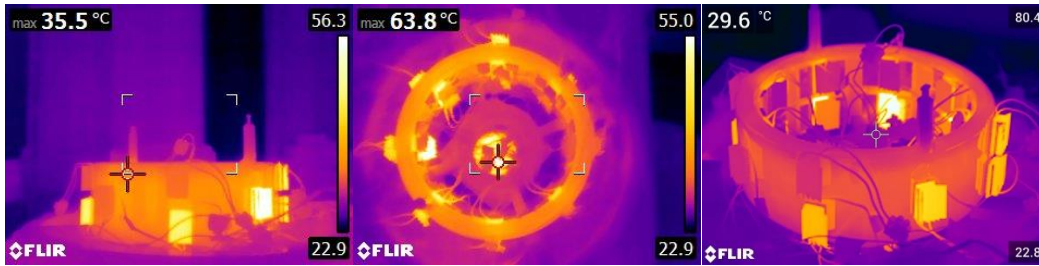
Figure 55: Thermocamera views.

4.1.1.2 TORODYNA prototype 1.0: tests and results

In order to validate the prototype, during the first tests a biphasic colloid was employed. In fact, the TORODYNA was filled with deionized water (DIW) and just a small amount of FF. Given the immiscibility between water and the hydrocarbon solvent of the FF, the resulting colloid was constituted mainly of DIW with travelling packets of FF. On one side, this allowed to employ only a small volume of FF to observe the impedance behaviour of TORODYNA; on the other, to have a clear signal, when the FF moved along the converter and trough the coils.

4.1.1.2.1 Impedance analysis

Considering the number of electronic devices employed, including cables and coils for the extraction system, analysing the impedance behaviour of TORODYNA was fundamental, also to exclude the presence of parasitic inductance. In fact, the large number of coils and magnetic material could lead to phenomena related to magnetic fields and currents, such as the mutual induction, in addition to the induced EMF. In this section, the two main electrical parameters are analysed in detail: inductance and resistance. Since from the impedance measurements it resulted to be negligible, the capacitance analysis is not reported here.

During the first test, the inductance was monitored. The inductive behaviour of the CERES reactor is analysed by measuring the inductance at terminals of the two poloidal coils connected in series. As mentioned before, the TORODYNA was filled with water and a small amount of FF in a biphasic state and the injection of 1 mL of FF (EFH1) into 1 L of water has been monitored as perturbation of the impedance of the system, since the FF acts as a high permeability core of a discrete inductor. In Figure 56b and e (with the FF injection taking place at the time marked with α) the increase of inductance of 45 nH with purely poloidal coil and of 65 nH with mixed poloidal/toroidal coil respectively is noticeable, confirming the

correctness of TORODYNA paradigm, especially considering that only 1 mL of FF was added to the converter. The value of L with only water differs in the two configurations as the concatenated magnetic flux is directly proportional to the coil area times the number of windings squared (2976.75 cm^2 in the former case and 6037.5 cm^2 in the latter, same ratio of ~2 is kept in the measurements). On the other hand, the difference in the measured increase of inductance is the result of a more efficient concatenation with complex fluid movements.
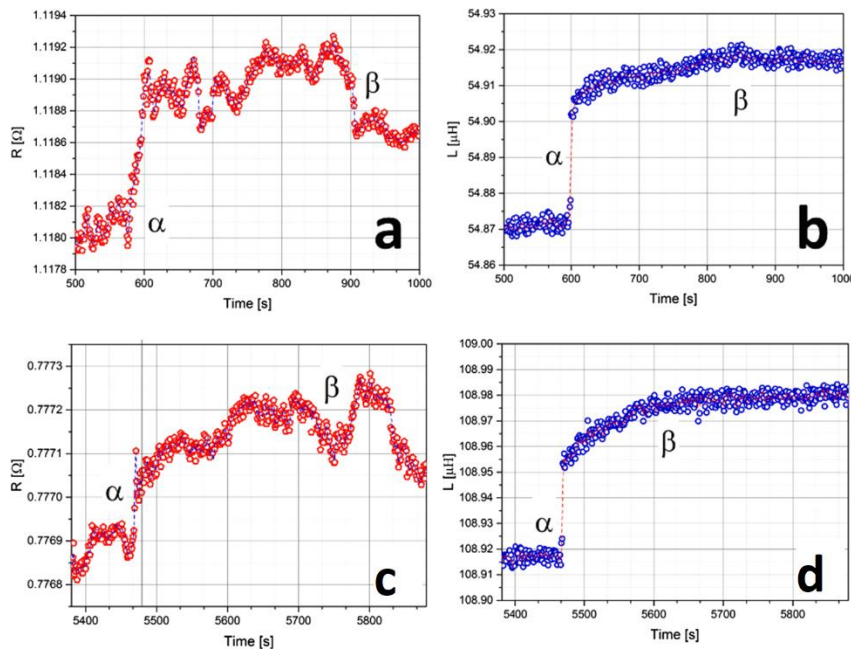
Figure 56: Effect of the injection of 1 mL of FF in 1 L of DIW. Series resistance (a) and inductance (b) versus time of poloidal extraction coil (c). Series resistance (d) and inductance (e) versus time of mixed toroidal/poloidal extraction coil (f) (197). Reproduced with permission.

Then, the inductance was fully characterized, during a 14 h long test (Figure 57). In the early stages, when Peltier cells are switched on and, after ~ 100 s, the DC current generator is activated, some variations occur. In fact, initially, the signal is very stable around 54.94 μH, but then it becomes perturbed by means of the Peltier modules. Subsequently, the DC current starts flowing into the coils and the series inductance decreases according to a linear trend, which slope drastically changes around 1000 s; finally, the signal stabilizes near 54.86 μH. The first decrease could be due to the Seebeck effect, influencing the electrical parameters of cables when their extremities are subjected to a thermal gradient, but becoming negligible in short time due to the high thermal conductivity of wires. The second

one could be due to the heating of FF inside the converter, which probably requires a certain time to initiate its cyclic motion.
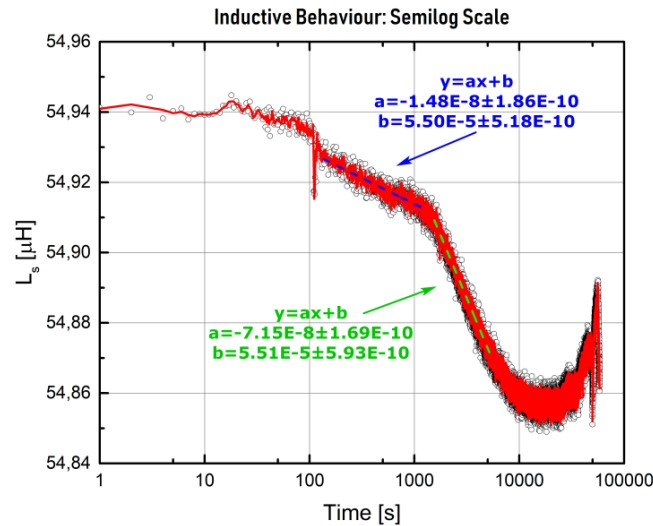
Figure 57: Inductance trend along 14 h, in semi logarithmic scale (198). Reproduced with permission.

After ~3 hours, when the motion is completely set up and steady, the inductance remains constant at the new value, slightly increasing before stopping the data collection, maybe due to the start-up of the automatic air conditioning in the lab.
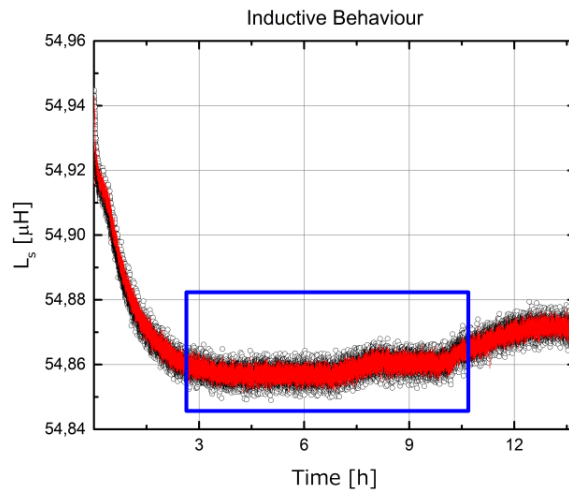
Figure 58: Focus on the inductance trend in steady-state conditions (198). Reproduced with permission.

Then, these experiments were repeated for the resistance characterization. The resistive part of impedance is used to monitor the energy output of the harvester, working on the equivalent circuit composed by the parallel between an ideal inductor (the extraction coil) and the impedance meter. So, the resistance variation, Figure 56a and d, of 800 μΩ for purely poloidal coil and 250 μΩ for mixed poloidal/toroidal coil, is due to the electromotive force generated in the experiment.

Then, the system resistance was analysed in the early stages (Figure 59). When the signal stabilizes around 1.10 Ω, with Peltier modules and the DC generator switched-on, the measure starts. Then, the FF injection occurs, so that the resistance rapidly increases up to 600 s (point 1), and then it saturates around 1.22 Ω (point 2). The increase in the resistance due to the FF is delayed possibly because the FF inertia affects the motion (the same delay observed for the inductance). Then, a long-term analysis is conducted showing that the resistance remains almost constant around 1.105 Ω (Figure 59b).

(a)   (b)
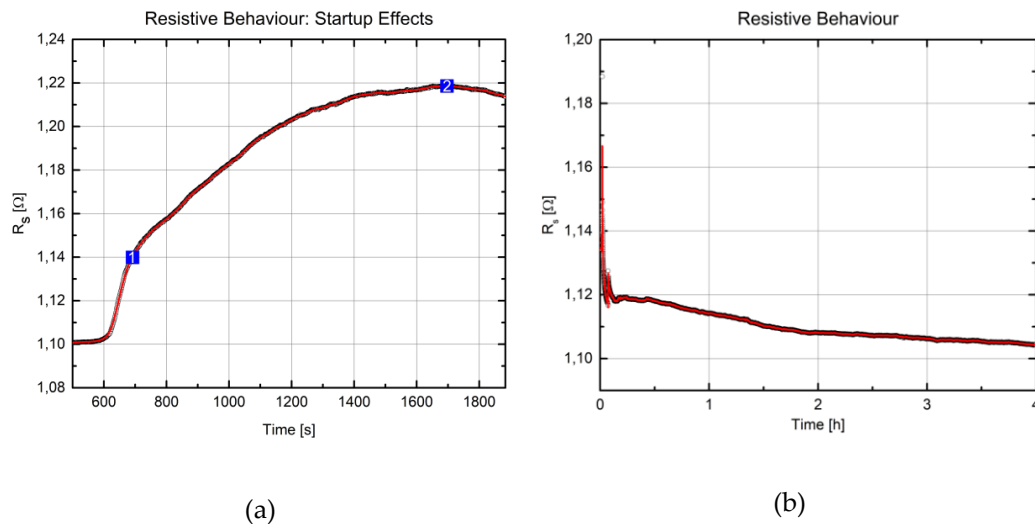
Figure 59: Early-stage (a) and long-term (b) resistance trend (198). Reproduced with permission.

In other experiments, the resistance showed a particular trend, after the injection of 1 mL of FF, after about 580 s, in the converter. In Figure 60, the red curve represents the Savitzky–Golay smoothing of the scatter plot, while the blue curve is a sinusoidal fitting. The green lines mark the temporal distance among successive peaks that, even if they could be random in time, they show a periodicity of 8 s. This value could be useful to determine the velocity of FF blobs inside the reactor given the distance between two adjacent windings (10 cm), resulting in a

FF speed of about 1.25 cm/s. In case of harmonic signal, the detection of higher order harmonics is expected. In fact, the sinusoidal fitting has a period of nearly 35 s, quite close to the fundamental period multiplied by 4.
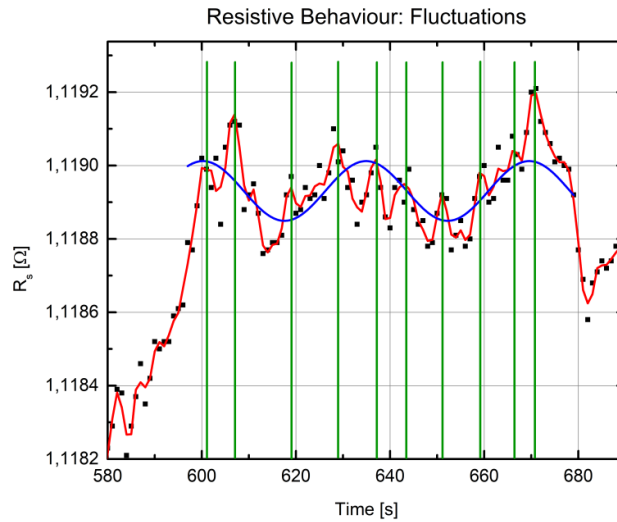
Figure 60: Fluctuations of resistance after the addition of 1mL of FF (198). Reproduced with permission.

With a closer look, the inverse chirp trend is evident (Figure 61), indicating the presence of possible density waves of FF within the converter theorized by the TORODYNA paradigm, and a strong confirmation of the paradigm itself.
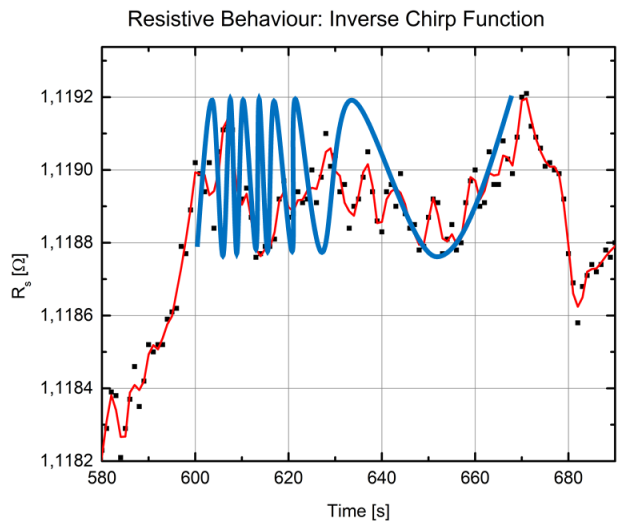
Figure 61: Inverse chirp function fitting the fluctuations occuring after the addition of 1 mL of FF (198). Reproduced with permission.

4.1.1.2.2   Thermal analysis

Afterwards, TORODYNA was filled with 10 mL of FF in DIW and a steady-state (SS) characterization was conducted, lasting several hours. The goal was to reach a long period during which the temperatures were stable at certain values within a negligible range, generating a horizontal plateau. As in the previous tests, the fluid was heated by the Peltier cells placed on the inner side (temperatures around 308.65 °C) and cooled by the Peltier cells placed on the outer one (temperature around 34.5 °C). Figure 62 clearly shows the fluid temperatures condition and the SS period. The entire toroidal axis is divided into 8 equally spaced segments, each of those portions is equipped with two thermocouples to monitor the fluid temperature on both sides. Therefore, 8 couples of curves were recorded but for sake of simplicity only one is shown.
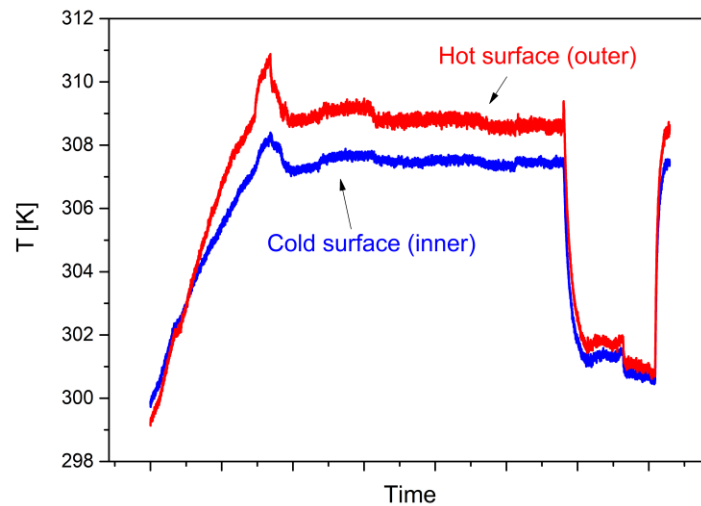
Figure 62: Experimental fluid temperatures.

In these conditions, the effective ΔT, between the inner and outer walls, submitted to the FF was 1.25 ± 0.1 °C (Figure 63a, dashed in red: Savitzky-Golay smoothing over 600 points). After the Peltier cells have been switched on at t = 0 (α), it took 1 h for reaching dynamically stable operation (γ). In order to characterize also the transient back to room temperature, after 2 h the system was switched off (δ) and on again (ε).

Analysing the temperature values coming from the 16 TCs in SS conditions along a period of 2 min, thermal fluctuations are evident (Figure 63b, dashed in black: Savitzky-Golay smoothing over 3 points, continuous in red: over 61 points). Developing a Fourier analysis on these values, a fundamental mode has been found with a period of about 150 s (s for single mode) and several other oscillation modes are present. Considering the winding periodicity (8 poloidal windings positioned every 10 cm) we can evidence the period corresponding to a packet of FF travelling across the whole toroidal axis (t for total mode, 360°) and multiples of two (720°) and three (1080°) complete turns (Figure 63c). There is also an excellent matching with impedance measurements, where monitoring of both the resistance and inductance component (Figure 63d and e) and consequent Fourier analysis (Figure 63f) evidences how all the most important spectral components (the fundamental s, the global t and the multiples at 720 and 1080°) are still present. Then, it is evident that the system can operate continuously while the thermal gradient is maintained across the converter. The periodicity of both inductance and thermal waves is a consequence of the movement of density waves across solenoids, each amplitude peak corresponding to the transit of a packet in one of the extraction sections.
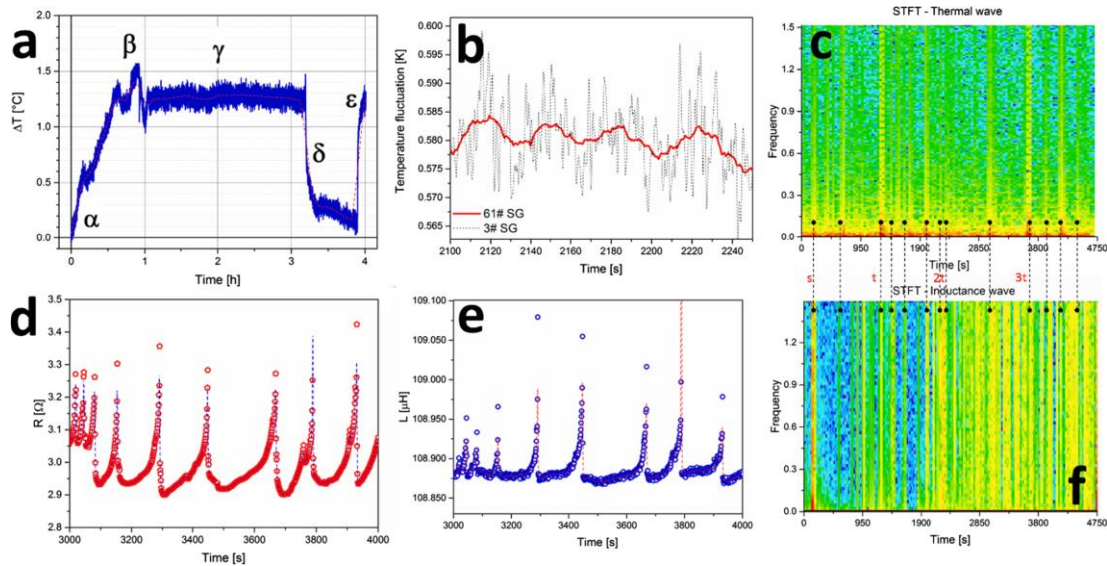
Figure 63: Steady-state operation. (a) Effective ΔT on the fluid. (b) Thermal waves. (c) Thermal waves evidenced by STFT with fundamental periods. Series resistance (d) and inductance (e) versus time showing oscillations in the steady state. (f) Inductance fluctuations as evidenced by STFT (197). Reproduced with permission.

4.1.1.2.3   Performance analysis

The TORODYNA efficiency can be evaluated by considering the parameters analysed in the impedance analysis applied to the equivalent circuits, which model the overall system. In this section, only the prototype with extraction system in poloidal configuration (Figure 49) is under analysis. It is worth to recall that, in this case, four coils were wound around the converter, with two of the three poloidal coils connected in series to perform impedance measurements and characterize the converter while the remaining two (one poloidal and one toroidal) were used to induce a magneto static field in the starting phase of the experiment. For the purpose of the analysis, only the series of two poloidal coils connected to the characterization system are considered. Figure 64 represents the equivalent circuit modelling the poloidal extraction system (R_p, L_p and C_p) connected to the characterization one (A represents the amperometer, which is not always connected to the rest of the circuit, and Z indicates the impedancemeter). As aforementioned, the measurements suggest that the capacitor C_p is negligible, but it is shown here for completeness.
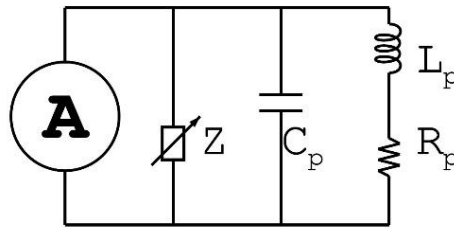
Figure 64: Equivalent circuit modelling the extraction system connected to the characterization one (198). Reproduced with permission.

Then, the impedance Z_p of the circuit was measured by means of an impedancemeter, corresponding to:

$$Z_p = R_p + jX_p$$

where R_p is the resistance, and X_p is the reactance (imaginary part of the impedance) that can be evaluated, considering C_p neglibile, by means of:

$$X_p = X_{L_p} + X_{C_p} = \omega L_p - \frac{1}{\omega C_p} = \omega L_p$$

Considering that the inductance L of a solenoid can be calculated using:

$$L = \frac{\mu A N^2}{l}$$

where μ is magnetic permeability of the material contained within the solenoid, A is the cross section of the solenoid (120.7 cm^2), N is the number of turns (80) and l the length of the coil (294 cm).

Here:

$$\mu = \mu_r \mu_0,$$

where μ_r is the magnetic permeability of the fluid within the converter and μ_0 is the magnetic permeability in vacuum:

$$\mu_r = 1 + \chi_m,$$

where χ_m is the magnetic susceptibility of FF EFH1 (2.64).

If the converter were totally filled with only air with $\mu_r = 1$, the resulting inductance would be 33 μH. If the reactor were completely filled with magnetite NPs, whose magnetic permeability corresponds to $\mu_r = 3.64$, the resulting inductance would be $L = 118$ μH. Since the inductance measured during the impedance analysis, after the injection of 1 mL of FF, was around 54.94 μH, the magnetic permeability of TORODYNA has to be $\mu_{r,eff} = 1.00666$. Consequently, the addition of a small amount of FF, with a vol. concentration equal to 7.9% of Fe_3O_4, corresponds to an increase in μ_r of 1%, with respect to the case of empty reactor.

As aforementioned, the resistive part of the impedance was used to evaluate the energy output of the harvester. In particular, the data shown in Figure 59a, before and after the injection, including the transient up to point 2, were employed. Since the resistance in alternate current (AC) before and after the injection were respectively $R_b = 1.1006$ Ω and $R_a = 1.2189$ Ω, the resulting variation $\Delta R = R_a - R_b$ is approximatively 0.11829 Ω. In order to evaluate the induced electromotive force (EMF), the system was modeled as a parallel between an impedance experiencing the variation of resistance and a voltage generator representing the EMF generated, both of them connected to a load representing the measurement system (Figure 65).
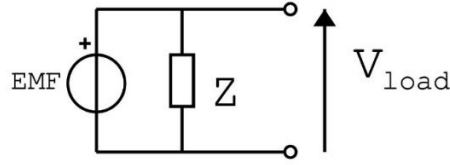
Figure 65: Equivalent circuit for the evaluation of EMF (198). Reproduced with permission.

Thus:

$$I_{meas} = \frac{V_{load}}{R},$$

then:

$$R = \frac{V_{meas} + EMF}{I_{meas}},$$

where V_{load} is the voltage drop across Z, while I_{meas} and V_{meas} are the output current and voltage of the impedancemeter, applied to perform the measurement.

Deriving with respect to EMF:

$$EMF = R\,I_{meas} - V_{meas}.$$

Considering that the current and the voltage provided by the impedancemeter were respectively 0.5 mA and 0.4 mV, the EMF before and after the FF injection are respectively $EMF_b = 150.3\,\mu V$ and $EMF_a = 209.5\,\mu V$ giving resulting in a $\Delta EMF = 59.2\,\mu V$. Since the measured resistance of the cable employed for the coils (R_c) is equal to 1.2292 Ω, the electrical power in output is:

$$P_e^{out} = \frac{\Delta EMF^2}{R_c} = 2.85\,nW.$$

In order to estimate a reasonable input thermal power, a thermal gradient of 50 °C between the two sides of the Peltier cell, cells is considered when they operate at 0.5 A and 2.3 V (operating conditions), corresponding to a coefficient of performance (COP) of 0.5, resulting in a heat absorbed by the cold side of:

$$Q_c = \frac{COP}{P_e} = 0.44\,J.$$

Since the TORODYNA have 32 Peltier modules installed, the overall thermal energy provided to the prototype is equal to 13.91 J. However, the ΔT between the external walls, T_w, and the fluid, T_f, is around 5 °C and considering the thermal conductivity of PLA being nearly 0.13 W m^{-1} K^{-1} and the wall thickness, t, 5 mm, and the internal hot area of the prototype, A_i, 0.052 m^2, the input thermal power corresponds to

$$q = k \frac{T_w - T_f}{t} A_i = 6.76 \, W,$$

giving an efficiency of conversion, evaluated as the ratio between the electrical power in output and the thermal power in input of:

$$\eta = \frac{P_e}{P_t} = \frac{2.85 \cdot 10^{-9}}{6.76} = 4.2 \, e^{-10}.$$

4.1.1.2.4   Numerical analysis

If the first goals were those of validating the TORODYNA paradigm and evaluating its initial performances then, a process of optimization started in order to investigate how the configuration of the magnetic field, combined to the thermal one, alters the flow development and, consequently, the electrical energy output. For doing so, the first step involved the development of numerical analysis for simulating the complex multiphysics phenomena governing the system, since the opaqueness of the walls and the FF itself did not allow optical visualizations of the flow, and at an early stage, we could not install acoustic velocimetry. Given the small size and large number of the suspended particles, the harvester was physically modelled as a two-phase system with an Eulerian-Eulerian approach, i.e. both phases, the solvent and the suspended colloidal particles, are treated mathematically as interpenetrating continua. Moreover, considering the small volume fraction of the solid phase, of the order of 10^{-2}, and the negligible inertia of the particles, the latter are assumed to be in thermal equilibrium with the surrounding flow and the model is conveniently formulated in terms of the mixture velocity and temperature. The solid phase is described through its volume fraction φ. The small ΔT, of the order of 1 °C, allowed to use of the Boussinesq approximation for natural convection. In the model, particles are subject to the hydrodynamic interaction with the solution, which includes the thermophoretic force, and to the magnetophoretic force due to the externally imposed magnetic field. Furthermore, the particle inertia is neglected, so that the slip between particles and mixture is due to the forces acting on the particles, that is, Stokes drag, Brownian forces, thermophoretic and

magnetophoretic forces. Then, the magnetization is assumed much weaker than the externally imposed magnetic field, due to the low volume fraction of the suspended particles. Finally, the confinement in the vertical direction is neglected, and only the flow in the core of the toroidal configuration is considered, so that the governing equations are solved in a parallelepiped domain between two vertical walls. With this method, the top and bottom portions of the vessel, where the vertical convective flow changes direction, are excluded by the simulation, which considers only the central portion of the vertical extent of the system. A scheme of the simplified flow domain is shown in Figure 66a and d, together with two of the investigated magnet configurations.
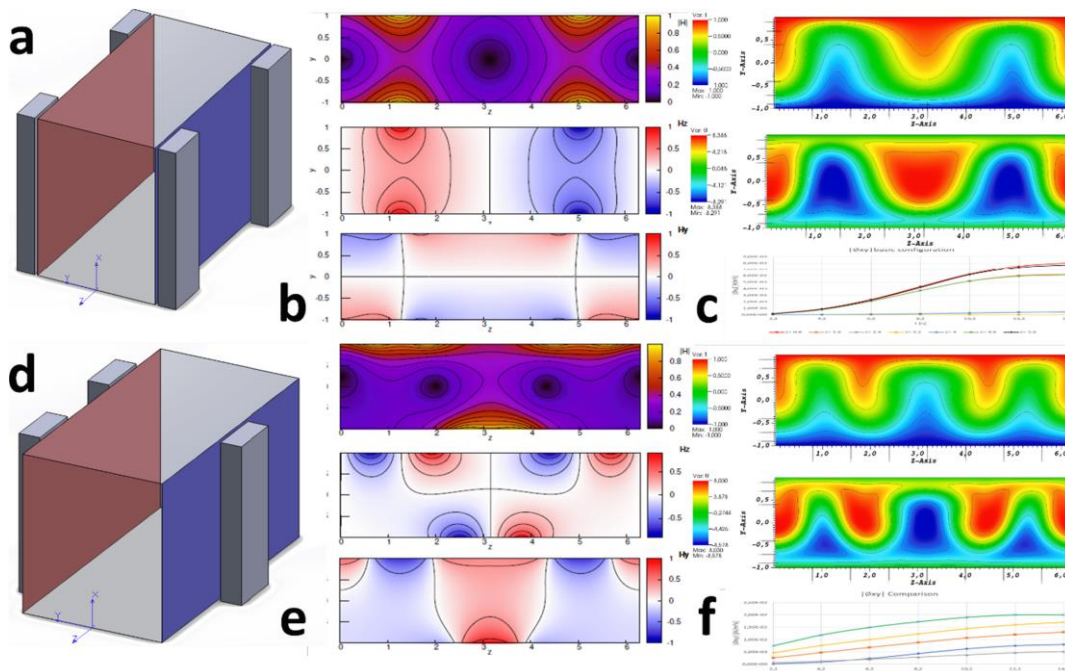
Figure 66: Investigated configurations with simplified flow domain (a) and (d). Solutions of Laplace equation for magnetic potential, from the top: magnetic field strength, toroidal component of magnetic field, poloidal component of magnetic field (b) and (e). Solutions of thermomagnetic advection equation, from the top: temperature, vertical component of velocity, toroidal component of magnetic flux (c) and (f) (197). Reproduced with permission.

The resulting partial differential equations are discretized with a mixed spectral-finite difference scheme: a Fourier-spectral discretization has been used along both the vertical and toroidal coordinates while finite differences are used along the poloidal axis. No-slip boundary condition for the velocity field and Dirichlet boundary conditions are imposed on the two vertical walls, while periodic boundary conditions are used in the other directions. A fourth order standard

Runge-Kutta method has been used for time integration. The magnetic field is generated by a set of permanent magnets, installed around the cell, arranged in vertical strips of opposite facing magnets Figure 66a and d. They are simulated by considering them as infinite in the vertical direction so that the magnetic field generated by the magnets is almost perpendicular (even if curved near the side edges) to the TORODYNA walls. Convection motion along the vertical axis are a direct consequence of the temperature gradients in the flow domain. Hotter volumes are associated with lower flux densities and the resulting motion is upwards near the warmer wall and downwards near the colder wall. Since the Rayleigh number is relatively small, the flow remains laminar, and the vertical component is always the dominating one. The other two velocity components, normal to the wall, i.e. directed across the vessel thickness, and along the toroidal axis, are a direct consequence of thermomagnetic force, as buoyancy does not act in such directions. Therefore, the position of the magnets and the intensity of the magnetic field directly modulate these components of the velocity, which is important for the creation of three-dimensional cells able to generate a flux of magnetized particles that can be intercepted by the coils. The simulations allow computation of the magnetic flux through an arbitrary surface, so that it is possible to understand where the extraction coils must be ideally located to increase energy extraction efficiency. From the results shown in Figure 66, it is evident that the asymmetry between upward and downward motion, induced by the magnetic field, brings a preferable configuration. The main finding is that, having purely poloidal coils, the configuration that maximizes the magnetic flux, and therefore the overall energy efficiency, corresponds to perfectly asymmetric magnets (i.e., shifted by half their pitch, Figure 66d) with a total phase mismatch along the toroidal direction of the magnetic fields generated by the opposite facing magnets. Such a configuration is potentially able to increase the magnetic flux up to 80% with respect to the basic configuration with directly opposing magnets. Therefore, the overall efficiency of the system could be further increased (197) (200).

4.1.1.2.5   Enhancements

 In order to improve the conversion efficiency and increasing the output electrical power of TORODYNA, many solutions are identified, to be applied in future developments of the project. A short list of improvements is here provided:

- increase m_{eff} of 100 times (100 % FF) in order to reach an output power of ~ 1µW;

- saturate the NP magnetization, resulting in a factor 10 to 100, reaching an output power in range 10 µW to 100 µW;
- use NPs with very high saturation, to reach a value of P_{out} comprised between 50 µW and 500 µW;
- provide a larger input electrical power, in order to increase Q_C. Then, if COP = 5, Q_C enlarges of 10 times, and the ouput power achieves 0.5 mW to 1 mW;
- smaller thickness of TORODYNA vessel, for enhancing thermomagnetic advection;
- smaller thickness of the walls, for enhancing heat transfer between heat source and the fluid.

On the other hand, for simply exploring the effects that some modifications of the prototype could bring, many ideas are proposed. Of course, many of them, before being practically applied, could be validate or not by means of numerical simulation, for example in COMSOL Multiphysics® environment. An exhaustive list is here provided:

- Peltier cells installed on top and bottom sides instead of inner and outer;
- different permanent magnets (or electromagnets) configurations and magnetization (instead of axial, longitudinal);

Finally, some improvements in the experimental setup could be:

- better sealings;
- installing fluid thermocouples with mechanical fittings;
- installing walls thermistor with a better adherence;
- enameled wire instead of rubber sheath, for enhancing electrical performance;
- utilisation of a cooling system for the Peltier modules (or single heat sinks), in order to improve their performance;
- transparent structure for performing optical visualization with biphasic fluid.

4.1.2 TORODYNA prototype 2.0

Considering the need of having a transparent structure, a borosilicate glass (Pyrex®) prototype has been designed and produced. In Figure 67 two pictures of the prototype are shown, where only the inner side is equipped with Peltier cells

and permanent magnets. Here, heat sinks were installed on the Peltier modules to improve their efficiencies.
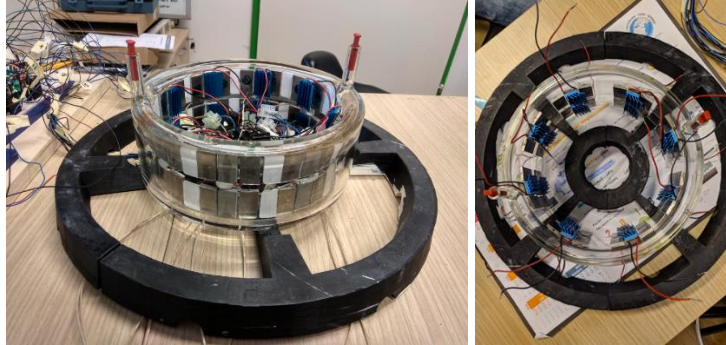
Figure 67: Isometric (left) and top (right) views of Pyrex® prototype.

The goal was that of observing the internal motion of the fluid throughout the converter in order to verify what we were expecting from theoretical models and numerical results. In this way, it was also possible to improve the design according to the observations. Since FF is opaque, some tracers were tested for the optical visualizations. Figure 68 shows a typical application for the TORODYNA converter. An industrial pipe mockup was created and TORODYNA 2.0 was installed on it, then it was filled with DIW and a few drops of blue ink were added to visualize the internal motion of the fluid. Then, mica powder was also tested as tracer, showing interesting results.
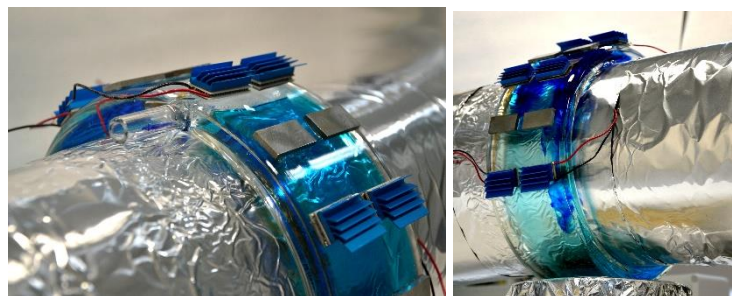
Figure 68: TORODYNA 2.0 filled with blue ink and installed on a pipe mockup.

Unfortunately, the complexity of the fluid dynamics induced by the geometry and thermomagnetic phenomena adding non trivial effects led us to evaluate the possibility of dealing with a simpler geometry. In fact, in the TORODYNA configuration, the motion generation and the energy recovery system are not linearly independent. In order to define a stable and unperturbed fluid motion with a stable electric output power, it is necessary to consider: the toroidal geometry, the

aspect ratio of the device, the structural materials and the colloid, the heat exchange between the waste heat and the solution and the choice of the magnets (magnitude and position). Therefore, we applied a simpler approach, decoupling the motion generation from the recovery system. Taking inspiration to what was made for the numerical simulations and in order to be able to validate the computational results with the experiments, we decided to take a step back and analyse a planar setup. Then, exploiting the periodicity of the geometry, only one thermomagnetic region was put under analysis, in order to focus on the fluid dynamic phenomena occurring in the orthogonal plane of the converter. On the other hand, for what concern the longitudinal dimension, a simplified setup was built for the analysis of the pure inductive effect of the ferromagnetic colloid. In this way, it was possible to do a proper electric characterization of the open-circuit voltage and short-circuit current generated by the magnetization and demagnetization of a FF, when it is subject to the action of a permanent magnet. Further improvements include the installation of optical visualization systems (cameras) to record the internal motion of the colloid and give a comparison with numerical simulations.

4.2   Planar setup

After having realized that a decoupling of longitudinal and transversal dimensions was needed in order to simplify the analysis, a planar experimental setup was designed and built. Furthermore, the need of comparing numerical and experimental results led to designing a setup the most similar to the computational model. First, a testing area of 200x100 mm^2 was designed. Different thicknesses were tested in order to evaluate the effect on the thermomagnetic phenomena. To generate a thermal gradient across the so-called "cell", a steel plate was installed on the bottom for heating by means of thermal tape, while a water based convective cell was installed on top for cooling. In order to maintain the testing area between a constant thermal gradient, the structure was made of Teflon, also for having adiabatic walls laterally. Permanent magnets or Helmotz coils are installed to set a permanent magnetic field. To guarantee transparency, the top cover was made of poly(methyl methacrylate) (Plexiglass). For each lateral side, N-type thermocouples were installed to monitor temperatures of the heating plate, cooling cell and of the FF under investigation. Finally, lateral holes allow the installation of ultrasound velocity profile (UVP) probes. The idea was to put the cell so that thermal gradient and gravity are parallel. Then, after setting a thermal gradient and a permanent magnetic field, observing the thermomagnetic rolls generated optically (by using optical tracers dispersed in the FF) and acoustically with the UVP system.

In Figure 69, two renderings show how the cell is made and how it works while Figure 70 shows a real picture of the cell where no subsystems are installed.
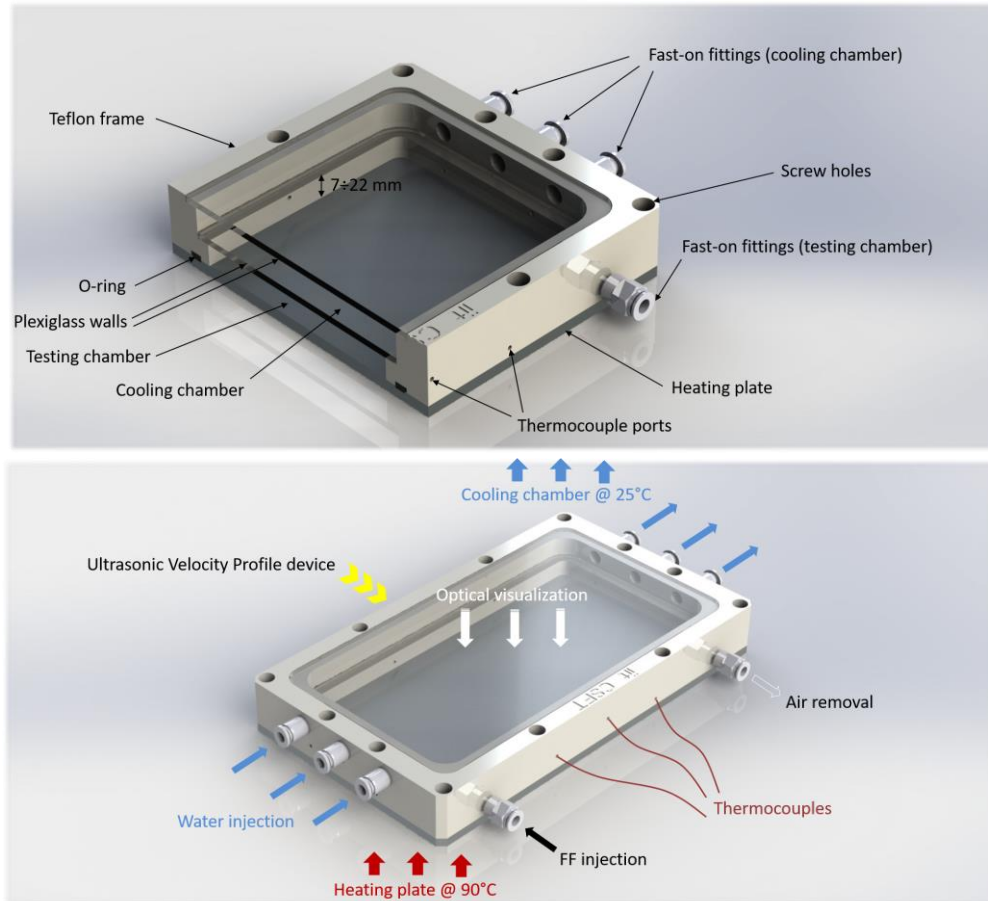
Figure 69: Isometric section (top) and view (bottom) of the rendered testing cell.
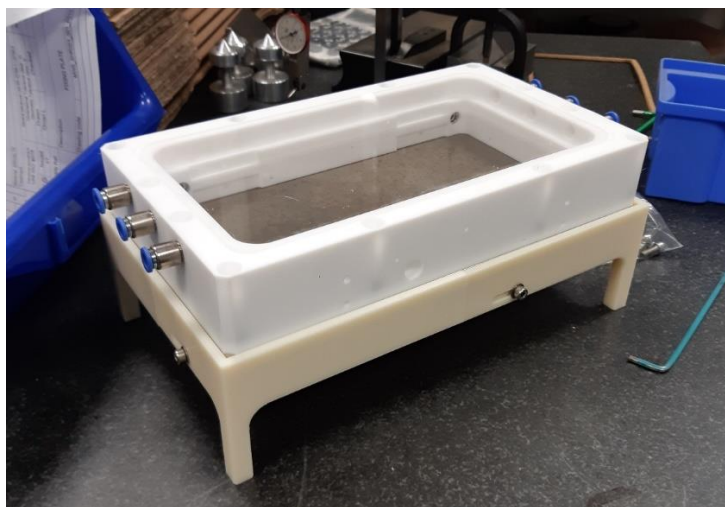
Figure 70: Picture of the testing cell with no sub-systems installed.

The experimental campaign is taking place at Hokkaido University, Laboratory of Flow Control, as part of a joint project with Istituto Italiano di Tecnologia but the results not yet available. The aim is to investigate experimentally both the fluid dynamics and the energy conversion capability of a hypothetical planar device.

4.3   Linear setup

4.3.1 Ferrofluid – Inductive effect

Then, a simplified linear setup was designed and built in order to characterize the inductive properties of FF when, magnetized, it moves through a coil. A peristaltic pump (Ismatec MCP) was used to generate a tunable motion through a fluorinated ethylene propylene (FEP) pipe with an inner (ID) and outer diameters (OD) of 10 and 12 mm respectively. The choice of such material will be explained in the next section. The Ismatec MCP provides a rotor system that allows pipes with a maximum internal diameter of 3.2 mm. This permits to generate at the maximum rotational speed a flow rate of 100 mL/min for each channel, up to 8 channels. A silicone pipe with internal and external diameters of 3.2 and 4 mm respectively, was coupled with the rotor system of the peristaltic pump; then, a series of intermediate pipes and adapters allowed connecting the testing pipe. The goal was that of having a laminar flow (Re < 2,000), in order to have a priori an idea of the velocity profile (Poiseuille flow (201)), since a laminar flow gives a different contribution to the electromotive force generated by the motion of the FF. However, in this early stage, magnetoviscous phenomena, turbulence effects introduced by the change of dimensions of the pipes due to the adapters and non-continuous flow generated by the peristaltic pump were not taken into account. For characterizing the inductive effects, a solenoidal coil is rolled up around the FEP pipe. The solenoid (Figure 71) is made of OFC wire (100 mm long and 2.5 mm in diameter) with 40 windings around the pipe.
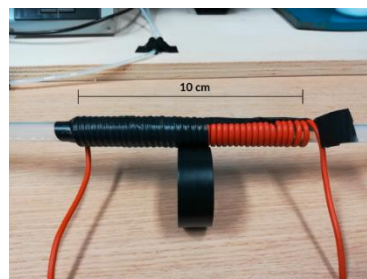
Figure 71: Solenoid wrapping the FEP pipe as characterization systems for inductive effects of FF.

A stack of 7 AlNiCo$_5$ permanent magnets were used in order to induce magnetization in the FF solution. Figure 72 shows the overall experimental setup.
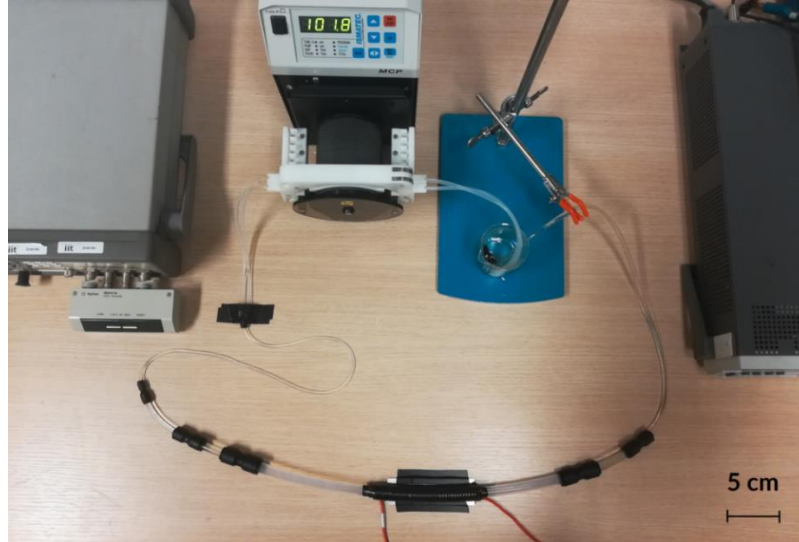
Figure 72: Experimental linear setup with peristaltic pump (top center) connected to the FF contained in a Becher and to the testing pipes, and the inductive electrode coupled with a stack of permanent magnets (bottom center) (146). Reproduced with permission.

The solenoid was connected to the SourceMeter-Keithley 2635A to perform an open-circuit voltage measurement, to the Semiconductor characterization system Keithley 4200-SCS coupled with a low-noise amplifier Keithley 4225-RPM (Tektronix, Inc., Beaverton, OR, USA) for measuring the short-circuit current, and to the impedancemeter Agilent E4980A for an impedance analysis. Since the different sensibility on the current and voltage measurement, two different instruments were used. In fact, the Keithley 4200-SCS has a current resolution of 10 aA if associated with the Keithley 4225-RPM amplifier. All the instrumentation is connected to a PC with LabVIEW^{TM} 2019 software (National Instruments, Austin, TX, USA). Three different Fe$_3$O$_4$ volumetric concentrations (2, 4 and 6 %) were tested, by diluting the FF EMG 901, in order to encompass a broader range of Magnetic Reynolds number. In fact, velocity spanned from 0 to 5 cm/s, respectively 0 and 10 arbitrary unit (A.U.). In order to evaluate V_{OC} and I_{SC} at the equilibrium, a data subset was selected when the measured values reached SS conditions. Then, a moving average filter (first-order polynomial Savitzky-Golay filter), with a fixed filtering window of 51 samples was applied, in order to minimize of the error band, due to the natural damping of the RLC circuit. Considering the different specifications of the instruments employed, 3 and 15 samples for second were acquired for the voltage and current respectively.
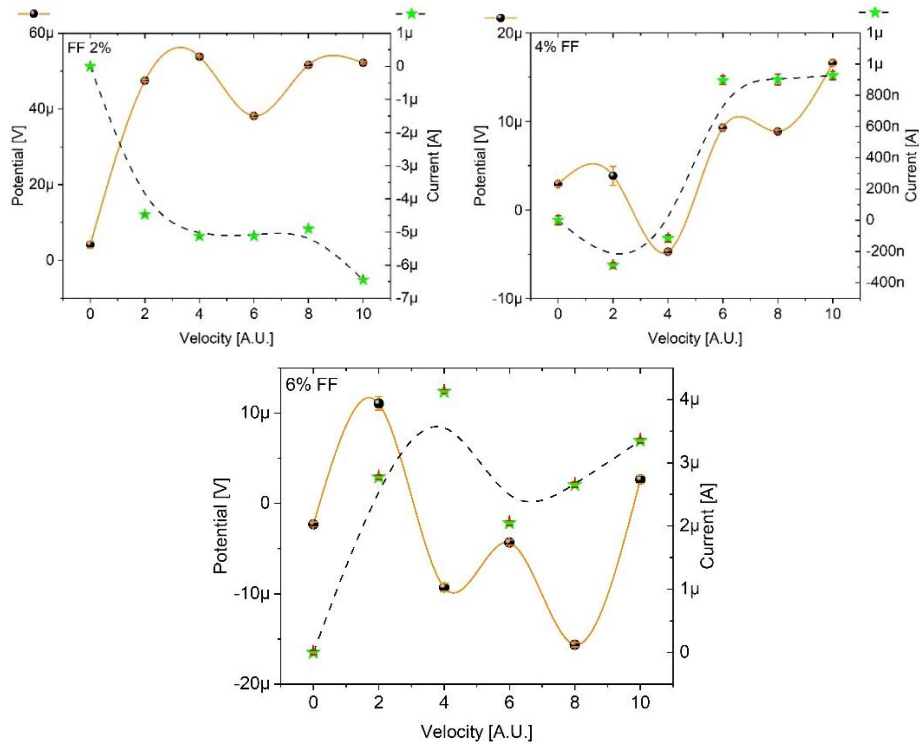
Figure 73: Comparison between harvested potentials and currents by means of the inductive electrode for FFs featuring increasing vol. concentration (2, 4 and 6%) of Fe_3O_4 (202). Reproduced with permission.

For what concerns the measurements at 2% vol. of FF (2% FF, Figure 73 top left), the trends of voltage and current are quite related, because when the mean velocity of the fluid reaches 3 cm/s (6 A.U.) there is a decrease and subsequently an increase of both parameters (in module). This is a direct evidence of the passive nature of the electrical characteristics of the device. Thus, it is possible to model the source as an electromotive force generator and the corresponding current associated to the resistive nature of the coil (146). From a fluid dynamic point of view, we suppose that the negative variation of the voltage at 3 cm/s can be associated to a fluid transition from laminar to turbulent flow due to magnetoviscous effects neglected during the setup design. This transition can generate recirculation zones, where the velocity profile of the fluid is not anymore described by a Poiseuille-like flow. Therefore, the evaluation of the mean velocity implies a reduction of the global electric characteristics of the system. This is an evidence of the nonlinear dependence of the motion generation with respect to recovery part of the system. However, increasing again the mean velocity of the fluid, voltage and current increase accordingly. Regarding the electrical power

analysis, the system reaches a voltage peak with a velocity of 2 cm/s (4 A.U.), where the associated electromotive force has a value of about 55 μV and the relative current has a value of 5.2 μA. Moreover, it is worth considering that the current generated in the device produces an induced magnetic field inside the coil that perturbs the motion of the magnetic fluid. At 2% FF, it is evident that this perturbation is negligible, because the current behaviour follows linearly the same voltage behaviour. Finally, supposing that the output power generated by the device is the product of V_{OC} and I_{SC}, it reaches P = 0.29 nW in a volume of V = 7.85 mL (considering the amount of FF contained in the volume of the pipe confined by the solenoid). Then, the power per unit volume of FF at a concentration of 2% is equal to 36.9 nW/L (@v = 2 cm/s). Note that in a real WHP application, the evaluation of the output power should be done considering different resistive loads and consequently, evaluating the voltage and the current in each working condition.

For what concerns the tests at 4% vol. (Figure 73, top right) the transition from laminar to turbulent is evident at 1 cm/s (2 A.U.). This is likely due to the increased magnetization of the FF, arising magneto viscous phenomena affecting the fluid dynamics, introducing a non-linear component in the fluid motion, due to the complex distribution of magnetic field along the motion direction. In this case, the mean velocity in the extraction region of the pipe may present more distributed recirculation modes along the normal direction of the flow. Since the electromotive force is mostly related to the internal product between the magnetization field and the velocity field, the values of voltage and currents are profoundly affected. Therefore, a tradeoff between the motion generation (velocity dependence) and the energy recovery (magnitude of the permanent magnets and concentration of the FF) is needed.

Last, with 6% FF, the laminar flow is not anymore present even at 1 cm/s. Therefore, the voltage and current characterization can provide helpful information about the fluid motion, but the results are not interesting for the output power characterization. However, in contrast to the previous cases, the voltage and current have an incomparable behaviour, probably due to an induced magnetic field generate by the current flow perturbing the fluid motion suggesting that this recovery technique may be more suitable for energy storage by means of batteries, supercapacitors, or in general devices that have a high intrinsic resistive and capacitive component. This also means that the electromotive force associated to the fluid motion can be increased simply introducing a larger density of coil in the extraction region.

This is the reason why in the following experiments we employed FFs with a vol. concentration of 2% vol. Further investigation could involve the analysis of FF behavior when the concentration is reduced to 1% and 0.5% vol. The relatively low performances obtained exploiting the FF inductive capability led us to consider different materials associated to other physical effects for the purpose of energy harvesting by means of colloids.

4.3.2 Colloidal titania – Triboelectric effect

As this stage, other ideas came out moving the focus from FF, to colloids in general. Starting from the recent findings described in 1.3.4, we considered triboelectric materials. In this case, the idea was that of exploiting the waste heat to generate the motion of colloidal TiO_2 (T) through a FEP pipe, governed by natural or Rayleigh-Bénard convection processes (203). Placing an aluminum ring electrode in contact with the pipe, electrostatic charges are accumulated due to the triboelectric effect between the fluid and the inner pipe walls. Inspired by the work of Ravelo et al. (204), a simple setup (Figure 74) similar to that shown in 4.3.1 was used.
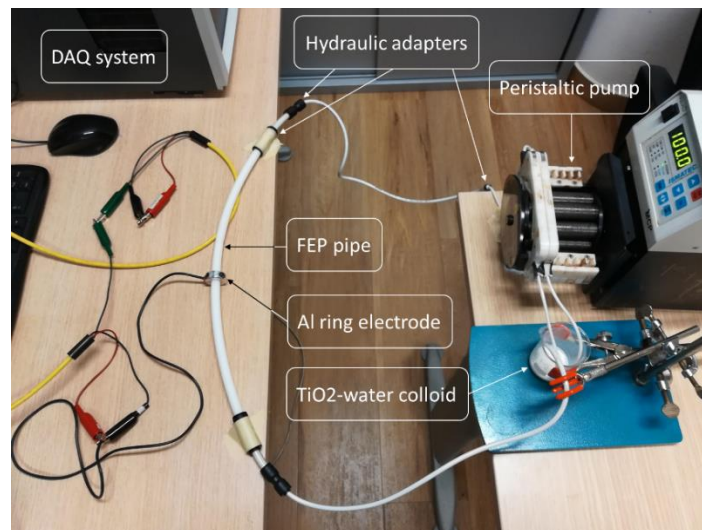
Figure 74: Photograph of experimental setup for the triboelectric characterization (155). Reproduced with permission.

Again, the same peristaltic pump (Ismatec MCP) generated a tunable motion of a colloidal solution of TiO_2 NPs (Evonik Degussa, Essen, Germany) and DIW through circular FEP pipe (ID=10 mm, OD=12mm). Its triboelectric features (154), and chemical compatibility with water-based suspensions drove the choice of FEP. The same fluid dynamics considerations made in the previous section for the FF

experiments drove the sizing of the pipe, resulting in maximum mean velocities within the pipe of the order of cm/s, which are reasonable values in a real device, supposing a motion triggered and governed by natural or Rayleigh-Bénard convection processes. In this case, the pump was placed in a different bench in order to mechanically isolate the characterization system. The region addressed to the accumulation of electrostatic charges was installed halfway of the pipe in order to reduce the fluid dynamics disturbance related to the variating pipe section and deal with a fully developed velocity profile. An aluminum ring (ID=12 mm, OD=28 mm, length=9 mm) in single electrode mode (SEM) configuration was clamped externally to the pipe for accumulating the charges generated by triboelectricity while characterizing the capacitive system. Considering the triboelectric coupling with FEP, Al was the perfect candidate since its tendency of accumulating positive charges on its surface. As reference electrode was used the ground of the measurement instruments, in order to guarantee the repeatability of the measurements. V_{OC} and I_{SC} measurements were conducted respectively by means of SourceMeter-Keithley 2635A and the Keithley 4200-SCS coupled with a Keithley 4225-RPM Remote Amplifier (Tektronix, Inc., Beaverton, OR, USA). All the instruments were connected to a PC with LabVIEW[TM] 2019 software (National Instruments, Austin, TX, USA). In this case, the impedance analysis was not conducted, since we are dealing with a single electrode device. In Figure 75, a schematic of the overall setup is shown.
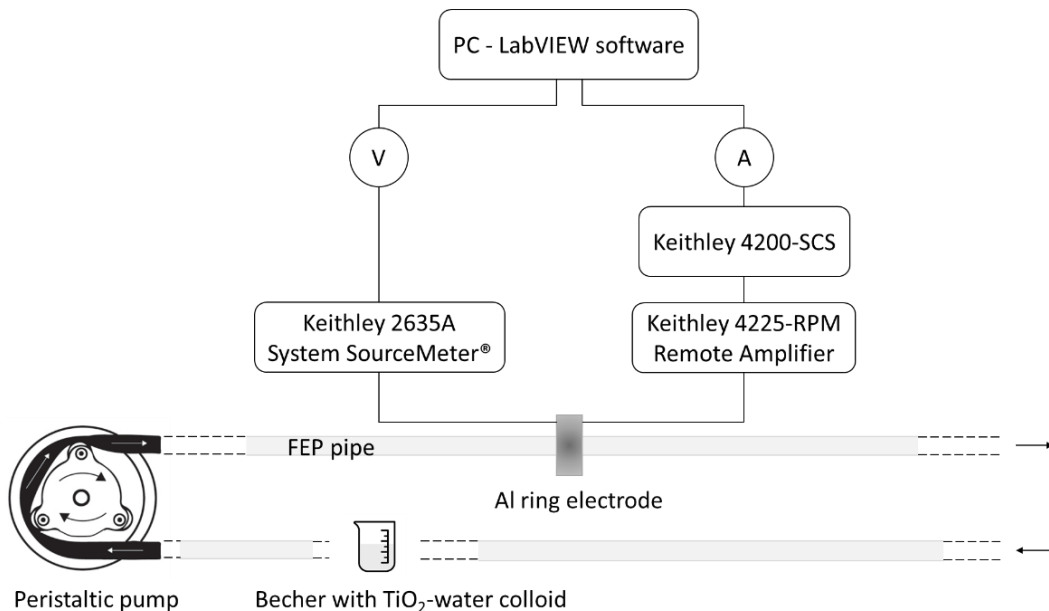
Figure 75: Schematic of experimental setup for triboelectric characterization (155). Reproduced with permission.

In order to verify the action of triboelectricity when the fluid is moving, a preliminary analysis (Figure 76) on the time evolution of voltage and current was conducted, varying the operational conditions of the pump using a 1% TiO_2 solution.
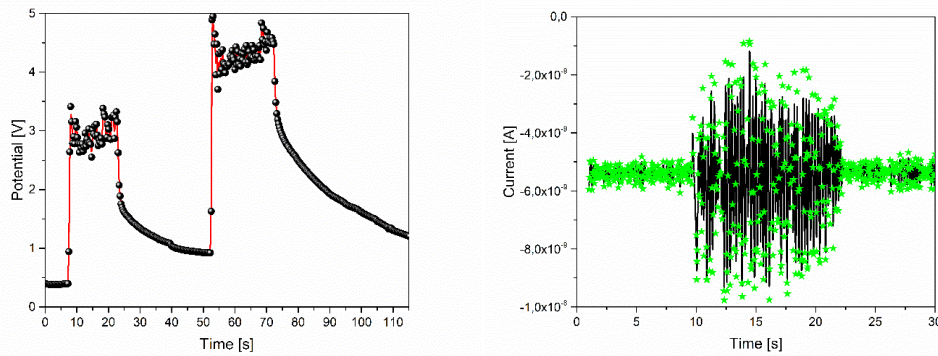
Figure 76: Evidence of triboelectricity from: Voltage-Time (left) and Current-Time (right) analysis of 1% TiO_2 solution (155). Reproduced with permission.

In Figure 76, a direct relation between the flow into the pipe and the charge accumulation on the ring electrode, is observed. In fact, when the pump is switched on (off), a steep increase (decrease) of the output voltage can be noticed. This is typical for a RC circuit, with the resistive component associated to the conductivity of the solution, the capacitive component to the geometrical properties of the electrodes and to the insulating properties of the polymer interface, and the current flow in the electrodes proportional to the velocity in the pipe (155).

Then, for evaluating V_{OC} and I_{SC} at the equilibrium, a data subset was selected when the measured values reached SS conditions. Then, a moving average filter (51 point, first-order polynomial Savitzky-Golay fitting) was applied in order to reduce the vibrational noise given by the pulsed motion of the fluid, minimizing the error band. Again, 3 and 15 samples for second were acquired for the voltage and current respectively. DIW and two suspensions at different concentrations (0.5 and 1%) of 30 nm TiO_2 NPs in DIW were tested (Figure 77). The electrical behavior of the device was analysed setting the peristaltic pump at five different fixed velocities: 1, 2, 3, 4 and 5 cm/s while observing the corresponding values of voltages and currents generated on the Al electrode by the colloid motion.
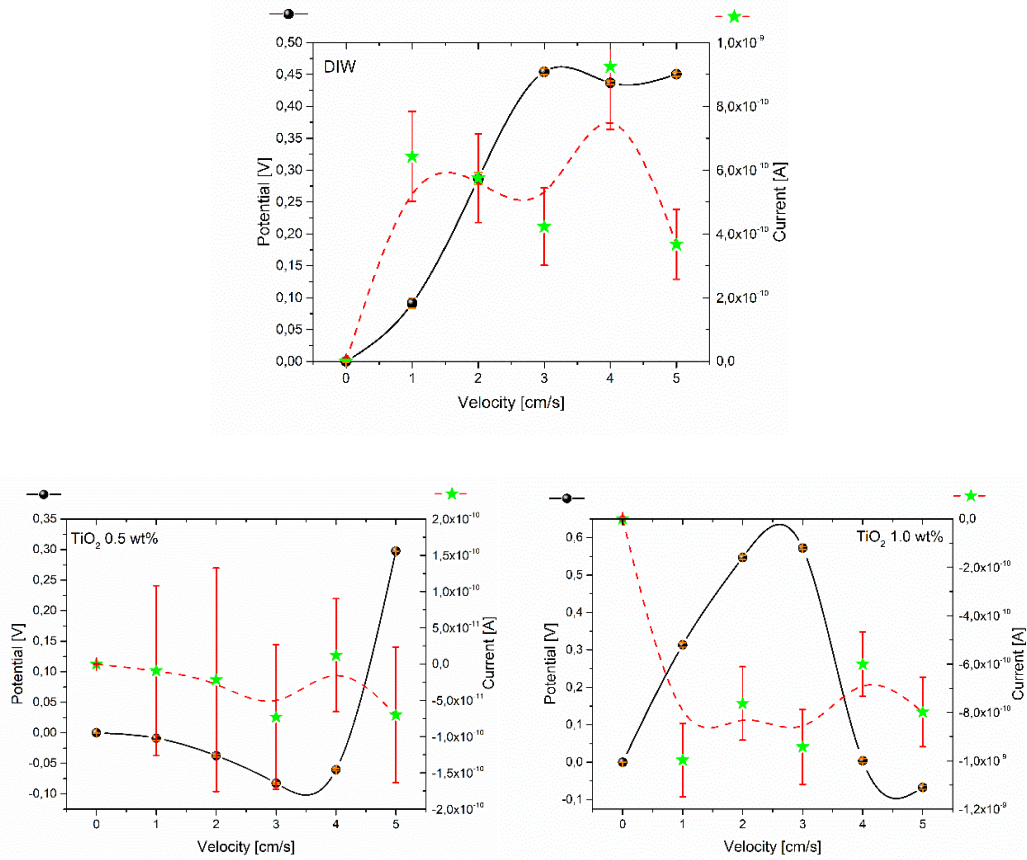
Figure 77: V_{OC} and I_{SC} VS mean velocity for DIW (top), 0.5% (bottom left) and 1% (bottom right) TiO$_2$-water suspension (155). Reproduced with permission.

With DIW (Figure 77 top), potential accumulated on the Al electrode increases with the mean flow velocity, reaching a plateau between 3 and 5 cm/s, with V_{OC} = 450 mV. The current values, instead, fluctuate with a peak at 4 cm/s of I_{SC} = 920 pA. The maximum ideal output power, defined as the product of V_{OC} and I_{SC}, is P_{max} = 402 pW generated at 4 cm/s. Considering the ring electrode having a reference surface S = 4.14 · 10^{-4} m^2, the output power per unit of area is P_A = 971 nW/m^2. On the other hand, the triboelectric effect of TiO$_2$-water suspension is not strong as it might be expected. Analysing Figure 77 (bottom left), the potential is negative up to 4 cm/s, while the current appears noisy and faintly negative, reaching at maximum -70 pA. The most interesting values are observed at v = 5 cm/s with V_{OC} = 298 mV, I_{SC} = 72 pA, P_{max} = 21 pW and P_A = 52 nW/m^2. Considering Figure 77 (bottom right), both voltage and current show an increase of magnitude with lower velocities (and up to 3 cm/s). Nevertheless, further increasing the mean velocity, the trend of voltage is inverted probably due a reduction of the friction between

solution and pipe walls, consequent to a drop of the flow velocity close to the walls. In fact, neutral tracers have shown a steep decrease in the peripheral flow velocity when exceeding 3 cm/s. More likely, this is due to sedimentation processes occurring in the suspension. The peak of the output power is at 3 cm/s, where V_{OC} = 575 mV, I_{SC} = 950 pA, P_{max} = 546 pW and P_A = 1.319 $\mu W/m^2$. As per the FF inductive case, a more detailed investigation, evaluating the electrical parameters in presence of a load, should be conducted.

For a deeper analysis, it is worth to evaluate the amount of energy, due to friction between the colloid and the pipe walls that is converted into electrical energy. Adopting a macroscopic approach, we estimated the electro-kinetic efficiency comparing the electrical power extracted by the harvester and the power loss due to the friction forces at the fluid-wall interface. First, considering only the portion of the pipe corresponding to the length of the Al electrode, L, (where the charge accumulation is possible), following the Darcy-Weisbach equation (205), the pressure drop Δp [Pa] due to viscous effects was evaluated as:

$$\Delta p = \rho f \frac{L}{D} \frac{\langle v \rangle^2}{2},$$

where $\langle v \rangle$ is the mean velocity [m/s] and f the Darcy friction factor expressed by the Colebrook-White equation (206), for a duct completely full, as:

$$\frac{1}{\sqrt{f}} = -2 \log\left(\frac{\varepsilon}{3.7D} + \frac{2.51}{Re\sqrt{f}}\right),$$

where ε is the pipe roughness [m] equal to 0.1 μm and D [m] is the pipe inner diameter and Re the associated Reynolds number. With these inputs, the resulting Δp is 1.36 mPa. To evaluate $P_{friction}$, the power due to the pressure loss, Δp was multiplied by the volumetric flow rate Q [m^3/s]:

$$Q = \langle v \rangle D^2 \frac{\pi}{4}.$$

Resulting in 2.73 pW due to friction losses with 1% TiO$_2$ at 3 cm/s, when the highest electrical power is extracted (0.546 nW). Then, the kinetic-electro conversion efficiency, η, is 20%, confronting $P_{friction}$ with $P_{electrical}$:

$$\eta = \frac{P_{electrical}}{P_{friction}} = \frac{V_{oc}I_{sc}}{Q\Delta p},$$

even if it could be further increased matching the direction of dipoles formed (207). Finally, it would be worth analysing how the harvesting mechanism affects the fluid

dynamics and consequently the system performances. In particular, how the accumulation of electrostatic charges and the consequent generation of an electrostatic attraction/repulsion region in correspondence of the electrode, influences the pressure losses. In fact, modeling the attraction/repulsion as an increase/decrease of roughness, a variation of 1 μm in the roughness generates a variation of 0.1% in the system efficiency (154). In this experimental campaign, the ratio between the pipe roughness (about 100 nm) and the TiO_2 NPs diameter (30 nm) was ≈ 3 but further investigation could be focused on how the roughness ratio affects the system performances, since it could be a driver in designing future colloidal triboelectric energy harvester. Furthermore, different suitable nanomaterials could be tested. Last, controlling the ferroelectric domains of the pipe wall could optimize and amplify the electrostatic charge distribution at the level of the extraction electrodes. Considering the originality and novelty of this work, a comparison with other TENGs is hard to make. Nevertheless, the work of Pjesky et al. is worth to mention, since NPs of TiO_2 and MgO were used to charge a PTFE tribocharger by means of a powder disperser showing that titania gained a higher net charge (208).

4.3.3 Barium titanate – Pyroelectric effect

Then, we started investigating pyroelectric materials. The same idea of exploiting the waste heat to generate a convective motion of a colloidal solution of $BaTiO_3$ (BT) and FF through a FEP pipe (ID=10 mm, OD=12mm) was applied. The colloid is heated up by means of a heating plate and then forced using the same peristaltic pump (Ismatec MCP). Since along the loop the fluid is subject to forced convection cooling, electrostatic charges are generated thanks to pyroelectric phenomena occurring on the BT NPs (Inframat® Advanced Materials^{TM}). A setup similar to that illustrated in 4.3.1 and 4.3.2 has been employed. In view of a multieffect colloid (4.3.5) and because of its particularly high gravitational stability, FF was employed in order to stabilize BT and hindering precipitation (209). The same fluid dynamics considerations made in the previous section for the FF experiments drove the sizing of the pipe. The pump was placed in a different bench in order to mechanically isolate the characterization system. Two titanium linear electrodes (SigmaAldrich, purity 99.98 %, width=5 mm, length=30 mm, thickness=0.2 mm, surface area=300 mm^2) spacing 150 mm were installed internally to the pipe, in direct contact with the fluid, for harvesting the current generated by pyroelectricity while characterizing the resistive system. As reference electrode was used the ground of the measurement instruments, in order to guarantee the repeatability of the

measurements. V_{OC} and I_{SC} measurements were conducted respectively by means of two identical SourceMeter-Keithley 2635A (Tektronix, Inc., Beaverton, OR, USA). All the instruments were connected to a PC with LabVIEW^{TM} 2019 software (National Instruments, Austin, TX, USA). In this case, no impedance analysis was conducted. In Figure 78, a schematic of the overall setup is shown.
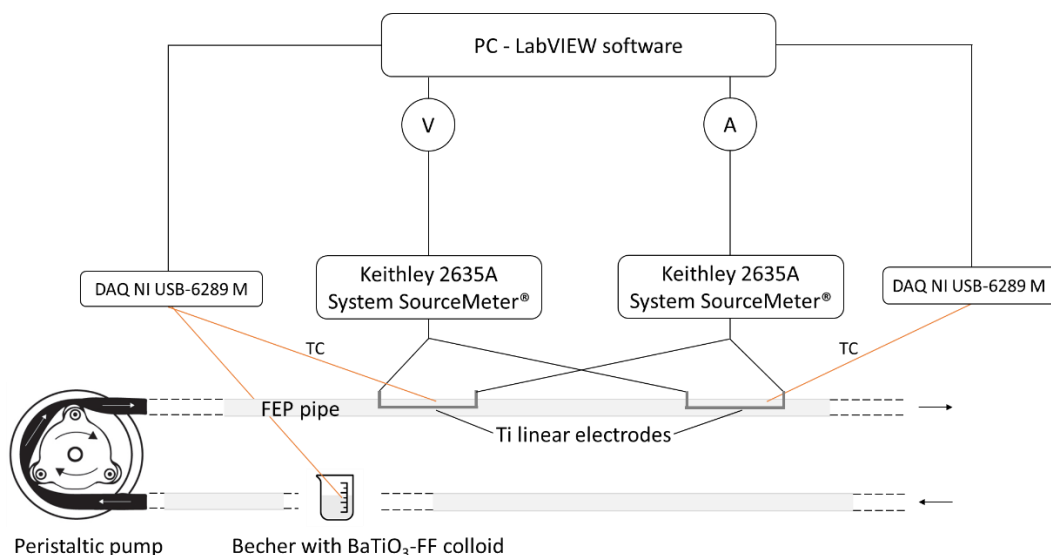
Figure 78: Schematic of experimental setup for pyroelectric characterization.

FF was diluted with Kerosene (Carlo Erba), compatible with the FF carrier fluid, in order to reach a 2% vol. concentration of Fe_3O_4 and then a 0.5% vol. of BT NPs (average diameter=300 nm, tetragonal crystalline structure) were dispersed by means of sonifier horn (Branson Digital Sonifier® Model 450). To ensure homogeneous dispersion during the entire duration of the experiments, a magnetic stirrer (Velp Scientifica) was used, coupled with a heating plate for providing different heating conditions. Two heating conditions have been investigated: low heating (LH), where the temperature increase in the reservoir (becher) was only due to mechanical stirring, and strong heating (SH), where the fluid was heated up to $\approx$ 60 °C before being pumped. The choice for this temperature was driven by a trade-off among the solvent evaporation rate, the cooling rate and the transient time needed to heat up the solution. As shown in Figure 78, temperature was monitored in correspondence of the reservoir and of the two electrodes, by means of N- type thermocouples (Eltec Cables and Instruments), connected to a DAQ NI USB-6289 M (National Instruments) controlled by LabVIEW^{TM} for data manipulation.

First, a thermal analysis was conducted and temperature values acquired by the TCs are reported in Figure 79, where the curves were smoothed by means of a first

order polynomial Savitzky-Golay fitting, over a window of 59 points. LH condition (left) and SH condition (right) show respectively only stirrer thermal agitation and heating up to 60 °C. Then, when the pump is switched-on, the temperature in the reservoir (T_B) abruptly drops due to colloid motion. After approximately 200 s SS conditions are achieved and the gradient between the two electrodes stabilizes (blue line) at 2.4 °C. Electrode 1 (E1) indicates the upstream electrode while E2 indicates the downstream one.
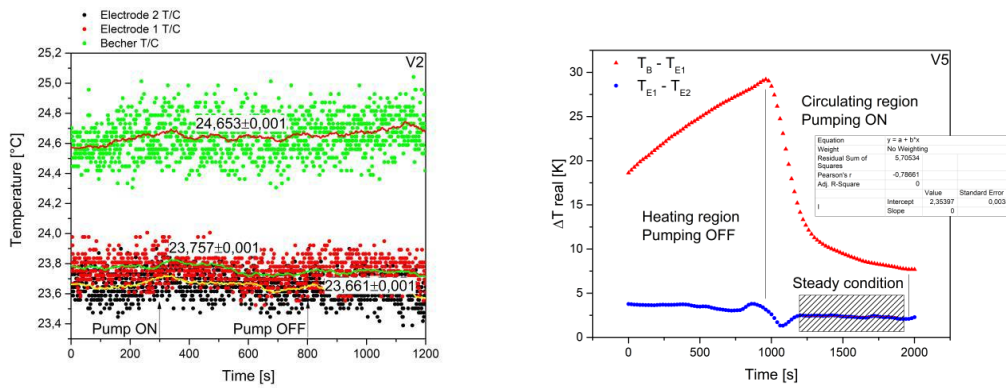
Figure 79: Temperature trend in typical LH (left) and SH (right) condition (209). Reproduced under the terms of the Creative Commons CC BY license.

In order to investigate different cooling rates, different velocities (0.2, 0.4, 0.6, 1.1, 2.2 cm/s) and Reynolds numbers (from 10 to 100) were set, guaranteeing a laminar flow regime in the entire velocity range. In Figure 80, voltage and current VS time in LH conditions for the colloid with 0.5% vol. of BT (0.5% BT) are provided.
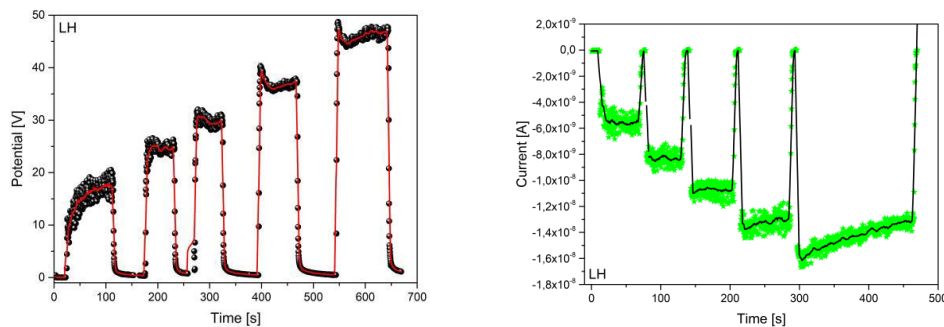
Figure 80: V_{OC} (left) and I_{SC} (right) VS time for 0.5% BT at different flow rates in low-heating condition (209). Reproduced under the terms of the Creative Commons CC BY license.

They show a quite stable trend, up to 0.6 cm/s; then, both potential and current are slowly moving to an asymptote, increasing and decreasing, respectively. This might be due to limitations in the extraction system and to the different entrance length *EL* related to the different velocities. In fact, *EL* identifies the length needed to the fluid for completely developing the flow profile in the pipe and is evaluated by means of:

$$EL = 0.06 \, Re \cdot d,$$

where d is the pipe diameter. In all the testing conditions, *EL* spans from 5 mm to 5,5 cm, leading to a completely developed profile in proximity of the first electrode in the case of low flow rates and in a not completely developed one for higher rates (> 1.1 cm/s).

Then, in order to verify the effective contribution to current and voltage due to pyroelectric effect thanks to BT NPs, the different components of the mixture (kerosene alone, FF and BT) have been analysed. First, kerosene was tested in both heating conditions. Neither pyro nor triboelectric behaviour was expected and no voltage or current was significantly measured above the noise floor indeed. However, 2% FF shown a remarkable triboelectric response, in both heating conditions. Thus, current and voltages were acquired in order to be subtracted from those related to 0.5% BT for isolating the pure pyroelectric component of energy harvesting. In Figure 81, voltage and current have been normalized respectively by the distance length between the two electrodes (electric field) and the electrode area (current density).
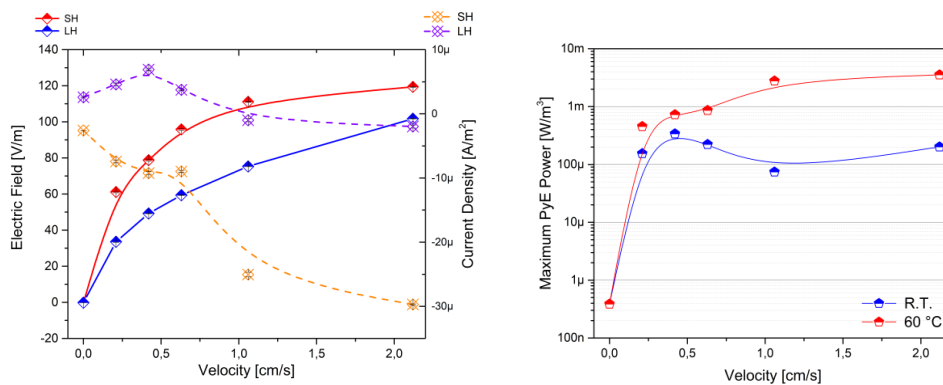
Figure 81: Electric field and current density (left) and maximum power (right) VS velocity of 0.5% BT in both heating conditions (209). Reproduced under the terms of the Creative Commons CC BY license.

Interestingly, the sign of current density changes by exploiting SH and pyroelectric effect, while the electric field does not change sign and slightly increases. Velocity has the effect of producing a steady but nonlinear increase in electric fields and a nonlinear increase in the currents density with SH and a fluctuating trend with LH. A significant increase in power production, especially at intermediate velocities and in SH condition, is observed. This could be due to a decrease of the colloid viscosity, leading to lower friction among NPs and surrounding solvent, allowing a larger number of NPs to reach the electrodes.

Finally, the conversion efficiency of the system is evaluated comparing all the input thermal power sources with the electrical power extracted. The first contribution to consider is the stirrer one, increasing the temperature of the colloid of ≈ 1.5 °C with respect to the room temperature of 23 °C, as reported in Figure 79 (left). According to the theory of mixing, the power transferred to the fluid during mechanical agitation depends on variables such as the size of the reservoirs and impeller (in this case a magnetic anchor), fluid properties such as viscosity, and stirred speed (209). The relationships between these variables are usually expressed in terms of dimensionless numbers, such as the impeller Reynolds number (Re) and the power number N_p. Re number of the stirred fluid can be expressed as (210):

$$Re = \frac{N_i \rho_m D^2}{\mu_m},$$

where Ni represents the stirring frequency [rps], D the anchor length [m] and ρ_m and μ_m are the mixture density [kg m^{-3}] and dynamic viscosity [kg m^{-1} s^{-1}], respectively.

The mixture density can be evaluated as (211):

$$\rho_m = (1 - \varphi - \vartheta)\rho_f + \varphi \rho_{FF} + \vartheta \rho_{BT},$$

with ρ_f representing the carrier fluid density, φ and ρ_{FF} concentration and density of magnetite, θ and ρ_{BT} concentration and density of barium titanate.

From the value of Re we could determine the regime to be turbulent inside the becher, and the dimensionless power number N_p equal to 0.35 (210) allowing the evaluation of the power transferred to the fluid during mixing:

$$P_{stir} = N_p \rho_m Ni^3 D^5.$$

The second contribution is provided by the heating plate in SH conditions. The amount of heat transferred to the fluid is:

$$Q_h = \Delta T_h \cdot m_b \cdot C,$$

with m_b representing the mass of the mixture [kg] contained in the becher and C being the specific heat capacity of the colloid [J kg^{-1} K^{-1}], evaluated as (212):

$$C = \frac{(1-\varphi-\vartheta)\rho_f C_f + \varphi \rho_{FF} C_{FF} + \vartheta \rho_{BT} C_{BT}}{\rho_m},$$

with C_f, C_{FF} and C_{BT} representing the specific heat capacities of the mixture components.

Considering that, in SH condition, the temperature difference, ΔT_h, is 37 °C, the thermal power is:

$$P_h = \dot{Q}_h = \frac{\Delta T_h m_b C}{t_h},$$

where t_h is time needed to reach the temperature of 60 °C.

Finally, the input power from both stirrer and heater must be normalized on the becher volume (V_b) considering the volume of fluid effectively drawn off (V_d), in order to consider as useful power, only the amount provided to the liquid actually used to produce the electrical output power.

Thus, the total input power P_I per unit volume, will be given by the sum of all the aforementioned contributions:

$$P_I = \frac{\overline{P_{stir} + P_h}}{V_{norm}} = \frac{1}{V_{norm} V_b}(P_{stir} V_d + P_h V_d),$$

where V_{norm} indicates the normalization volume obtained accounting the distance between the two electrodes and the electrodes area, and the thermal-electro efficiency is expressed as:

$$\eta = \frac{P_{electrical}}{P_{thermal}} = \frac{V_{oc} I_{sc}}{P_I}.$$

The efficiency values are reported in Table 12, showing promising results especially in SH conditions.

Table 12: Thermal-electro efficiency values at different velocities, in both LH and SH conditions (209).

	V_1 [m/s]	V_2 [m/s]	V_3 [m/s]	V_4 [m/s]	V_5 [m/s]
η^{LH} [%]	0.28	0.31	0.14	0.03	0.04
η^{SH} [%]	0.7	0.57	0.45	0.87	0.56

4.3.4 Ferrofluid – Triboelectric and pyroelectric effect

After having evaluated the inductive capability of FF and driven by the findings of 4.3.3, we also investigate its triboelectric and pyroelectric properties with surprising unprecedented results. Employing the same setups of 4.3.2 and 4.3.3 we analysed the potentials and currents generated on the capacitive and resistive electrodes respectively at different flows velocities in a range far from saturation, testing: V1= 0.22, V2= 0.44, V3= 0.66, V5=1.1, V10=2.2 mm/s, respectively 2, 4, 6, 8, 10 A.U..

On the capacitive electrode, Figure 82 shows, as expected for triboelectric phenomena, increasing potentials and currents with increasing speed, up to a maximum of about 48 V and 2.8 nA. In this case, a directly proportional correlation between velocity and potential and currents, differently to what observed in 4.3.2, probably due to a higher stability of the colloid employed.
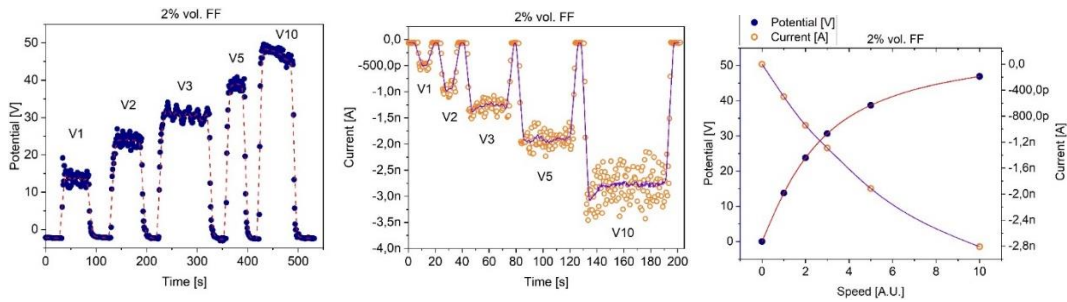
Figure 82: Recorded potential and current on the capacitive electrode versus time (top left and right) and speed (bottom) (202). Reproduced with permission.

On the other hand, we measured both potentials and currents as a function of the fluid velocity when the recorded temperature in the becher was 60 °C and we compared the values with the case when the colloid was flowing at room temperature (RT). As expected, increasing the fluid velocity, a more abrupt

temperature drop occurs and then Figure 83 shows a gradual increase in recorded potentials and currents. With respect to the RT conditions, the electrical outputs are clearly higher, confirming that a pyroelectric phenomenon is taking place in the FF NPs.
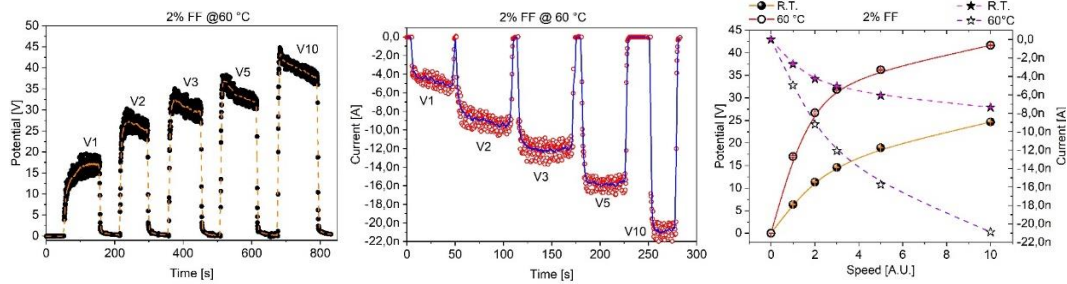
Figure 83: Recorded potential and current on the resistive electrode versus time in SH conditions (left, center) and speed in both heating conditions (right) (202). Reproduced with permission.

Considering that at RT the max potential recorded is about 25 V it is evident that the capacitive electrode is better performing for exploiting triboelectricity, while the measured current up to 22 nA, one order of magnitude higher than for the capacitive electrode, suggests that the resistive one better suits for collecting charges generated by pyroelectricity.

In order to verify that the measured voltages and currents are effectively produced from the energy conversion processes taking place, and that the measurement system does not introduce any bias, we analysed the electric conductivity at room temperature of the FF with different concentrations (0.5, 1, 2, 4, 6 and 8 % vol.), conducting an impedance spectrum analysis (Figure 84).
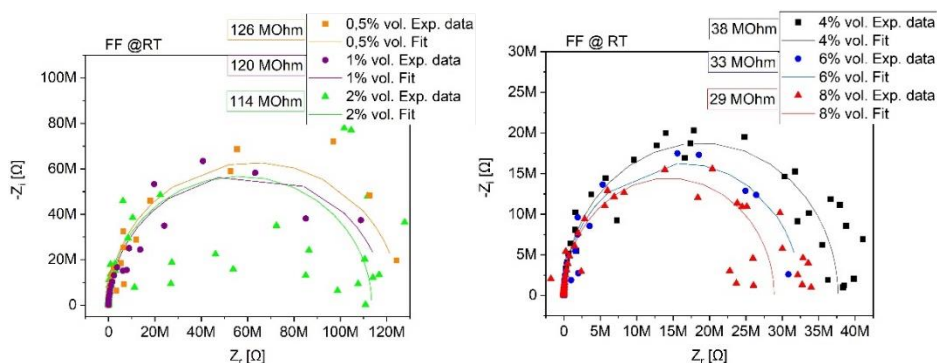
Figure 84: Impedance spectrum analysis at room temperature of FF at different concentrations (202). Reproduced with permission.

In Figure 84 intercepts with x-axis represent the values of electronic resistance of the material and are indicated in the boxes along with FF solid volumes. It is evident that FF behaves as a quasi-ideal capacitor (circular lines properly fit the experimental data) at all volume concentrations tested, with very high values of electric resistance (coloured boxes in figure).

Since, neither pyro nor triboelectric behaviour was observed above the noise floor in the kerosene, as mentioned in 4.3.3, all the contributions are attributable to the sole Fe_3O_4 component suggesting that FF behaves as both a triboelectric and a pyroelectric material. Furthermore, while the capacitive electrode is more efficient for accumulating charges developed by triboelectricity (up to 48 V), the resistive one, being in direct contact with the FF, is essential to collect the charges displaced by pyroelectricity (up to 22 nA). In comparison (4.3.1), exploiting electromagnetic induction harvesting leads to extracted currents of 3 orders of magnitude higher, while the EMF is of 6 orders of magnitude lower with respect to the one obtained with the triboelectric harvesting. Thus, FF is an interesting candidate for triboelectric and pyroelectric harvesters. Moreover, FF magnetic properties are appealing, especially in robotic applications when they can be exploited for controlling the fluid dynamics in order to optimize energetic system but also for developing mobility system, similarly to what already happens in biomedical nano/micro robotics.

4.3.5 Mixed colloid - Multieffect

Finally, we explored the potential of a multieffect conversion system combining together the effects of electromagnetic induction, triboelectricity and pyroelectricity, using a mixed colloid and focusing on synergistic effects that could arise. We built a similar setup to that already employed in 4.3.1, 4.3.2 and 4.3.3 with all the three extraction systems installed (Figure 85). FF EMG 901 was diluted with kerosene, compatible with the FF carrier fluid, in order to reach a 2% vol. concentration of Fe_3O_4. $BaTiO_3$ (1% vol.) and TiO_2 (1% vol.) NPs were dispersed by means of a horn sonicator (Branson Digital Sonifier Model 450) operating for 30 min at 100 W, with a duty cycle of 10 s of rest each 10 s of operation. The mixed colloid (2%FF + 1%BT + 1%T) was stored in a Becher where a magnetic stirrer was used to maintain its compositional and thermal homogeneity, and a heater to provide the desired thermal power. Then, it was pumped through the FEP pipe by means of the peristaltic pump setting the fluid velocity, between 0.22 mm/s and 2.2 cm/s. The titanium resistive electrode, placed directly in contact with the colloid

collected charges by mechanical drag. The OFC solenoid, wound around the pipe, collected charges by electromagnetic induction and the aluminum capacitive electrode anchored externally, in contact with the pipe, collected charges by dielectric polarization. Each electrode was coupled with one of the functional components of the colloid, showing pyroelectric (colloidal $BaTiO_3$), magnetic (FF), and triboelectric (colloidal TiO_2) properties, respectively. In particular, the resistive titanium electrode permitted to harvest charges accumulated in the fluid whose equivalent is a voltage generator, while the colloid itself acts as a primary circuit. This circuital analogy is valid even when the external velocity of the fluid is zero: in fact, spatial temperature gradients are able to initiate density gradients by diffusion, which ultimately produce an electromotive force on the inner electrode (213).
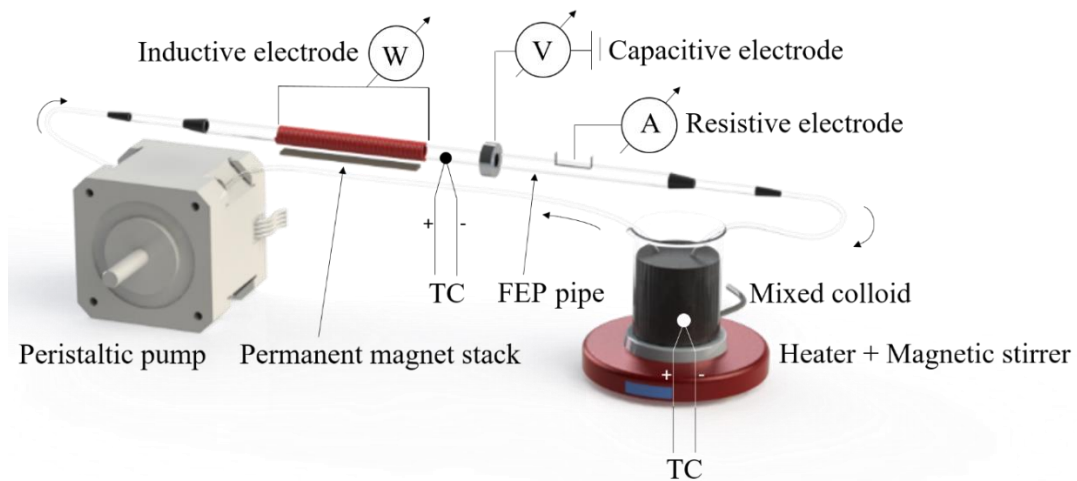
Figure 85: Rendering of the multieffect setup.

Furthermore, the ferroelectric behavior shown by the FEP pipe (Figure 86) allowed bringing the polymer to an electrical remanence state and taking advantage of its dielectric displacement, when interacting with the moving colloid and NPs surfaces.
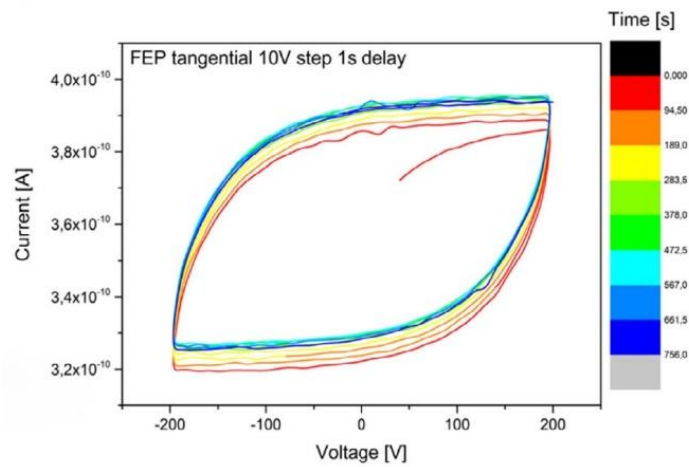
Figure 86: Electrical minor hysteresis cycle measured tangentially to the FEP pipe (213). Reproduced with permission.

We can think at the system as a spring storing energy until the pipe reaches its electrical remanence state, where it can polarize the charges of the moving fluid and increase the conversion efficiency. When the colloid moves very fast to a specific direction (e.g. forward), the friction between the fluid and the pipe walls can rotate the pipe polarization state and eventually reach its electrical coercivity, where the net polarization is zero (spring released). Here, the pipe is not anymore able to polarize the fluid and we lose conversion efficiency. If the same forward direction is maintained, the fluid can transfer again energy on the pipe walls and bring their polarization to the negative remanence, restoring its polarization capabilities and conversion efficiency (spring compressed) (213).

First, we characterized the inductive electrode with the fluid in SH conditions, showing small electromotive forces and currents corresponding to power up to the hundreds of pW (Figure 87a), slightly lower, but of the same magnitude, than the powers extracted with only 2% FF (4.3.1). Obviously, the inductive capability of the colloid is not enhanced by the other components, having BT and T no magnetic moment. Actually, it is likely reduced due to interference and viscosity factors. In order to take into account independently the effects of magnetic field (generated by the permanent magnets), temperature, and concentration of FF, a complete analytical model has been developed (214). Then, we analysed the external capacitive electrode, on which the potential accumulated was higher when compared with the setup with titania only (4.3.2), both at room temperature or in SH conditions (Figure 87b).
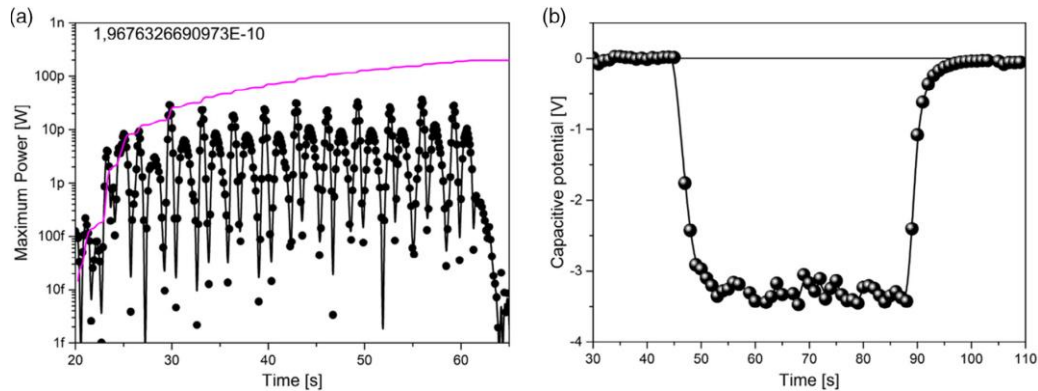
Figure 87: a) Power output of the inductive electrode when mixed colloid (SH conditions) flows at 0.22 mm/s. b) Potential measured on the capacitive electrode when mixed colloid (SH conditions) flows at 6 mm/s (213). Reproduced with permission.

Finally, we characterized the resistive electrode, when the fluid was heated up to 60 °C (SH conditions), showing typical SC current profiles as shown in Figure 88a, in the range of tens of nA. The potential that settles on the resistive electrode can be in the range of hundreds of V, as in Figure 88b.
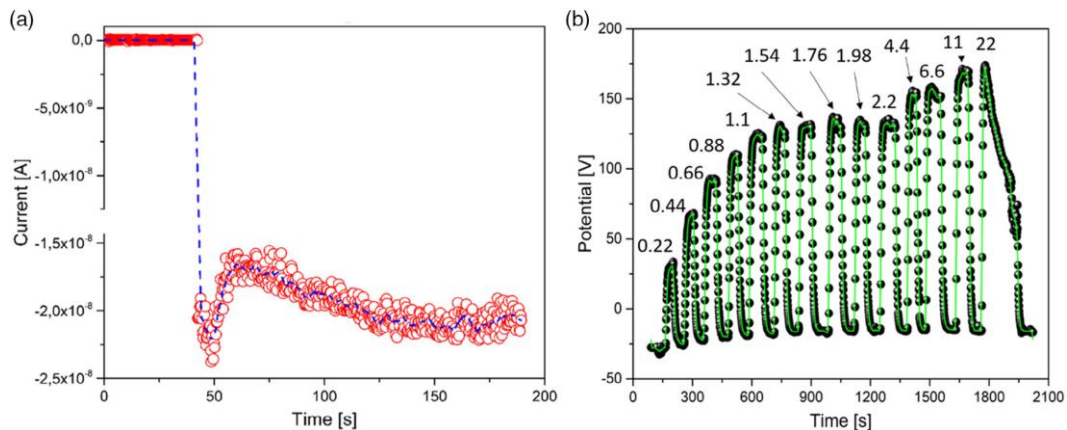
Figure 88: Resistive electrode, SH conditions. Typical profile of current extracted when mixed colloid flows at of 2.2 cm/s (a) and of potential measured (b), where for each potential peak the corresponding speed is indicated in mm/s (213). Reproduced with permission.

Furthermore, potential is sensitive to the magnitude and direction of the colloid velocity. In fact, inverting the flux an inversion of the potential sign was observed (Figure 89).
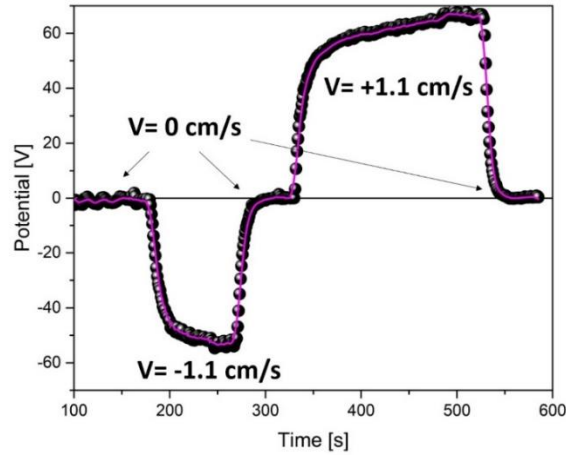
Figure 89: Sensitivity of potential to the colloid direction (213). Reproduced with permission.

With respect to the experiments with only the pyroelectric effect (4.3.3), the generated potential is approximately 365% higher and the current 54% higher. This remarkable result is the first proof of the synergistic effects enabled in the multieffect setup (213). Considering that typical Rayleigh–Bénard convection, triggered by a thermal gradient of 1 °C, generates diffusive patterns flowing at 1.2 cm/s (215), velocity profiles in function of acquisition time (Figure 90) show the fast dynamics of the system in harvesting energy even at speeds lower than 1 mm/s. In fact, the multieffect setup features a maximum power output of 700 nW at 1 cm/s, while 150 nW is extracted at 1 mm/s, corresponding to a thermal gradient of 0.1 °C, showing a higher conversion efficiency at lower speed, probably due to unfavorable effects of dynamic viscosity
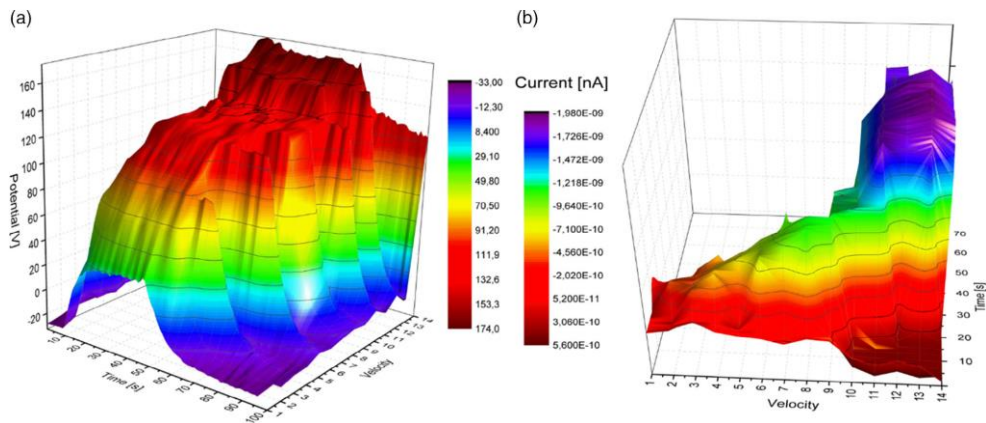
Figure 90: OC voltages (a) and SC currents (b) VS time [s] and fluid velocity [mm/s], collected by the resistive electrode in LH conditions (213). Reproduced with permission.

The most interesting results were found characterizing the resistive electrode with the mixed colloid in LH conditions. In these conditions, specific power, electric field and the current density of the setup in function of the fluid velocity is shown in Figure 91, considering respectively the colloid volume, distance between resistive and reference electrode in the becher and the electrode area. The multieffect setup reaches the maximum output power at 1 cm/s, corresponding to a thermal gradient in the order of 1 °C.
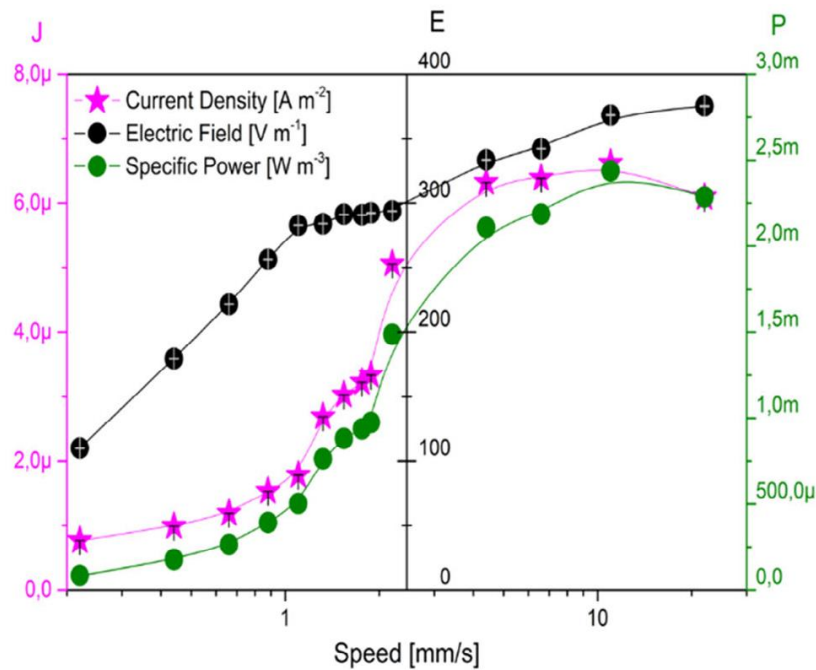
Figure 91: Overall specific power, electric field and current density VS fluid velocity, measured on the resistive electrode in LH conditions (213). Reproduced with permission.

Thus, if it is clear that BT and T NPs, having no net magnetization, cannot provide any induction, the pure triboelectric component is greatly enhanced by the mixed colloid, as well as the pyroelectric component, by synergistic effects. The inductive component is slightly diminished. At the same time, each materials suits better with different solvents. Thus, in view of a practical application, a non-mixed colloid is preferred.

4.4   Planar converter

In view of the last findings, the final step of CERES project conceived a planar energy harvester and converter. The results obtained with the experimental linear setup were applied to a device with planar geometry, inspired by the planar

experimental setup described in 4.2, within which the functional colloid flow through channels designed ad hoc for this particular configuration. The invention, called Multieffect liqUid State Thermal hArvesteR (mu-star, μ*), was internationally patented (PT190513) and is here described. The μ* converter has been imagined for installation and use in three main application domains, resulting in as many configuration:

- flat surfaces - "flat" configuration;
- curved surfaces - "soft" configuration;
- cylindrical surfaces - "ring" configuration.

4.4.1 Flat configuration

The flat configuration is a rectangular parallelepiped with variable dimensions according to the application (e.g. 200x100x20 mm). The top layer is in thermal and physical contact with the hot reservoir and the bottom layer with the cold one. The hot surface might be either an illuminated plane, to whom solar radiation transfers energy, or a portion where waste heat has been conveyed (for example: the heat sink of an engine, of a domestic appliance, of an electronic circuit that needs to dissipate thermal energy, the ceiling or window/wall of a greenhouse). The cold surface might be either a shaded area, or a radiator in thermal contact with the environment, or a radiator in thermal contact with a cooling circuit.

It is composed of 3 different layers as shown in Figure 92.
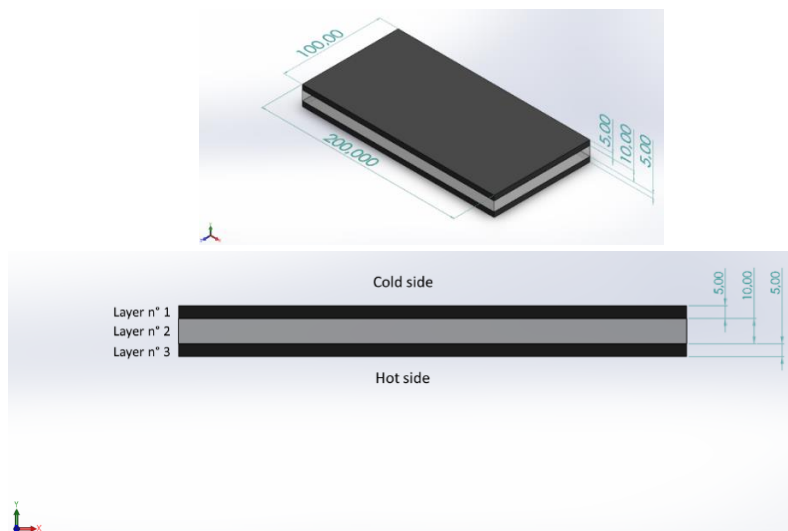
Figure 92: Isometric (top) and side (bottom) views of flat configuration.

In order:

- a top external metal/ceramic layer with very high thermal conductivity (for example aluminium, copper, PERLUCOR®);
- an intermediate polymeric hollow layer with very low thermal conductivity (for example PTFE);
- a bottom external metal layer with very high thermal conductivity (for example aluminium, copper).

The intermediate layer (number 2) comprises three adjacent volumes, physically separated, as shown Figure 93. Such volumes are named as:

- "Tribo" region, through which water based colloidal TiO_2 (or an alternative triboelectric nanomaterial) flows;
- "Pyro" region, through which water/oil based colloidal $BaTiO_3$ (or an alternative pyroelectric nanomaterial) flows;
- "Induction" region, through which water/oil based colloidal Fe_3O_4 (or an alternative superparamagnetic nanomaterial) flows;
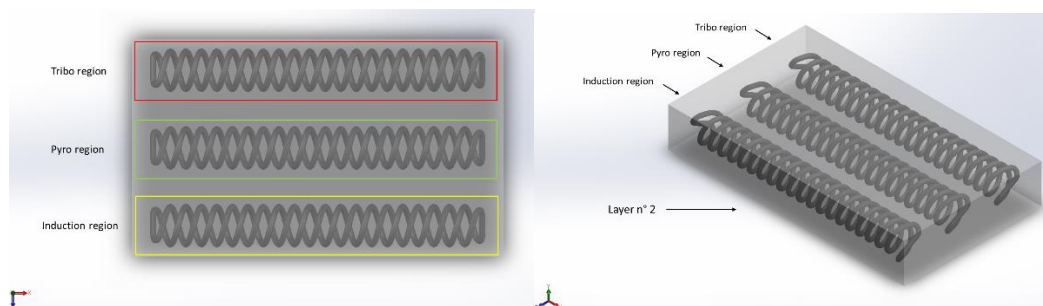
Figure 93: Top (left) and isometric (right) views of Layer n° 2 with the Tribo, Pyro and Induction regions highlighted, in the flat and soft configuration.

Within each region a different nanofluid flows through an helicoidal channel hosted within layer number 2 and confined in each single region as shown in Figure 93. The helicoidal channel could either be a duct within the same layer 2-block material (for example, PTFE), or a polymeric tube positioned within layer 2 (for example made in PTFE-FEP or PVDF). The typical inner diameter of the channel ranges from 3 to 5 mm. Each channel has an inlet for the injection of their respective functional colloid and an outlet for exhausting air during the filling operations. The fabrication of harvesting panels, therefore, must include besides assembly also the operation of filling with the colloids. Openings must be sealable with a pressure cap

that is removed to inject the colloid and allow air to exit, and replaced before setting the device into operation.

Along the channels in "Tribo" and "Pyro" regions, halfway between the top and bottom surfaces, electrodes are installed as shown in Figure 94. According to the last findings, in the "Tribo" region, aluminum electrodes are placed externally to the channel, while in the "Pyro" region titanium electrodes are installed internally, in contact with the fluid.
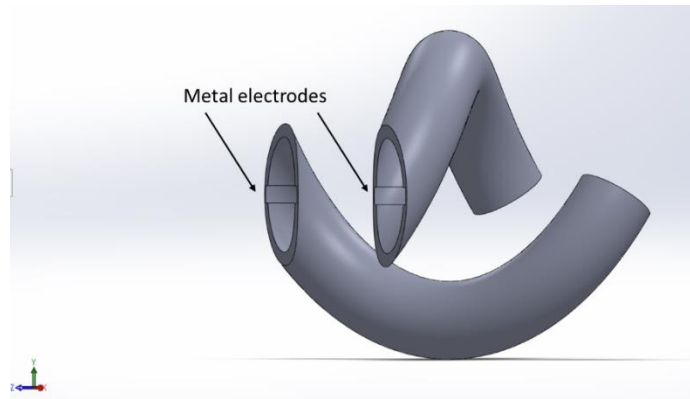
Figure 94: Section view of the channels in "Tribo" and "Pyro" regions, with electrodes highlighted.

Along the channels, in the "Induction" region, halfway between the top and bottom surfaces, two ring-shaped magnets are coupled with an OFC induction coil (Figure 95).
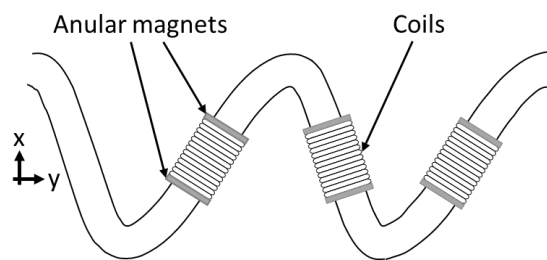
Figure 95: Side view of the channels in "Induction" region, with coils and magnets highlighted.

It is fundamental that the helicoidal channels has an asymmetric profile as the one shown in Figure 96, in order to allow the fluid to follow a preferential direction. Let us consider again that portion of tube that is "far" from the top (cold) and bottom (hot) surfaces. Looking at the orthogonal section, the angle between the straight

portion of the tube and the hot side is approximately 45°, while the angle between the cold side and the straight portion of the tube is approximately 60°. When a fluid particle inside the channel is close to the "cold side", it is forced to move toward the "hot side" going from left to right thanks to the geometry of the channel itself. The explanation of this resides in the better exploitation of the buoyancy and gravitational forces: heating facilitates buoyancy, cooling facilitates gravitational sedimentation.
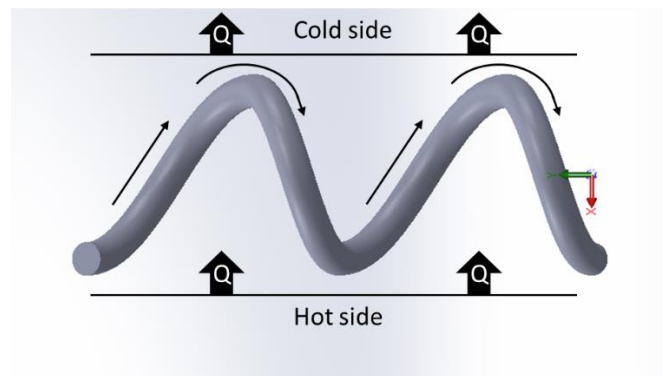
Figure 96: Lateral view of helicoidal channels with fluid motion highlighted.

During an operative scenario, thanks to Rayleigh-Bénard natural convection triggered by the thermal gradient across the device, the 3 nanofluids start flowing through the 3 channels. Then, the device start operating, cooling the hot surface and generating electricity by means of capacitive, resistive and inductive electrodes. Such electricity is made available to the user for external loads. According to 4.3.5, in order to increase the efficiency of the converter, it is important that the three regions are physically separated to be resilient toward a naturally dynamic reality, where physical parameters may exceptionally explore a vast configuration space.

Finally, in order to estimate the impact on society of a multieffect WHP CERES, typical application scenarios have been hypothesized, defining practical application domains (wearable patch, satellite electronic board, domestic electric appliance, car heat exchanger, house wall, industrial plant) and reasonable device geometries (thickness and surface area). Results are summarized in Table 13, including the output power, computed by means of a MATLAB script (213), of a conversion system exploiting the same features reported in our experiments (mixture components and concentrations), but different geometry and volume of colloid employed.

Table 13: Input parameters for the MATLAB script exploited for performing numerical simulation of the output power of the multieffect WHP CERES.

Application	Thickness [m]	Area [m^2]	ΔT [K]	Power [W]
Wearable	0.05	0.01	10	395 μ
Space	0.1	0.01	30	6 m
Domestic	0.15	0.1	25	33 m
Automotive	0.2	1	100	2
Building	0.07	25	30	73
Industrial	0.5	1500	150	11 k

Outcomes can be also graphically visualized in Figure 97.
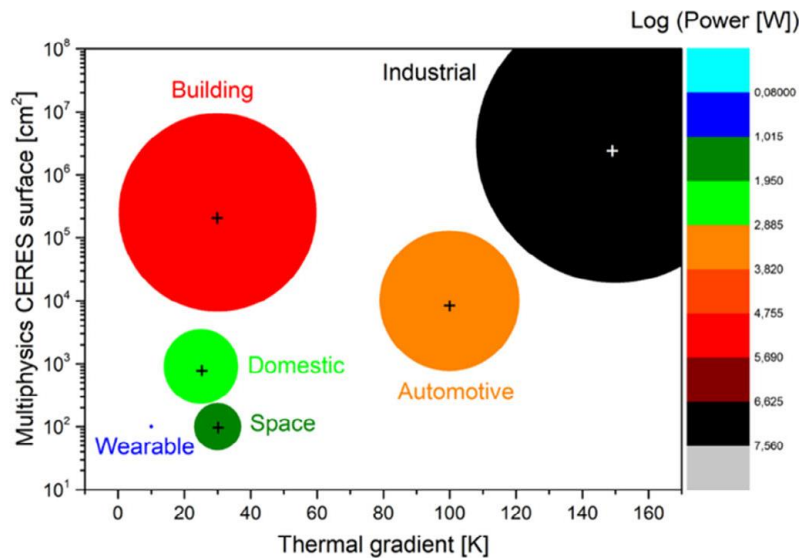
Figure 97: Output power of the multieffect WHP CERES in specific application scenarios, as per numerical analysis. The bubble diameter and colour are proportional to log (power) (213). Reproduced with permission.

In in Figure 97 extracted power ranges from 395 µW in the wearable device to 11 kW in the industrial plant, operating over 150 °C of ΔT. In the analysis, no materials optimization was considered, but it is clear that progress in employing higher efficiency colloidal mixtures could easily increase the amount of energy extracted (213).

4.4.2 Soft configuration

The application domain is similar to the flat option, but with a specific design for curved surfaces. In fact, the soft configuration is a flexible rectangular parallelepiped composed, similarly to the flat case, of 3 different layers (Figure 92):

- a top elastomeric layer with very high thermal conductivity (for example fabricated in thermally conductive silicone, elastomer with elongated liquid metal inclusions, mixture of PDMS and carbon nanotubes, mixtures of rubbers and graphene, "thubber");
- an intermediate polymeric hollow layer with very low thermal conductivity (for example fabricated in silicone, PTFE);
- a second external elastomeric layer with very high thermal conductivity (for example fabricated in thermally conductive silicone, elastomer with elongated liquid metal inclusions, mixture of PDMS and carbon nanotubes, mixtures of rubbers and graphene, "thubber").

The layer number 2 (Figure 93) comprises three adjacent volumes, physically separated and containing the same fluids and with the same channels and electrode systems, as in the flat configuration. Of course, considering the application, a higher degree of flexibility in the channel system is required, in comparison to the flat case.

4.4.3 Ring configuration

The ring configuration is a hollow torus (with cross section presenting flat lateral sides) featuring variable dimensions, with inner diameter that the ring can be installed around a hot pipe, conveying fluids (for example hot water for heating, hot fumes/exhaust pipes, oil transportation pipes). Imagining cutting open the device along the poloidal axis, the ring is composed by three different layers, as shown in Figure 98 (where the channels have been linearized for the sake of clarity):

- an outer metal/ceramic layer with very high thermal conductivity (for example aluminium, copper, PERLUCOR®);

- an intermediate polymeric hollow layer with very low thermal conductivity (for example PTFE), comprising a volume where three pipes are helically revolving around the inner opening of the ring;

- an inner metal layer with very high thermal conductivity (for example aluminium, copper).
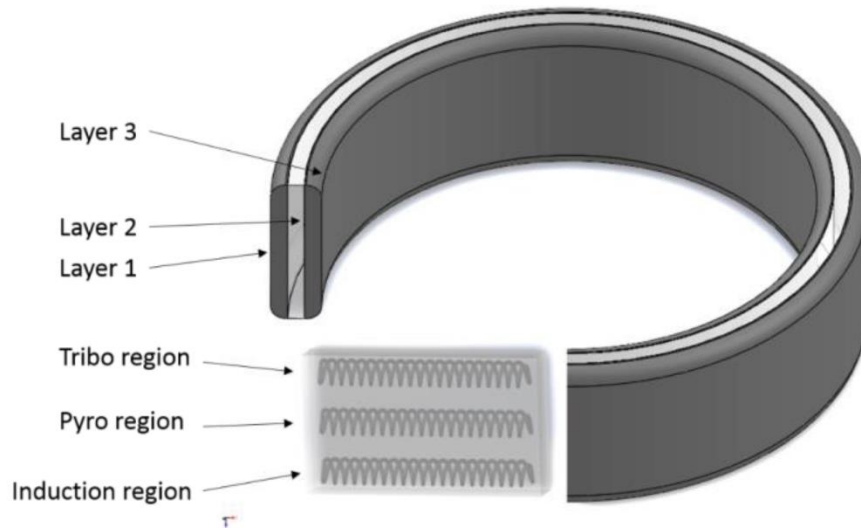
Figure 98: Section of the ring configuration with internal channels highlighted.

Conclusions

In this work the context of the present research project has been outlined, highlighting energy and climate global issues, the state-of-the-art of technologies addressing them, as well as the reasons for the urgent need of novelties. In fact, anthropogenic energy systems have a huge environmental impact: most of all, the greenhouse gases emissions and energy losses. Although some highly damaging processes have been either completely eliminated or reduced to acceptable levels some serious problems still remain, related to exponentially increasing global population in complex high-energy demanding societies. Fortunately, in parallel with the development of powered devices, several approaches for reducing energy losses exist and nowadays, many waste heat recovery, waste heat to power, energy harvesting and conversion systems are available. The most interesting have been described and sorted according to their typical practical application.

Starting from the purpose of space exploration in extreme environments, the engineering feasibility of an energy harvesting and storage system called Colloidal EneRgEtic System (CERES) is proposed as a starting point to address waste heat to power and energy harvesting with nonconventional solutions, combining the nanoscale properties of solid material and the advantages of fluids. In particular, exploiting magnetic, triboelectric and pyroelectric colloids. At this point, the main steps and milestones related to the PhD project are described and discussed, starting from the initial conceptual idea and the first prototype, showing how and why the design has evolved, the test conducted and the main findings and, at last, future optimizations. First, with TORODYNA, ferrofluids have been investigated, exploiting a combination of thermal gradient (simulating the waste heat from any kind of source) and magnetic field to trigger a driven thermomagnetic advection in a toroidal converter. Then, with dedicated induction coils, coupled with permanent magnets, electromagnetic induction force and consequently electrical power are generated. The analysis showed interesting results, suggesting that low ferrofluid concentrations ($\leq$ 2% vol.) perform better due to antagonistic magnetoviscous effects. Furthermore, this recovery technique may be more suitable for energy storage by means of batteries, supercapacitors, or in general devices that have a high intrinsic resistive and capacitive component. At the same time, in order to improve the conversion efficiency and increasing the electrical power output, many solutions have been identified, to be applied in future developments of the project.

Then, exploiting the periodicity of the geometry, only one thermomagnetic region was analysed, in order to focus on the fluid dynamic phenomena, occurring in the orthogonal plane of the converter. The experimental investigation was coupled with numerical simulations, suggesting a specific thermomagnetic configuration for optimizing the performances. On the other hand, for what concerns the longitudinal dimension, a simplified setup was built for the analysis of the pure inductive effect of the ferromagnetic colloid. The relatively low performances obtained exploiting the ferrofluid inductive capability led us to consider different colloids (suspension of TiO_2 and $BaTiO_3$ nanoparticles) associated to other physical effects: tribo and pyroelectricity. The first promising results, with relatively high conversion efficiencies, led us to patent a device (mu-star) based on these materials and physical principles suitable industrial, automotive, domestic, space and wearable applications. Then, we also investigated the ferrofluids capability of showing triboelectric and pyroelectric-like phenomena, reaching surprising results. In summary, exploiting electromagnetic induction harvesting leads to currents of 3 orders of magnitude higher, while the electromotive force is of 6 orders of magnitude lower with respect to the one obtained with the triboelectric harvesting. Thus, ferrofluids proved being an interesting candidate for triboelectric and pyroelectric harvesters. Moreover, ferrofluid magnetic properties are particularly appealing, especially in robotic applications when they can be exploited for controlling the fluid dynamics in order to optimize energetic systems but also for developing mobility systems, similarly to what already happened in biomedical nano/micro robotics. Finally, we explored the potential of a multieffect conversion system combining together the effects of electromagnetic induction, triboelectricity and pyroelectricity, using a mixed colloid and noticing synergistic effects that increase the system efficiency, yet with some operational drawbacks.

Further steps in the CERES project involve:

- device design enhancements for thermo-fluid dynamics optimization;
- energy extraction system should be analysed, designed and calibrated ad hoc for the specific application, device and materials employed, in order to optimize the harvesting efficiency;
- customized synthesis of colloids under analysis, for avoiding sedimentation and agglomeration during operation;
- a complete computational heat and mass transfer analysis for obtaining insights on the micro and nanoscale phenomena occurring inside the device before, during and after operations;

- technological readiness level advancements with application in industrial, automotive, domestic and space exploration fields possibly with the aid of incubators.

Finally, a sustainability analysis, for example by means of fuzzy logic based methodologies, would be fundamental to verify that the energetic cost of production, both for materials and device, maintenance and disposal is lower than the energy effectively harvested and converted, similarly to what happens with new environmental friendly technologies.

References

1. Smil, V. *Energy Transitions: History, Requirements, Prospects.* 1st. Santa Barbara, Praeger, 2010.

2. Fischedick, M., et al. *Climate Change 2014: Mitigation of Climate Change. IPCC Working Group III Contribution to AR5 of the Intergovernmental Panel on Climate Change.* Cambridge University Press, 2021.

3. *Industrial energy efficiency and climate change mitigation.* Worrell, E., Bernstein, L. and Roy, J. et al. 109. Springer, 2009, Energy Efficiency, Vol. 2, 109.

4. *Industrial waste heat: Estimation of the technically available resource in the EU per industrial sector, temperature level and country.* Papapetrou, M., Kosmadakis, G. and Cipollina, A. et al. 2018, Applied Thermal Engineering, Vol. 138, pp. 207-216.

5. *Waste Heat Recovery in the EU industry and proposed new technologies.* Agathokleous, R., Bianchi, B., Panayiotou, G. and et al. 2019, Energy Procedia, Vol. 161, pp. 489-496.

6. *International Comparison of Light-Duty Vehicle Fuel Economy 2005-2015.* Paris: IEA, 2017.

7. Sovran, G. and Blaser, D. *A Contribution to Understanding Automotive Fuel Economy and Its Limits*. SAE International, 2003. SAE Technical Paper.

8. Ling-Chin, J., Bao, H. and Ma, Z. et al. *State-of-the-Art Technologies on Low-Grade Heat Recovery and Utilization in Industry*, Energy Conversion - Current Technologies and Future Trends. [book auth.] I. H. Al-Bahadly. IntechOpen. 2018.

9. Hunnicutt, T. BlackRock Plans Environmentally Conscious Money. *reuters.com.* [Online] 22 01 2019. [Cited: 16 11 2021.] https://www.reuters.com/article/us-blackrock-funds-environment/blackrock-plans-environmentally-conscious-money-market-fund-idUSKCN1PG2MU.

10. Masson-Delmotte, V., P. Zhai, A. and Pirani, S. L. et al. *Climate Change 2021: The Physical Science Basis. Contribution of Working Group I to the Sixth Assessment Report of the Intergovernmental Panel on Climate Change.* IPCC. Cambridge University Press, 2021.

11. *Short-lived climate forcers have long-term climate impacts via the carbon–climate feedback.* Fu, B., Gasser, T., Li, B. et al. 2020, Nat. Clim. Chang., Vol. 10, pp. 851–855.

12. NASA. Mitigation and Adaptation. *NASA: Climate Change and Global Warming.* [Online] 30 11 2021. [Cited: 06 12 2021.] https://climate.nasa.gov/solutions/adaptation-mitigation/.

13. Agency, European Environmental. *What is the difference between adaptation and mitigation?* European Environmental Agency. [Online] 09 11 2021. [Cited: 12 06 2021.] https://www.eea.europa.eu/help/faq/what-is-the-difference-between.

14. Nations, United. Goal 13 | Department of Economic and Social Affairs. *Sustainable Development.* [Online] 30 11 2021. [Cited: 06 12 2021.] https://sdgs.un.org/goals/goal13.

15. Government, United Nations and UK. *COP26 Goals.* UN Climate Change Conference (COP26). [Online] 15 11 2021. [Cited: 06 12 2021.] https://ukcop26.org/cop26-goals/.

16. Ehsan Masood, Jeff Tollefson. *'COP26 hasn't solved the problem': scientists react to UN climate deal.* Nature. 599, 2021, pp. 355-356.

17. *Water Vapour and Its Role in the Earth's Greenhouse.* Stephens, G. L. and Tjemkes, S. A. 1993, Australian Journal of Physics, Vol. 46, p. 149.

18. *Climate change and carbon dioxide: An introduction.* Keeling, C. D. Proceedings of the National Academy of Sciences of the United States of America. Vol. 94 (16), pp. 8273–8274.

19. Le Treut, H., Somerville, R. and Cubasch, U. et al. *Historical Overview of Climate Change Science in Climate Change 2007: The Physical Science Basis. Contribution of Working Group I to the Fourth Assessment Report.* International Panel on Climate Change. s.l. : Cambridge University Press, 2007.

20. *Conf. on Exploitation of Waste Heat Potentials in Europe.* Boštjan, G. and Erlih, S. Dubrovnik, Croatia, 2017.

21. Soin, N. Chapter 10 - Magnetic Nanoparticles-Piezoelectric Polymer Nanocomposites for Energy Harvesting. *Magnetic Nanostructured Materials.* Elsevier, 2018, Vol. Micro and Nano Technologies, pp. 295-322.

22. *Energy and exergy analysis of an organic Rankine for power generation from waste heat recovery in steel industry.* Kaşka, Ö. 2014, Energy Conversion and Management, Vol. 77, pp. 108-117.

23. *Design and exergy analysis of waste heat recovery system and gas engine for power generation in Tehran cement factory.* Naeimia, A., Bidia, M., Ahmadib, M. et al. Elsevier, 2019, Thermal Science and Engineering Progress, Vol. 9, pp. 299-307.

24. *Estimating the global waste heat potential.* Forman, C. et al. Elsevier, 2016, Renewable and Sustainable Energy Reviews, Vol. 57, pp. 1568-1579.

25. *Waste Heat to Power: Technologies, Current Applications, and Future Potential.* Garofalo, E., Bevione, M., Cecchini, L. et al. Wiley, 2020, Energy Technology, Vol. 8, 11, p. 2000413.

26. *Industrial waste heat – tapping into a neglected efficiency potential.* Pehnt, M., J., Bödeker and Arens, M. 2011. ECEE 2011 Summer Study. pp. 691–70.

27. *Spatial modelling of industrial heat loads and recovery potentials in the UK.* McKenna, R. C. and Norman, J. B. Elsevier, 2010, Energy Policy, Vol. 38, 10, pp. 5878-5891.

28. *Heat recovery potentials and technologies in industrial zones.* Huang, F., Zheng, J., Baleynaud J. M. et al. 2016, Journal of the Energy Institute, Vol. 90, pp. 1-11.

29. Caton, J. A. *A Comparison of Lean Operation and Exhaust Gas Recirculation: Thermodynamic Reasons for the Increases of Efficiency.* SAE International, 2013. SAE Technical Paper.

30. *Review of engine cooling technologies for modern engines.* J., Pang H. H. and Brace C. SAGE Journals, 2004, Proceedings of the Institution of Mechanical

Engineers, Part D: Journal of Automobile Engineering, Vol. 218, 11, pp. 1209-1215.

31. *IC-Engine Downsizing and Pressure-Wave Supercharging for Fuel Economy.* Guzzella, L. et al. SAE International, 2000, SAE Technical Paper.

32. *Automotive exhaust power and waste heat recovery technologies.* Rajoo, S. et al. Nova Science Publishers, 2014, Automotive Exhaust Emissions and Energy Recovery, pp. 265-281.

33. *The Application of Availability and Energy Balances to a Diesel Engine.* Alkidas, A. C. ASME, 1988, Journal of Engineering for Gas Turbines and Power, Vol. 110, 3, pp. 462-469.

34. *A Second Law Analysis of High Efficiency Low Emission Gasoline Engine Concepts.* Farrell, J. et al. SAE International, 2006, SAE Technical Paper.

35. Perrot, P. *A to Z of Thermodynamics.* Oxford : Oxford University Press, 1998.

36. Energy, US Department of. *Industrial Technologies Program.* Washington DC, 2008. pp. 1-112.

37. *A brief history of cardiac pacing.* Aquilina, O. PubMed Central, 2006, Images Paediatric Cardiology, Vol. 8, 2, pp. 17-81.

38. *Sensor Mania! The Internet of Things, Wearable Computing, Objective Metrics, and the Quantified Self 2.0.* Swan, M. MDPI, 2012, Journal of Sensor and Actuator Networks, Vol. 1, 3, pp. 217-253.

39. *Efficient retrieval of life log based on context and content.* Kiyoharu, A. et al. New York : Association for Computing Machinery, 2004. Proceedings of the the 1st ACM workshop on Continuous archival and retrieval of personal experiences (CARPE'04). pp. 22–31.

40. Erturk, A. and Inman, D. J. *Piezoelectric Energy Harvesting.* John Wiley & Sons, 2011.

41. FAO. *Human energy requirements - Report of a Joint FAO/WHO/UNU Expert Consultation.* Food and Nutrition. 2001. Technical Report Series 1.

42. *Human-powered wearable computing.* Starner, T. IBM, 1996, IBM Systems Journal, Vol. 35, 3.4, pp. 618-629.

43. *Characterizing Smartwatch Usage in the Wild.* Liu, X. New York : Association for Computing Machinery, 385–398. Proceedings of the 15th Annual International Conference on Mobile Systems, Applications, and Services (MobiSys '17).

44. *Individual differences in normal body temperature: longitudinal big data analysis of patient records.* Obermeyer, Z. British Medical Association, 2017, British Medical Journal, Vol. 359.

45. *Thermodynamic analysis and optimization of an air Brayton cycle for recovering waste heat of blast furnace slag.* Zhang, Z., Chen, L., Yang, B. et al. 2015, Applied Thermal Engineering, Vol. 90, pp. 742-748.

46. *An investigation on the performance of a Brayton cycle waste heat recovery system for turbocharged diesel engines.* 2013, Journal of Mechanical Science and Technology, Vol. 27, pp. 1721–1729.

47. *Brayton cycle for internal combustion engine exhaust gas waste heat recovery.* Galindo, J., Serrano, J.R., Dolz, V. et al. SAGE journals, 2015, Advances in Mechanical Engineering, Vol. 7, 6.

48. *Energetical, exergetical and economical optimization analysis of combined power generation system of gas turbine and Stirling engine.* Entezari, A., Manizadeh, A. and Ahmadi, R. Elsevier, Energy Conversion and Management, Vol. 159, pp. 189-203.

49. *A thermoacoustic Stirling electrical generator for cold exergy recovery of liquefied nature gas.* Hou, M., Wu, Z., Yu, G. et al. Elsevier, Applied Energy, Vol. 226, pp. 389-396.

50. *A survey on waste heat recovery: Electric power generation and potential prospects within Pakistan.* Zeb, K., Ali, S.M., Khan, B. et al. Elsevier, 2016, Renewable and Sustainable Energy Reviews, Vol. 75, pp. 1142-1155.

51. Srl, Exergy International. ORC Heat recovery from industrial processes. *Exergy: innovative organic rankine cycle company.* [Online] 1 12 2021. [Cited: 17

12 2021.] https://www.exergy-orc.com/application/heat-recovery-from-industrial-process.

52. *Exergoeconomic comparison of TLC (trilateral Rankine cycle), ORC (organic Rankine cycle) and Kalina cycle using a low grade heat source.* Yari, M. et al. Elsevier, 2015, Energy, Vol. 83, pp. 712-722.

53. *The viability of ultra low temperature waste heat recovery using organic Rankine cycle in dual loop data center applications.* Ebrahimi, K. et al. Elsevier, 2017, Applied Thermal Engineering, Vol. 126, pp. 393-406.

54. *Performances of an ORC power unit for Waste Heat Recovery on Heavy Duty Engine.* Cipollone, R. et al. Elsevier, 2017, Energy Procedia, Vol. 129, pp. 770-777.

55. *Efficiency Prediction for Axial-Flow Turbines Operating with Nonconventional Fluids.* Macchi, E. and Perdichizzi, A. ASME, 1981, Journal of Engineering for Gas Turbines and Power, Vol. 103, 4, pp. 718–724.

56. *Preliminary Design and Simulation of a Turbo Expander for Small Rated Power Organic Rankine Cycle (ORC).* Capata, R. and Hernandez, G. MDPI , 2014, Energies, Vol. 7, pp. 7067-7093.

57. *Application of Rankine Cycle to Passenger Vehicle Waste Heat Recovery - A Review.* Zhou, F. et al. SAE International, 2016, SAE International Journal of Materials and Manufacturing, Vol. 9, 2, pp. 224–235.

58. *Waste Heat Recovery of Passenger Car Using a Combination of Rankine Bottoming Cycle and Evaporative Engine Cooling System.* Oomori, H. and Ogino, S. SAE Internationanl, 1993, SAE Technical Paper, Vol. 930880.

59. *Thermodynamic analysis of dual-loop organic Rankine cycle using zeotropic mixtures for internal combustion engine waste heat recovery.* Ge, Z. et al. Elsevier, 2018, Energy Conversion and Management, Vol. 166, pp. 201-214.

60. *Parametric and working fluid analysis of a dual-loop organic Rankine cycle (DORC) used in engine waste heat recovery.* Shu, G. et al. Elsevier, 2014, Applied Energy, Vol. 113, pp. 1188-1198.

61. *Analyzing the optimization of an organic Rankine cycle system for recovering waste heat from a large marine engine containing a cooling water*

system. Yang, M. H. et al. Elsevier, 2014, Energy Conversion and Management, Vol. 88, pp. 999-1010.

62. *Analysis of an electricity–cooling cogeneration system based on RC–ARS combined cycle aboard ship.* Shu, G. et al. Elsevier, 2013, Energy Conversion and Management, Vol. 76, pp. 1053-1060.

63. *Thermodynamic analysis of a dual-loop organic Rankine cycle (ORC) for waste heat recovery of a petrol engine.* Wang, E. et al. Heat Powered Cycles Conference, Nottingham, 2016.

64. *A review of turbocompounding as a waste heat recovery system for internal combustion engines.* Aghaali, H. and Angstrom, H. E. Elsevier, 2015, Renewable and Sustainable Energy Reviews, Vol. 49, pp. 813-824.

65. *A technical review on waste heat recovery from compression ignition engines using organic Rankine cycle.* Chintala, V. et al. Elsevier, 2018, Renewable and Sustainable Energy Reviews, Vol. 81, Part 1, pp. 493-509.

66. *Thermal power fluctuations in waste heat to power systems: An overview on the challenges and current solutions.* Jiménez-Arreola, M. et al. Elsevier, 2018, Applied Thermal Engineering, Vol. 134, pp. 576-584.

67. *Organic Rankine Cycles (ORC) for mobile applications – Economic feasibility in different transportation sectors.* Pili, R. et al. Elsevier, 2017, Applied Energy, Vol. 204, pp. 1188-1197.

68. *A thermodynamic feasibility study of an Organic Rankine Cycle.* Lion, S. et al. Springer, 2017, International Journal of Energy and Environmental Engineering, Vol. 8, pp. 81–98.

69. Sarkar, D. *Thermal Power Plant-Design and Operation.* Elsevier, 2015.

70. Besarati, S. M. and Goswami, D. Y. *Advances in Concentrating Solar Thermal Research and Technology.* Woodhead Publishing Series, 2017. pp. 157–178. Vol. 8.

71. *Comparative analysis of a bottoming transcritical ORC and a Kalina cycle for engine exhaust heat recovery.* Yue, C. et al. Elsevier, 2015, Energy Conversion and Management, Vol. 89, pp. 764-774.

72. *Heat recovery from Diesel engines: A thermodynamic comparison between Kalina and ORC cycles.* Bombarda, P. et al. Elsevier, 2010, Applied Thermal Engineering, Vol. 30, 2-3, pp. 212-219.

73. *Exergy analysis of a hydrogen and water production process by a solar-driven transcritical CO2 power cycle with Stirling engine.* Naseri, A., Bidi, M., Ahmadi, M. H. et al. Elsevier, 2017, Journal of Cleaner Production, Vol. 158, pp. 165-181.

74. *Parametric analysis of carbon dioxide transcritical and supercritical power cycles using low grade heat source.* Baheta, A. T. and Emad, M. A. ARPN Journals, 2015, ARPN Journal of Engineering and Applied Sciences, Vol. 10, 21.

75. *Experimental investigations into power generation with low grade waste heat and R245fa Organic Rankine Cycles (ORCs).* Li, L., Ge, Y. T. and Luo, X. et al. Elsevier, 2017, Applied Thermal Engineering, Vol. 115, pp. 815-824.

76. *Cooling, Heating, Generating Power, and Recovering Waste Heat with Thermoelectric Systems.* Bell, L. E. Science, 2008, Science, Vol. 321, 5895, pp. 1457-1461.

77. Rowe, D. *Thermoelectrics Handbook.* Taylor & Francis Group, 2006.

78. *Thermoelectric power generation systems recovering heat from combustible solid waste in Japan.* Kajikawa, T. IEEE, 1996, Fifteenth International Conference on Thermoelectrics. Proceedings ICT '96, pp. 343-351.

79. *Power Generation from Waste Heat Using Heat Pipe and Thermoelectric Generator.* Remeli, M. F. Elsevier, 2015, Energy Procedia, Vol. 75, pp. 645-650.

80. *Autonomous Sensor System With Power Harvesting for Telemetric Temperature Measurements of Pipes.* Dalola, S. et al. IEEE, 2009, IEEE Transactions on Instrumentation and Measurement, Vol. 58, pp. 1471-1478.

81. *Design and characterization of small thermoelectric generators for environmental monitoring devices.* Bonin, R. et al. Elsevier, 2013, Energy Conversion and Management, Vol. 73, pp. 340-349.

82. *Thermoelectric Power Generation from Waste Heat of Natural Gas Water Heater.* Ding, L. C. et al. Elsevier, 2017, Energy Procedia, Vol. 110, pp. 32-37.

83. *Development and multi-objective optimization of geothermal-based organic Rankine cycle integrated with thermoelectric generator and proton exchange membrane electrolyzer for power and hydrogen production.* Gholamian, E. et al. Elsevier, 2018, Energy Conversion and Management, Vol. 174, pp. 112-125.

84. *Employing thermoelectric generator for power generation enhancement in a Kalina cycle driven by low-grade geothermal energy.* Zare, V. and Palideh, V. Elsevier, 2018, Applied Thermal Engineering, Vol. 130, pp. 418-428.

85. *Experiments and simulations on low-temperature waste heat harvesting system by thermoelectric power generators.* Hsu, C.T., Huang, G.Y., Chu, H.S. et al. Elsevier, 2011, Applied Energy, Vol. 88, 4, pp. 1291-1297.

86. *Development of high-efficiency thermoelectric power generation system.* Sano, S., Mizukami, H. and Kaibe, H. 2003, Komatsu Technical Report, Vol. 49, 152.

87. *Thermal design of automobile exhaust based thermoelectric generators: Objectives and challenges.* Saqr, K. M. et al. KSAE, 2008, International Journal of Automotive Technology, Vol. 9, 2, pp. 155-160.

88. *Automotive Applications of Thermoelectric Materials.* Yang, J. and Stabler, F. R. Springer Nature, 2009, Journal of Electronic Materials, Vol. 38, 7, pp. 1245-1251.

89. *Thermoelectric Conversion of Exhaust Gas Waste Heat into Usable Electricity.* Meisner, G. P. San Diego, 2010. General Motors Global Research Development 16th Directions in Engine Efficiency and Emissions Research (DEER) Conf.

90. *A case study on compatibility of automotive exhaust thermoelectric generation system, catalytic converter and muffler.* Liu, X. et al. Elsevier, 2014, Case Studies in Thermal Engineering, Vol. 2, pp. 62-66.

91. *Waste heat recovery from the exhaust of low-power diesel engine using thermoelectric generators.* Haidar, J. G. and Ghojel, J. I. Beijing : IEEE, 2001. ICT2001: Proceedings of the 20th International Conference on Thermoelectrics. pp. 1-6.

92. *Thermoelectric power generation system for future hybrid vehicles using hot exhaust gas.* Kim, S. K. et al. Springer Nature, 2011, Journal of Electronic Materials, Vol. 40, pp. 778-783.

93. *Heat-Pipe Assisted Thermoelectric Generators for Exhaust Gas Applications.* Goncalves, L. M. et al. Vancouver : ASME, 1387-1396. Proceedings of the ASME 2010 International Mechanical Engineering Congress and Exposition. Vols. Volume 5: Energy Systems Analysis, Thermodynamics and Sustainability; NanoEngineering for Energy; Engineering to Address Climate Change, Parts A and B.

94. Smith, K. and Thornton, M. *Feasibility of Thermoelectrics for Waste Heat Recovery in Conventional Vehicles.* National Renewable Energy Lab, U.S. Department of Energy. 2009.

95. *Thermoelectric Converters of Human Warmth for Self-Powered Wireless Sensor Nodes.* Leonov, V. et al. IEEE, 2007, IEEE Sensors Journal, Vol. 7, 5, pp. 650-657.

96. *Pulse Oximeter Fully Powered by Human Body Heat.* Torfs, T. et al. International Frequency Sensors Association, 2007, Sensors & Transducers Journal, Vol. 80, 6, pp. 1230-1238.

97. *Wearable electronics self-powered by using human body heat: The state of the art and the perspective.* Leonov, V. and Vullers, R. J. M. AIP Publishing, 2009, Journal of Renewable and Sustainable Energy, Vol. 1, 062701.

98. *Wearable Autonomous Wireless Electro-encephalography System Fully Powered by Human Body Heat.* Torfs, T. et al. IEEE, 2008, Sensors, pp. 1269-1272.

99. *A Batteryless 19 microW MICS/ISM-Band Energy Harvesting Body Sensor Node SoC for ExG Applications.* Zhang, Y. et al. IEEE, 2013, IEEE Journal of Solid-State Circuits, Vol. 48, 1, pp. 199-213.

100. *Characterization of Human Body-Based Thermal and Vibration Energy Harvesting for Wearable Devices.* Wahbah, M. et al. IEEE, 2014, IEEE Journal on Emerging and Selected Topics in Circuits and Systems, Vol. 4, 3, pp. 354-363.

101. *Wearable solar thermoelectric generator driven by unprecedentedly high temperature difference.* Jung, Y. S. et al. Elsevier, 2017, Nano Energy, Vol. 40, pp. 663-672.

102. *On thermoelectric and pyroelectric energy harvesting.* Sebald, G., Guyomar, D. and Agbossou, A. IOP Publishing Ltd, 2009, Smart Materials and Structures, Vol. 18, p. 125006.

103. *Harvesting wind energy with pyroelectric nanogenerator PNG using the vortex generator mechanism.* Raouadi, M. and Touayar, O. Elsevier, 2018, Sensors and Actuators A: Physical, Vol. 273, pp. 42-48.

104. *A triboelectric and pyroelectric hybrid energy harvester for recovering energy from low-grade waste fluids.* Jiang, D. et al. Elsevier, 2020, Nano Energy, Vol. 70, p. 104459.

105. *The Prospect and Analysis of Nanogenerator for Wearable Devices.* Yu, J,Y. and Liu, L. Springer, Cham, 2019, Advances in Body Area Networks I, Vols. Internet of Things (Technology, Communications and Computing).

106. *Thermal Energy Harvesting Using Pyroelectric and Piezoelectric Effect.* Kang, M. and Yeatman, E. M. IOP Publishing, 2016, Journal of Physics: Conference Series, Vol. 773, 012073.

107. *Characterization of Pyroelectric Materials for Energy Harvesting from Human Body.* Potnuru, A. and Tadesse, Y. Taylor and Francis Online, 2014, Integrated Ferroelectrics, Vol. 150, 1, pp. 23-50.

108. *A pyroelectric generator as a self-powered temperature sensor for sustainable thermal energy harvesting from waste heat and human body heat.* Sultana, A. et al. Elsevier, 2018, Applied Energy, Vol. 221, pp. 299-307.

109. *Hybrid Photothermal Pyroelectric and Thermogalvanic.* Ding, T. et al. Wiley, 2018, Advanced Energy Materials, Vol. 8, 1802397.

110. *A wearable pyroelectric nanogenerator and self-powered breathing sensor.* Xue, H. et al. Elsevier, 2017, Nano Energy, Vol. 38, pp. 147-154.

111. *Flexible triboelectric generator.* Fan, F. R. Elsevier, 2012, Nano Energy, Vol. 1, 2, pp. 328-334.

112. *Toward Large-Scale Energy Harvesting by a Nanoparticle-Enhanced Triboelectric Nanogenerator.* Zhu, G. et al. ACS, 2013, Nano Letters, Vol. 13, 2, pp. 847–853.

113. *Nanoscale Triboelectric-Effect-Enabled Energy Conversion for Sustainably Powering Portable Electronics.* Wang. S. et al. ACS, 2012, Nano Letters, Vol. 12, 12, pp. 6339–6346.

114. *Rotary Triboelectric Nanogenerator Based on a Hybridized Mechanism for Harvesting Wind Energy.* Xie, Y. et al. ACS, 2013, ACS Nano, Vol. 7, 8, pp. 7119–7125.

115. *Integrated Multilayered Triboelectric Nanogenerator for Harvesting Biomechanical Energy from Human Motions.* Bai, P. et al. ACS, 2013, ACS Nano, Vol. 7, 4, pp. 3713–3719.

116. *The Energy Harvesting Eel: a small subsurface ocean/river power generator.* Taylor, G. et al. IEEE, 2001, IEEE Journal of Oceanic Engineering, Vol. 26, 4, pp. 539-547.

117. *Water-Solid Surface Contact Electrification and its Use for Harvesting Liquid-Wave Energy.* Lin, Z. H. et al. Wiley, 2013, Angewandte Chemie, Vol. 52, 48, pp. 12545-12549.

118. *Demonstration of the triboelectricity effect by the flow of liquid water in the insulating pipe.* Ravelo, B. et al. Elsevier, 2011, Journal of Electrostatics, Vol. 69, 6, pp. 473-478.

119. *Spontaneous electrical charging of droplets by conventional pipetting.* Choi, D. et al. Springer Nature Limited, 2013, Scientific Reports, Vol. 3, 2037.

120. *Water-Through Triboelectric Nanogenerator Based on Ti-Mesh for Harvesting Liquid Flow.* Park, H. Y. et al. Springer Nature, 2018, Journal of the Korean Physical Society, Vol. 72.

121. Tegusi, T. *Novel materials for magnetic refrigeration.* Van der Waals-Zeeman Institute. 2003. PhD Thesis.

122. Prieto, M. et al. *Urban Energy Systems for Low-Carbon Cities.* Elsevier, 2018. pp. 181–239. Vol. 5.

123. Administration, U.S. Energy Information. *Construction cost data for electric generators installed in 2019*. Independent statistics and analysis: U.S. Energy Information Administration. [Online] https://www.eia.gov/electricity/generatorcosts/.

124. Ebrahimi, M., Keshavarz, A. *Combined Cooling, Heating and PowerDecision-Making - Decision-Making, Design and Optimization.* Elsevier, 2015. pp. 35–91.

125. *Lecture at Washington State University.* Valdimarsson, P. Washington DC, 2003.

126. Limited, Kalina Power. 2016.

127. *Summer Study on Energy Efficiency in Industry.* Arvay, P. et al. Washington, DC : American Council for an Energy Efficient Economy, 2011. ACEEE, pp. 1–12.

128. *Thermoeconomic analysis of multi-stage recuperative Brayton cycles: Part II – Waste energy recovery using CO2 and organic Rankine power cycles.* Mohammadi, K. and McGowan, J. Elsevier, 2019, Energy Conversion and Management, Vol. 185, pp. 920-934.

129. *Optimization and application of Stirling engine for waste heat recovery from a heavy-duty truck engine.* Güven, M. et al. Elsevier, 2019, Energy Conversion and Management, Vol. 180, pp. 411-424.

130. *Integration of Kalina cycle in a combined heat and power plant, a case study.* Ogriseck, S. Elsevier, 2009, Applied Thermal Engineering, Vol. 29, 14-15, pp. 2843-2848.

131. *Potential of carbon dioxide transcritical power cycle waste-heat recovery systems for heavy-duty truck engines.* Li, X. et al. Elsevier, 2019, Applied Energy, Vol. 250, pp. 1581-1599.

132. *A survey on waste heat recovery: Electric power generation and potential prospects within Pakistan.* Zeb, K. et al. Elsevier, 2017, Renewable and Sustainable Energy Reviews, Vol. 75, pp. 1142-1155.

133. *Smart Fluid Systems: The Advent of Autonomous Liquid Robotics.* Chiolerio, A., Quadrelli, M. B. Wiley Online Library, 2017, Advanced Science, Vol. 4, 7, p. 1700036.

134. *Autonomous robots for harsh environments: a holistic overview of current solutions and ongoing challenges.* Wong, C. et al. Taylor & Francis Online, 2018, Systems Science & Control Engineering, Vol. 6, 1, pp. 213-219.

135. *Exploration of Extreme Environments with Current and Emerging Robot Systems.* Kalita, H. and Thangavelautham, J. Springer Nature, 2020, Curr Robot Rep, Vol. 1, pp. 97–104.

136. *MallARD: An Autonomous Aquatic Surface Vehicle for Inspection and Monitoring of Wet Nuclear Storage Facilities.* Groves, K. et al. MDPI, 2019, Robotics, Vol. 8, 47.

137. *Self-Sufficient Energy Harvesting in Robots using Nanotechnology.* Zein, Basma El. Hilaris, 2013, Advances in Robotics & Automation, Vol. 2, 3.

138. *Three-dimensional piezoelectric polymer microsystems for vibrational energy harvesting, robotic interfaces and biomedical implants.* Han, M., Wang, H., Yang, Y. et al. Springer Nature Limited, 2019, Nature Electronics, Vol. 2, pp. 26–35.

139. *Energy harvesting from walking motion of a humanoid robot using a piezoelectric composite.* Cha, Y. and Seokmin, H. IOP Publishing, 2016, Smart Materials and Structures, Vol. 25.

140. *Soft Robotics: Biological Inspiration, State of the Art, and Future Research*. Trivedi, D., Rahn, C. D., Kier, W. M. et al. Hindawi, 2008, Applied Bionics and Biomechanics, vol. 5, 520417, pp. 19.

141. *Energy Harvesting in Soft Robot Locomotion with Complex Dynamics.* S. A. Katiyar, F. Iida and S. G. Nurzaman. Bangkok, IEEE, 2019. International Conference on Cybernetics and Intelligent Systems (CIS) and IEEE Conference on Robotics, Automation and Mechatronics (RAM). pp. 475-480.

142. *Bioinspired underwater locomotion of light-driven liquid crystal gels.* Hamed Shahsavan, Amirreza Aghakhani, Hao Zeng, Yubing Guo, Zoey S.

Davidson, Arri Priimagi, Metin Sitti. PNAS, 2020. Proceedings of the National Academy of Sciences. Vol. 117 (10), pp. 5125-5133.

143. *Colloidal Energetic Systems.* Chiolerio, A. and Quadrelli, M. B. Wiley, 2018, Energy Technology, Vol. 7, 5, p. 1800580.

144. Spaldin, N. A. *Magnetic Materials: Fundamentals and Applications.* Cambridge Univarsity Press, 2010. Vol. 1.

145. Odenbach, S. *Magnetoviscous Effects in Ferrofluids*. Springer, 2002.

146. Cecchini, L. *Multiphase colloidal system: electrical charaterization of triboelectric and ferromagnetic colloids*. Department of Electronics and Telecommunications, Politecnico di Torino. 2019. Master Thesis.

147. *The force on a magnetic dipole*. Boyer, T. H. AIP Publishing, 1988, American Journal of Physics, Vol. 56, 8, p. 688 .

148. Aliofkhazraei, M. Handbook of Nanoparticles. Springer, 2016.

149. *Convective instability of ferromagnetic fluids*. Finlayson, B. Cambridge University Press, 1970, Journal of Fluid Mechanics, Vol. 40, 4, pp. 753-767.

150. Odenbach, S. *Ferrofluids: Magnetically Controllable Fluids and Their Applications*. New York : Springer, 2002. pp. 88–89.

151. *Thermomagnetic convective flows in a vertical layer of ferrocolloid: Perturbation energy analysis and experimental study*. Suslov, S. A. APS, 2012, Phys. Rev. E, Vol. 86, 1, p. 016301 .

152. *Convection in a vertical layer of stratified magnetic fluid*. Bozhko, A. A. et al. Institute of Physics, University of Latvia, 2013, Magnetohydrodynamics, Vol. 49, 1, pp. 143–152.

153. *Triboelectric effect: A new perspective on electron transfer process*. Pan, S. and Zhang, Z. AIP Publishing, 2017, J. Appl. Phys., Vol. 122, p. 144302.

154. Wang, Z. et al. *Triboelectric Nanogenerators*. Springer, 2016.

155. Triboelectric Characterization of Colloidal TiO2 for Energy Harvesting Applications. Garofalo, E. et al. s.l. : MDPI, 2020, Nanomaterials , Vol. 10, p. 1181.

156. *Hybridization of Magnetism and Piezoelectricity for an Energy Scavenger based on Temporal Variation of Temperature.* Carlioz, L. et al. EDA Publishing, 2008, DTIP of MEMS/MOEMS.

157. *Nonlinear pyroelectric energy harvesting from relaxor single crystals.* Khodayari, A., Pruvost, S. and Sebald, G. et al. IEEE, 2009, IEEE Transactions on Ultrasonics, Ferroelectrics, and Frequency Control, Vol. 56, 4, pp. 693-699.

158. *Energy harvesting based on Ericsson pyroelectric cycles in a relaxor ferroelectric ceramic.* Sebald, G., Pruvost, S. and Guyomar, D. IOP Publishing Ltd, 2007, Smart Materials and Structures, Vol. 17, 015012.

159. *Pyroelectric Energy Harvesting Using the Olsen Cycle on Relaxor Ferroelectric 8/65/35 PLZT.* Lee, F. et al. Atlanta, Georgia: ASME, 2012. ASME 2012 Third International Conference on Micro/Nanoscale Heat and Mass Transfer. pp. 597-604.

160. *Waste heat energy harvesting using the Olsen cycle on 0.945Pb(Zn1/3Nb2/3)O3– 0.055PbTiO3 single crystals.* McKinley, I. M. et al. IOP Publishing Ltd, 2012, Smart Materials and Structures, Vol. 21, 035015.

161. *Pyroelectric energy harvesting using Olsen cycles in purified and porous poly(vinylidene fluoride-trifluoroethylene) [P(VDF-TrFE)] thin films.* Navid, A. and Pilon, L. IOP Publishing Ltd, 2011, Smart Materials and Structures, Vol. 20, 2, p. 025012.

162. *Pyroelectric Energy Harvesting: With Thermodynamic-Based Cycles.* Mohammadi, S. and Khodayari, A. Hindawi, 2012, Smart Materials Research, Vol. 2012.

163. *New approach to waste-heat energy harvesting: pyroelectric energy conversion.* Pandya, S., et al. 2019, NPG Asia Mater, Vol. 11, p. 26.

164. *Colloidal soft matter under external control.* Löwen, H. IOP Publishing, 2001, Journal of Physics: Condensed Matter, Vol. 13, 24.

165. Sindel, J. et al. *Surface and Colloid Chemistry.* Encyclopedia of Materials: Science and Technology. Elsevier, 2001, pp. 1–10.

166. *Wetting and Dispersing Agents.* F. O. Pirrung et al. Swiss Chemical Society, 2002, Chimia , Vol. 56, 5, p. 170.

167. *Magnetic properties of ferrofluid emulsions: model of non-interacting droplets*. Ivanov, A.O. [ed.] University of Latvia Institute of Physics. 2, 2011, Magnetohydrodynamcs, Vol. 47, pp. 129–134.

168. *On the temperature dependence of ferrofluid susceptibility*. Dikansky, Y. et al. EDP Sciences, 2018. EPJ Web Conf. Vol. 185 .

169. *Ferromagnetic Colloid for Studying Magnetic Structures*. Elmore, W. C. American Physical Society, 1938, Physical Review, Vol. 54, p. 309.

170. Papell, S. S. *Low viscosity magnetic fluid obtained by the colloidal suspension of magnetic particles*. US-PATENT-3,215,572|NASA-CASE-XLE-01512 [ed.] US Gov. Public Use Permitted. 1965.

171. Rosensweig, R. E. *Ferrohydrodynamics*. [ed.] Courier Corporation. Mineola : Dover Publication, Inc., 2013.

172. *Ferrofluids - Magnetisable Liquids and Their Application in Density Separation*. Odenbach, S. Hindawi Publishing Corporation, 1998, Physical Separation in Science and Engineering, Vol. 9.

173. Odenbach, S. *Colloidal Magnetic Fluids - Basics, Development and Application of Ferrofluids*. Springer, 2009.

174. *Flow electrification of liquids*. Touchard, G. Elsevier, 2001, Journal of Electrostatics, Vols. 51-52, pp. 440-447.

175. *Numerical simulation of the electrical double layer development: physicochemical model at the solid and dielectric liquid interface for laminar flow electrification phenomenon*. EL-Adawy, M. et al. IEEE, 2011, IEEE Transactions on Dielectrics and Electrical Insulation, Vol. 18, 5, pp. 1463-1475.

176. *A semi-quantitative tribo-electric series for polymeric materials: The influence*. Diaz, A. and Félix-Navarro, R.M. Elsevier, 2004, J. Electrost., Vol. 62, pp. 277–290.

177. *Molecular structure engineering of dielectric fluorinated polymers for enhanced performances of triboelectric*. Kim, M.P. et al. Elsevier, 2018, Nano Energy, Vol. 53, pp. 37–45.

178. *Triboelectricity in polymers: effects of the ionic nature of carbon–carbon bonds in the polymer main chain on charge due to yield of mechano-anions produced by heterogeneous scission of the carbon–carbon bond by mechanical fracture*. Sakaguchi, M. et al. Elsevier, 2004, J. Electrost., Vol. 62, 1, pp. 35-50.

179. *Where is water in the triboelectric series?* Burgo, T. et al. Elsevier, 2016, Journal of Electrostatics, Vol. 80, pp. 30-33.

180. *Enhanced Triboelectric Nanogenerators and Triboelectric Nanosensor Using Chemically Modified TiO2 Nanomaterials*. Lin, Z. H. et al. ACS, 2013, ACS Nano, Vol. 7, 5, pp. 4554–4560.

181. *Triboelectric charging of powders: A review*. Matsusaka, S. et al. Elsevier, 2010, Chemical Engineering Science, Vol. 65, 22, pp. 5781-5807.

182. *Pyroelectric energy harvesting using liquid-based switchable thermal interfaces*. Cha, G. and Ju, Y. S. Elsevier, 2013, Sensors and Actuators A: Physical, Vol. 189, pp. 100-107.

183. Isse, A. *Crystal Hybridized Pyro-Piezoelectric Ferrofluidic Harvester*. Arxiv, 2020.

184. *Self-powered colloidal wurtzite-structure quantum dots photodetectors*. Jin, L. et al. Wiley, 2018, Adv. Opt. Mater., Vol. 6, 21, pp. 1–8.

185. Woods, L. C. *Theory of tokamak transport : new aspects for nuclear fusion reactor design*. Wiley, 2006.

186. *Effective heat capacity of ferrofluids – Analytical approach*. Mousavi, N. S. S. and Kumar, S. Elsevier, 2014, International Journal of Thermal Sciences, Vol. 84, pp. 267-274.

187. *Electronic cooling using an automatic energy transport device based on thermomagnetic effect*. Xuan, Y. and Lian, W. Elsevier, 2011, Applied Thermal Engineering, Vol. 31, 8-9, pp. 1487-1494.

188. *Energy harvesting via ferrofluidic induction*. Monroe, J. G. et al. Baltimore, 2015. SPIE Sensing Technology + Applications, Energy Harvesting and Storage: Materials, Devices, and Applications VI. Vol. 94930G.

189. *Electromagnetic induction by ferrofluid in an oscillating heat pipe*. Monroe, J. G. et al. AIP Publishing, 2015, Applied Physics Letters, Vol. 106, 26, p. 263901.

190. *On the energy harvesting and heat transfer ability of a ferro-nanofluid oscillating heat pipe*. Monroe, J. G. et al. Elsevier, 2019, International Journal of Heat and Mass Transfer, Vol. 132, pp. 162-171.

191. *Energy scavenging from ultra-low temperature gradients*. Kishore R. A. et al. RSC, 2019, Energy & Environmental Science, Vol. 12, 3, pp. 1008-1018.

192. *Energy harvesting near room temperature using a thermomagnetic generator with a pretzel-like magnetic flux topology*. Waske, A. et al. Springer Nature, 2019, Nature Energy, Vol. 4, pp. 68–74.

193. *Harvesting low-grade heat energy using thermo-osmotic vapour transport through nanoporous membranes*. Straub, A. et al. Springer Nature, 2016, Nature Energy, Vol. 1, p. 16090.

194. *Skin-Inspired Low-Grade Heat Energy Harvesting Using Directed Ionic Flow through Conical Nanochannels*. Xie, G. et al. Wiley, 2018, Advanced Energy Materials, Vol. 8, 22, p. 1800459.

195. *A new miniaturized engine based on thermomagnetic effect of magnetic fluids*. Zhou, L. et al. Springer Nature, 2009, Frontiers of Energy and Power Engineering in China, Vol. 3, pp. 160–166.

196. *Characteristics of thermo-magnetic driven motor using magnetic fluid*. Yamaguchi, H. et al. Elsevier, 2004, Journal of Magnetism and Magnetic Materials, Vols. 272–276, Part 3, pp. 2362-2364.

197. *Waste heat to power conversion by means of thermomagnetic hydrodynamic energy harvester*. Chiolerio, A. et al. Elsevier, 2020, Applied Energy, Vol. 277, p. 115591.

198. Mattiussi, F. *A Thermomagnetic Energy Harvester CERES PROJECT*. Politecnico di Torino, 2018. Thesis.

199. *Calibration curves for thermistors*. Steinhart, J. S., Hart, S. R. Elsevier, 1968, Deep Sea Research and Oceanographic Abstracts, Vol. 15, 4, pp. 497-503.

200. Fortunato, G. *Thermofluiddynamics of colloidal systems*. Dipartimento di Ingegneria Meccanica ed Aerospaziale, Politecnico di Torino. 2019. Thesis.

201. *Poiseuille and his law*. Pfitzner, J. Wiley Online, 1976, Anaesthesia, Vol. 31, pp. 273-275.

202. *On the pyroelectric and triboelectric phenomena in ferrofluids*. Garofalo, E. et al. Wiley, 2022, Advanced Materials Technologies, p. 2200127.

203. *Rayleigh-bénard convection*. Bergé, P. and Dubois, M. Taylor & Francis Online, 1984, Contemporary Physics, Vol. 25, 6, pp. 535-582.

204. *Demonstration of the triboelectricity effect by the flow of liquid water in the insulating pipe*. Ravelo, B. et al. Elsevier, 2011, Journal of Electrostatics, Vol. 69, 6, pp. 473-478.

205. *The History of the Darcy-Weisbach Equation for Pipe Flow Resistance*. Brown, G.O. et al. Washington, 2002. Environmental and Water Resources History Sessions at ASCE Civil Engineering Conference and Exposition. pp. 34–43.

206. *Experiments with fluid friction in roughened pipes*. Colebrook, C. F. and White, C. M. Royal Society Publishing, 1937, Proc. R. Soc. Lond. A, Vol. 161, pp. 367–381.

207. *Matching the Directions of Electric Fields from Triboelectric and Ferroelectric Charges in Nanogenerator Devices for Boosted Performance*. Šutka, A. et al. Cell Press, 2020, iScience, Vol. 23, 4, p. 101011.

208. *Relative Chargeability of Nanostructured and Conventional Particles by Tribocharging*. Pjesky, S. C. and Maghirang, R. G. Taylor & Francis Online, 2009, Particulate Science and Technology, Vol. 27, 2, pp. 193-202.

209. *Liquid-state pyroelectric energy harvesting*. Bevione, M. et al. Cambridge University Press, 2020, MRS Energy & Sustainability, Vol. 7, E38.

210. *Mechanically Stirred Vessels*. Hemrajani, R.R. and Tatterson, G.B. Wiley Online Library, 2003, Handbook of Industrial Mixing.

211. *Effective heat capacity of ferrofluids - Analytical approach*. Mousavi, N. S. and Kumar, S. Elsevier, 2014, International Journal of Thermal Sciences, Vol. 84, 1, pp. 267-274.

212. *Convective Transport in Nanofluids*. Buongiorno, J. ASME, 2006, Journal of Heat Transfer, Vol. 128, 3, pp. 240-250.

213. *Multiphysics-Enabled Liquid State Thermal Harvesting: Synergistic Effects between Pyroelectricity and Triboelectrification*. Chiolerio, A. et al. Wiley Online, 2021, Energy Technol., Vol. 9, p. 2100544.

214. *The magnetic body force in ferrofluids*. Cecchini, L. and Chiolerio, A. IOP Publishing, 2021, J. Phys. D: Appl. Phys., Vol. 54, 35, p. 355002.

215. Kays, W. et al. *Convective Heat and Mass Transfer*. New York : McGraw-Hill Professional, 2004. Vol. 4th edition.

216. *Thermomagnetic energy harvesting with first order phase change materials*. Post, A. et al. AIP Publishing, 2013, Journal of Applied Physics, Vol. 114, 033915.

217. *Energy harvesting via fluidic agitation of a magnet within an oscillating heat pipe*. Monroe, J. G. et al. Elsevier, 2018, Applied Thermal Engineering, Vol. 129, pp. 884-892.

218. *Flexible triboelectric generator*. Wang, Z. et al. Elsevier, 2012, Nano Energy, Vol. 1, pp. 328–334.

219. *Modeling of triboelectric charge accumulation dynamics at the metal-insulator*. Ghaffarinejad, A. and Yavand Hasani, J. Springer Nature, 2019, Appl. Phys. A, Vol. 125, p. 259.

220. *How to measure the pyroelectric coefficient?* Jachalke, S. et al. AIP Publishing, 2017, Applied Physics Reviews, Vol. 4, p. 021303.

August 17, 2022

Letter of Permission

We, the Magnetohydrodynamics Journal (University of Latvia), herewith grant the permission to reproduce the requested figures (Figure 2 on p.145, Figure 3 on p. 146, and Figure 6 on p. 149) from the article

Author(s)	Title	Source
A.A. Bozhko G.F. Putin A.S. Sidorov S.A. Suslov	CONVECTION IN A VERTICAL LAYER OF STRATIFIED MAGNETIC FLUID	Magnetohydrodynamics, vol. 49 (2013), no. 1-2, pp. 143-152.

in the thesis by
Author: Erik Garofalo
Affiliation: Istituto Italiano di Tecnologia, Genova, Italy

The author (Erik Garofalo), in his turn, fully acknowledges the original publication, copyright agreement and the permanent link to the web site of Magnetohydrodynamics (http://www.mhd.sal.lv).

A. Cēbers
Editor in Chief
Magnetohydrodynamics www.mhd.sal.lv

CCC Marketplace™

Order Confirmation

Thank you, your order has been placed. An email confirmation has been sent to you. Your order license details and printable licenses will be available within 24 hours. Please access Manage Account for final order details.

This is not an invoice. Please go to manage account to access your order history and invoices.

CUSTOMER INFORMATION

Payment by invoice: You can cancel your order until the invoice is generated by contacting customer service.

📑 Billing Address

Dr. Erik Garofalo
Via Livorno 60
Torino, Torino 10144
Italy

+39 3341728122
erik.garofalo@iit.it

📍 Customer Location

Dr. Erik Garofalo
Via Livorno 60
Torino, Torino 10144
Italy

📄 PO Number (optional)

N/A

💳 Payment options

Invoice

PENDING ORDER CONFIRMATION

Confirmation Number: Pending

Order Date: 12-Aug-2022

---

1. Journal of Physics : Condensed Matter

0.00 USD

Order License ID	Pending	**Publisher**	IOP Publishing
ISSN	0953-9984	**Portion**	Chart/graph/table/figure
Type of Use	Republish in a thesis/dissertation		

LICENSED CONTENT

Publication Title	Journal of Physics : Condensed Matter	**Country**	United Kingdom of Great Britain and Northern Ireland
Author/Editor	Institute of Physics (Great Britain)	**Rightsholder**	IOP Publishing, Ltd
Date	01/01/1989	**Publication Type**	Journal
Language	English		

REQUEST DETAILS

Portion Type	Chart/graph/table/figure	**Distribution**	Worldwide
Number of charts / graphs / tables / figures requested	1	**Translation**	Original language of publication
		Copies for the disabled?	No
Format (select all that apply)	Print	**Minor editing privileges?**	No
Who will republish the content?	Academic institution	**Incidental promotional use?**	No
Duration of Use	Current edition and up to 5 years	**Currency**	USD
Lifetime Unit Quantity	Up to 499		
Rights Requested	Main product		

NEW WORK DETAILS

Title	PhD Candidate	**Institution name**	Istituto Italiano di Tecnologia
Instructor name	Erik Garofalo	**Expected presentation date**	2022-10-05

ADDITIONAL DETAILS

Order reference number	N/A	**The requesting person / organization to appear on the license**	Erik Garofalo

REUSE CONTENT DETAILS

Title, description or numeric reference of the portion(s)	Figure 1	**Title of the article/chapter the portion is from**	N/A
Editor of portion(s)	N/A	**Author of portion(s)**	Erik Garofalo
Volume of serial or monograph	N/A	**Issue, if republishing an article from a serial**	N/A
Page or page range of portion	1	**Publication date of portion**	1989-01-01

RIGHTSHOLDER TERMS AND CONDITIONS

These special terms and conditions are in addition to the standard terms and conditions for CCC's Republication Service and, together with those standard terms and conditions, govern the use of the Works. As the User you will make all reasonable efforts to contact the author(s) of the article which the Work is to be reused from, to seek

consent for your intended use. Contacting one author who is acting expressly as authorised agent for their co-author(s) is acceptable. User will reproduce the following wording prominently alongside the Work: the source of the Work, including author, article title, title of journal, volume number, issue number (if relevant), page range (or first page if this is the only information available) and date of first publication; and a link back to the article (via DOI); and if practicable, and IN ALL CASES for new works published under any of the Creative Commons licences, the words "© IOP Publishing. Reproduced with permission. All rights reserved" Without the express permission of the author(s) and the Rightsholder of the article from which the Work is to be reused, User shall not use it in any way which, in the opinion of the Rightsholder, could: (i) distort or alter the author(s)' original intention(s) and meaning; (ii) be prejudicial to the honour or reputation of the author(s); and/or (iii) imply endorsement by the author(s) and/or the Rightsholder. This licence does not apply to any article which is credited to another source and which does not have the copyright line '© IOP Publishing Ltd'. User must check the copyright line of the article from which the Work is to be reused to check that IOP Publishing Ltd has all the necessary rights to be able to grant permission. User is solely responsible for identifying and obtaining separate licences and permissions from the copyright owner for reuse of any such third party material/figures which the Rightsholder is not the copyright owner of. The Rightsholder shall not reimburse any fees which User pays for a republication license for such third party content. This licence does not apply to any material/figure which is credited to another source in the Rightsholder's publication or has been obtained from a third party. User must check the Version of Record of the article from which the Work is to be reused, to check whether any of the material in the Work is third party material. Third party citations and/or copyright notices and/or permissions statements may not be included in any other version of the article from which the Work is to be reused and so cannot be relied upon by the User. User is solely responsible for identifying and obtaining separate licences and permissions from the copyright owner for reuse of any such third party material/figures where the Rightsholder is not the copyright owner. The Rightsholder shall not reimburse any fees which User pays for a republication license for such third party content. User and CCC acknowledge that the Rightsholder may, from time to time, make changes or additions to these special terms and conditions without express notification, provided that these shall not apply to permissions already secured and paid for by User prior to such change or addition. User acknowledges that the Rightsholder (which includes companies within its group and third parties for whom it publishes its titles) may make use of personal data collected through the service in the course of their business. If User is the author of the Work, User may automatically have the right to reuse it under the rights granted back when User transferred the copyright in the article to the Rightsholder. User should check the copyright form and the relevant author rights policy to check whether permission is required. If User is the author of the Work and does require permission for proposed reuse of the Work, User should select 'Author of requested content' as the Requestor Type. The Rightsholder shall not reimburse any fees which User pays for a republication license. If User is the author of the article which User wishes to reuse in User's thesis or dissertation, the republication licence covers the right to include the Version of Record of the article, provided it is not then shared or deposited online. User must include citation details. Where User wishes to share their thesis or dissertation online, they should remove the Version of Record before uploading it. User may include a Preprint or the Accepted Manuscript (after the embargo period) in the online version of the thesis or dissertation, provided they do so in accordance with the Rightsholder's policies on sharing Preprints or Accepted Manuscripts. User may need to obtain separate permission for any third party content included within the article. User must check this with the copyright owner of such third party content. Any online or commercial use of User's thesis or dissertation containing the article, including publication via ProQuest, would need to be expressly notified in writing to the Rightsholder at the time of request and would require separate written permission from the Rightsholder. As well as CCC, the Rightsholder shall have the right to bring any legal action that it deems necessary to enforce its rights should it consider that the Work infringes those rights in any way. For content reuse requests that qualify for permission under the STM Permissions Guidelines, which may be updated from time to time, the STM Permissions Guidelines supplement the terms and conditions contained in this license.

Total Items: 1   Total Due: 0.00 USD

LANGUAGES   ▼

SEARCH

ipcc   REPORTS   SYNTHESIS REPORT   WORKING GROUPS   ACTIVITIES   NEWS

CALENDAR

COPYRIGHT

Unless otherwise stated, the information available on this website, including text, logos, graphics, maps, images and electronic downloads is the property of the IPCC and is protected by intellectual property laws.

You may freely download and copy the material contained on this website for your personal, non-commercial use, without any right to resell or redistribute it or to compile or create derivative works there from, subject to more specific restrictions that may apply to specific materials.

For such personal, non-commercial usages, reproduction of limited number of figures or short excerpts of IPCC material is authorized free of charge and without formal written permission provided that the original source is properly acknowledged, with mention of the complete name of the report, the publisher and the numbering of the page(s) or the figure(s). Permission can only be granted to use the material exactly as it is in the report. Please be aware that figures cannot be altered in any way, including the full legend. For media

use it is sufficient to cite the source while using the original graphic or figure. In line with established Internet usage, any external website may provide a hyperlink to the IPCC website or to any of its pages without requesting permission.

For any other use, permission is required. To obtain permission, please email a scanned copy of a letter on official letterhead addressed to the Secretary of the IPCC with all relevant details. All communications by mail should be addressed to:

IPCC Secretariat

World Meteorological Organization

7bis Avenue de la Paix,

P.O. Box No. 2300

CH-1211 Geneva 2,

Switzerland

All e-mail communications should be addressed to ipcc-sec@wmo.int.

Follow the IPCC

The Intergovernmental Panel on Climate Change (IPCC) is active socially – choose your network:

Engage with the IPCC

There are many ways to be involved and participate in the IPCC world.

LEARN MORE

ABOUT   COPYRIGHT   DISCLAIMER   PRIVACY POLICY

Creative Commons License Deed

Attribution-NonCommercial-NoDerivatives 4.0 International (CC BY-NC-ND 4.0)

This is a human-readable summary of (and not a substitute for) the license.

You are free to:

Share — copy and redistribute the material in any medium or format

The licensor cannot revoke these freedoms as long as you follow the license terms.

Under the following terms:

Attribution — You must give appropriate credit, provide a link to the license, and indicate if changes were made. You may do so in any reasonable manner, but not in any way that suggests the licensor endorses you or your use.

NonCommercial — You may not use the material for commercial purposes.

NoDerivatives — If you remix, transform, or build upon the material, you may not distribute the modified material.

No additional restrictions — You may not apply legal terms or technological measures that legally restrict others from doing anything the license permits.

Notices:

You do not have to comply with the license for elements of the material in the public domain or where your use is permitted by an applicable exception or limitation.

No warranties are given. The license may not give you all of the permissions necessary for your intended use. For example, other rights such as publicity, privacy, or moral rights may limit how you use the material.

Hindawi

Smart Materials Research

+ Journal Menu   PDF

Article Sections

Pyroelectric Energy Harvesting: With Thermodynamic-Based Cycles

Saber Mohammadi✉[1] and Akram Khodayari[1]

Show more

Academic Editor: Mickaël Lallart

Published: 05 Apr 2012

Abstract

This work deals with energy harvesting from temperature variations using ferroelectric materials as a microgenerator. The previous researches show that direct pyroelectric energy harvesting is not effective, whereas thermodynamic-based cycles give higher energy. Also, at different temperatures some thermodynamic cycles exhibit different behaviours. In this paper pyroelectric energy harvesting using Lenoir and Ericsson thermodynamic cycles has been studied numerically and the two cycles were compared with each other. The material used is the PMN-25 PT single crystal that is a very interesting material in the framework of energy harvesting and sensor applications.

1. Introduction

Small, portable, and lightweight power generation systems are currently in very high demand in commercial markets, due to a dramatic increase in the use of personal electronics and communication equipments. The simple way to satisfy these demands is to utilize batteries; however, nonrechargeable batteries are becoming useless upon discharging, and rechargeable batteries require portable power generation units to recharge them. Thus, a portable small-scale power generation system that can either replace batteries entirely or recharge them to extend their lifetime is of considerable interest. There are several different classes of small-scale power generators currently being researched. The power generation technique that is investigated in this

Smart Materials Research

+ Journal Menu   PDF   ⤓

Article Sections

Copyright

Follow us:

About us

Contact us

Careers

Blog

Journals

Article Processing Charges

Print editions

JOHN WILEY AND SONS LICENSE
TERMS AND CONDITIONS

Aug 12, 2022

This Agreement between Istituto Italiano di Tecnologia ("You") and John Wiley and Sons ("John Wiley and Sons") consists of your license details and the terms and conditions provided by John Wiley and Sons and Copyright Clearance Center.

License Number	5366490480451
License date	Aug 12, 2022
Licensed Content Publisher	John Wiley and Sons
Licensed Content Publication	ENERGY TECHNOLOGY (ELECTRONIC)
Licensed Content Title	Waste Heat to Power: Technologies, Current Applications, and Future Potential
Licensed Content Author	Alessandro Chiolerio, Fabio Mattiussi, Luca Cecchini, et al
Licensed Content Date	Sep 7, 2020
Licensed Content Volume	8
Licensed Content Issue	11
Licensed Content Pages	22
Type of use	Dissertation/Thesis

Requestor type	Author of this Wiley article
Format	Print
Portion	Figure/table
Number of figures/tables 5	
Will you be translating?	No
Title	PhD candidate
Institution name	Istituto Italiano di Tecnologia
Expected presentation date	Oct 2022
Portions	figure 7, 10
Requestor Location	Istituto Italiano di Tecnologia Via Livorno 60 Torino, Torino 10144 Italy Attn: Istituto Italiano di Tecnologia
Publisher Tax ID	EU826007151
Total	0.00 USD

Terms and Conditions

TERMS AND CONDITIONS

Clearance Center Inc., ("CCC's Billing and Payment terms and conditions"), at the time that
you opened your RightsLink account (these are available at any time at
http://myaccount.copyright.com).

Terms and Conditions

- The materials you have requested permission to reproduce or reuse (the "Wiley
  Materials") are protected by copyright.

- You are hereby granted a personal, non-exclusive, non-sub licensable (on a stand-
  alone basis), non-transferable, worldwide, limited license to reproduce the Wiley
  Materials for the purpose specified in the licensing process. This license, **and any
  CONTENT (PDF or image file) purchased as part of your order,** is for a one-time
  use only and limited to any maximum distribution number specified in the license.
  The first instance of republication or reuse granted by this license must be completed
  within two years of the date of the grant of this license (although copies prepared
  before the end date may be distributed thereafter). The Wiley Materials shall not be
  used in any other manner or for any other purpose, beyond what is granted in the
  license. Permission is granted subject to an appropriate acknowledgement given to the
  author, title of the material/book/journal and the publisher. You shall also duplicate the
  copyright notice that appears in the Wiley publication in your use of the Wiley
  Material. Permission is also granted on the understanding that nowhere in the text is a
  previously published source acknowledged for all or part of this Wiley Material. Any
  third party content is expressly excluded from this permission.

- With respect to the Wiley Materials, all rights are reserved. Except as expressly
  granted by the terms of the license, no part of the Wiley Materials may be copied,
  modified, adapted (except for minor reformatting required by the new Publication),
  translated, reproduced, transferred or distributed, in any form or by any means, and no
  derivative works may be made based on the Wiley Materials without the prior
  permission of the respective copyright owner.**For STM Signatory Publishers
  clearing permission under the terms of the STM Permissions Guidelines only, the
  terms of the license are extended to include subsequent editions and for editions
  in other languages, provided such editions are for the work as a whole in situ and
  does not involve the separate exploitation of the permitted figures or extracts,**
  You may not alter, remove or suppress in any manner any copyright, trademark or
  other notices displayed by the Wiley Materials. You may not license, rent, sell, loan,
  lease, pledge, offer as security, transfer or assign the Wiley Materials on a stand-alone
  basis, or any of the rights granted to you hereunder to any other person.

- The Wiley Materials and all of the intellectual property rights therein shall at all times
  remain the exclusive property of John Wiley & Sons Inc, the Wiley Companies, or
  their respective licensors, and your interest therein is only that of having possession of
  and the right to reproduce the Wiley Materials pursuant to Section 2 herein during the
  continuance of this Agreement. You agree that you own no right, title or interest in or
  to the Wiley Materials or any of the intellectual property rights therein. You shall have
  no rights hereunder other than the license as provided for above in Section 2. No right,
  license or interest to any trademark, trade name, service mark or other branding
  ("Marks") of WILEY or its licensors is granted hereunder, and you agree that you
  shall not assert any such right, license or interest with respect thereto

- NEITHER WILEY NOR ITS LICENSORS MAKES ANY WARRANTY OR
  REPRESENTATION OF ANY KIND TO YOU OR ANY THIRD PARTY,

EXPRESS, IMPLIED OR STATUTORY, WITH RESPECT TO THE MATERIALS OR THE ACCURACY OF ANY INFORMATION CONTAINED IN THE MATERIALS, INCLUDING, WITHOUT LIMITATION, ANY IMPLIED WARRANTY OF MERCHANTABILITY, ACCURACY, SATISFACTORY QUALITY, FITNESS FOR A PARTICULAR PURPOSE, USABILITY, INTEGRATION OR NON-INFRINGEMENT AND ALL SUCH WARRANTIES ARE HEREBY EXCLUDED BY WILEY AND ITS LICENSORS AND WAIVED BY YOU.

- WILEY shall have the right to terminate this Agreement immediately upon breach of this Agreement by you.

- You shall indemnify, defend and hold harmless WILEY, its Licensors and their respective directors, officers, agents and employees, from and against any actual or threatened claims, demands, causes of action or proceedings arising from any breach of this Agreement by you.

- IN NO EVENT SHALL WILEY OR ITS LICENSORS BE LIABLE TO YOU OR ANY OTHER PARTY OR ANY OTHER PERSON OR ENTITY FOR ANY SPECIAL, CONSEQUENTIAL, INCIDENTAL, INDIRECT, EXEMPLARY OR PUNITIVE DAMAGES, HOWEVER CAUSED, ARISING OUT OF OR IN CONNECTION WITH THE DOWNLOADING, PROVISIONING, VIEWING OR USE OF THE MATERIALS REGARDLESS OF THE FORM OF ACTION, WHETHER FOR BREACH OF CONTRACT, BREACH OF WARRANTY, TORT, NEGLIGENCE, INFRINGEMENT OR OTHERWISE (INCLUDING, WITHOUT LIMITATION, DAMAGES BASED ON LOSS OF PROFITS, DATA, FILES, USE, BUSINESS OPPORTUNITY OR CLAIMS OF THIRD PARTIES), AND WHETHER OR NOT THE PARTY HAS BEEN ADVISED OF THE POSSIBILITY OF SUCH DAMAGES. THIS LIMITATION SHALL APPLY NOTWITHSTANDING ANY FAILURE OF ESSENTIAL PURPOSE OF ANY LIMITED REMEDY PROVIDED HEREIN.

- Should any provision of this Agreement be held by a court of competent jurisdiction to be illegal, invalid, or unenforceable, that provision shall be deemed amended to achieve as nearly as possible the same economic effect as the original provision, and the legality, validity and enforceability of the remaining provisions of this Agreement shall not be affected or impaired thereby.

- The failure of either party to enforce any term or condition of this Agreement shall not constitute a waiver of either party's right to enforce each and every term and condition of this Agreement. No breach under this agreement shall be deemed waived or excused by either party unless such waiver or consent is in writing signed by the party granting such waiver or consent. The waiver by or consent of a party to a breach of any provision of this Agreement shall not operate or be construed as a waiver of or consent to any other or subsequent breach by such other party.

- This Agreement may not be assigned (including by operation of law or otherwise) by you without WILEY's prior written consent.

- Any fee required for this permission shall be non-refundable after thirty (30) days from receipt by the CCC.

- These terms and conditions together with CCC's Billing and Payment terms and conditions (which are incorporated herein) form the entire agreement between you and

WILEY concerning this licensing transaction and (in the absence of fraud) supersedes all prior agreements and representations of the parties, oral or written. This Agreement may not be amended except in writing signed by both parties. This Agreement shall be binding upon and inure to the benefit of the parties' successors, legal representatives, and authorized assigns.

- In the event of any conflict between your obligations established by these terms and conditions and those established by CCC's Billing and Payment terms and conditions, these terms and conditions shall prevail.

- WILEY expressly reserves all rights not specifically granted in the combination of (i) the license details provided by you and accepted in the course of this licensing transaction, (ii) these terms and conditions and (iii) CCC's Billing and Payment terms and conditions.

- This Agreement will be void if the Type of Use, Format, Circulation, or Requestor Type was misrepresented during the licensing process.

- This Agreement shall be governed by and construed in accordance with the laws of the State of New York, USA, without regards to such state's conflict of law rules. Any legal action, suit or proceeding arising out of or relating to these Terms and Conditions or the breach thereof shall be instituted in a court of competent jurisdiction in New York County in the State of New York in the United States of America and each party hereby consents and submits to the personal jurisdiction of such court, waives any objection to venue in such court and consents to service of process by registered or certified mail, return receipt requested, at the last known address of such party.

WILEY OPEN ACCESS TERMS AND CONDITIONS

Wiley Publishes Open Access Articles in fully Open Access Journals and in Subscription journals offering Online Open. Although most of the fully Open Access journals publish open access articles under the terms of the Creative Commons Attribution (CC BY) License only, the subscription journals and a few of the Open Access Journals offer a choice of Creative Commons Licenses. The license type is clearly identified on the article.

The Creative Commons Attribution License

The Creative Commons Attribution License (CC-BY) allows users to copy, distribute and transmit an article, adapt the article and make commercial use of the article. The CC-BY license permits commercial and non-

Creative Commons Attribution Non-Commercial License

The Creative Commons Attribution Non-Commercial (CC-BY-NC)License permits use, distribution and reproduction in any medium, provided the original work is properly cited and is not used for commercial purposes.(see below)

Creative Commons Attribution-Non-Commercial-NoDerivs License

The Creative Commons Attribution Non-Commercial-NoDerivs License (CC-BY-NC-ND) permits use, distribution and reproduction in any medium, provided the original work is properly cited, is not used for commercial purposes and no modifications or adaptations are made. (see below)

Use by commercial "for-profit" organizations

Use of Wiley Open Access articles for commercial, promotional, or marketing purposes requires further explicit permission from Wiley and will be subject to a fee.

Further details can be found on Wiley Online Library
http://olabout.wiley.com/WileyCDA/Section/id-410895.html

Other Terms and Conditions:

v1.10 Last updated September 2015

Questions? customercare@copyright.com or +1-855-239-3415 (toll free in the US) or +1-978-646-2777.

AIP PUBLISHING LICENSE
TERMS AND CONDITIONS

Aug 12, 2022

This Agreement between Istituto Italiano di Tecnologia ("You") and AIP Publishing ("AIP Publishing") consists of your license details and the terms and conditions provided by AIP Publishing and Copyright Clearance Center.

License Number	5366491345883
License date	Aug 12, 2022
Licensed Content Publisher	AIP Publishing
Licensed Content Publication	Journal of Renewable and Sustainable Energy
Licensed Content Title	Wearable electronics self-powered by using human body heat: The state of the art and the perspective
Licensed Content Author	Vladimir Leonov, Ruud J. M. Vullers
Licensed Content Date	Nov 1, 2009
Licensed Content Volume	1
Licensed Content Issue	6
Type of Use	Thesis/Dissertation
Requestor type	Student

Format	Print

Portion	Figure/Table

Number of figures/tables	1

Will you be translating?	No

Title	PhD candidate

Institution name	Istituto Italiano di Tecnologia

Expected presentation date	Oct 2022

Portions	figure 1

Requestor Location	Istituto Italiano di Tecnologia Via Livorno 60 Torino, Torino 10144 Italy Attn: Istituto Italiano di Tecnologia

Total	0.00 USD

Terms and Conditions

AIP Publishing -- Terms and Conditions: Permissions Uses

AIP Publishing hereby grants to you the non-exclusive right and license to use and/or distribute the Material according to the use specified in your order, on a one-time basis, for the specified term, with a maximum distribution equal to the number that you have ordered. Any links or other content accompanying the Material are not the subject of this license.

1. You agree to include the following copyright and permission notice with the reproduction of the Material:"Reprinted from [FULL CITATION], with the permission of AIP Publishing." For an article, the credit line and permission notice must be

printed on the first page of the article or book chapter. For photographs, covers, or tables, the notice may appear with the Material, in a footnote, or in the reference list.

2. If you have licensed reuse of a figure, photograph, cover, or table, it is your responsibility to ensure that the material is original to AIP Publishing and does not contain the copyright of another entity, and that the copyright notice of the figure, photograph, cover, or table does not indicate that it was reprinted by AIP Publishing, with permission, from another source. Under no circumstances does AIP Publishing purport or intend to grant permission to reuse material to which it does not hold appropriate rights.
   You may not alter or modify the Material in any manner. You may translate the Material into another language only if you have licensed translation rights. You may not use the Material for promotional purposes.

3. The foregoing license shall not take effect unless and until AIP Publishing or its agent, Copyright Clearance Center, receives the Payment in accordance with Copyright Clearance Center Billing and Payment Terms and Conditions, which are incorporated herein by reference.

4. AIP Publishing or Copyright Clearance Center may, within two business days of granting this license, revoke the license for any reason whatsoever, with a full refund payable to you. Should you violate the terms of this license at any time, AIP Publishing, or Copyright Clearance Center may revoke the license with no refund to you. Notice of such revocation will be made using the contact information provided by you. Failure to receive such notice will not nullify the revocation.

5. AIP Publishing makes no representations or warranties with respect to the Material. You agree to indemnify and hold harmless AIP Publishing, and their officers, directors, employees or agents from and against any and all claims arising out of your use of the Material other than as specifically authorized herein.

6. The permission granted herein is personal to you and is not transferable or assignable without the prior written permission of AIP Publishing. This license may not be amended except in a writing signed by the party to be charged.

7. If purchase orders, acknowledgments or check endorsements are issued on any forms containing terms and conditions which are inconsistent with these provisions, such inconsistent terms and conditions shall be of no force and effect. This document, including the CCC Billing and Payment Terms and Conditions, shall be the entire agreement between the parties relating to the subject matter hereof.

This Agreement shall be governed by and construed in accordance with the laws of the State of New York. Both parties hereby submit to the jurisdiction of the courts of New York County for purposes of resolving any disputes that may arise hereunder.

V1.2

Questions? customercare@copyright.com or +1-855-239-3415 (toll free in the US) or +1-978-646-2777.

SPRINGER NATURE LICENSE
TERMS AND CONDITIONS

Aug 12, 2022

This Agreement between Istituto Italiano di Tecnologia ("You") and Springer Nature ("Springer Nature") consists of your license details and the terms and conditions provided by Springer Nature and Copyright Clearance Center.

License Number	5366520617120
License date	Aug 12, 2022
Licensed Content Publisher	Springer Nature
Licensed Content Publication	Journal of the Korean Physical Society
Licensed Content Title	Water-Through Triboelectric Nanogenerator Based on Ti-Mesh for Harvesting Liquid Flow
Licensed Content Author	Hong-Yeol Park et al
Licensed Content Date	Mar 13, 2018
Type of Use	Thesis/Dissertation
Requestor type	non-commercial (non-profit)
Format	print
Portion	figures/tables/illustrations
Number of figures/tables/illustrations	5

Will you be translating?	no
Circulation/distribution	1 - 29
Author of this Springer Nature content	no
Title	PhD candidate
Institution name	Istituto Italiano di Tecnologia
Expected presentation date	Oct 2022
Portions	figure 1
Requestor Location	Istituto Italiano di Tecnologia Via Livorno 60 Torino, Torino 10144 Italy Attn: Istituto Italiano di Tecnologia
Total	0.00 USD

Terms and Conditions

Springer Nature Customer Service Centre GmbH
Terms and Conditions

This agreement sets out the terms and conditions of the licence (the **Licence**) between you and **Springer Nature Customer Service Centre GmbH** (the **Licensor**). By clicking 'accept' and completing the transaction for the material (**Licensed Material**), you also confirm your acceptance of these terms and conditions.

1. Grant of License

1. 1. The Licensor grants you a personal, non-exclusive, non-transferable, world-wide licence to reproduce the Licensed Material for the purpose specified in your order only. Licences are granted for the specific use requested in the order and for no other use, subject to the conditions below.

1. 2. The Licensor warrants that it has, to the best of its knowledge, the rights to license reuse of the Licensed Material. However, you should ensure that the material you are requesting is original to the Licensor and does not carry the copyright of another entity (as credited in the published version).

1. 3. If the credit line on any part of the material you have requested indicates that it was reprinted or adapted with permission from another source, then you should also seek permission from that source to reuse the material.

2. Scope of Licence

2. 1. You may only use the Licensed Content in the manner and to the extent permitted by these Ts&Cs and any applicable laws.

2. 2. A separate licence may be required for any additional use of the Licensed Material, e.g. where a licence has been purchased for print only use, separate permission must be obtained for electronic re-use. Similarly, a licence is only valid in the language selected and does not apply for editions in other languages unless additional translation rights have been granted separately in the licence. Any content owned by third parties are expressly excluded from the licence.

2. 3. Similarly, rights for additional components such as custom editions and derivatives require additional permission and may be subject to an additional fee. Please apply to Journalpermissions@springernature.com/bookpermissions@springernature.com for these rights.

2. 4. Where permission has been granted **free of charge** for material in print, permission may also be granted for any electronic version of that work, provided that the material is incidental to your work as a whole and that the electronic version is essentially equivalent to, or substitutes for, the print version.

2. 5. An alternative scope of licence may apply to signatories of the [STM Permissions Guidelines](#), as amended from time to time.

3. Duration of Licence

3. 1. A licence for is valid from the date of purchase ('Licence Date') at the end of the relevant period in the below table:

Scope of Licence	Duration of Licence
Post on a website	12 months
Presentations	12 months
Books and journals	Lifetime of the edition in the language purchased

4. Acknowledgement

4. 1. The Licensor's permission must be acknowledged next to the Licenced Material in print. In electronic form, this acknowledgement must be visible at the same time as the figures/tables/illustrations or abstract, and must be hyperlinked to the journal/book's

homepage. Our required acknowledgement format is in the Appendix below.

5. Restrictions on use

5. 1. Use of the Licensed Material may be permitted for incidental promotional use and minor editing privileges e.g. minor adaptations of single figures, changes of format, colour and/or style where the adaptation is credited as set out in Appendix 1 below. Any other changes including but not limited to, cropping, adapting, omitting material that affect the meaning, intention or moral rights of the author are strictly prohibited.

5. 2. You must not use any Licensed Material as part of any design or trademark.

5. 3. Licensed Material may be used in Open Access Publications (OAP) before publication by Springer Nature, but any Licensed Material must be removed from OAP sites prior to final publication.

6. Ownership of Rights

6. 1. Licensed Material remains the property of either Licensor or the relevant third party and any rights not explicitly granted herein are expressly reserved.

7. Warranty

IN NO EVENT SHALL LICENSOR BE LIABLE TO YOU OR ANY OTHER PARTY OR ANY OTHER PERSON OR FOR ANY SPECIAL, CONSEQUENTIAL, INCIDENTAL OR INDIRECT DAMAGES, HOWEVER CAUSED, ARISING OUT OF OR IN CONNECTION WITH THE DOWNLOADING, VIEWING OR USE OF THE MATERIALS REGARDLESS OF THE FORM OF ACTION, WHETHER FOR BREACH OF CONTRACT, BREACH OF WARRANTY, TORT, NEGLIGENCE, INFRINGEMENT OR OTHERWISE (INCLUDING, WITHOUT LIMITATION, DAMAGES BASED ON LOSS OF PROFITS, DATA, FILES, USE, BUSINESS OPPORTUNITY OR CLAIMS OF THIRD PARTIES), AND
WHETHER OR NOT THE PARTY HAS BEEN ADVISED OF THE POSSIBILITY OF SUCH DAMAGES. THIS LIMITATION SHALL APPLY NOTWITHSTANDING ANY FAILURE OF ESSENTIAL PURPOSE OF ANY LIMITED REMEDY PROVIDED HEREIN.

8. Limitations

8. 1. _**BOOKS ONLY:**_ Where **'reuse in a dissertation/thesis'** has been selected the following terms apply: Print rights of the final author's accepted manuscript (for clarity, NOT the published version) for up to 100 copies, electronic rights for use only on a personal website or institutional repository as defined by the Sherpa guideline (www.sherpa.ac.uk/romeo/).

8. 2. For content reuse requests that qualify for permission under the STM Permissions Guidelines, which may be updated from time to time, the STM Permissions Guidelines

supersede the terms and conditions contained in this licence.

9. Termination and Cancellation

9. 1. Licences will expire after the period shown in Clause 3 (above).

9. 2. Licensee reserves the right to terminate the Licence in the event that payment is not received in full or if there has been a breach of this agreement by you.

<u>Appendix 1 — Acknowledgements:</u>

For Journal Content:
Reprinted by permission from [**the Licensor**]: [**Journal Publisher** (e.g. Nature/Springer/Palgrave)] [**JOURNAL NAME**] [**REFERENCE CITATION** (Article name, Author(s) Name), [**COPYRIGHT**] (year of publication)

For **Advance Online Publication papers:**
Reprinted by permission from [**the Licensor**]: [**Journal Publisher** (e.g. Nature/Springer/Palgrave)] [**JOURNAL NAME**] [**REFERENCE CITATION** (Article name, Author(s) Name), [**COPYRIGHT**] (year of publication), advance online publication, day month year (doi: 10.1038/sj.[JOURNAL ACRONYM].)

For Adaptations/Translations:
Adapted/Translated by permission from [**the Licensor**]: [**Journal Publisher** (e.g. Nature/Springer/Palgrave)] [**JOURNAL NAME**] [**REFERENCE CITATION** (Article name, Author(s) Name), [**COPYRIGHT**] (year of publication)

<u>Note: For any republication from the British Journal of Cancer, the following credit line style applies:</u>

Reprinted/adapted/translated by permission from [**the Licensor**]: on behalf of Cancer Research UK: : [**Journal Publisher** (e.g. Nature/Springer/Palgrave)] [**JOURNAL NAME**] [**REFERENCE CITATION** (Article name, Author(s) Name), [**COPYRIGHT**] (year of publication)

For **Advance Online Publication** papers:
Reprinted by permission from The [**the Licensor**]: on behalf of Cancer Research UK: [**Journal Publisher** (e.g. Nature/Springer/Palgrave)] [**JOURNAL NAME**] [**REFERENCE CITATION** (Article name, Author(s) Name), [**COPYRIGHT**] (year of publication), advance online publication, day month year (doi: 10.1038/sj.[JOURNAL ACRONYM])

For Book content:
Reprinted/adapted by permission from [**the Licensor**]: [**Book Publisher** (e.g. Palgrave Macmillan, Springer etc) [**Book Title**] by [**Book author**(s)] [**COPYRIGHT**] (year of publication)

Other Conditions:

Version 1.3

Questions? customercare@copyright.com or +1-855-239-3415 (toll free in the US) or +1-978-646-2777.

JOHN WILEY AND SONS LICENSE
TERMS AND CONDITIONS

Aug 12, 2022

This Agreement between Istituto Italiano di Tecnologia ("You") and John Wiley and Sons ("John Wiley and Sons") consists of your license details and the terms and conditions provided by John Wiley and Sons and Copyright Clearance Center.

License Number	5366521243220
License date	Aug 12, 2022
Licensed Content Publisher	John Wiley and Sons
Licensed Content Publication	Advanced Materials Technologies
Licensed Content Title	On the Pyroelectric and Triboelectric Phenomena in Ferrofluids
Licensed Content Author	Erik Garofalo, Matteo Bevione, Luca Cecchini, et al
Licensed Content Date	May 13, 2022
Licensed Content Volume	0
Licensed Content Issue	0
Licensed Content Pages	7
Type of use	Dissertation/Thesis
Requestor type	Author of this Wiley article

Format	Print
Portion	Figure/table
Number of figures/tables	10
Will you be translating?	No
Title	PhD candidate
Institution name	Istituto Italiano di Tecnologia
Expected presentation date	Oct 2022
Portions	figure 1-4, 6
Requestor Location	Istituto Italiano di Tecnologia Via Livorno 60 Torino, Torino 10144 Italy Attn: Istituto Italiano di Tecnologia
Publisher Tax ID	EU826007151
Total	0.00 USD

Terms and Conditions

TERMS AND CONDITIONS

Terms and Conditions

- The materials you have requested permission to reproduce or reuse (the "Wiley Materials") are protected by copyright.

- You are hereby granted a personal, non-exclusive, non-sub licensable (on a stand-alone basis), non-transferable, worldwide, limited license <u>to reproduce the Wiley Materials for the purpose specified in the licensing process.</u> This license, **and any CONTENT (PDF or image file) purchased as part of your order,** is for a one-time use only and limited to any maximum distribution number specified in the license. The first instance of republication or reuse granted by this license must be completed within two years of the date of the grant of this license (although copies prepared before the end date may be distributed thereafter). The Wiley Materials shall not be used in any other manner or for any other purpose, beyond what is granted in the license. Permission is granted subject to an appropriate acknowledgement given to the author, title of the material/book/journal and the publisher. You shall also duplicate the copyright notice that appears in the Wiley publication in your use of the Wiley Material. Permission is also granted on the understanding that nowhere in the text is a previously published source acknowledged for all or part of this Wiley Material. Any third party content is expressly excluded from this permission.

- With respect to the Wiley Materials, all rights are reserved. Except as expressly granted by the terms of the license, no part of the Wiley Materials may be copied, modified, adapted (except for minor reformatting required by the new Publication), translated, reproduced, transferred or distributed, in any form or by any means, and no derivative works may be made based on the Wiley Materials without the prior permission of the respective copyright owner.**For STM Signatory Publishers clearing permission under the terms of the [STM Permissions Guidelines](#) only, the terms of the license are extended to include subsequent editions and for editions in other languages, provided such editions are for the work as a whole in situ and does not involve the separate exploitation of the permitted figures or extracts,** You may not alter, remove or suppress in any manner any copyright, trademark or other notices displayed by the Wiley Materials. You may not license, rent, sell, loan, lease, pledge, offer as security, transfer or assign the Wiley Materials on a stand-alone basis, or any of the rights granted to you hereunder to any other person.

- The Wiley Materials and all of the intellectual property rights therein shall at all times remain the exclusive property of John Wiley & Sons Inc, the Wiley Companies, or their respective licensors, and your interest therein is only that of having possession of and the right to reproduce the Wiley Materials pursuant to Section 2 herein during the continuance of this Agreement. You agree that you own no right, title or interest in or to the Wiley Materials or any of the intellectual property rights therein. You shall have no rights hereunder other than the license as provided for above in Section 2. No right, license or interest to any trademark, trade name, service mark or other branding ("Marks") of WILEY or its licensors is granted hereunder, and you agree that you shall not assert any such right, license or interest with respect thereto

- NEITHER WILEY NOR ITS LICENSORS MAKES ANY WARRANTY OR REPRESENTATION OF ANY KIND TO YOU OR ANY THIRD PARTY, EXPRESS, IMPLIED OR STATUTORY, WITH RESPECT TO THE MATERIALS OR THE ACCURACY OF ANY INFORMATION CONTAINED IN THE MATERIALS, INCLUDING, WITHOUT LIMITATION, ANY IMPLIED WARRANTY OF MERCHANTABILITY, ACCURACY, SATISFACTORY

QUALITY, FITNESS FOR A PARTICULAR PURPOSE, USABILITY, INTEGRATION OR NON-INFRINGEMENT AND ALL SUCH WARRANTIES ARE HEREBY EXCLUDED BY WILEY AND ITS LICENSORS AND WAIVED BY YOU.

- WILEY shall have the right to terminate this Agreement immediately upon breach of this Agreement by you.

- You shall indemnify, defend and hold harmless WILEY, its Licensors and their respective directors, officers, agents and employees, from and against any actual or threatened claims, demands, causes of action or proceedings arising from any breach of this Agreement by you.

- IN NO EVENT SHALL WILEY OR ITS LICENSORS BE LIABLE TO YOU OR ANY OTHER PARTY OR ANY OTHER PERSON OR ENTITY FOR ANY SPECIAL, CONSEQUENTIAL, INCIDENTAL, INDIRECT, EXEMPLARY OR PUNITIVE DAMAGES, HOWEVER CAUSED, ARISING OUT OF OR IN CONNECTION WITH THE DOWNLOADING, PROVISIONING, VIEWING OR USE OF THE MATERIALS REGARDLESS OF THE FORM OF ACTION, WHETHER FOR BREACH OF CONTRACT, BREACH OF WARRANTY, TORT, NEGLIGENCE, INFRINGEMENT OR OTHERWISE (INCLUDING, WITHOUT LIMITATION, DAMAGES BASED ON LOSS OF PROFITS, DATA, FILES, USE, BUSINESS OPPORTUNITY OR CLAIMS OF THIRD PARTIES), AND WHETHER OR NOT THE PARTY HAS BEEN ADVISED OF THE POSSIBILITY OF SUCH DAMAGES. THIS LIMITATION SHALL APPLY NOTWITHSTANDING ANY FAILURE OF ESSENTIAL PURPOSE OF ANY LIMITED REMEDY PROVIDED HEREIN.

- Should any provision of this Agreement be held by a court of competent jurisdiction to be illegal, invalid, or unenforceable, that provision shall be deemed amended to achieve as nearly as possible the same economic effect as the original provision, and the legality, validity and enforceability of the remaining provisions of this Agreement shall not be affected or impaired thereby.

- The failure of either party to enforce any term or condition of this Agreement shall not constitute a waiver of either party's right to enforce each and every term and condition of this Agreement. No breach under this agreement shall be deemed waived or excused by either party unless such waiver or consent is in writing signed by the party granting such waiver or consent. The waiver by or consent of a party to a breach of any provision of this Agreement shall not operate or be construed as a waiver of or consent to any other or subsequent breach by such other party.

- This Agreement may not be assigned (including by operation of law or otherwise) by you without WILEY's prior written consent.

- Any fee required for this permission shall be non-refundable after thirty (30) days from receipt by the CCC.

- These terms and conditions together with CCC's Billing and Payment terms and conditions (which are incorporated herein) form the entire agreement between you and WILEY concerning this licensing transaction and (in the absence of fraud) supersedes all prior agreements and representations of the parties, oral or written. This Agreement may not be amended except in writing signed by both parties. This Agreement shall be binding upon and inure to the benefit of the parties' successors, legal representatives,

and authorized assigns.

- In the event of any conflict between your obligations established by these terms and conditions and those established by CCC's Billing and Payment terms and conditions, these terms and conditions shall prevail.

- WILEY expressly reserves all rights not specifically granted in the combination of (i) the license details provided by you and accepted in the course of this licensing transaction, (ii) these terms and conditions and (iii) CCC's Billing and Payment terms and conditions.

- This Agreement will be void if the Type of Use, Format, Circulation, or Requestor Type was misrepresented during the licensing process.

- This Agreement shall be governed by and construed in accordance with the laws of the State of New York, USA, without regards to such state's conflict of law rules. Any legal action, suit or proceeding arising out of or relating to these Terms and Conditions or the breach thereof shall be instituted in a court of competent jurisdiction in New York County in the State of New York in the United States of America and each party hereby consents and submits to the personal jurisdiction of such court, waives any objection to venue in such court and consents to service of process by registered or certified mail, return receipt requested, at the last known address of such party.

WILEY OPEN ACCESS TERMS AND CONDITIONS

Wiley Publishes Open Access Articles in fully Open Access Journals and in Subscription journals offering Online Open. Although most of the fully Open Access journals publish open access articles under the terms of the Creative Commons Attribution (CC BY) License only, the subscription journals and a few of the Open Access Journals offer a choice of Creative Commons Licenses. The license type is clearly identified on the article.

The Creative Commons Attribution License

The [Creative Commons Attribution License (CC-BY)](#) allows users to copy, distribute and transmit an article, adapt the article and make commercial use of the article. The CC-BY license permits commercial and non-

Creative Commons Attribution Non-Commercial License

The [Creative Commons Attribution Non-Commercial (CC-BY-NC)License](#) permits use, distribution and reproduction in any medium, provided the original work is properly cited and is not used for commercial purposes.(see below)

Creative Commons Attribution-Non-Commercial-NoDerivs License

The [Creative Commons Attribution Non-Commercial-NoDerivs License](#) (CC-BY-NC-ND) permits use, distribution and reproduction in any medium, provided the original work is properly cited, is not used for commercial purposes and no modifications or adaptations are made. (see below)

Use by commercial "for-profit" organizations

Use of Wiley Open Access articles for commercial, promotional, or marketing purposes requires further explicit permission from Wiley and will be subject to a fee.

Further details can be found on Wiley Online Library
http://olabout.wiley.com/WileyCDA/Section/id-410895.html

Other Terms and Conditions:

v1.10 Last updated September 2015

Questions? customercare@copyright.com or +1-855-239-3415 (toll free in the US) or +1-978-646-2777.

Home | Help ⌄ | Live Chat | Sign in | Create Account
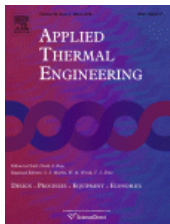
Industrial waste heat: Estimation of the technically available resource in the EU per industrial sector, temperature level and country

Author:
Michael Papapetrou,George Kosmadakis,Andrea Cipollina,Umberto La Commare,Giorgio Micale

Publication: Applied Thermal Engineering

Publisher: Elsevier

Date: 25 June 2018

© 2018 The Authors. Published by Elsevier Ltd.

Creative Commons Attribution-NonCommercial-No Derivatives License (CC BY NC ND)

BACK   CLOSE WINDOW

CCC

RightsLink

SPRINGER NATURE

A thermodynamic feasibility study of an Organic Rankine Cycle (ORC) for heavy-duty diesel engine waste heat recovery in off-highway applications

Author: Simone Lion et al

Publication: International Journal of Energy and Environmental Engineering

Publisher: Springer Nature

Date: Apr 24, 2017

Copyright © 2017, The Author(s)

CCC

RightsLink

Home | Help ⌄ | Live Chat | Erik Garofalo ⌄

Waste heat to power conversion by means of thermomagnetic hydrodynamic energy harvester
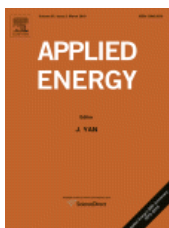
Author:

Alessandro Chiolerio,Erik Garofalo,Fabio Mattiussi,Marco Crepaldi,Giuseppe Fortunato,Michele Iovieno

Publication: Applied Energy
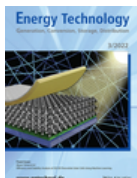
Publisher: Elsevier

Date: 1 November 2020

Journal Author Rights

BACK   CLOSE WINDOW

CCC
RightsLink

?
Help ∨

Live Chat

Multiphysics-Enabled Liquid State Thermal Harvesting: Synergistic Effects between Pyroelectricity and Triboelectrification

Author: Alessandro Chiolerio, Erik Garofalo, Matteo Bevione, et al

Publication: ENERGY TECHNOLOGY (ELECTRONIC)

Publisher: John Wiley and Sons

Date: Sep 8, 2021

© 2021 The Authors. Energy Technology published by Wiley-VCH GmbH

Wiley offers a professional reprint service for high quality reproduction of articles from over 1400 scientific and medical journals. Wiley's reprint service offers:

• Peer reviewed research or reviews
• Tailored collections of articles
• A professional high quality finish
• Glossy journal style color covers
• Company or brand customisation
• Language translations
• Prompt turnaround times and delivery directly to your office, warehouse or congress.

Please contact our Reprints department for a quotation. Email corporatesaleseurope@wiley.com or corporatesalesusa@wiley.com or corporatesalesDE@wiley.com.
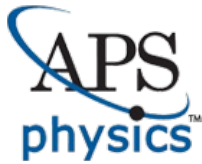
American Physical Society
Reuse and Permissions License

12-Aug-2022

This license agreement between the American Physical Society ("APS") and Erik Garofalo ("You") consists of your license details and the terms and conditions provided by the American Physical Society and SciPris.

Licensed Content Information

License Number:	**RNP/22/AUG/056667**
License date:	12-Aug-2022
DOI:	10.1103/PhysRevE.86.016301
Title:	Thermomagnetic convective flows in a vertical layer of ferrocolloid: Perturbation energy analysis and experimental study
Author:	Sergey A. Suslov et al.
Publication:	Physical Review E
Publisher:	American Physical Society
Cost:	USD $ 0.00

Request Details

Does your reuse require significant modifications: No

Specify intended distribution locations:	Worldwide
Reuse Category:	Reuse in a thesis/dissertation
Requestor Type:	Student
Items for Reuse:	Figures/Tables
Number of Figure/Tables:	1
Figure/Tables Details:	figure 1
Format for Reuse:	Print
Total number of print copies:	Up to 1000

Information about New Publication:

University/Publisher:	Istituto Italiano di Tecnologia
Title of dissertation/thesis:	Energy harvesting of low-grade waste heat with colloid-based technology
Author(s):	Erik Garofalo
Expected completion date:	Oct. 2022

License Requestor Information

Name:	Erik Garofalo
Affiliation:	Individual
Email Id:	g.erik1992@gmail.com
Country:	Italy

American Physical Society
Reuse and Permissions License

TERMS AND CONDITIONS

The American Physical Society (APS) is pleased to grant the Requestor of this license a non-exclusive, non-transferable permission, limited to Print format, provided all criteria outlined below are followed.

1. You must also obtain permission from at least one of the lead authors for each separate work, if you haven't done so already. The author's name and affiliation can be found on the first page of the published Article.

2. For electronic format permissions, Requestor agrees to provide a hyperlink from the reprinted APS material using the source material's DOI on the web page where the work appears. The hyperlink should use the standard DOI resolution URL, http://dx.doi.org/{DOI}. The hyperlink may be embedded in the copyright credit line.

3. For print format permissions, Requestor agrees to print the required copyright credit line on the first page where the material appears: "Reprinted (abstract/excerpt/figure) with permission from [(FULL REFERENCE CITATION) as follows: Author's Names, APS Journal Title, Volume Number, Page Number and Year of Publication.] Copyright (YEAR) by the American Physical Society."

4. Permission granted in this license is for a one-time use and does not include permission for any future editions, updates, databases, formats or other matters. Permission must be sought for any additional use.

5. Use of the material does not and must not imply any endorsement by APS.

6. APS does not imply, purport or intend to grant permission to reuse materials to which it does not hold copyright. It is the requestor's sole responsibility to ensure the licensed material is original to APS and does not contain the copyright of another entity, and that the copyright notice of the figure, photograph, cover or table does not indicate it was reprinted by APS with permission from another source.

7. The permission granted herein is personal to the Requestor for the use specified and is not transferable or assignable without express written permission of APS. This license may not be amended except in writing by APS.

8. You may not alter, edit or modify the material in any manner.

9. You may translate the materials only when translation rights have been granted.

10. APS is not responsible for any errors or omissions due to translation.

11. You may not use the material for promotional, sales, advertising or marketing purposes.

12. The foregoing license shall not take effect unless and until APS or its agent, Aptara, receives payment in full in accordance with Aptara Billing and Payment Terms and Conditions, which are incorporated herein by reference.

13. Should the terms of this license be violated at any time, APS or Aptara may revoke the license with no refund to you and seek relief to the fullest extent of the laws of the USA. Official written notice will be made using the contact information provided with the permission request. Failure to receive such notice will not nullify revocation of the permission.

14. APS reserves all rights not specifically granted herein.

15. This document, including the Aptara Billing and Payment Terms and Conditions, shall be the entire agreement between the parties relating to the subject matter hereof.